



Development of Methods to Evaluate Dynamic Fracture Toughness  
of Metallic Materials at Very High Loading Rates Under Limited  
Plastic Deformation Conditions

CHIAMAKA EMILIA IKENNA-UZODIKE, BEng (Hons), MSc

SCHOOL OF ENGINEERING  
Engineering Building, Gillow Avenue  
LANCASTER UNIVERSITY

Doctor of Philosophy  
Academic Year: 2019 - 2024

Academic Principal Supervisor: Prof. Andrew Kennedy  
TWI Supervisor: Dr Yin Jin Janin  
Academic co-Supervisor: Dr Wei Wen  
February 2024

## **ABSTRACT**

The measurement of mechanical properties of metallic materials at high strain rates has been challenging, notwithstanding the application of steel for intermediate and dynamic loading conditions. This is due to a lack of sophisticated measuring tools which will require a very high-speed camera to capture the stages of deformation, with little availability of recent machines capable of testing at high strain rates when compared with testing at quasi-static strain rates.

The quasi-static testing procedure has been well-established with different international standards. Still, the dynamic testing procedures are very limited as they are being modified from the quasi-static testing. It is quite challenging to characterize the dynamic fracture toughness owing to limitations in the existing standards such as BS 7448-3:2005. With the effect of inertia during the experiment of high strain rates, many oscillations are generated which masks the true path of the load-displacement curve.

The concern spans from significant oscillations encountered with the stress-strain curve, making it difficult to obtain the dynamic mechanical properties of the material. Hence, it is difficult to include dynamic properties in the design of structures, and this results in catastrophic failure whenever the material fails under dynamic loading, and thus safety is not satisfied. As dynamic deformation occurs with limited plastic deformation, the material fails without warning like showing significant necking before failure.

In this research, X65 steel material was investigated and characterized at quasi-static and dynamic conditions using several techniques like instrumented Charpy test, tensile testing (flat and round specimen), fracture toughness test, and drop weight test, which led to the proposed methods of determining high strain rates material properties. An EDM notched and fatigue pre-cracked Charpy-sized specimens were utilised in this investigation. Quasi-static fracture toughness testing was used to characterize the material properties at low strain rates, which were applied in the machine learning algorithm to predict the material's fracture toughness.

The finite element analysis was utilised to support the investigation of the stress and strain distribution in a single-edge notched bend (SENB) specimen at varying loading rates to determine the effect of loading rates and crack driving force for the dynamic fracture toughness measurement. ABAQUS was employed in performing the FEM simulations. The ductile and damage model parameters were determined from experimental data using the Johnson-Cook model.

Analytical solutions were also implied through the application of irreversible thermodynamics of dislocation evolution to predict the stress-strain curve at an elevated strain rate. Damage constants for FEM calculations utilising the Johnson-Cook model and the undelaying plasticity theory to capture the impact of the strain rate were both utilised. The thermal diffusivity method was applied to characterize the material behaviour at high loading rates, as it is being affected by the change in temperature to undergo an adiabatic process at dynamic loading. The change in temperature at elevated loading rates was taken into consideration in dislocation density theory for the application of body-centered cubic materials.

Due to the difficulty in determining data from the VHS Instron machine on dynamic fracture toughness, the low-blow Charpy test was implemented to determine the varying strain rate properties to correlate with the simulated results. Results from the experimental results show that material strength is affected by rates of loading and increases with loading rates, whereas fracture toughness decreases with the loading rates.

Finally, the machine learning approach was considered to predict the stress-strain curve and fracture toughness data. The training sets were derived from experimental data with certain features including the strain rate to train the model. The random forest and multilayer perceptron regressor algorithm were utilised in this work for its application with small data sets and to reduce overfitting. The results showed that it is promising to predict material properties from the machine learning algorithm to reduce the cost of material testing. However, this has a limitation from the available number of datasets, which need to be derived from experiments to increase the accuracy of the prediction of dynamic fracture toughness.

## **ACKNOWLEDGEMENTS**

To my dear husband, Ikenna Uzodike, and children, Sochima and Chimamaka, I am very grateful for all your endless support and unconditional love, without which it would have been difficult to complete this study. My supervisors, Dr. Yin Jin Janin, who gave all her support and motherly advice, Professor Andrew Kennedy, and Dr. Wei Wen, thank you so much for guiding me through this long journey with your expertise and enhanced knowledge. Dear Professor Pedro EJ Rivera-Diaz-del-Castillo, Dr. Marius Gintalas, and Dr. Artūras Tadžijėvas, your experienced contributions are deeply appreciated. To the TWI technical team, Alex, and Mathew, I am grateful for your patience with all the unexpected technical discussions and for making the experiments worth the time. To Professor Darren Williams, Director of Joining 4.0 Innovation Centre, and my PhD mentor, Professor James Taylor, thank you for all your support when I needed them most.

To all those whose names were not mentioned, the TWI family, Lancaster University team, my parent, sisters, and brothers, all your time, help, and support to make this piece of work complete are forever appreciated. And finally, a very special thank you to God Almighty for keeping me alive and healthy to the end of this study.

This publication was made possible by the sponsorship and support of Lloyd's Register Foundation (LRF). The work was enabled through, and undertaken at, the National Structural Integrity Centre (NSIRC), a postgraduate engineering facility for industry-led research into structural integrity established and managed by TWI through a network of both national and international Universities.

Lloyd's Register Foundation helps to protect life and property by supporting engineering-related education, public engagement, and the application or research. [www.lrfoundation.org.uk](http://www.lrfoundation.org.uk)



# TABLE OF CONTENTS

ABSTRACT .....	i
ACKNOWLEDGEMENTS.....	iii
LIST OF FIGURES.....	viii
LIST OF TABLES .....	xv
LIST OF EQUATIONS.....	xvii
LIST OF ABBREVIATIONS .....	xx
1 INTRODUCTION.....	21
1.1 Background Information.....	21
1.2 Aims and Objectives .....	24
1.3 Thesis Structure.....	25
2 LITERATURE REVIEW.....	27
2.1 Introduction of the material .....	27
2.2 Fractures in metallic structures .....	29
2.3 Strain rate effect on the properties of a material .....	30
2.3.1 Strain rate effects on tensile properties and dislocation density .....	30
2.3.2 Effects of strain rates on the fracture toughness .....	33
2.4 History of dynamic testing.....	35
2.4.1 Testing methods for dynamic strain rates ( $10^1 - 10^7 \text{ s}^{-1}$ ).....	37
2.5 Testing procedures to determine dynamic fracture toughness. ....	40
2.5.1 BS 7448 Part 3 procedure.....	41
2.5.2 ASTM E1921 procedure.....	42
2.5.3 ASTM E1820 procedure.....	43
2.6 Analytical solutions for stress intensity factor under impact load .....	44
2.6.1 Theory of stress intensity factor, $K$ under quasi-static conditions....	44
2.6.2 Dynamic Fracture Initiation Toughness $K_{Id}$ .....	48
2.7 Yield strength response under impact load.....	50
2.8 Constitutive laws to predict dynamic material behaviour.....	51
2.8.1 Plastic deformation in ductile metallic materials .....	52
2.8.2 Dislocation evolution theory .....	53
2.8.3 Dislocation motion in metallic materials.....	56
2.8.4 Theory of the Johnson-Cook Model .....	58
2.8.5 Johnson-Cook failure model.....	60
2.8.6 Theory of thermal diffusivity and temperature rise during high strain rate testing. ....	61
2.9 Dislocation evolution theory in BCC metals .....	62
2.10 FEM application of JC parameters for Dynamic/Explicit model.....	65
2.11 Theory of machine learning for stress-strain curve prediction and fracture toughness prediction.....	66
2.11.1 Theory of MLPRegressor .....	67
2.11.2 Theory of Random Forest Regressor .....	69

2.12 Knowledge gap .....	72
<b>3 EXPERIMENTAL METHODS .....</b>	<b>75</b>
3.1 Overview .....	75
3.2 Introduction .....	76
3.2.1 Test specifications.....	77
3.3 Tensile testing.....	80
3.3.1 Quasi-static tensile tests .....	80
3.3.2 High strain rate tensile testing .....	83
3.4 Fracture Toughness Testing .....	87
3.4.1 Test specimen preparation.....	88
3.4.2 Fatigue Pre-cracking .....	89
3.4.3 Testing procedure .....	92
3.5 Qualitative Toughness Measurement Tests.....	93
3.5.1 Impact drop weight test .....	93
3.5.2 Instrumented Charpy testing .....	95
3.6 Dynamic Fracture Toughness Measurement Test .....	98
3.6.1 Testing Procedure of high velocity test with an impactor.....	99
3.6.2 Dynamic Fracture toughness analysis of DIC system with GOM correlate software.....	101
3.7 Machine learning methodology .....	104
3.7.1 Stress-Strain Prediction using MLPRegressor. ....	104
<b>4 EXPERIMENTAL ANALYSIS OF X65 STEEL TENSILE PROPERTIES.....</b>	<b>107</b>
4.1 Introduction .....	107
4.2 Quasi-static tensile results of X65 steel. ....	108
4.2.1 Round smooth tensile test.....	108
4.2.2 Round-notched tensile tests.....	111
4.3 High strain rate tensile test results of X65 steel .....	114
4.3.1 Summary of the high strain rate tensile test .....	115
4.4 Interpretation of tensile test data.....	116
4.4.1 Thermal diffusivity effect.....	117
4.4.2 Johnson-Cook plasticity parameter determination .....	120
4.4.3 Determination of JC constants A, B, and n.....	121
4.4.4 Determination of JC constants C.....	122
4.4.5 Determination of Johnson-Cook ductile damage parameter .....	125
4.4.6 Rise in temperature during plastic deformation .....	127
4.5 Analytical approach to thermomechanical model in BCC metals .....	128
4.6 FEA modelling of tensile tests.....	131
4.7 Discussion on Tensile Testing Analysis .....	136
4.7.1 Different methods of high strain rate testing.....	136
4.7.2 Effect of strain rate on tensile testing .....	137
4.7.3 Temperature rise effect on material behaviour during plastic deformation. ....	140

5 FRACTURE TOUGHNESS DETERMINATION AT DIFFERENT LOADING RATES ON X65 STEEL .....	141
5.1 Introduction .....	141
5.2 Quasi-static fracture toughness property of X65 steel .....	141
5.2.1 Quasi-static fracture toughness testing results of X65 steel.....	141
5.2.2 Resistance curve measurement of fracture toughness .....	144
5.3 Dynamic/High strain rate fracture toughness results for X65 steel .....	146
5.4 Instrumented Charpy test.....	147
5.5 Low blow Instrumented Charpy test.....	149
5.6 FEA modelling of fracture toughness on SENB sample.....	152
5.6.1 FEA model preparation and the geometry.....	152
5.7 FEM results on high strain rate model .....	154
5.7.1 FEA model prediction at high loading rates.....	158
5.8 Discussion on Fracture Toughness.....	161
5.8.1 Loading Rate Effects on Fracture Toughness of Steel.....	161
5.8.2 Effect of loading rate on testing procedure.....	163
5.8.3 Concluding remarks .....	165
5.9 Machine learning results for toughness and stress-strain curve predictions .....	166
5.9.1 Fracture toughness prediction.....	166
5.9.2 Stress-Strain Prediction using machine learning.....	169
5.9.3 Machine learning Summary.....	171
6 CONCLUSIONS.....	173
6.1.1 Material characterisation .....	173
6.1.2 Fracture behaviour .....	174
6.1.3 Finite element analysis and machine learning.....	175
7 RECOMMENDATION FOR FUTURE WORK .....	179
REFERENCES.....	181
APPENDICES .....	197
Appendix A Experiments Conducted and the Conditions .....	197
Published Paper .....	221



## LIST OF FIGURES

Figure 2-1 Pipeline steels production and their developments (Barsanti et al.)	28
Figure 2-2 (a) Increase in the tensile properties (b) Rise in temperature and stacking fault energy (He et al., 2020).	31
Figure 2-3 Strain rate sensitivity plot of true stress at a true strain of 0.1 (Tiamiyu, Szpunar, & Odeshi, 2019)	31
Figure 2-4 Flow stress dependence on shear strain rate for 1100-0 aluminium (Clifton, 1983).	32
Figure 2-5 Dislocation and flow stress increase with increasing strain rate for OFE copper (Huang, M., Rivera-Díaz-del-Castillo, Bouaziz, & van der Zwaag, 2009).	33
Figure 2-6: ABS-C steel behaviour at temperature and strain rate change on crack toughness (Wiesner & MacGillivray, 2019)	34
Figure 2-7 Plots of load vs. load line displacement of different strain rates (Srinivas & Kamat, 2001).	35
Figure 2-8 Material testing techniques for high strain rates (Meyers, 1994)	36
Figure 2-9 Diagram showing a schematic representation of a cam plastometer (Meyers, 1994).	38
Figure 2-10 Set-up of Split Hopkinson pressure bar test showing notched splitting tension cylinder (Lambert & Allen Ross, 2000) (Lambert and Allen Ross, 2000).	38
Figure 2-11 The SHPB strain gauge signals from the splitting tension test (Lambert & Allen Ross, 2000).	39
Figure 2-12 Figure 2 5 (a) Triangular line-wave generator (b) Mousetrap plane-wave generator (Meyers, 1994).	40
Figure 2-13 D.C signal conditioners and amplifiers test systems (British Standard Institution,2005).	42
Figure 2-14 A.C transducers test system (British Standard Institution,2005).	42
Figure 2-15 Ductile-to-brittle fracture toughness master curve (a) for 1T specimens (ASTM standard) (b) for A533B steel at 95% upper and 5% lower bounds (Zhu & Joyce, 2012).	43
Figure 2-16 Infinite plate under tensile stress with a crack length of $2a$ (Anderson, T. L., 2017).	45
Figure 2-17 The near crack tip and in-plane stresses of an elastic material (Anderson, T. L., 2017).	46

Figure 2-18 Typical load versus displacement curve shown with the corresponding region on the transition curve (© TWI). .....	48
Figure 2-19 Three-point bend specimen schematic view of deformation (Rubio, Fernandez-Saez, & Navarro, 2003).....	49
Figure 2-20 Set-up of Split Hopkinson pressure bar using 3-point bend specimen (Rubio, Fernandez-Saez, & Navarro, 2003). .....	50
Figure 2-21 Tensile test results of dynamic loading on mild steel (Compbell & Cooper, 1966).....	51
Figure 2-22 Ductile-brittle transition of ferritic steel (Anderson, P. M., Hirth, & Lothe, 2017) .....	53
Figure 2-23 Burgers circuit defining the Burgers vector (a) edge dislocation (b) screw dislocation (Hull & Bacon, 2001). .....	54
Figure 2-24 X65 steel microstructure showing (a) pearlite colonies in isolation; (b) pearlite colonies interconnected (Wang, Atrens, Cousens, & Kinaev, 1999). .....	55
Figure 2-25 ABAQUS Damage initiation criteria for ductile material.....	66
Figure 2-26 Process of determining JC plasticity and damage parameters for FEA.....	66
Figure 2-27 Stress-Strain curve for experiment and prediction (ANN) at (a) 18 % and (b) 24 % volume fraction of $\alpha$ (Gangi Setti & Rao, 2014).....	67
Figure 2-28 MPL Regressor framework with one hidden layer ( <a href="https://scikit-learn.org/stable/modules/neural_networks_supervised.html">https://scikit-learn.org/stable/modules/neural_networks_supervised.html</a> ) .....	68
Figure 2-29 A convolutional neural network with pooling layers connected two full layers for stress-strain curve prediction (Koenuma, Yamanaka, Watanabe, & Kuwabara, 2020).....	69
Figure 2-30 Numerical (black) and estimated (red) biaxial tensile curves trained with DNN-2D (Koenuma, Yamanaka, Watanabe, & Kuwabara, 2020). ....	70
Figure 2-31 Random Forest Regressor sample tree (Li et al., 2018) .....	71
Figure 2-32: Random Forest prediction sample (Ganesh et al., 2021).....	71
Figure 2-33 Project plan for scientific contribution to dynamic fracture toughness measurement.....	74
Figure 3-1 2-D diagram of Charpy-sized specimen. ....	78
Figure 3-2 Three-point bend EDM-notched specimens (a) $a/W_0$ of 0.2( $\approx$ 2 mm notch) and (b) $a/W_0$ of 0.5 ( $\approx$ 5mm notch).....	78
Figure 3-3 Three-point bend configuration showing the point of impact, $F$ . .....	80

Figure 3-4 Round dog-bone samples showing the un-notched (a), and notched samples (b, c, & d).....	82
Figure 3-5 A tensile test set up showing the extensometer across the gauge on round specimen (© TWI).....	83
Figure 3-6 Flat dog-bone sample for high-strain tensile testing.....	84
Figure 3-7 Instron machine with sample sprayed with speckle set-up for testing. ....	85
Figure 3-8 GOM data analysis for tensile testing at high strain rate initial stage .....	86
Figure 3-9 GOM data analysis for tensile testing at high strain rate extension stage.....	86
Figure 3-10 GOM data analysis for tensile testing at high strain rate fracture stage .....	87
Figure 3-11 Determination of R-curve and the data spacing (British Standard Institution, 2021) .....	88
Figure 3-12 Engineering diagram of Charpy-sized specimen with EDM notched. ....	88
Figure 3-13 Single edged notched sample showing the three dimensions; crack length (a), the thickness (b), and the width (W). ....	89
Figure 3-14 Fatigue crack of cyclic loading introduced at the tip of a machined notch (Anderson, T. L., 2017).....	90
Figure 3-15 Opened specimen for crack surface shape investigation showing machine notched on top, and ductile fracture bottom. (a) $a/W$ of 0.5, (b) $a/W$ of 0.2. (© TWI).....	90
Figure 3-16 SEN(B) sample with EDM notched and the fatigue pre-cracking (image from TWI).....	91
Figure 3-17 Cracked specimens showing the EDM notched, fatigue pre-cracked and fractured surfaces for, (a) $a_0/W$ of 0.2, (b) $a_0/W$ of 0.5. (© TWI) .....	91
Figure 3-18 Set up for fracture toughness test with a pre-cracked notch specimen mounted (© TWI). ....	92
Figure 3-19 Specimen undergoing impact drop weight testing (Zwick Roell) ...	94
Figure 3-20 Charpy testing machine with specimen placed horizontally on it (© TWI).....	96
Figure 3-21 Charpy sample with EDM notched and fatigue pre-cracked. ....	97
Figure 3-22 A schematic diagram of the Charpy impact test machine .....	97
Figure 3-23 Impact drop tower .....	99

Figure 3-24 VHS Instron machine (© TWI).....	101
Figure 3-25 Three bend sample with speckle pattern for fracture toughness test .....	103
Figure 3-26 Sample with the surface component under high strain rate deformation.....	103
Figure 3-27 (a) Correlation table showing the applied features (b) Fracture toughness prediction with Regression Tree method (Daghigh et al., 2020). .....	105
Figure 3-28 Generated curves from test data of composite with mean squared errors between 25 – 75 % (Yang, Kim, Ryu, & Gu, 2020) .....	106
Figure 4-1 Stress-strain curve of X65 material for static testing .....	108
Figure 4-2 Tensile properties and the measurement errors .....	109
Figure 4-3 Round Un-notched stress-strain curve showing two identical results of tested specimens M04 13 and M04 14 from X65 steel. ....	110
Figure 4-4 Comparison of Engineering and True stress-strain curves for X65 steel.....	110
Figure 4-5 Round (Notched and un-notched) samples variation of yield strength in X65 steel.....	112
Figure 4-6 Notched tensile test stress-strain curves.....	113
Figure 4-7 Comparison of the notched and smooth round tensile curve .....	113
Figure 4-8 Comparison of all stress-strain curves at different displacement rates .....	114
Figure 4-9 Comparison of yield stress for un-notched, notched round specimen and flat specimens at different strain rates. ....	116
Figure 4-10: Comparison of ultimate tensile strength for un-notched, notched round specimen and flat specimens at different strain rates which increases with strain rate. ....	116
Figure 4-11 Thermal diffusion distance covered the entire curve.....	118
Figure 4-12 Plot to show thermal diffusion distance at 216 s <sup>-1</sup> strain rate. ....	119
Figure 4-13 Plot to show thermal diffusion distance at 400 s <sup>-1</sup> strain rate.....	119
Figure 4-14 Plot to show thermal diffusion distance at 600 s <sup>-1</sup> strain rate. ....	120
Figure 4-15 Natural logarithm of flow stress and strain. ....	122
Figure 4-16 Plot for obtaining the Johnson-Cook C constant. ....	123

Figure 4-17 Comparison of obtained X65 steel Johnson-Cook parameters with (Cortis, Nalli, Sasso, Cortese, & Mancini, 2022) and (El-Danaf et al., 2013) JC parameters using same ductile damage parameter ( $d_1 - d_5$ ) .....	124
Figure 4-18 Different stress triaxialities obtained from experimental data .....	126
Figure 4-19 Fracture strain Vs stress triaxiality plot fitted for round tensile tests. ....	126
Figure 4-20 Analytical temperature rise comparison for different strain rates. ....	128
Figure 4-21 Two models compared with the experimental data at $216 \text{ s}^{-1}$ . ....	129
Figure 4-22 Two models compared with the experimental data at $400 \text{ s}^{-1}$ . ....	129
Figure 4-23 Stress-strain curve comparing the effect of temperature rise at $400 \text{ s}^{-1}$ . ....	130
Figure 4-24 Stress-strain curve comparing the effect of temperature rise at $600 \text{ s}^{-1}$ . ....	130
Figure 4-25 Mesh Sensitivity analysis for the round tensile specimen .....	133
Figure 4-26 Mesh Sensitivity analysis for the flat tensile specimen at $600 \text{ s}^{-1}$ strain rate .....	133
Figure 4-27 FEA model of un-notched round specimen (a) showing the location of stress (b) showing the boundary conditions.....	134
Figure 4-28 FEA Model simulation and experimental data for un-notched sample .....	134
Figure 4-29 Notched Tensile testing sample in FEA model simulation.....	135
Figure 4-30 Round notched sample comparing different data set. ....	135
Figure 4-31 Flat tensile specimen FEA modelled in Abaqus. ....	135
Figure 4-32 Comparison of simulation and experiment for (a) $216 \text{ s}^{-1}$ and (b) $400 \text{ s}^{-1}$ with flat specimen. ....	136
Figure 4-33 strain rate effect during compression test on cylindrical specimens (a) 7075-T6 aluminium and (b) alloy titanium 6% Al-4% V (Maiden & Green, 1966) .....	138
Figure 4-34 Strain rate effect during compression test on (a) pure titanium (b) tantalum (Meyers, 1994).....	139
Figure 4-35 Copper tested at $10^4 \text{ s}^{-1}$ strain rate at initial temperature 298 K, shows variation in the temperature during dynamic deformation (Andrade, Meyers, Vecchio, & Chokshi, 1994). ....	140
Figure 5-1 Force-CMOD curve for X65 blunt notch $a_0/W$ of 0.5 .....	142
Figure 5-2 Force-CMOD curve for X65 blunt notch $a_0/W$ of 0.2 .....	143

Figure 5-3 Graphical representation of the fracture toughness values .....	144
Figure 5-4 Resistance curve for X65 steel at room temperature with SENB specimen ( $B=W=10\text{mm}$ ) at $a_0/W = 0.5$ mm .....	145
Figure 5-5 Resistance curve for X65 steel at room temperature with SENB specimen ( $B=W=10\text{mm}$ ) at $a/W = 0.2$ mm.....	146
Figure 5-6 Charpy test result of force-displacement curve at room temperature with varying crack lengths, $a$ [mm].....	148
Figure 5-7 Comparison of fracture toughness for pre-cracked specimen at different crack lengths ( $B = W \approx 10 \text{ mm}$ ) .....	149
Figure 5-8 Comparison of J toughness measurement for full and low blow Charpy tests.....	151
Figure 5-9 Comparison of CTOD toughness measurement for full and low blow Charpy tests. ....	151
Figure 5-10 SENB geometry showing the pre-cracked region.....	153
Figure 5-11 Varying mesh density on different partition. ....	153
Figure 5-12 Mesh Sensitivity analysis for the three-point bend specimen .....	154
Figure 5-13 FEA model for 1 m/s displacement rate at 0.002 seconds .....	155
Figure 5-14 Load versus displacement of X65 steel at 4880 mm/s displacement rate .....	156
Figure 5-15 Load versus displacement of X65 steel at 3880 mm/s displacement rate. ....	156
Figure 5-16 Comparison of time steps with the experiment at 4880 mm/s.....	157
Figure 5-17 Comparison of time steps with the experiment at 3880 mm/s.....	157
Figure 5-18 Energy increase with the displacement rate from the FEA model. ....	158
Figure 5-19 Comparison of energy obtained from drop weight test with FEA model at 5.23 m/s.....	159
Figure 5-20 FEA model for 5.3 m/s displacement rate at 0.002 seconds .....	160
Figure 5-21 FEA result on the 15 m/s displacement rate at 0.002 seconds ...	160
Figure 5-22 FEA model on 20 m/s at 0.00095 seconds, the striker passing through the sample without bending.....	160
Figure 5-23 The striker cut through the sample with no significant bending at 20 m/s within 0.002 seconds. ....	161
Figure 5-24 Ductile to brittle transition curve for ferritic steels (© TWI). ....	163

Figure 5-25 Loading rate effect on HY80 steel (Anderson, T. L., 2017) .....	163
Figure 5-26 (a) Quasi-static Load-time plot (b) Dynamic Load-time plot (Wiesner & MacGillivray, 2019).....	165
Figure 5-27 Pearson matrix showing the correlation of the features applied for the machine learning prediction.....	167
Figure 5-28 Prediction of fracture toughness values with Random Forest Regressor ML results showing the true and predicted toughness values.	168
Figure 5-29 Comparison of predicted fracture toughness with the true toughness result.....	168
Figure 5-31 Un-notched tensile tests plot of trained and true dataset .....	169
Figure 5-32 Round notched tensile tests plot of trained and true dataset. ....	170
Figure 5-33 Controlled drop weight tests plot of trained and true dataset. ....	170
Figure A-1 Impact drop weight tested samples showing the level of crack extension .....	203
Figure A-2 Fractured notch of impact drop weight test samples.....	204

## LIST OF TABLES

Table 2-1 Chemical composition of API 5L X65 alloy steel (in wt.%) .....	28
Table 2-2 Johnson-Cook constitutive model parameters for X65 steel .....	60
Table 3-1 The X65 tensile properties tested by the supplier with a cylindrical specimen cut from a Longitudinal orientation at 20°C.....	76
Table 3-2 Experiments conducted for the study. ....	77
Table 3-3 Three-point bend specimen dimensions with allowable tolerances ..	79
Table 3-4 Mechanical properties of X65 assumed during testing. ....	79
Table 3-5 Velocity range with corresponding strain rates.....	84
Table 3-6 Fatigue details for the 3-point bend specimens.....	91
Table 3-7 Mass applied and the corresponding work capacity in Joules at a velocity of 5296 mm/s.....	93
Table 3-8 Displacement rate conditions for the tests performed with the Charpy machine.....	98
Table 4-1 Tensile properties of round un-notched X65 steel tested at 21°C ..	109
Table 4-2 Material properties measured with round notched tensile specimen under quasi-static loading.....	112
Table 4-3 Material properties measured with flat tensile specimens. ....	115
Table 4-4 Mechanical properties of X65 grade steel. ....	115
Table 4-5 Thermal diffusion distant at each displacement rates.....	118
Table 4-6 Tensile test conditions for JC constants determination at room temperature .....	121
Table 4-7 Result of B and n from linear regression method. ....	122
Table 4-8 Regular JC obtained parameters.....	124
Table 4-9 JC ductile damage parameters (dimensionless) .....	127
Table 4-10 FEA elements distribution in mesh sensitivity analysis with round tensile specimen.....	132
Table 4-11 FEA elements and node distribution in mesh sensitivity analysis for the flat specimen. ....	132
Table 5-1 Fracture toughness results under quasi-static loading at room temperature summarised for the $a_0/W \approx 0.5$ . ....	143



Table 5-2 Fracture toughness results under quasi-static loading at room temperature summarised for the $a_0/W$ of 0.2 .....	144
Table 5-3 Fracture test results of dynamic loading of $V= 5400$ mm/s analysed with ISO 12135:2016 and CTOD of ASTM E1820-20b on SENB specimens. ....	147
Table 5-4 Low blow Charpy test of dynamic loading of $V= 5400$ mm/s analysed with ISO 12135:2016 and CTOD of ASTM E1820-20b on SENB specimens for $a_0/W = 0.5$ .....	150
Table 5-5 Low blow Charpy test of dynamic loading of $V= 5400$ mm/s analysed with ISO 12135:2016 and CTOD of ASTM E1820-20b on SENB specimens for $a_0/W = 0.2$ .....	150
Table 5-6 FEA elements and node distribution in mesh sensitivity analysis for three-point bend sample.....	154
Table A.1 High strain rate loading condition tensile test data for X65 steel...	197
Table A.2 Test data for controlled drop weight test with blunt notch of $a_0/W \approx 0.2$ .....	198
Table A.3 Fracture toughness test under quasi-static condition at ambient temperature for $a_0/W$ 0.5 with specimen geometry $B=W=10$ .....	205
Table A.4 Fracture toughness test under quasi-static condition at ambient temperature for $a_0/W \approx 0.2$ with specimen geometry $B=W=10$ .....	205
Table A.5 Instrumented Charpy test data and the absorbed energies for $a_0/W \approx 0.5$ .....	206
Table A.6 Instrumented Charpy test data and the absorbed energies for $a_0/W \approx 0.2$ .....	207
Table A.7 Fracture test for resistance curve on the blunt notch specimen of $a_0/W \approx 0.5$ and 0.2.....	219
Table A.8 Fracture test for resistance curve on the pre-cracked specimen of $a_0/W \approx 0.5$ .....	219
Table A.9 Fracture test for resistance curve on the pre-cracked specimen of $a_0/W \approx 0.2$ .....	220

# LIST OF EQUATIONS

(2-1).....	30
(2-2).....	30
(2-3).....	31
(2-4).....	32
<b>(2-5)</b> .....	<b>36</b>
<b>(2-6)</b> .....	<b>43</b>
<b>(2-7)</b> .....	<b>44</b>
<b>(2-8)</b> .....	<b>44</b>
<b>(2-9)</b> .....	<b>44</b>
(2-10).....	44
(2-11).....	45
(2-12).....	46
(2-13).....	46
(2-14).....	46
(2-15).....	46
(2-16).....	47
(2-17).....	47
(2-18).....	49
(2-19).....	49
(2-20).....	49
(2-21).....	49
(2-22).....	51
(2-23).....	54
(2-24).....	54
(2-25).....	55
(2-26).....	56
(2-27).....	56
(2-28).....	56

(2-29).....	57
(2-30).....	57
(2-31).....	57
(2-32).....	58
(2-33).....	58
(2-34).....	58
(2-35).....	59
(2-36).....	61
(2-37).....	61
(2-38).....	61
(2-39).....	62
(2-40).....	62
(2-41).....	62
(2-42).....	62
(2-43).....	63
(2-44).....	63
(2-45).....	64
(2-46).....	64
(2-47).....	64
(3-1).....	95
(3-2).....	98
(3-3).....	100
(3-4).....	100
(3-5).....	100
<b>(4-1)</b> .....	<b>110</b>
<b>(4-2)</b> .....	<b>110</b>
<b>(4-3)</b> .....	<b>121</b>
<b>(4-4)</b> .....	<b>122</b>
<b>(4-5)</b> .....	<b>123</b>

<b>(4-6)</b> .....	123
<b>(4-7)</b> .....	125
<b>(4-8)</b> .....	125

## LIST OF ABBREVIATIONS

ECA	Engineering Critical assessment
EDM	Electric discharge machining
BS	British standard
ISO	International standard organization
FEA	Finite element analysis
FEM	Finite element model
SENB	single-edge notched bend
DIC	Digital image correction
a/W	Crack length to specimen width ratio
C(T)	Compact tension
SENT	Single edge notch tension
BCC	Body-Centered Cubic
FCC	Face-Centered Cubic
HCP	Hexagonal close packed
JC	Johnson-Cook
CTOD	Crack tip opening displacement
LEFM	Linear elastic fracture mechanics
EPFM	Elastic-plastic fracture mechanics
ANN	Artificial neural network
MLP	Multilayer perceptron
TWI	The Welding Institute
SIF	Stress intensity factor

# 1 INTRODUCTION

## 1.1 Background Information

As the complexity of engineering structures increases in recent design, sophisticated methods are required to assess safety and structural integrity. Various factors affect the integrity of such structures, for example, imperfections or flaws in the materials, which can be introduced during production and fabrication, or environmental effects such as corrosion and fatigue. The presence of stress concentrations (notches, holes, grooves, and fillets) and residual stresses also affect material performance. Components may fail by ductile or brittle fracture depending on the loads, strain rates, environmental contaminants, and/or service temperature.

Liberty Ships was one example of brittle crack failure that occurred amid World War II in the 1940s (Kobayashi, H. & Onoue, 1943) . This resulted in the evolution of an innovative fracture mechanics analysis technique aimed at improving the grasp of fracture behaviour in metallic materials. Stresses, flaws, and material properties (especially fracture toughness), if any of these three elements is critical, it will be potentially unsafe. The approach to determine the relationship and dependence between these three elements can be demonstrated using a fracture mechanics-based approach. Thus, fracture mechanics principles form the basis for Engineering Critical Assessment (ECA) outlined in BS 7910 (British Standard Institution,2019aa), which is a procedure used to determine flaw acceptability under specified loading conditions.

Fracture is simply a type of failure that occurs in metallic materials through rapid and unstable propagation of a crack. Fracture mechanics studies a material's resistance to fracture in two categories: linear elastic fracture mechanics (LEFM) and elastic-plastic fracture mechanics (EPFM) which apply to brittle and ductile materials respectively. These are utilised to determine the behaviour of flaws which depends on the local conditions at the crack tip, material properties, and loadings. The crack driving force can be characterized by different parameters including stress intensity factor ( $K$ ), and J-integral ( $J$ ). Fracture toughness properties, CTOD, and  $J$  are obtained experimentally and used to derive the  $K$  parameter using a formula. The stress intensity factor,  $K$  is used to characterize the material resistance that occurs within the elastic yield region in LEFM, while the CTOD derived through a strain-based approach,

and J derived through an energy-based approach represents fracture resistance in EPFM. The EPFM considers plastic deformation in the post-yield region. These fracture resistance parameters can be determined experimentally through direct fracture toughness tests of representative materials. The specimens may be manufactured in different geometries such as single-edge notch tension (SENT), compact tension (CT), and single-edge notch bend (SENB). Whenever the fracture toughness is less than the crack driving force, it results in fracture.

The mechanical properties of metals are well studied under quasi-static (strain rate  $\approx 10^{-5} \text{ s}^{-1}$ ) (Burdekin, Zhao, Tkach, Wiesner, & Xu, 2004) conditions and their properties have been applied in design and assessment, but material response under dynamic loading conditions (strain rate greater than  $1 \text{ s}^{-1}$ ) are still under active investigation as shown in Table 1. as it is applied to different equipment and conditions. Materials that exhibit ductile behaviour under normal loading conditions may fail in a brittle manner at higher strain rates. This becomes necessary to establish testing methods to determine fracture toughness properties under dynamic loading.

**Table 1. Some typical components of engineering and their loading rates (Wiesner and MacGillivray, 2019)**

<b>Application</b>	<b><math>\dot{\epsilon}</math>, <math>\text{s}^{-1}</math></b>	<b>K, <math>\text{MPam}^{0.5\text{s}^{-1}}</math></b>
Storage tanks, pressure vessels	$10^{-6}$ to $10^{-4}$	$10^{-2}$ to 1
Bridges, cranes, earthmoving earthquake loading	$10^{-2}$ to 0.1	10 to $10^3$
Marine collisions	0.1 to 10	$10^2$ to $10^4$
Transport on land, aircraft undercarriage	10 to $10^3$	$10^3$ to $10^6$
Explosion, ballistics	$10^4$ to $10^6$ above	$10^7$ to $10^{10}$ above

The testing procedures including BS EN ISO 12737:2005, BS ISO 12135, and ASTM E1820 are well-established for the determination of fracture toughness at low strain rates (quasi-static). Currently, BS 7448-3 (British Standard Institution,2005) specifies

the procedure for fracture toughness testing at a stress intensity factor rate higher than  $3 \text{ MPa}\cdot\text{m}^{0.5}\text{s}^{-1}$ .

Under high loading rate conditions, the material behaviours are most affected by significant inertia effects, such that large oscillations are captured in the load-time and load-displacement records. With the presence of these oscillations, it becomes difficult to differentiate between the actual material response (i.e. crack driving force) and the loading effects on the experiment device (i.e. shock wave in load cell). The current drop weight test machines available in the market are equipped with sensors to record impact time and force. However, the recorded signal includes a certain degree of oscillation as a result of the shock wave upon impact. As the speed of impact is greater than that of regular tests, the recording of material response will require more sophisticated equipment.

The determination of dynamic fracture toughness is complicated since its mechanics involve inertia forces, reflected stress waves, and rate-dependent material behaviour. In a simple context, fracture toughness properties are sensitive to microstructural and chemical changes in a material (Quinn, Sundar, & Lloyd, 2003) (Kleebe, Pezzotti, & Ziegler, 1999) as well as nonlinear effects such as inertia effects, strain rate sensitivity of the material, reflected stress waves, and thermal softening due to adiabatic heating as documented by (Molinari, Mercier, & Jacques, 2014) and (Owen, Zhuang, Rosakis, & Ravichandran, 1998).

This project applies to applications where the material resistance to fracture initiation may be low with a very critical important safety margin in the aspect of delivering structural integrity assessment. Failure of structures by fracture is rare, but once it occurred can be catastrophic and may result in loss of lives and cost. Some failures that occurred in the past resulting from poor design and improper welding such as the John Thompson pressure vessel in 1965 (Hayes, 1996), King's Bridge, Melbourne of 10 July 1962 (Evison, 1964), and Alexander L. Kielland platform in the North Sea on 27 March 1980 (Moan, 1985) (Almar-Naess, Haagenen, Lian, Moan, & Simonsen, 1984), among others, formed the basis from which lessons were learned and hence preventive measures became very imperative. As failure occurrence results from a critical combination of low toughness, high stresses, and a flaw, proper procedures need to be in place to assess these conditions.



To improve safety and structural reliability, industries such as the oil and gas sector and energy generation sector utilize failure analysis in assessing defective components including steel pipelines, pressure vessels, platforms, blades, and gas turbine components. Since environments can affect material properties such as the pipelines embedded in marine environments experiencing impact from the effect of waves or other structures, it is therefore necessary that the effect of this impact is assessed at different strain rates, and as such fracture toughness testing at high strain rates becomes unavoidable. Fracture mechanics and structural integrity assessment require some factors such as fracture toughness, to determine the proximity to failure resulting from both brittle and plastic collapse. Failure assessment diagram hence determines the level of acceptable flaw in a material to prevent failure from occurring.

## **1.2 Aims and Objectives**

This project aims to recommend an alternative method to determine high strain rates dynamic fracture toughness from the combination of analytical solutions, experimental data, computational data, and machine learning.

The objectives of the project include:

- To investigate the crack driving force under various strain, temperature, and strain rates which are representative of dynamic loading conditions.
- To identify the gap and limitations associated with the current testing procedures for dynamic fracture toughness.
- To propose improvements for the determination of dynamic fracture toughness.
- To establish a prediction model based on the experimental evidence and material behaviour model (Johnson-Cook and dislocation density)
- To investigate the dynamic fracture toughness properties as affected by the notch depth in metallic material.
- To investigate the prediction of fracture toughness properties using a machine learning algorithm.

### 1.3 Thesis Structure

Chapter 2 describes the research work and theories to identify the gaps, limitations, and recent techniques. It also reviews the procedure for finite element modelling and theories of machine learning employed in this work.

Chapter 3 details the experiments carried out to determine the mechanical properties. The experimental data were analysed to establish parameters for the Johnson-Cook (JC) model, and these parameters were implemented in the analytical and finite element model to characterize the behaviour of the material at low and high strain rates.

Chapter 4 presents the results from different analytical methods used, including the theoretical models, experimental approach, and numerical model (considering the behaviour of the material at varying strain rates ranging from  $10^{-5} \text{ s}^{-1}$  to  $10^2 \text{ s}^{-1}$ ). Chapter 5 discusses results from the instrumented Charpy and fracture toughness tests. It also describes the procedures and outcome of the machine learning algorithm in the prediction of stress-strain behaviour and fracture toughness of the material. The results focused on the similarities and differences between the quasi-static and dynamic material behaviour. Proposed suggestions for the next revision of the BS 7448 - 3 procedure was also included.

Chapter 6 concludes the work, while Chapter 7 makes recommendations for future work.



## **2 LITERATURE REVIEW**

### **2.1 Introduction of the material**

This study employed API 5L X65 grade steel material which is used widely in oil and gas industries. Based on their high strength and low yield ratio to ultimate tensile ratio, they are also used in pressure vessel systems, petrochemicals, boiler equipment, sugar industries, and power generation amongst others (Billingham, Healy, & Bolt, 1997).

The development of pipeline steels has been reported by (Barsanti, Pozzoli, & Hillenbrand, 2001) and presented in Figure 2-1 which the X65 steel falls in the controlled-rolled or thermo-mechanical treated (TM) steels and was established in the 1970's. The controlled thermo-mechanical rolling process is conducted in conjunction with the addition of micro-alloying elements. High toughness is a vital property in the selection of materials for pipeline application to ensure the structural integrity of pipes over the operational period.

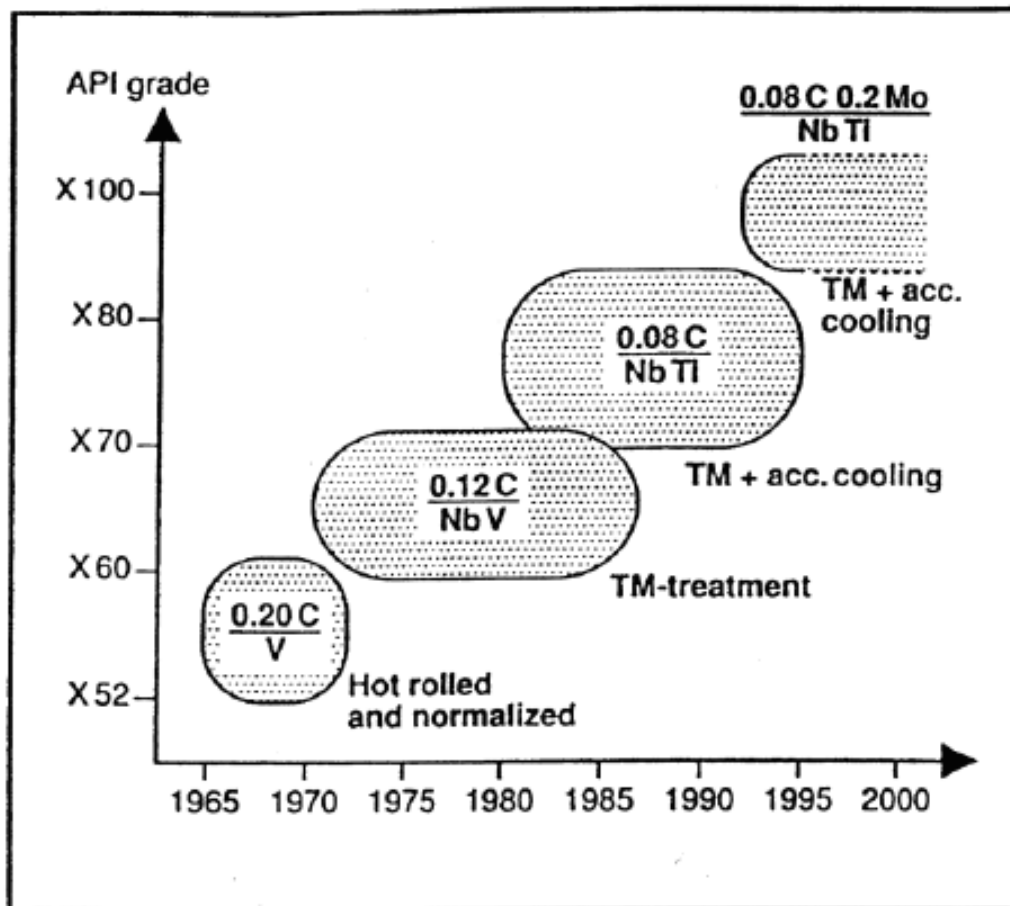


Figure 2-1 Pipeline steels production and their developments (Barsanti et al.)

The X65 material is an alloy steel with a crystal structure of body-centered cubic (BCC). Table 2-1 shows the chemical composition of the material. Nickel is added to improve the ductility and toughness of the material while carbon is added for its ability to improve the strength and hardness. Manganese, an austenite forming element is for increased strength, toughness, and hardenability. Sulphur functions in improving weldability and increasing machinability.

Table 2-1 Chemical composition of API 5L X65 alloy steel (in wt.%)

<b>Element</b>	<b>Mn</b>	<b>C</b>	<b>Si</b>	<b>Ni</b>	<b>Al</b>	<b>P</b>	<b>N</b>	<b>Sn</b>	<b>Mo</b>
<b>Wt %</b>	1.45	0.1	0.2	0.004	0.035	0.02	0.003	0.002	0.04
<b>Element</b>	<b>V</b>	<b>Nb</b>	<b>Ti</b>	<b>S</b>	<b>Cr</b>	<b>Co</b>	<b>B</b>	<b>Fe</b>	
<b>Wt %</b>	0.069	0.054	0.041	0.005	0.04	0.002	0.001	Bal	

X65 steel has a specific minimum yield strength of 450 MPa and is very ductile at room temperature. There are different ways in which failure can occur in the pipeline, which could result from corrosion along grain boundaries without the presence of stress as observed by (Henthorne & Parkins, 1966), fatigue, stress corrosion cracking, and fracture which could result from quasi-static or dynamic loading conditions. The fracture was examined under dynamic loading conditions in this study.

## **2.2 Fractures in metallic structures**

Failure in engineering design could be caused by different factors including poor design, inappropriate operation, negligence in construction, incorrect selection of material, error in stress analysis, as well as improper material testing to determine the material properties under different conditions. For any material whether existing or new to be employed in engineering construction, rigorous testing is highly recommended to demonstrate legislation compliance and integrity.

(Griffith, 1921) established the quantitative relationship that exists between flaw size and applied stress using the elliptical hole for engineering stress analysis introduced by (Inglis, 1913). Griffith's fracture theory based on the first law of thermodynamics predicted flaw-strength relationships well on glass specimens but was unsuccessful with metals.

Modifications were made to Griffith's theory by (Irwin, 1947), (Orowan, 1949), and (Mott, 1948). Irwin modified Griffith's theory and introduced Westergaard's (Westergaard, 1939) solution to describe crack tip characterization. This was later known as the 'stress intensity factor' - a fracture toughness measurement parameter. (Wells, 1961) in 1961 attempts in applying LEFM to low and medium-strength steels were unsuccessful as the materials were too ductile, but the fracture face split up during plastic deformation and this resulted in the development of today's crack-tip opening displacement. (Rice, 1968) research on nonlinear elastic deformation showed that line integral could be used to represent nonlinear energy release rate, and it was called the J-integral. All three fracture toughness measurement parameters (SIF, CTOD, and J) were established for a time-independent fracture mechanism.

## 2.3 Strain rate effect on the properties of a material

Characterization of dynamic loading conditions requires a combination of material science, mechanics, computation, and dynamics. The kinetic energy equation (2-1) describes energy as being absorbed by the target and applies to materials under dynamic loading.

$$E_k = \frac{1}{2}mv^2 \quad (2-1)$$

Quasi-static experiments are not affected by the time of the experiment and time is insignificant to material properties at low loading rates. However, dynamic deformation is time-dependent because of the strain-rate effect on the deformation, and strain rate is the rate of change of strain with time expressed in the equation (2-2).

$$\dot{\varepsilon} = \frac{d\varepsilon}{dt} \quad (2-2)$$

### 2.3.1 Strain rate effects on tensile properties and dislocation density

When a body is affected by rapid loading, the material response differs from the body under the quasi-static loading condition. Bullets at high speed can perforate a metal and such is a core example of a dynamic loading. Some factors influence dynamic occurrences such as inner kinetics and inertia which were carefully studied by (Grady, 1982). (Tam & Calladine, 1991) research utilised two different materials due to their behaviour during plastic deformation (aluminium alloy and mild steel), they concluded that the inertia and strain-rate effect from moving striker impacted the samples under different conditions.

Research by (He et al., 2020) demonstrated strain rate effects on tensile properties of which the employed alloy  $\text{Fe}_{50}\text{Mn}_{30}\text{Co}_{10}\text{Cr}_{10}$  tested under varying strain rates showed an initial decrease in the yield strength, elongation, ultimate tensile strength, and increase as the strain rate increases up to  $10^3 \text{ s}^{-1}$  as shown in Figure 2-2. (He et al., 2020) also recorded an increase in the stacking fault energy at high strain rates as dynamic loading is affected by adiabatic heating leading to temperature rise that causes reverse transformation of e-martensite to austenite.

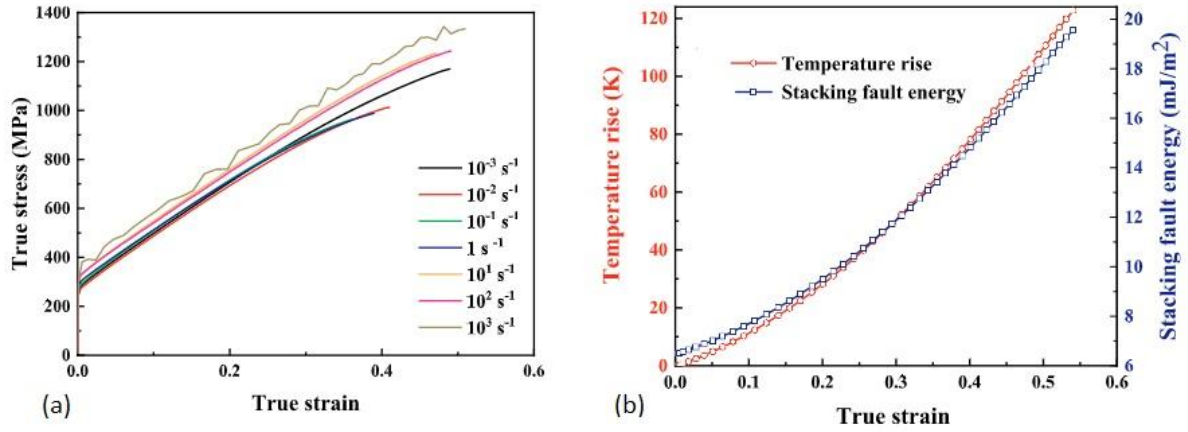


**Figure 2-2 (a) Increase in the tensile properties (b) Rise in temperature and stacking fault energy (He et al., 2020).**

To determine strain rate sensitivity,  $m$ , under dynamic loading in the equation (2-3),

$$m = \frac{\partial \log \sigma_T}{\partial \log \dot{\epsilon}_T} \quad (2-3)$$

where  $\sigma_T$  and  $\dot{\epsilon}_T$  represent true stress and true strain rate respectively. (Tiamiyu, Szpunar, & Odeshi, 2019) utilised AISI 321 stainless steels with different grain sizes (ultra-fine 0.24  $\mu\text{m}$ , fine 3  $\mu\text{m}$ , and coarse 37  $\mu\text{m}$ ) and observed a change in strain rate sensitivity in the fine and coarse grain sizes while the ultrafine remains unchanged as shown in Figure 2-3.

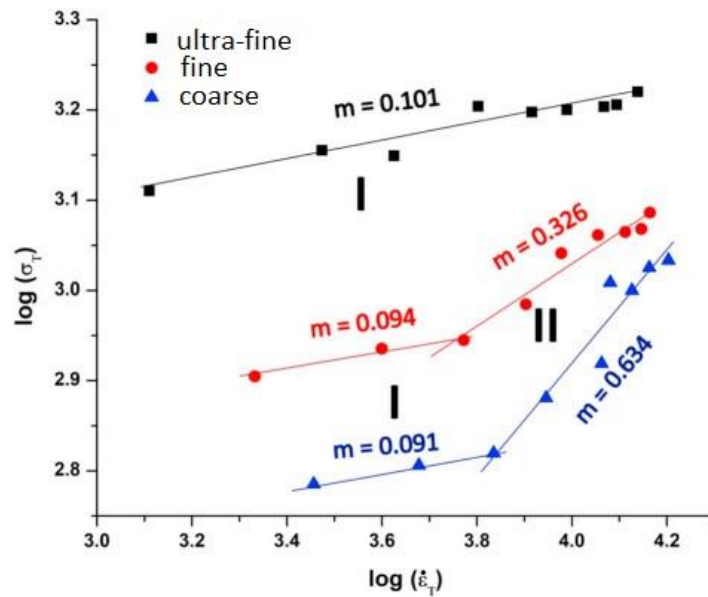


**Figure 2-3 Strain rate sensitivity plot of true stress at a true strain of 0.1 (Tiamiyu, Szpunar, & Odeshi, 2019)**



Increased strain rate increases the flow stress during deformation and has been demonstrated by (Clifton, 1983) for 1100-0 aluminium as shown in Figure 2-4, and (Huang, M., Rivera-Díaz-del-Castillo, Bouaziz, & van der Zwaag, 2009) for the OFE copper in Figure 2-5 with an increase in dislocation density at higher strain rates.

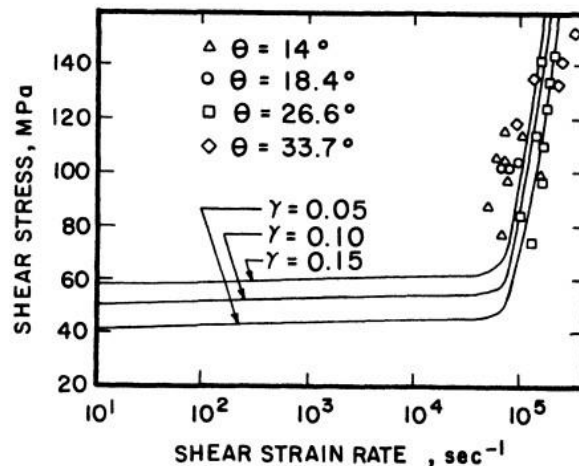


**Figure 2-4 Flow stress dependence on shear strain rate for 1100-0 aluminium (Clifton, 1983).**

A mesh length theory developed by (Kuhlmann-Wilsdorf, 1970) described strengthening of metals by dislocation cells and predicts the linear increase of flow stress with the square root of the dislocation density as presented in equation (2-4),

$$\sigma = \sigma_0 + Gb\rho^{1/2} \quad (2-4)$$

where  $\sigma$  is the flow stress,  $G$  is the shear modulus,  $b$  is the Burgers vector,  $\rho$  is the dislocation density,  $\sigma_0$  is a material constant. It is necessary to mention that the strengthening mechanism in metals and alloys either exhibits the hardening or softening processes (Chao & Varma, 1991). Where the increase in internal stresses brings about hardening the effect, the decrease in the internal stresses through relaxation causes the softening effect. The thermally activated relaxation process was found by (Korbel & Światkowski, 1972) to be time-dependent and this is applicable at high strain rates where the plastic deformation reduces the relaxation process thereby resulting in higher flow stress.

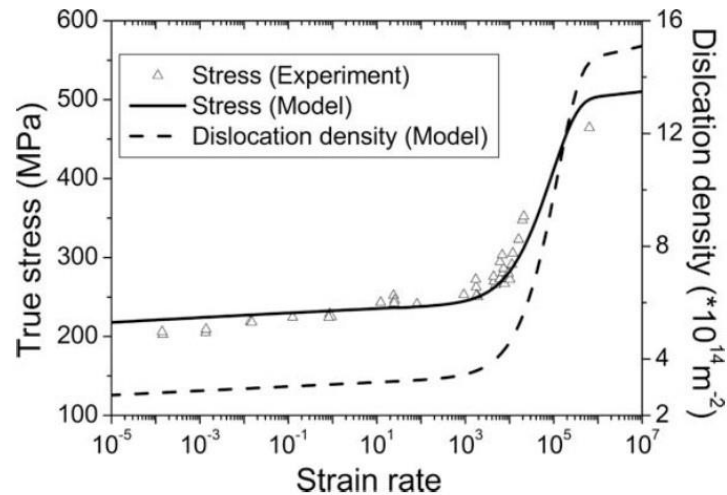


**Figure 2-5 Dislocation and flow stress increase with increasing strain rate for OFE copper (Huang, M., Rivera-Díaz-del-Castillo, Bouaziz, & van der Zwaag, 2009).**

### 2.3.2 Effects of strain rates on the fracture toughness

The fracture toughness dependent on strain rates is very complicated as different materials behave differently. While some materials show an increased toughness at high loading rates, others experience a decline in fracture toughness (Meyers, 1994). This dynamic behaviour of materials at high loading rates was studied by (Wiesner & MacGillivray, 2019) and the loading rate effect was found to depend on overall material behaviour depending on the brittle to ductile transition curve where the test was conducted. **Error! Reference source not found.** shows a decrease in the crack toughness  $K_{Ic}$  with loading rate, while the temperature increases the sensitivity to the loading rate.

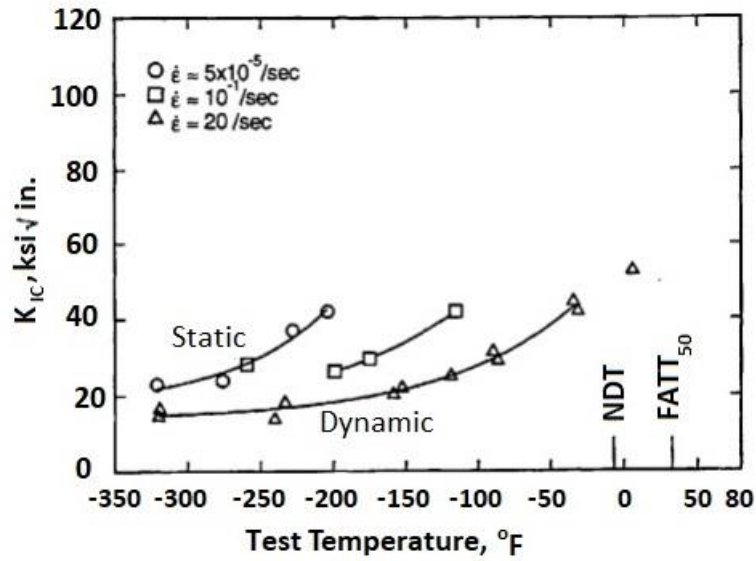


**Figure 2-6: ABS-C steel behaviour at temperature and strain rate change on crack toughness (Wiesner & MacGillivray, 2019)**

The research work by (Srinivas & Kamat, 2001) to test the strain rate effects on mild steel was done in the displacement rates of 0.1, 1, 10, and 50  $\text{mm min}^{-1}$  which were a correspondence of the strain rates  $10^{-5}$ ,  $10^{-4}$ ,  $10^{-3}$ , and  $10^{-2} \text{ s}^{-1}$ , respectively as shown in Figure 2-7. (Srinivas & Kamat, 2001) concluded that the fracture toughness of mild steel increased at the range of  $10^{-5} - 10^{-3} \text{ s}^{-1}$  where the maximum value was determined, and a drastic drop of fracture toughness beyond this strain rate at  $10^2 \text{ s}^{-1}$ .

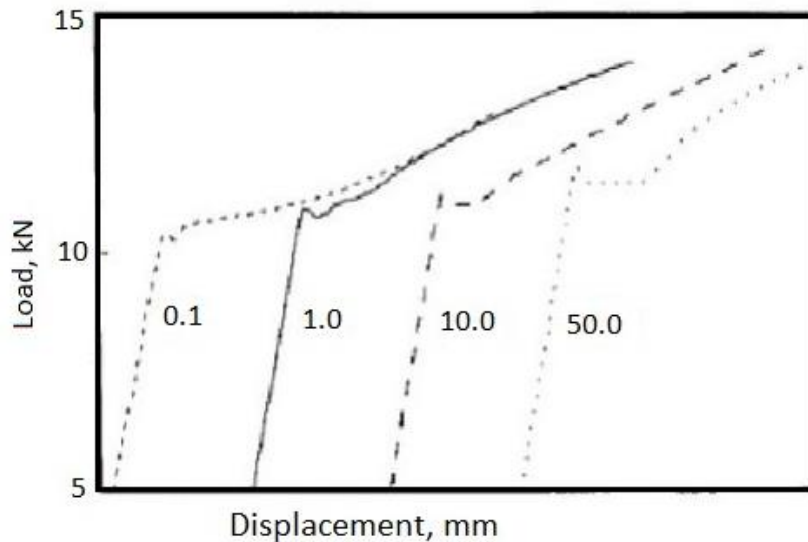


**Figure 2-7 Plots of load vs. load line displacement of different strain rates (Srinivas & Kamat, 2001)**

## **2.4 History of dynamic testing**

Since materials behave differently under various loading conditions, it is therefore difficult to predict their response from the first principles theories, hence, each material has to be tested to determine its mechanical properties at such conditions. Some of the features affecting material properties include strain, strain rates, temperature, and environments. The presence of oscillations in the mechanical testing of dynamic fracture toughness is an issue and the oscillations mask the true response of a material under dynamic loading. Different testing techniques for various strain rates are shown in Figure 2-8.

STRAIN RATES, s <sup>-1</sup>	COMMON TESTING METHODS	DYNAMIC CONSIDERATIONS	
10 <sup>7</sup>	<b>HIGH VELOCITY IMPACT</b> -Explosives -Normal plate impact -Pulsed laser -Exploding foil -Incl. plate impact (pressure-shear)	SHOCK-WAVE PROPAGATION	INERTIAL FORCES IMPORTANT
10 <sup>6</sup>		SHEAR-WAVE PROPAGATION	
10 <sup>5</sup>		PLASTIC-WAVE PROPAGATION	
10 <sup>4</sup>	<b>DYNAMIC-HIGH</b> -Taylor anvil tests -Hopkinson Bar -Expanding ring	MECHANICAL RESONANCE IN SPECIMEN AND MACHINE IS IMPORTANT	
10 <sup>3</sup>			
10 <sup>2</sup>	<b>DYNAMIC-LOW</b> High-velocity hydraulic, or pneumatic machines: cam plastometer	TESTS WITH CONSTANT CROSS-HEAD VELOCITY STRESS THE SAME THROUGHOUT LENGTH OF SPECIMEN	
10 <sup>1</sup>			
10 <sup>0</sup>	<b>QUASI-STATIC</b> Hydraulic, servo-hydraulic or screw-driven testing machines	VISCO-PLASTIC RESPONSE OF METALS	INERTIAL FORCES NEGLIGIBLE
10 <sup>-1</sup>			
10 <sup>-2</sup>			
10 <sup>-3</sup>			
10 <sup>-4</sup>			
10 <sup>-5</sup>	<b>CREEP AND STRESS-RELAXATION</b> -Conventional testing machines -Creep testers		
10 <sup>-6</sup>			
10 <sup>-7</sup>			
10 <sup>-8</sup>			
10 <sup>-9</sup>			

**Figure 2-8 Material testing techniques for high strain rates (Meyers, 1994)**

There are applicable testing methods available depending on the intended strain rates as grouped in Figure 2-8. It was classified under creep and stress relation for extremely low strain rates ( $10^{-9} - 10^{-5} \text{ s}^{-1}$ ), quasi-static ( $10^{-5} - 10^0 \text{ s}^{-1}$ ), and dynamic ( $10^1 - 10^7 \text{ s}^{-1}$ ) testing methods. The dynamic testing method is further split into dynamic high, dynamic low, and high-velocity impact. Strain rates are determined from the machine velocity,  $v_0$  and the gauge length,  $l_0$  as represented in equation (2-5).

$$\dot{\epsilon}_{tensile} = \frac{\Delta \epsilon}{\Delta t} = \frac{v_0}{l_0} \quad (2-5)$$

### **2.4.1 Testing methods for dynamic strain rates ( $10^1 - 10^7 \text{ s}^{-1}$ )**

To understand material behaviour under dynamic loading which entails the application of external force to a body at a very high rate of change of the applied force, experimental methods are designed to replicate dynamic deformation to produce strain rates ranging from  $10^1$  to  $10^7 \text{ s}^{-1}$ .

Dynamic stress is known to travel through a body at a specific known velocity and is hence referred to as waves. Thus, the process of dynamic deformation is associated with wave propagation, unlike the quasi-static condition which is in an equilibrium state. (Taylor, 1948) conducted experiments involving plastic deformation as a wave process (elastic and plastic wave) at very high strain rates. His work formed the fundamentals for testing to determine the dynamic yield strength.

A specialized machine capable of withstanding high loading conditions with a bespoke device to perform dynamic tensile testing. It also requires a highly skilled person for machine and specimen setup. Dynamic testing can be costly, making quasi-static testing to be generally acceptable for most design purposes regardless of loading conditions. Though structures are designed to withstand quasi-static loading, but extreme conditions exist in which the structure experiences impact loading such as collision or drop impact. Consideration of dynamic loading behaviour in the design for in-service loading becomes imperative to material response and safety of the structure.

#### **High-velocity hydraulic - Dynamic low-testing methods**

To achieve dynamic low testing, different techniques could be used such as the high-velocity hydraulic, or pneumatic machine such as the cam plastometer. A drop hammer machine could be utilised such that a large mass is freely dropped from a predefined height to fracture the specimen.

The cam plastometer machine shown in Figure 2-9 provides an efficient coupling between the specimen and the driver, in which the cam is rotated at a specified constant velocity throughout the experiment. The cam follower is engaged at a certain point to compress the sample placed on the elastic bar, and the sample is deformed in one cycle. Dynamic low with a range of strain rates of  $0.1 - 100 \text{ s}^{-1}$  is attained using this method.

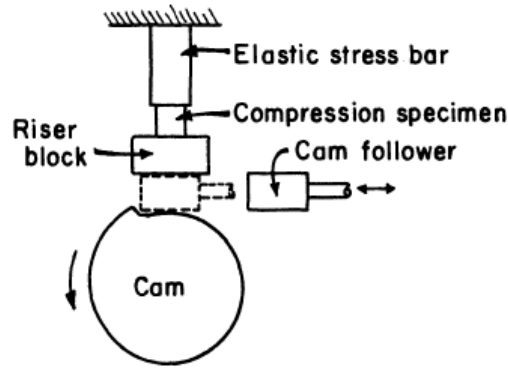


**Figure 2-9 Diagram showing a schematic representation of a cam plastometer (Meyers, 1994).**

### **Split Hopkinson pressure bar**

From the analogy of an elastic wave travelling through a cylindrical bar from which the wave's propagation velocity is calculated, the Hopkinson bar experiment was established.

Hopkinson pressure bar (HPB) experiment became very versatile in material testing at high strain rates. (Lambert & Allen Ross, 2000) utilised HPB to test the strain rate effect on fracture toughness of concrete material within the interval of strain rates  $2s^{-1}$  to  $8 s^{-1}$  and established that an increased strain rate increases fracture toughness. Their analysis combined theoretical analysis and experiment on quasi-brittle material using split Hopkinson pressure bar procedure shown in Figure 2-10, and the generated strain signal is shown in Figure 2-11.

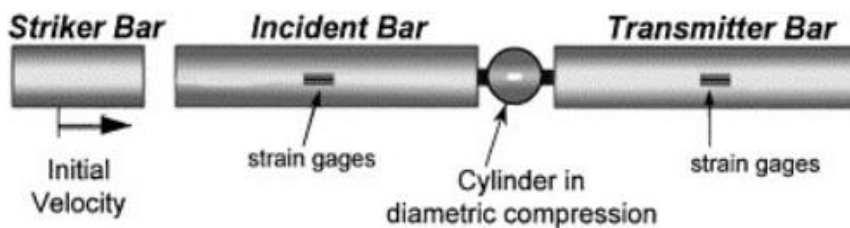


**Figure 2-10 Set-up of Split Hopkinson pressure bar test showing notched splitting tension cylinder (Lambert & Allen Ross, 2000) (Lambert and Allen Ross, 2000).**

The Hopkinson pressure bar test has been widely accepted in strain rate testing between the range of  $10^2 - 10^4 s^{-1}$ . This test involves a striker bar/projectile impacting the incident bar to produce a pulse of length with respect to the specimen. The elastic wave produced travels through the incident bar to the specimen (cylinder in Figure

2-10) placed between the incident and the transmitter bar. The two strain gages on the incident and transmitter bars which are used to measure the direct pulse, transmitted, and reflected pulse shown in Figure 2-11 from which stress-strain relationships are derived.

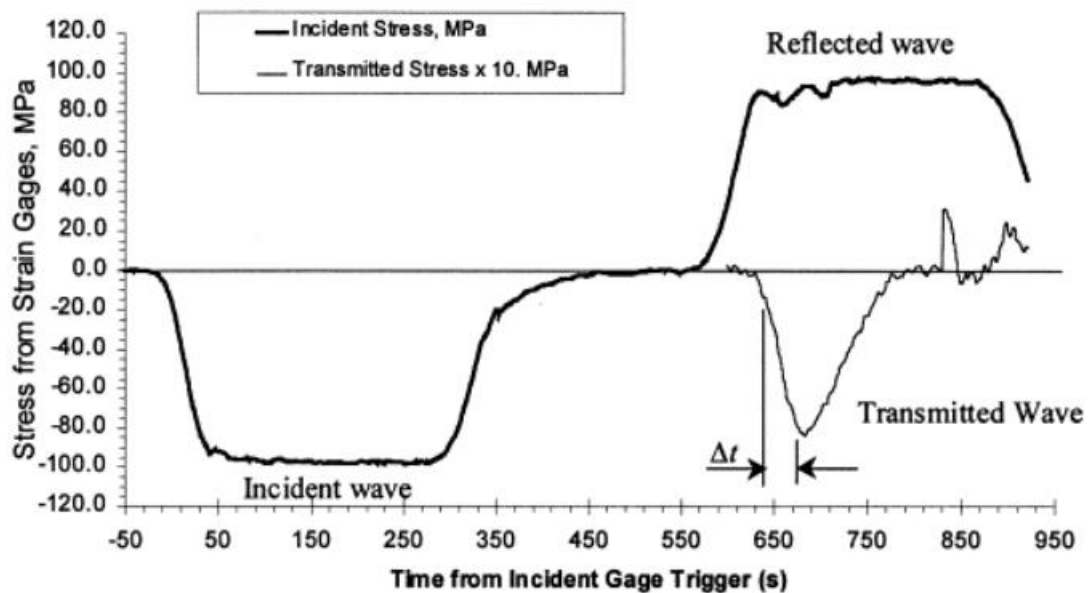


**Figure 2-11 The SHPB strain gauge signals from the splitting tension test (Lambert & Allen Ross, 2000).**

Other researchers (Fan, Xu, Han, Liu, & Huang, 2023), (Marais, Tait, Cloete, & Nurick, 2004), and (Lee & Kim, 2003), also employed the Split Hopkinson pressure bar test for dynamic fracture testing.

An instrumented Charpy test may also be applied to determine dynamic fracture toughness properties. Charpy tests have been around since the 1940s and are used to determine the impact of energy at a given temperature and environmental condition. (Kobayashi, T., Kim, & Morita, 2001) has analysed the Charpy test and its progress since its first presentation in 1901. Using the Charpy impact test, they developed a testing and evaluation system for determining dynamic fracture toughness.

### **High-velocity impact testing techniques**

To create a high-velocity impact, explosive-driven devices are used. The techniques developed are aimed at converting a point explosion produced by the detonator into a



plane detonation. Using a line-wave generator, the point detonation determined is transformed into a line detonation. The plane-wave generator is then used to convert the line explosion to a plane detonation.

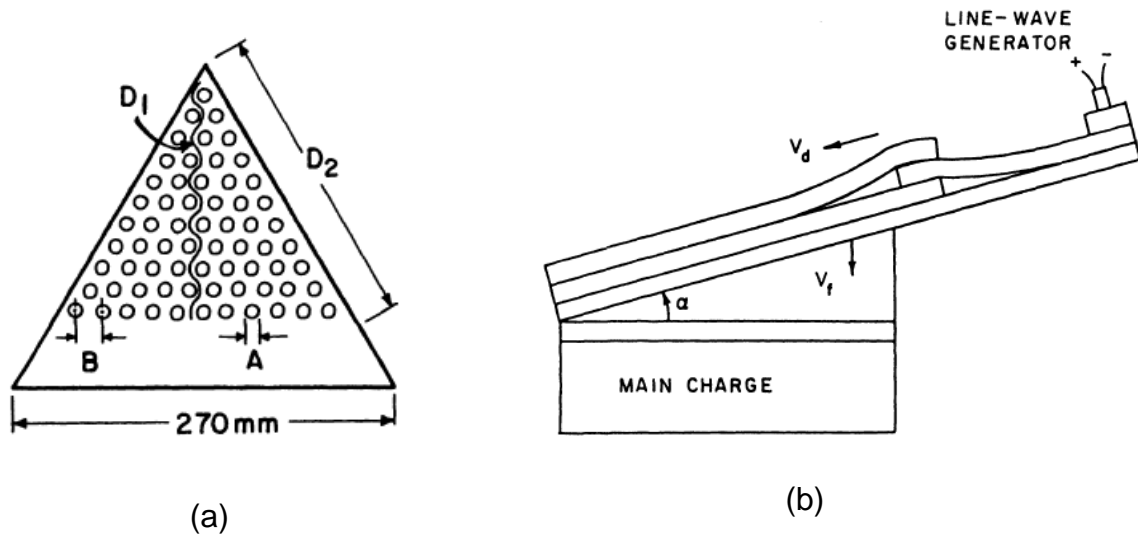


**Figure 2-12 Figure 2 5 (a) Triangular line-wave generator (b) Mousetrap plane-wave generator (Meyers, 1994).**

## 2.5 Testing procedures to determine dynamic fracture toughness.

Large oscillations are present in the load vs time and load vs displacement records of laboratory tests with high loading rates because a considerable inertia effect has the greatest impact on the material behaviour. It becomes challenging to distinguish between material response (such as crack driving force) and loading effects on experiment apparatus (such as shock wave in load cell) when these oscillations are present.

Since its mechanics entail inertia forces, reflected stress waves, and rate-dependent material behaviour, dynamic fracture toughness becomes difficult to quantify. In a straightforward setting, the qualities of a material's fracture toughness are susceptible to microstructural and chemical alterations (Quinn, Sundar, & Lloyd, 2003) (Kleebe, Pezzotti, & Ziegler, 1999). According to (Molinari, Mercier, & Jacques, 2014), and (Owen, Zhuang, Rosakis, & Ravichandran, 1998), there are a few nonlinear phenomena connected to dynamic fracture, including inertia effects, strain rate sensitivity of the material, reflected stress waves, and thermal softening brought on by

adiabatic heating. Dynamic fracture toughness properties are affected by the strain rates at which cracks propagate.

Some procedures have been developed to test materials for fracture toughness at high strain rates such as BS 7448-3, ASTM E180, and E1921. These procedures have specified loading rates in which the tests are to be carried and provide no method for extrapolation at higher rates making it insufficient to be utilised in testing at rates beyond the specified range in the procedures. The material behaviour at increased strain rates changed the process of deformation to adiabatic from fully isothermal since the time is limited for the escape of generated heat out of the material body during deformation.

Some of the mechanical testing methods at high strain rates enumerated in Section 2.3.2 do not follow any specified testing procedure and require very complex equipment. However, the instrumented Charpy testing is included and recommended in ASTM E1921 and E1820 for the determination of dynamic fracture toughness. The testing method in BS 7448-3 is now obsolete and requires substantial revision to include the technological advancement in test machines and recording devices/sensors. It also lacks the appropriate guidance to address the issue of oscillation in the load versus displacement curve.

### **2.5.1 BS 7448 Part 3 procedure**

Test procedures such as BS EN ISO 12135, and ASTM E1820 were developed for testing fracture toughness at quasi-static loading conditions to establish resistance curves or a single fracture toughness parameter. Annex A17 of procedure ASTM E1820 guides the use of Charpy impact-sized specimens, but it is difficult to achieve all the criteria due to specimen size. The British Standards Institute published the BS 7448-3 procedure, which describes the method to determine fracture toughness at high strain rates.

BS 7448-3 includes the evaluation of fracture toughness in terms of stress intensity factor ( $K_{Ic}$ ), crack tip opening displacement (CTOD), and the critical J fracture toughness for metallic materials under stress intensity factor rate ranging from  $3\text{MPa}\cdot\text{m}^{0.5}\cdot\text{s}^{-1}$  and  $3000\text{MPa}\cdot\text{m}^{0.5}\cdot\text{s}^{-1}$ . This testing method was last revised in 2005 but is deemed unsuitable for modern testing machines.

The recording equipment described in the procedure refers to oscilloscopes for reading output signals of frequency to carry out the determination of fracture toughness. These are no longer in use. The sinewave function generator in which the oscilloscope is connected to is shown in Figure 2-13. Figure 2-14 shows the transducers' instrumentation. Both are now obsolete.

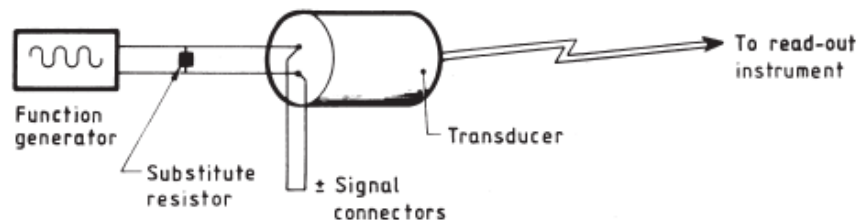


**Figure 2-13 D.C signal conditioners and amplifiers test systems (British Standard Institution,2005).**

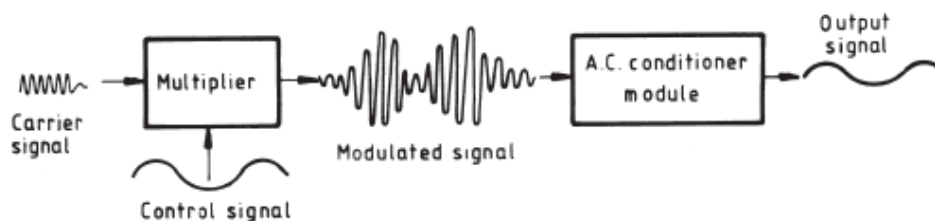


**Figure 2-14 A.C transducers test system (British Standard Institution,2005).**

Recent equipment available in the market for testing fracture toughness at high strain rates requires the use of high-speed cameras to capture the deformation stages for analysis in software. The TWI, Cambridge facility's high loading rate servo-hydraulic test equipment can test up to a displacement rate of 20 m/s. Digital Image Correlation (DIC) measures the force, displacement, and time factors, which offers an alternative method of data recording to supplement the conventional approach.

### **2.5.2 ASTM E1921 procedure**

In this process, the reference temperature and the master cleavage toughness curve that define the ductile-brittle transition shown in Figure 2-15 are measured based on at least six repeat tests. This test procedure was developed due to insufficient information in ASTM E399 (obtains  $K_c$  values on a lower shelf which is insensitive to temperature) and E1820 (obtains  $K_{Jc}$  from the procedure) to determine the reference temperature  $T_0$  in the transition range for ferritic steels and was first developed in 1997

with ASTM E1921-22a (E1921-22a, 2022) as the current version. The ferritic steels used in this procedure have a yield strength ranging from 275 MPa to 825 MPa (Zhu & Joyce, 2012). The loading rate required for testing in this procedure is  $1 \text{ MPa m}^{0.5} \text{ s}^{-1}$  and the crack aspect ratio  $a/W$  is 0.5 for all specimens.

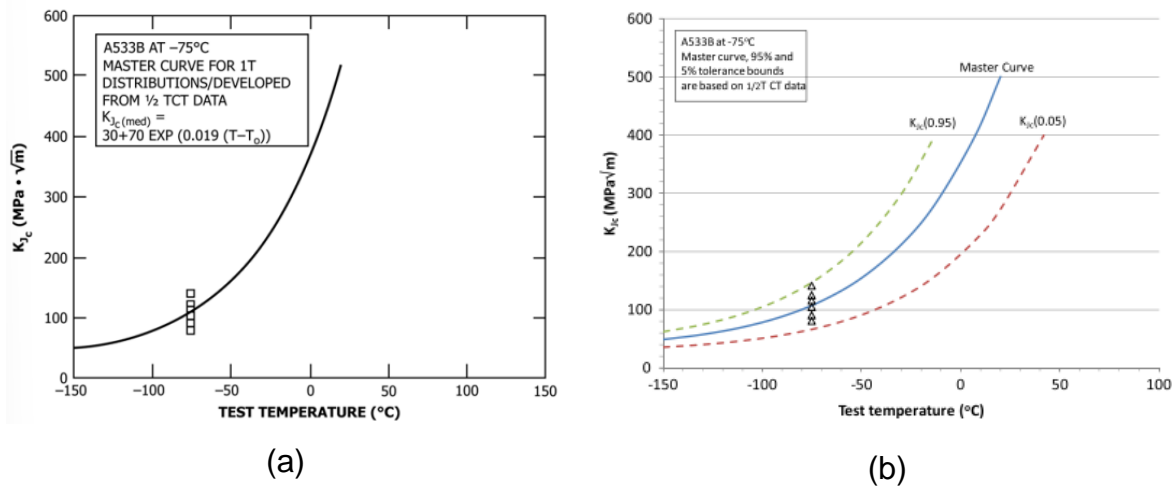


**Figure 2-15 Ductile-to-brittle fracture toughness master curve (a) for 1T specimens (ASTM standard) (b) for A533B steel at 95% upper and 5% lower bounds (Zhu & Joyce, 2012)**

### 2.5.3 ASTM E1820 procedure

In designing for safety, critical cases using ductile high-strength steel, the understanding of behaviour of defects and cracks are important. ASTM has standards for fracture toughness test as well as BSI which allows toughness to be measured in critical values of stress intensity ( $K$ ),  $J$ , and CTOD. It could be measured as a single-point value or tearing resistance curve. This testing method is similar to BS 7448 but differs most in the equations for calculating CTOD. The  $J$ -integral for ASTM E1820 (E1820-23b, 2023) derives CTOD directly from the  $J$ -integral using the equation (2-6), while BS 7448 assumes the rotation of the specimen about a fixed point in the uncracked ligament.

$$\delta = \frac{J}{m\sigma_Y} \tag{2-6}$$

where  $m$  which is a function of material property and crack size is expressed as,

$$m = A_0 - A_1 * \left(\frac{\sigma_{YS}}{\sigma_{TS}}\right) + A_2 * \left(\frac{\sigma_{YS}}{\sigma_{TS}}\right)^2 - A_3 * \left(\frac{\sigma_{YS}}{\sigma_{TS}}\right)^3 \quad (2-7)$$

with,

$$A_0 = 3.18 - 0.22 * (a_0/W), \quad A_1 = 4.32 - 2.23 * (a_0/W), \quad (2-8)$$

$$A_2 = 4.44 - 2.29 * (a_0/W), \quad A_3 = 2.05 - 1.06 * (a_0/W).$$

for SE(B) specimen and

$$A_0 = 3.62, \quad A_1 = 4.21, \quad A_2 = 4.33, \quad A_3 = 2.00 \quad (2-9)$$

for C(T) specimen, while CTOD calculation in the equation (2-6) requires  $\sigma_{YS}/\sigma_{TS} \geq 0.5$ .

All testing procedures for obtaining fracture toughness indicated the loading rate in which the test could be conducted but provided no provision for interpolating at higher loading rates, hence limiting the possibility of measuring fracture toughness at high strain rates. Both ASTM E1921 and E1820 recommend the use of instrumented Charpy testing utilised in this work for fracture toughness testing, however, the procedures are not sufficient to extrapolate results to higher strain rates. BS 7910 (British Standard Institution,2019aa) also has a formula that estimates dynamic fracture toughness from that of quasi-static with a correction factor  $r$  in equation (2-10). This equation is only beneficial if the  $T_0$  is known. It is believed that this solution can be overly conservatism in some cases.

$$r = 9.9 \exp \left[ \left( \frac{T_{0,st}}{190} \right)^{1.66} + \left( \frac{\sigma_Y}{722} \right)^{1.09} \right] \quad (2-10)$$

## 2.6 Analytical solutions for stress intensity factor under impact load

### 2.6.1 Theory of stress intensity factor, $K$ under quasi-static conditions

The energy criterion and stress intensity factor are two approaches for fracture analysis. Defining fracture toughness as a measure of how resistant a material is to fracture is critical. Linear elastic fracture mechanics (LEFM) stress distribution is

mostly applied to account for the effects of crack size, applied force, and specimen geometry, and determine crack driving force, which is expressed as stress intensity factor,  $K$ .

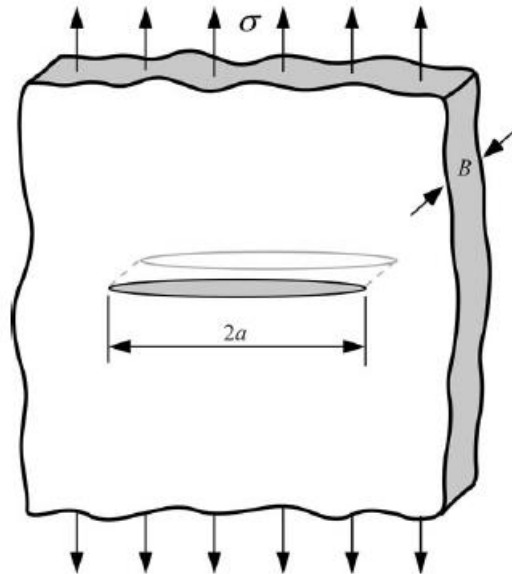


**Figure 2-16 Infinite plate under tensile stress with a crack length of  $2a$  (Anderson, T. L., 2017).**

The stress intensity factor (SIF) measures the magnitude of the elastic stress field singularity in the homogeneous linear-elastic body. Equation (2-11) is the expression of the  $K$ -factor for an infinite plate under uniform stress normal to a crack size  $2a$  as shown in Figure 2-16.

$$K_I = \sigma\sqrt{\pi a} \quad (2-11)$$

where  $\sigma$  is applied stress and  $a$  is the crack length. The stress components shown in Figure 2-17 are proportional to a common constant  $K_I$  in the equations (2-13), (2-14), and (2-15), if known will be used to determine all the stress distribution of the material at the crack tip. The constant  $K_I$  is the stress intensity factor while the subscript  $I$  represents the opening mode I. However, if the material is assumed to fail when stress and strain are critically combined, then a critical stress intensity  $K_{Ic}$  will be required for fracture occurrence, and thus the  $K_{Ic}$  defines fracture toughness. In a finite plate, the  $K$  value has been derived with consideration to the specimen geometry as in Equation (2-12).

$$K = \sigma\sqrt{\pi a}f(a/W) \quad (2-12)$$

where  $f(a/W)$  represents a dimensionless shape function and depends on the test geometry which could be a compact tension test or a three-point bend test. The static stress  $K$  is not suitable for dynamic  $K$  determination since time is considered during dynamic deformation. Section 2.6.2 detailed the dynamic stress  $K$  determination.

The SIF is a fracture toughness parameter for linear elastic fracture whereby the maximum stress is easily determined. For non-linear elastic fracture, the crack opening displacement (COD), and the energy-based methods (J integral) have been employed to measure fracture toughness.

$$\sigma_{xx} = \frac{K_I}{\sqrt{2\pi r}} \cos\left(\frac{\theta}{2}\right) \left[1 - \sin\left(\frac{\theta}{2}\right) \sin\left(\frac{3\theta}{2}\right)\right] \quad (2-13)$$

$$\sigma_{yy} = \frac{K_I}{\sqrt{2\pi r}} \cos\left(\frac{\theta}{2}\right) \left[1 + \sin\left(\frac{\theta}{2}\right) \sin\left(\frac{3\theta}{2}\right)\right] \quad (2-14)$$

$$\tau_{xy} = \frac{K_I}{\sqrt{2\pi r}} \cos\left(\frac{\theta}{2}\right) \sin\left(\frac{\theta}{2}\right) \cos\left(\frac{3\theta}{2}\right) \quad (2-15)$$

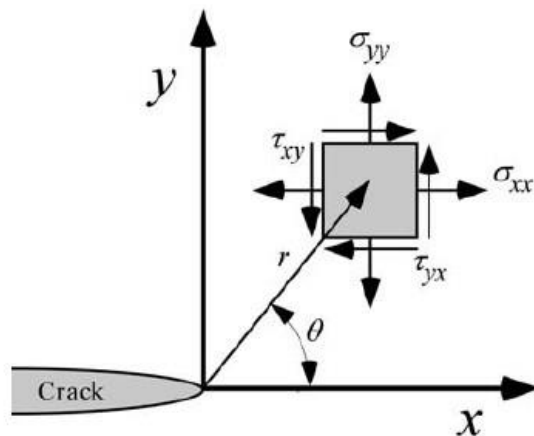


Figure 2-17 The near crack tip and in-plane stresses of an elastic material (Anderson, T. L., 2017)

Metals react spontaneously to dynamic load, and this could cause fracture with limited plastic deformation. Microscopic events that cause fracture in materials occur mostly in the plastic zone and are thus ignored in linear elastic materials. As a result, in the presence of a very tiny plastic zone, fracture cannot form in the singularity-dominated zone. Thus, whether stress intensity is a valid failure criterion in inelastic deformation analysis near the crack tip in materials is raised.

In this project, a Charpy-sized single-edge notched bend (SENB) sample was utilised to ascertain the mechanical properties. Fracture toughness was expressed in terms of  $J$  (equation (2-17)) following BS ISO 12135 for the static fracture toughness of materials, hence,  $K$  can be derived from  $J$  in equation (2-16).

$$K_{J0.2BL} = \sqrt{\frac{EJ_{0.2BL}}{1 - \nu^2}} \quad (2-16)$$

$$J = \frac{K^2}{E'} = m S_Y \delta \quad (2-17)$$

Where  $E' = E$  for plane stress and  $E' = E/(1 - \nu^2)$  for plane strain,  $S_Y$  is the yield strength. Figure 2-18 shows the relationship between fracture toughness and temperature, such that fracture toughness increases with temperature within transition region. The load-displacement curves differ from region to region. The lower shelf region produces a curve of brittle fracture showing the peak load to fracture, while the transition and upper shelf show a curve with the plastic region before fracture making the material behave in a ductile manner before fracture.



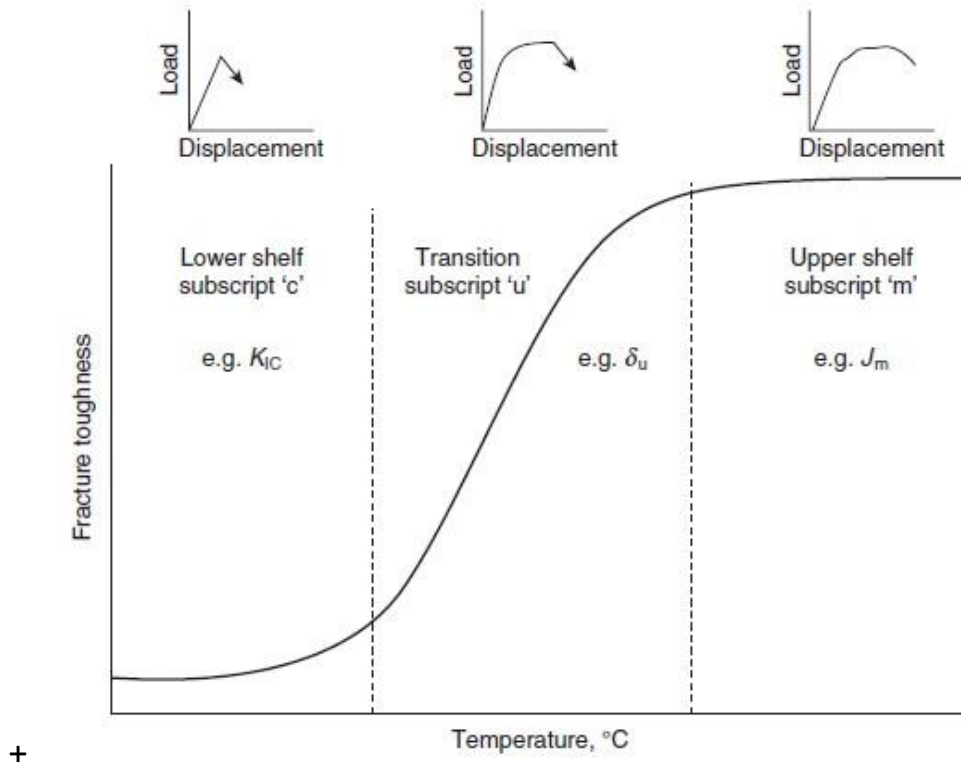


**Figure 2-18 Typical load versus displacement curve shown with the corresponding region on the transition curve (© TWI).**

### 2.6.2 Dynamic Fracture Initiation Toughness $K_{Id}$

When the time-dependent factors are considered in dynamic loading conditions, the stress intensity factor changes from the static measure to adopt the transient element. Dynamic fracture toughness determines the ability of a material to withstand fracture propagation under rapid loading. Inertia effects, material rate dependency, and reflected stress waves frequently aggravate dynamic fracture concerns.

(Rokach, 1998) and (Rubio, Fernandez-Saez, & Navarro, 2003) evaluated  $K_{Id}$  using two items; the temporal evolution of the  $SIF$  and the time to fracture measurement. The temporal evolution of the  $SIF$  was hinged on CMOD, the input load, and load point displacement as seen in Figure 2-19. Dynamic  $SIF$  expressed in Equation (2-18) is a simplified formula of which the derivation was detailed in (Kishimoto, Aoki, & Sakata, 1980). The derivation does not consider the plasticity effect.

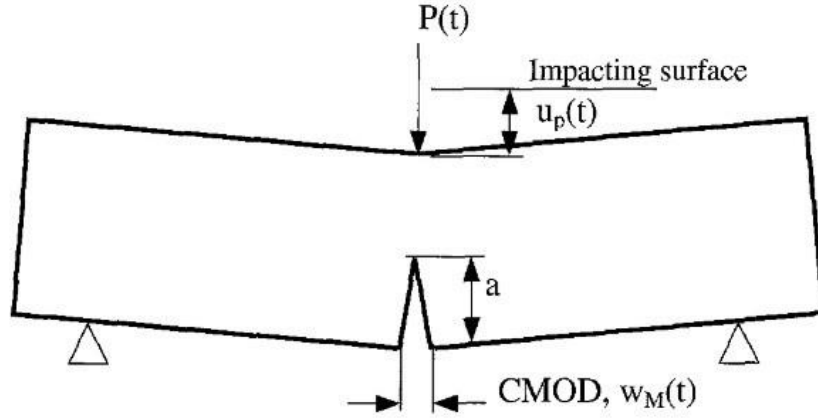


**Figure 2-19 Three-point bend specimen schematic view of deformation (Rubio, Fernandez-Saez, & Navarro, 2003)**

$$K_I(t) = \frac{K_{Is}\omega_I}{P(t)} \int_0^t P(\tau) \sin\omega_I(t - \tau) d\tau \quad (2-18)$$

where,

$$K_{Is} = \frac{3}{2} \frac{P(t)\beta}{B\sqrt{W}} \frac{\sqrt{a/W}}{(1 + 2a/W)(1 - a/W)} f(a/W) \quad (2-19)$$

and,

$$f(a/W) = (1.99 - a/W (1 - a/W)(2.15 - 3.93 a/W + 2.7(a/W)^2)) \quad (2-20)$$

Where  $a/W$  is a ratio of crack length,  $a$ , and specimen width,  $W$ .  $\beta$  could be defined as the ratio between specimen span,  $S$ , and its width,  $W$ , ensuring that the inertia effect has been considered in the fundamental frequency,  $\omega_I$ . Hence,  $K_{Id}$  is expressed in equation (2-21) from (Rubio, Fernandez-Saez, & Navarro, 2003) as a function of  $K_I(t)$  derived from Equation (2-18).  $K_{Id}$  may be obtained experimentally as the stress intensity factor (SIF)  $K_I$  value, which is measured at crack growth initiation time,  $t_f$ . This derivation also utilised a modified split Hopkinson pressure bar device Figure 2-20 for the analysis at a SIF loading rate,  $\dot{K}_I = 10^6 \text{ MPa m}^{0.5} \text{ s}^{-1}$ . Therefore, it is necessary to identify both the temporal evolution of SIF during the specimen loading procedure and the precise moment at which cracks start to appear during the experiment.

$$K_{Id} = K_I(t_f) \quad (2-21)$$

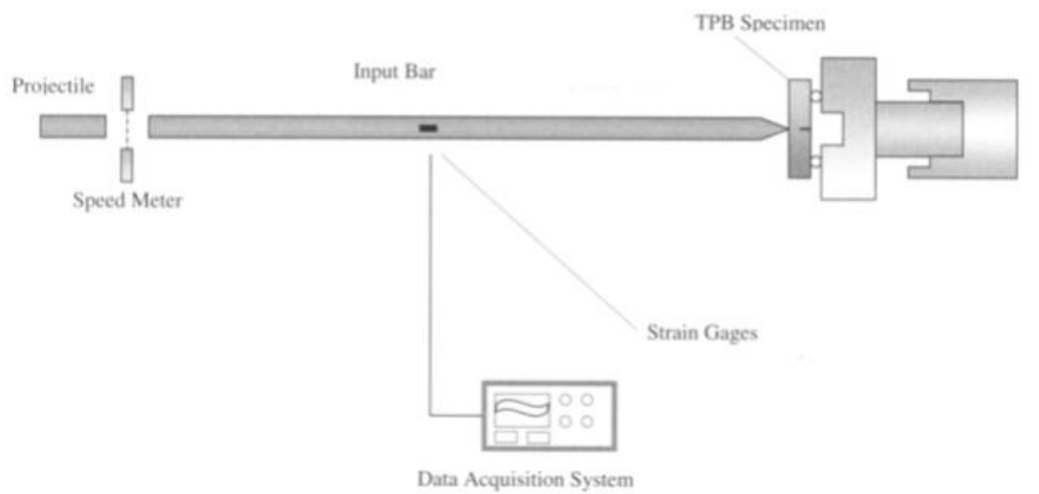
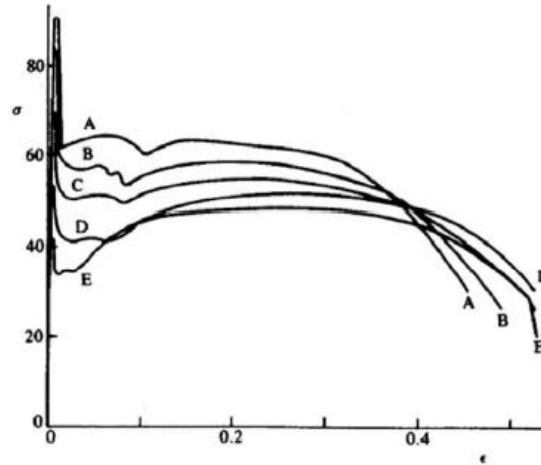


**Figure 2-20 Set-up of Split Hopkinson pressure bar using 3-point bend specimen (Rubio, Fernandez-Saez, & Navarro, 2003).**

## 2.7 Yield strength response under impact load

Yield strength is a mechanical property that determines the resistance of materials to deformation when a driving force is applied for plastic deformation. Yield strength is determined in the laboratory with a regular tensile specimen. Similar to toughness, yield strength is also affected by the loading rate.

(Compbell & Cooper, 1966) results Figure 2-21 showed the decreasing fracture strain with increasing strain rate depicting that at an increased strain rate, materials gravitate to being brittle. (Jasper & Manjoine, 1945) investigation on strain rate effect on mild steel showed an increased lower yield and ultimate tensile strengths under dynamic loading.



Dynamic uniaxial tensile tests on mild steel<sup>(8,16)</sup> at various mean plastic strain rates. A:  $\dot{\epsilon} = 106 \text{ s}^{-1}$ ; B:  $\dot{\epsilon} = 55 \text{ s}^{-1}$ ; C:  $\dot{\epsilon} = 2 \text{ s}^{-1}$ ; D:  $\dot{\epsilon} = 0.22 \text{ s}^{-1}$ ; E:  $\dot{\epsilon} = 0.001 \text{ s}^{-1}$ . 1 unit of ordinate is  $10^3 \text{ lbf/in}^2$  or  $6.895 \text{ MN/m}^2$ .

**Figure 2-21 Tensile test results of dynamic loading on mild steel (Compbell & Cooper, 1966).**

Dynamic yield strength presented by (Kuntiyawichai & Burdekin, 2003) is expressed in Equation (2-22) as a function of yield strength and strain rate.

$$\frac{f_{yd}}{f_y} = 1 + 0.0473 \log\left(\frac{\dot{\epsilon}}{\dot{\epsilon}_0}\right) \quad (2-22)$$

where the reference strain rate  $\dot{\epsilon}_0$  was taken as  $5 \times 10^{-6} \text{ s}^{-1}$ . Equation (2-22) is only applicable for an assumed constant strain rate and not suitable for cyclic loading.

## 2.8 Constitutive laws to predict dynamic material behaviour

Constitutive laws are used in structural analysis to relate applied stress to strains during deformation. Constitutive equations are usually employed to report the state of deformation under different conditions. It is used to express flow stress during deformation as a function of strain, strain rates, temperature, and dislocation density. Some of the parameters in these equations are known material constants, experimentally derived constants, or fitted parameters to agree with the equations.

Two types of constitutive equations were utilised in this study to determine the flow stress of the material at varying strain rates; one was based on the physical equation with a broad range of material properties, and the other relied on experimental factors for its parameter derivations.

The equations are the Taylor equation employing dislocation density for BCC metals adopted from (Galindo-Nava & Rivera-Díaz-del-Castillo, 2012) and the well-known Johnson-Cook equation, which the parameters were determined from experimental data. Other existing equations with reduced constants include Zerilli-Armstrong, (Zerilli & Armstrong, 1987), (Rusinek, Zaera, & Klepaczko, 2007), amongst others. The review of these constitutive equations will be reduced to the first two (dislocation evolution and Johnson-Cook) which were applied in this work.

### **2.8.1 Plastic deformation in ductile metallic materials**

A pure metal in its simplest form consists of a single crystal with a specific orientation and the plastic flow stress is determined through the interaction of dislocation within the crystal. However, most metals are polycrystalline with the addition of alloying elements. The alloying element can be used for different purposes such as maximum strength, wear resistance, hardness, corrosion resistance, and toughness. These elements can be introduced into the steel either substitutional or interstitially element distorting the crystal lattice.

Work hardening reduces the ductility of steel when subjected to plastic deformation (cold working) at a temperature below its recrystallization range. Due to this plastic deformation on the steel, the shear stress needed to plastically deform the steel increases continuously with an increase in dislocation density. This is due to the multiplication of dislocation, which continues until dislocation becomes sessile.

(Andrade, Meyers, Vecchio, & Chokshi, 1994) and (Meyers, 1994) demonstrated that metals have the tendency to transit from ductile to brittle fracture mode under high loading rates. This means the transition curve will shift to the left-hand side when a material is subject to a high strain rate. (Capelle, Furtado, Azari, Jallais, & Pluvinage, 2013) studied the ductile-brittle transition temperature of API 5L X65 steel used in transporting of dense CO<sub>2</sub> considering the geometry, loading rate, and loading mode. They found that X65 steel is suitable for dense CO<sub>2</sub> transportation having obtained through experiment and calculation, transition temperatures lower than -80°C as expected utilising the Charpy test and fracture mechanics' test.

The constitutive equation described in this project models the plasticity behaviour of the selected material. The FCC metals have constant impact energy and do not

undergo crystal structure transformation with temperature changes, and hence are preferred for application in low temperatures. Metallic materials with BCC crystal structure on the other hand exhibit a transitional behaviour in an s-shape form as in Figure 2-22 with a distinct lower shelf behaviour at lower temperatures and an improved toughness in the upper shelf region i.e higher temperatures.

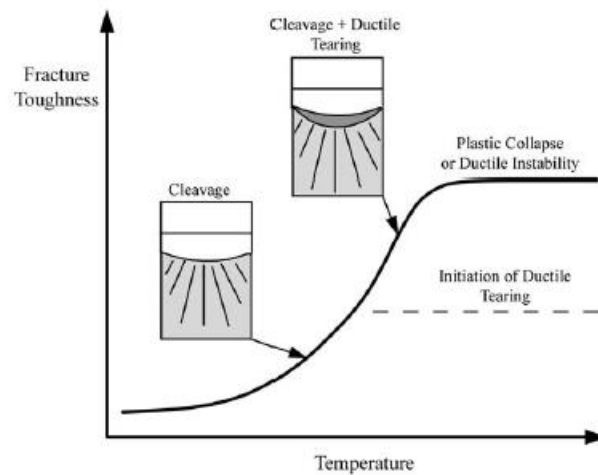


**Figure 2-22 Ductile-brittle transition of ferritic steel (Anderson, P. M., Hirth, & Lothe, 2017)**

### 2.8.2 Dislocation evolution theory

The crystal structure/microstructure of a metallic component will inevitably contain micro or atomic-scale defects. With the addition of alloying elements, they are typically present as irregularity within a crystal structure. It is not uncommon for these irregularities to be manifested as dislocation (with either an extra or missing plane of atoms).

Hence, dislocation becomes central in determining such alloy mechanical properties at plastic deformation. Dislocation evolution and interactions with other crystal defects improve the material's capacity to withstand high strain, resulting in an increase in the material's strength owing to twin growth and interactions with dislocation.

Factors such as density of dislocation  $\rho$ , the distance dislocation moved  $L$ , and their Burgers vector  $b$ , determine the plastic strain that is obtained after dislocation motion. The shear strain resulting from such a slip system is shown in Equation (2-23).

$$\gamma = \rho b L \quad (2-23)$$

The time-dependent variable of the shear strain which is derived by the differentiation of the shear strain gives the shear strain rate in Equation (2-24) which is known as the Orowan relation.

$$\dot{\gamma} = b \rho_m V_d \quad (2-24)$$

Where  $\dot{\gamma}$  is the plastic shear strain rate,  $\rho_m$  is the average mobile dislocation density per unit volume,  $b$  is the magnitude of burgers vector as shown in Figure 2-23, and  $V_d$  is the average velocity of mobile dislocations.

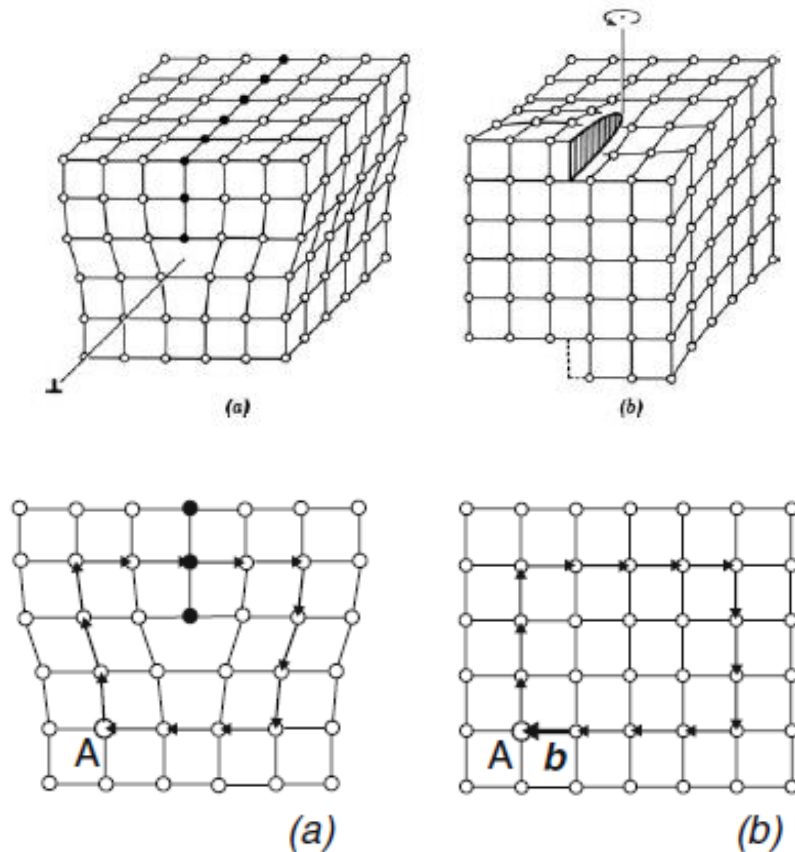


**Figure 2-23 Burgers circuit defining the Burgers vector (a) edge dislocation (b) screw dislocation (Hull & Bacon, 2001).**

(Wang, Atrens, Cousens, & Kinaev, 1999) showed that the X65 steel microstructure is rich in bands of pearlite and ferrite as shown in Figure 2-24 with a grain size of about 10  $\mu\text{m}$  and it is a BCC metal. The difference in the crystallography of cross slip,

dislocation slip, and the mechanism of double kink dislocation motion in Peierls-Nabarro relief (Malygin, 2012) which determines the direction of dislocation lines are the major differences in the deformation behaviour of BCC and FCC metal. Cross-slip in FCC metals has been widely studied; (Duesbery, 1998) utilised copper, (Prakash, Weygand, & Bitzek, 2017) was on nanocrystalline aluminium, and (Nohring & Curtin, 2017) on FCC solid solution alloy.

Following an analysis by (Klepaczko & Brara, 2001), a straightforward relationship for the evolution of total dislocation density demonstrates that, independent of temperature, dislocation density is essentially linear to deformation in the first stages of hardening. As a result, the accumulation of dislocation density from the beginning value to the saturation point is taken into account while analysing the change of mobile dislocation density with plastic strain. During plastic deformation, the rise in dislocation density requires a continuous increase in the applied stress for deformation to progress as stated in Equation (2-25).

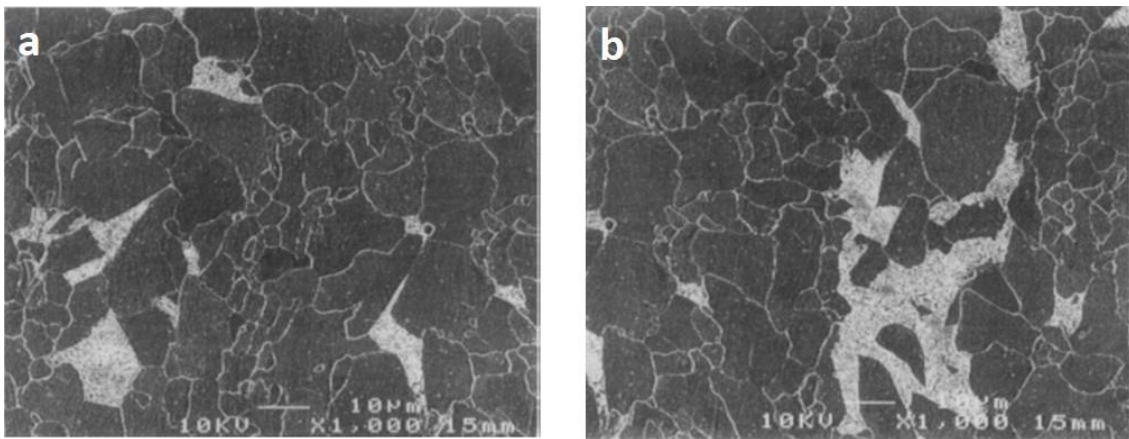


**Figure 2-24 X65 steel microstructure showing (a) pearlite colonies in isolation; (b) pearlite colonies interconnected (Wang, Atrens, Cousens, & Kinaev, 1999).**

$$\frac{d\rho}{d\varepsilon_p} = M - K_a(\rho - \rho_0) \quad (2-25)$$

Where  $M = \frac{1}{bl}$  is the multiplication factor,  $l$  is the dislocation mean free path,  $b$  is the Burgers factor,  $\rho_0$  is the initial dislocation density before deformation,  $K_a$  is the dislocation annihilation factor which may depend on both strain rate and temperature.



The mobile dislocation density relates to total dislocation density in the linear relation  $\rho_m = f\rho$ , where  $f$  is a fraction  $\leq 1.0$  depending on  $\rho$  and temperature. The dislocation velocity,  $v$  is determined through thermal activation which overcomes local obstacles to dislocation motion and (Bammann & Aifantis, 1982) proposed a general expression in Equation (2-26)

$$v = v_0 \exp\left(-\frac{G}{KT}\right) \quad (2-26)$$

Where  $K$  is Boltzmann's constant and  $T$  is the absolute temperature. The reference dislocation velocity is,  $v_0 = \frac{d}{t_w}$ , where  $t_w$  is the time dislocation waits for an obstacle and  $d$  is the distance moved by dislocation between the obstacles. The study of the dislocation dynamics of material crystals formed, moved, and retained during inelastic deformation can aid in determining the plastic behaviour of such materials. This indicates that the appropriate theory of crystal plasticity should consist of the motion, multiplication, and interaction of these dislocations. (Huang, M., Rivera-Díaz-del-Castillo, Bouaziz, & van der Zwaag, 2009), (Voyiadjis & Abed, 2005), applied Orowan's relation of plastic deformation as a dynamic process in which the plastic shear strain rate,  $\dot{\gamma}$  is established from the motion of dislocation with an average velocity  $V_d$ , in the relation  $\dot{\gamma} = b\rho_m V_d$ . The plastic strain rate,  $\dot{\epsilon}_p$  can be defined in terms of mobile dislocation density and dislocation velocity as shown in Equation (2-27),

$$\dot{\epsilon}_p = \bar{m} b \rho_m v \quad (2-27)$$

where  $\bar{m} = \left(\frac{2}{3} M_{ij} M_{ij}\right)^{\frac{1}{2}}$  can represent the Schmidt orientation factor. One important thing to note is that the mobility velocity and mobility density of dislocation increase with the increase of external forces/stresses.

### 2.8.3 Dislocation motion in metallic materials

Taylor's equation of dislocation expresses the shear flow stress  $\tau$  as a function of the total dislocation density  $\rho$  which is shown in Equation (2-28),

$$\tau = \alpha\mu b\sqrt{\rho} \quad (2-28)$$

where  $\alpha$  is an empirical coefficient describing the interaction between dislocations, taken as 0.2 for FCC metals and about 0.4 for BCC metals by (Nabarro, Basinski, & Holt, 1964). (Lavrentev, 1980) discovered that the term defining dislocations interaction,  $\alpha$  values, is constant in FCC metals such as copper but varies with strain rates in BCC metal. Both the stationary and mobile dislocation density need to be addressed in the evolution (accumulation) relations for high-strain rate issues for BCC flow stress that is associated with hardening stress. The expression in Equation (2-29) was formulated by (Huang, M., Rivera-Díaz-del-Castillo, Bouaziz, & van der Zwaag, 2009) for FCC metals' dislocation density analysis.

$$\frac{d\rho}{dt} = \frac{\tau_f \dot{\gamma}}{2E} - \frac{d\rho^-}{dt}. \quad (2-29)$$

The expression in Equation (2-29) with other formulas as detailed in (Huang, M., Rivera-Díaz-del-Castillo, Bouaziz, & van der Zwaag, 2009) work resulted to Equation (2-30) differentiating dislocation density with respect to shear strain. The dislocation evolution of FCC model at high strain rates considered the phonon drag effect and cross slip.

$$\begin{aligned} \frac{d\rho}{d\gamma} = \frac{\tau_0}{\mu b^2} \left[ 1 - \exp\left(-\frac{\dot{\gamma}}{\dot{\gamma}_0}\right) \right] + \frac{\beta}{b} \sqrt{\rho} \\ - \frac{\mu b^4}{8\pi x V} \frac{v_D}{\dot{\gamma}} \times \exp\left[-A \ln\left(\frac{\mu b^4}{16\pi x V} \frac{v_D}{\dot{\gamma}}\right) + \frac{\tau V}{\mu b^3}\right] \rho. \end{aligned} \quad (2-30)$$

where  $\mu$  represents the shear modulus,  $b$  represents the magnitude of the Burgers vector,  $\dot{\gamma}$  denotes the shear strain rate,  $V$  is the activation volume,  $\beta$  as a constant accounting for the interaction between dislocations,  $v_D$  is Debye frequency,  $x$  represents the stacking fault energy,  $\tau$  is the shear stress,  $\tau_0$ ,  $\dot{\gamma}$ , and  $A$  are fitted parameters. True normal stress and strain were derived from  $\sigma = M\tau$  and  $\varepsilon = \gamma/M$  respectively, with  $M$  being the Taylor factor.

Using the same model, it analytically expresses the flow stress  $\sigma$  in Equation (2-31) proposed by (Kocks & Mecking, 2003) for plastic deformation,

$$\sigma = \sigma_0 + \alpha M \mu b \sqrt{\rho} \quad (2-31)$$

where  $\mu$  represents shear modulus, and  $b$  denotes the magnitude of the Burgers vector.

## 2.8.4 Theory of the Johnson-Cook Model

Plastic deformation sets in when the elastic limit of stress in a ductile material is exceeded, and it can exist in both dynamic and quasi-static deformation. Strain rate and not the velocity of deformation is regarded as the important parameter in producing dynamic deformation as shown in Equation (2-32) which can be in the range of  $10$  to  $10^8 \text{ s}^{-1}$ .

$$\dot{\varepsilon} = \frac{d\varepsilon}{dt} \quad (2-32)$$

From the classification Figure 2-8, the lower strain rates need not consider the effect of inertial forces due to the effect of wave propagation since equilibrium is reached. However, a higher strain rate has an increased effect of these inertial forces. Material's constitutive properties are used to determine the deviatoric response of a continuum subjected to some random thermomechanical loading, which is reflected in a change of shape at a material element. The material constitutive properties can be modelled in terms of elastic, plastic, and viscous characteristics. The generic equation (2-33),

$$\sigma = f(\varepsilon \dot{\varepsilon} T) \quad (2-33)$$

describes the constitutive behaviour relating to material flow stress, strain, strain rate, and temperature. This constitutive equation is used to describe plastic deformation at a high strain rate. Since plastic deformation is an irreversible process that depends on the path, the reaction of the material at a certain stress-strain ( $\sigma$ - $\varepsilon$ ) point is reliant on the distortion substructure made. As there exist varieties of distortion substructures that are reliant on strain rate, stress state, and temperature, it is necessary that the term "deformation history" be added to the above function, hence equation (2-34);

$$\sigma = f(\varepsilon \dot{\varepsilon} T \text{ deformation history}) \quad (2-34)$$

Metals and other materials such as polymers deform plastically by shear and are thus driven by shear stresses. Hence, shear stresses and strains ( $\tau$  and  $\gamma$ ) are being considered rather than the scalar quantities of effective stress and effective strain ( $\sigma_{eff}$  and  $\varepsilon_{eff}$ ), since we know that shear stresses are important components in plastic deformation.

The investigation of material behaviour at a high strain rate for industrial applications requires accurate description. JC parameters are applied in analysis such as FEM in Abaqus to model the plasticity and ductile damage effect. (Johnson, Hoegfeldt, Lindholm, & Nagy, 1983) applied the basic principles of parabolic hardening, temperature effect, and strain rate effect to propose a constitutive Equation (2-35).

$$\sigma = (A + B\varepsilon^n) \left(1 + C \ln \frac{\dot{\varepsilon}}{\dot{\varepsilon}_0}\right) \left(1 - \frac{T - T_r^m}{T_m - T_r}\right) \quad (2-35)$$

where  $A$ ,  $B$ ,  $n$ ,  $C$ , and  $m$  are material constants representing the yield stress at reference conditions, a strain hardening coefficient, a strain hardening constant, a strengthening coefficient of strain rate, and a temperature constant respectively.  $\sigma$  is the effective stress,  $\varepsilon$  is the equivalent plastic strain,  $\dot{\varepsilon}$  is the strain rate,  $\dot{\varepsilon}_0$  is the reference strain rate taken as  $1 \text{ s}^{-1}$ . With this equation, Johnson and Cook tested materials to determine their material constants, and the JC equation has been widely accepted in plastic deformation analysis.

The JC constants were not determined from first principles but the use of experimental data to fit the model employing some optimisation approach. (Dorogoy & Rittel, 2009) used the regression analysis method to determine JC constants. Other optimisations methods were employed to determine material behaviour using experimental data by researchers, for example, genetic algorithm (GA) was utilised by (Dimatteo, Vannucci, & Colla, 2013) to predict the mean flow stress of a rolling process which was found to perform better than the industrial process previously applied.

JC model parameters were also determined by optimisation methods for different materials such as (Huang, Z. P., Gao, Wang, & Wang, 2016) utilised cluster global algorithm, and (Karkalos & Markopoulos, 2018) used the fireworks algorithm which was introduced in 2010 by (Tan & Zhu, 2010) for AISI 316L stainless steel. The derived JC plastic constants obtained in the literature for X65 steel are shown in Table 2-2.

**Table 2-2 Johnson-Cook constitutive model parameters for X65 steel**

<b>A (MPa)</b>	<b>B (MPa)</b>	<b>n</b>	<b>C</b>	<b>m</b>	<b>Source</b>
<b>464</b>	401	0.439	0.047	0.464	(Cortis, Nalli, Sasso, Cortese, & Mancini, 2022)
<b>500</b>	857	0.34257	0.032604	-	(El-Danaf et al., 2013)

### **2.8.5 Johnson-Cook failure model**

For model representation and simulation in finite element tools such as Abaqus, constitutive equations are incorporated. The JC ductile and damage models are used extensively in Abaqus to model dynamic/explicit conditions for plastic deformation. JC damage initiation criterion is ductile damage suitable to predict damage onset due to growth, nucleation, and coalescence of voids in ductile material. JC dynamic failure model was utilised as it is suitable for metals deforming at a very high strain rate. The pressure stress and deviatoric stress are set to zero, and element deletion is chosen (for flow stress in tension) such that elements that meet the failure criterion are deleted. In the case of quasi-static simulations that require element removal, models such as Progressive Damage and Failure, Gurson metal plasticity are recommended.

These parameters were also used in other simulations such as metal forming derived by (Murugesan & Jung, 2020) to determine the flow stress. Methods such as the Levenberg-Marquardt algorithm were proposed by (Shrot & Baker, 2011) to determine the JC constants through the process of chip morphology and cutting force during machining. (Bobbili, Ramakrishna, Madhu, & Gogia, 2015) adopted the approach of artificial neural network for material behaviour at high strain rates which was concluded to perform better than the JC model on the 7017-aluminium alloy. (Osorio-Pinzon, Abolghasem, & Casas-Rodriguez, 2019) utilised the analytical approach to estimate JC constants for temperature distribution during the machining process. The JC damage parameter is defined in Equation (2-36) (Sharma, Chandel, Bhardwaj, Singh, & Mahajan, 2018).

$$D = \sum \frac{\Delta \varepsilon}{\varepsilon_f} \geq 0 \quad (2-36)$$

where  $\Delta \varepsilon$  is the incrementation in plastic strain,  $\varepsilon_f$  is the equivalent plastic strain to fracture, and  $D$  is an internal variable increasing monotonically with plastic deformation up to the value of 1 during total failure occurrence. Equation (2-37) was adopted as seen in (Banerjee, Dhar, Acharyya, Datta, & Nayak, 2015), (Zhang, Outeiro, & Mabrouki, 2015) and (Murugesan & Jung, 2020) for modelling JC damage constants.

$$\varepsilon_f = \left( d_1 + d_2 \exp \left( d_3 \frac{\sigma_m}{\sigma_{eq}} \right) \right) (1 + d_4 \ln \dot{\varepsilon}_p^*) (1 + d_5 T^*) \quad (2-37)$$

Where  $d_1$  through  $d_5$  are damage constants,  $\sigma_m$  is the mean stress, and  $\sigma_{eq}$  is the equivalent stress.

### 2.8.6 Theory of thermal diffusivity and temperature rise during high strain rate testing.

When temperature increases, the dislocation kinetics/interaction increases. The dislocation density usually decreases as the temperature increases due to enhanced annihilation and hence, metals soften when heated. Thermal diffusivity is used to describe the behaviour of a material when reacting to change in temperature by characterizing the conduction of heat which is unsteady. Thermal diffusivity,  $\varphi$  describing the rate at which temperature spreads in a material is shown in Equation (2-38) as a ratio of heat conductivity and heat capacity at constant pressure,

$$\varphi = \frac{\lambda}{\rho C_p} \quad (2-38)$$

where  $\lambda$  is thermal conductivity,  $\rho$  is the mass density and  $C_p$  is the heat capacity.

At quasi-static tensile or compressive testing, little or no significant temperature increase is observed which made its plastic deformation an isothermal process. However, this is not the case of dynamic testing as the material has little or no time for heat exchange with the environment and the heat is trapped within the specimen, giving rise to an adiabatic process. Thermal diffusion distance,  $d_\varphi$  measures the distance this heat travels within the specimen and is given in Equation (2-39).

$$d_{\phi} = 2\sqrt{\phi t} \quad (2-39)$$

This can be represented in terms of strain and strain rate since  $\dot{\varepsilon} = \varepsilon/t$  as in Equation (2-40).

$$d_{\phi} = 2\sqrt{\phi \frac{\varepsilon}{\dot{\varepsilon}}} \quad (2-40)$$

Where  $\varepsilon$  is the strain and  $\dot{\varepsilon}$  the strain rate. The increased strain rate test reduces the deformation time to yield a reduced thermal diffusion distance. The deformation work at this high rate is converted to heat to increase the attendant temperature of the specimen. The effect of this temperature rise on material behaviour is profound due to thermal softening, that could lead to shear instability. By considering that a fraction of this temperature rise is converted into heat during plastic deformation, the associated temperature rise could be determined with a constitutive equation (2-41)

$$\Delta T = \frac{\beta}{\rho C_p} \int_0^{\varepsilon_f} \sigma d\varepsilon = \frac{0.9}{\rho C_p} \int_0^{\varepsilon_f} \sigma d\varepsilon \quad (2-41)$$

By taking the work to heat ratio  $\beta$ , 0.8-0.9 was determined for 4340 steel by (Mason, Rosakis, & Ravichandran, 1994). The JC flow stress is utilised which was substituted to determine equation (2-42) and  $m$  assumed equal to 1 for simpler derivation as adopted from (Meyers, 1994).

$$\int_{T_0^*}^{T_f^*} \frac{dT^*}{1 - T^{*m}} = \frac{0.9(1 + C \log \dot{\varepsilon}/\dot{\varepsilon}_0)}{\rho C_p (T_m - T_r)} \int_0^{\varepsilon_f} (\sigma + B\varepsilon^n) d\varepsilon \quad (2-42)$$

## 2.9 Dislocation evolution theory in BCC metals

Body-Centered Cubic (BCC) is a crystal structure of ferritic steel that exhibits ductile to brittle transition (Figure 2-22.) in which the metal would be ductile at room temperature but become brittle at lower temperature or at extremely high strain rates. The plastic deformation that occurs in metals at room temperature are by dislocation motion.

In this study, dislocation evolution analyses which captured the effect of dislocation density as well as JC model was used to model the flow stress of X65 steel at high strain rate. It went further to represent the high strain rate as an adiabatic process capturing the rise in temperature during plastic deformation. The determined ductile and damage constants were employed for FEM analysis to model high strain rate material behaviour and fracture toughness. Also, machine learning algorithm was applied to predict the stress-strain curve and fracture toughness of X65 steel.

In the analytical approach, modifications were made to existing irreversible thermodynamic model to incorporate the behaviour of the material at high strain rates. At low strain rate, plastic deformation is regarded to undergo an isothermal process allowing exchange of heat with the environment. This process makes it fit to model quasi-static plastic deformation with a constant temperature. (Galindo-Nava & Rivera-Díaz-del-Castillo, 2012) have applied the Kocks-Mecking formulation corresponding with dislocation evolution in Equation (2-43) considering dynamic recovery and cell formation effects in their model for BCC metals, where the temperature effect remains constant. Kocks-Mecking (KM) theory accounts for both generation and annihilation of dislocation.

$$\frac{d\rho}{d\gamma} = \frac{k_1}{b} \sqrt{\rho} - f\rho \quad (2-43)$$

This model was for quasi-static loading conditions and was modified in this research to describe the plasticity in BCC metals using API 5L X65 specimen considering high strain rate effect. This theory is based on thermostatistical description of dislocation annihilation, formation energy, and statistical entropy. It describes the stress-strain response for the specimen. (Anderson, T. L., 2017) explained that BCC metals have increased dislocation cross-slip rate and therefore its dislocation evolution is modified from Equation (2-43) by expanding the coefficients of dislocation mean free path  $k_1\sqrt{\rho}$  and dynamic recovery,  $f_{BCC}\rho$  by a factor of  $(48/12).(8/12) = 8/3$  as shown in the Equation (2-44).

$$\frac{d\rho}{d\gamma} = \frac{3k_1}{8b} \sqrt{\rho} - \frac{8}{3}f_{BCC}\rho \quad (2-44)$$

Where  $f_{BCC}$  is the coefficient of dynamic recovery for BCC metal,  $k_1$  is the coefficient of dislocation storage and  $b$  is the magnitude of Burgers vector. The coefficients



parameters are determined from fitting the experimental data. The  $f_{BCC}$  parameter was determined from Equation (2-45) and the extensive derivation approach was derived in (Galindo-Nava & Rivera-Díaz-del-Castillo, 2012) studies.

$$f_{BCC} = \frac{N_A}{w_a} \rho_a V_{sys} \quad (2-45)$$

$$= \frac{N_A \rho_a b^2 l^*}{w_a} \frac{T \Delta S_{BCC}}{\frac{1}{2} \mu b^3 + \sigma_Y A_{act} b^3 + \frac{l^*}{b} \delta(T) (E_f + k_B T \ln c_m) - 2N k_B T \ln \left( \frac{\dot{\epsilon}_0 + \vartheta}{\dot{\epsilon}} \right)}$$

In this work, the X65 steel which is a BCC metal was utilised for all testing at quasi-static and high strain rates. With the application of high strain rate on BCC metals, the plastic deformation was often adiabatic, causing rise in temperature in the specimen. This temperature rise causes thermal softening and affects the material behaviour. This work has considered the effect of this temperature rise in plastic deformation for X65 steel at high strain rate incorporating the (Galindo-Nava & Rivera-Díaz-del-Castillo, 2012) formulation for low strain rates. The dynamic recovery coefficient  $f_{BCC}$  was modified from equation (2-41), in which the flow stress  $\sigma$  in the temperature change was derived by adopting the JC formulation in Equation (2-35) and the final temperature  $T_f$  is presented in Equation with change in temperature as a factor of strain and strain rate as shown in the Equation (2-46).

$$T_f = \left[ 1 - \left( 1 - \frac{T_0}{T_m} \right) \exp \left[ - \frac{0.9 \left( 1 + C \ln \frac{\dot{\epsilon}}{\dot{\epsilon}_0} \right) \left( \sigma_0 \varepsilon + \frac{\beta \varepsilon^{n+1}}{n+1} \right)}{\rho c_p (T_m - T_0)} \right] \right] \times T_m \quad (2-46)$$

The change in temperature affected the dynamic recovery coefficient  $f_{BCC}$ , and this was embedded in Equation (2-44)(2-45) to yield the modification shown in Equation (2-47).

$$f_{BCC} = \frac{N_A}{w_a} \rho_a V_{sys} \quad (2-47)$$

$$= \frac{N_A \rho_a b^2 l^*}{w_a} \frac{\Delta T \Delta S_{BCC}}{\frac{1}{2} \mu b^3 + \sigma_Y A_{act} b^3 + \frac{l^*}{b} \delta(T) (E_f + k_B T \ln c_m) - 2N k_B T \ln \left( \frac{\dot{\epsilon}_0 + \vartheta}{\dot{\epsilon}} \right)}$$

The determined flow stress was compared with the flow stress for JC model, and the determined JC parameters were applied to FEM to simulate the material behaviour at dynamic strain rates.

## 2.10 FEM application of JC parameters for Dynamic/Explicit model

The finite element method has been advanced in predicting physical parameters for plastic deformation process, such as stresses generated, strains, forces, and temperatures. The accuracy of FEM modelling depends on the constitutive model for the flow stress description in plastic deformation behaviour. FEM is applied in modelling both static and dynamic conditions using Abaqus/Standard or Abaqus/Explicit respectively. There are different constitutive models that could be applied in Abaqus to model the plasticity hardening (Isotropic, Kinematic, Multilinear-Kinematic, Johnson-Cook, User, and Combined) and damage for ductile metals including: Ductile damage, Johnson-Cook damage, Shear damage, FLD (Forming Limit diagram) damage, FLSD (Forming limit stress diagram) damage, M-K (Marciniak-Kuczynski) damage, MSFLD (M schenborn-Sonne forming limit diagram) damage parameters of a material. Figure 2-25 shows some damage initiation criteria in ABAQUS and the Ductile criteria was applied with the Johnson-Cook parameters for metallic parent material.

The Johnson-Cook plasticity and damage parameters were utilised to investigate the behaviour of X65 material at high strain rates. The JC parameters required for the investigation were determined from experimental analysis and optimization method using the steps in Figure 2-26. Round tensile tests were done to determine the quasi-static material properties while flat tensile tests were to determine the material properties at high strain rates. Both sample configurations were selected due to the type of machine fixture available to support the experiments. JC model is widely used for fracture analysis in Abaqus model, for example, (Flores-Johnson et al., 2012) determined the JC ductile constants for 316L austenitic steel plate to model a weld and utilise the shear failure fracture criterion to capture the plastic strain induced by post-weld plastic damage. (Sharma, Chandel, Bhardwaj, Singh, & Mahajan, 2018) investigation showed the use of JC parameters for impact modelling in Abaqus/Explicit which shows spalling and scabbing occurring at impact velocity of 852 m/s.

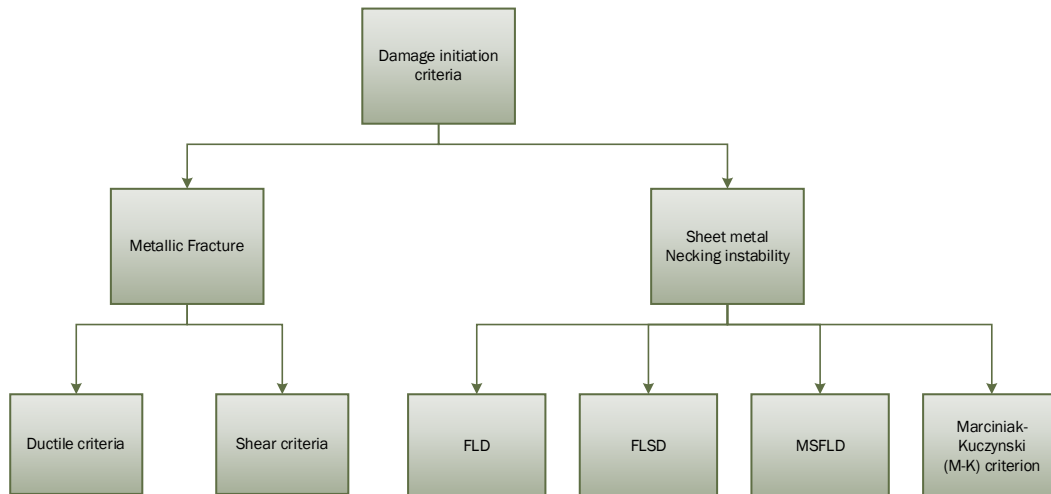


**Figure 2-25 ABAQUS Damage initiation criteria for ductile material**

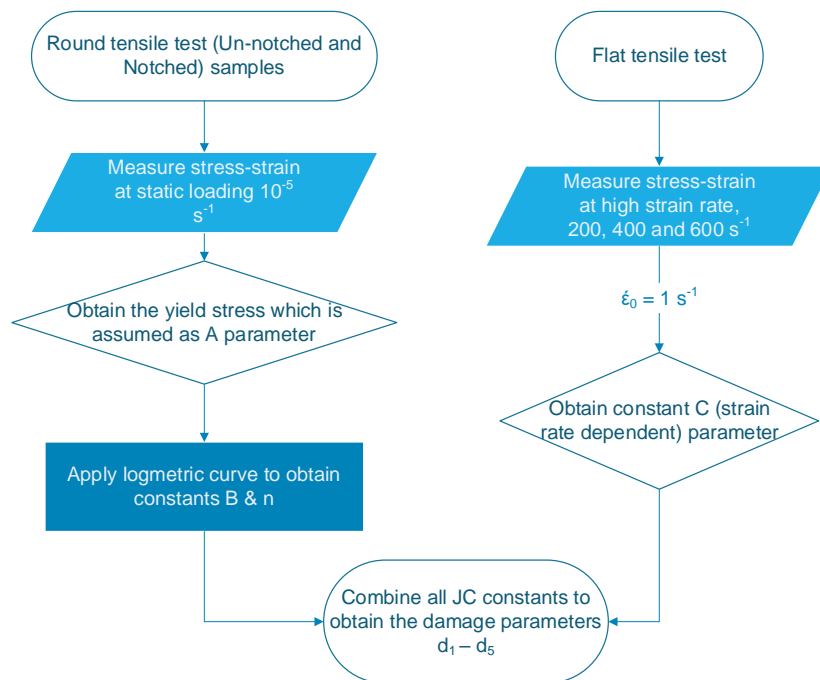


**Figure 2-26 Process of determining JC plasticity and damage parameters for FEA.**

## 2.11 Theory of machine learning for stress-strain curve prediction and fracture toughness prediction

Several approaches have been employed in the prediction of stress-strain curves using artificial neural networks (ANN). The flow of 316 stainless steel was studied by (Gupta, Singh, Reddy, & Hariharan, 2012) using ANN model for the regime of dynamic

strain aging. They utilise features like range of temperature and strain rates between  $10^{-4}$  to  $10^{-2} \text{ s}^{-1}$  in their studies. (Gangi Setti & Rao, 2014) predicted stress strain curve of near beta titanium alloy as a volume fraction of alpha ( $\alpha$ ) and beta ( $\beta$ ). They utilised the strain and volume fraction of  $\alpha$  as the inputs and stress as the output. They employed multilayer perceptron architecture with back propagation and obtained a stress-strain curve as shown in Figure 2-27, in which the pattern correlation coefficient  $R$  of 0.99 and 0.97 respectively show a good correlation in the experimental and calculated (ANN) stress-strain curve.

To advance the method of fracture toughness prediction, the Multi-Layer Perceptron (MLP) Regressor was used for stress-strain curve prediction, and further the Random Forest Regression was applied to predict fracture toughness of X65 steel from experimental data available. Random Forest Regressor was used due to its high level of accuracy over decision tree algorithm in their prediction results and the ability to reduce overfitting.

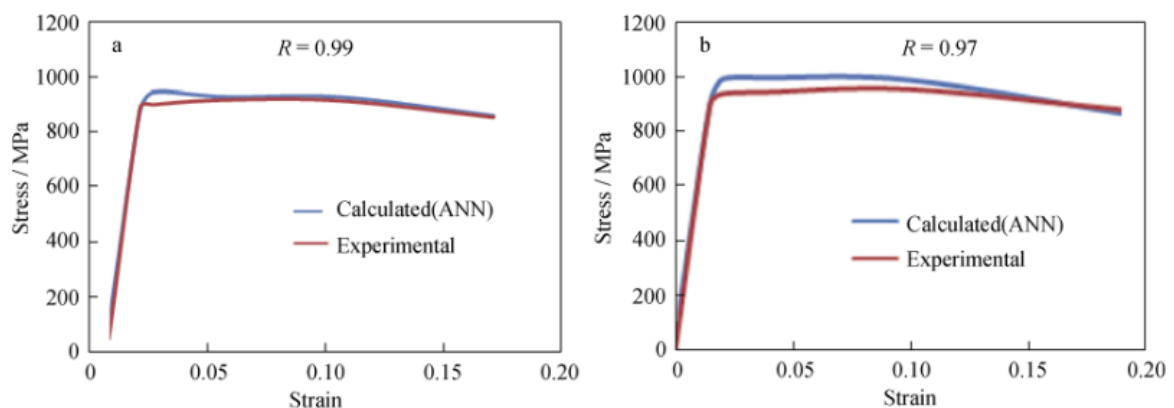


**Figure 2-27 Stress-Strain curve for experiment and prediction (ANN) at (a) 18 % and (b) 24 % volume fraction of  $\alpha$  (Gangi Setti & Rao, 2014).**

### 2.11.1 Theory of MLPRegressor

MLPRegressor is a Scikit-learn neural network model that optimizes using the stochastic gradient descent or the squared error using Limited-memory Broyden–Fletcher–Goldfarb–Shanno (LBFGS) for training. As the name implies, Multilayer Perceptron contains several perceptron arranged into layers which uses back-propagation for its training. MLPRegressor model uses the iteration method for its training at each time step to compute the partial derivative of loss function with respect

to the parameters of the model. As with other algorithms, this model comprises of regularization term in addition to the loss function to prevent overfitting of the model. This model was adopted owing to its ability to perform problems of optimization that consists of many variables, and its support for multi-output regression with more than a target.

The scikit-learn project is mainly imported in Python programs and thus requires basic knowledge of Python programming. (Buitinck et al., 2013) designed the API for machine learning software and discussed how it is mapped in Python programming language. Most of the easy-to-read codes are being imported to perform assigned tasks. A sample of three layers MLP with an input layer, one hidden layer, and a scalar output layer is shown in Figure 2-28. Scikit-learn is a module in python that integrates varying machine learning algorithms capable of solving unsupervised and supervised problems for small to medium scale (Pedregosa et al., 2011).

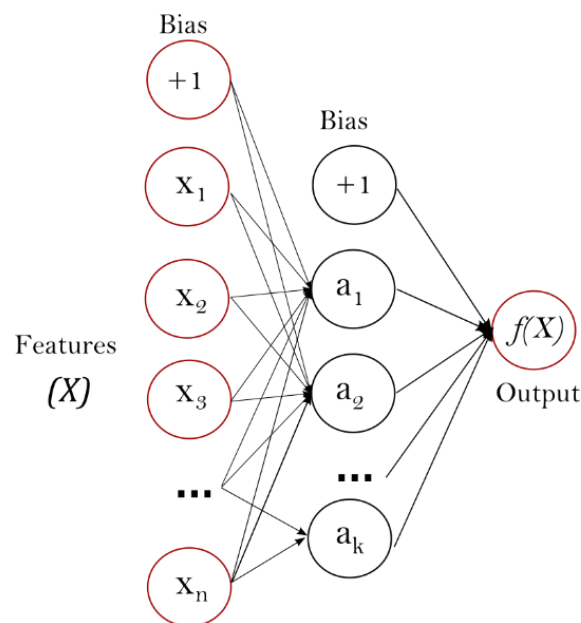


**Figure 2-28 MLP Regressor framework with one hidden layer ([https://scikit-learn.org/stable/modules/neural\\_networks\\_supervised.html](https://scikit-learn.org/stable/modules/neural_networks_supervised.html))**

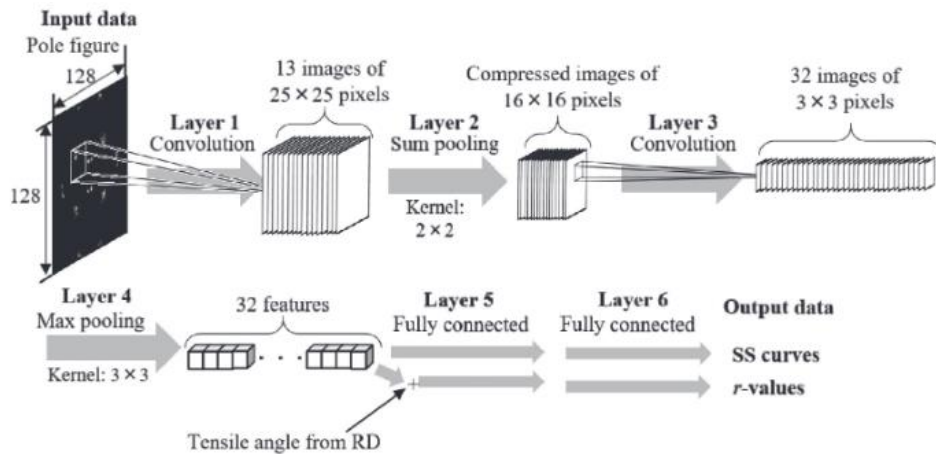


**Figure 2-29 A convolutional neural network with pooling layers connected two full layers for stress-strain curve prediction (Koenuma, Yamanaka, Watanabe, & Kuwabara, 2020)**

### 2.11.2 Theory of Random Forest Regressor

The fracture toughness of X65 material was also predicted using the Random Forest regressor model. The model can be utilised for the classification and regression of supervised learning that fits some classifying decision trees to sub-samples of the applied dataset. The output for regression is obtained by the individual trees returning the mean or average prediction to control over-fitting and improve the predictive accuracy.

The algorithm was first created in 1995 by (Ho, 1995) using another method of random subspace (Ho, 1998). A random forest uses an ensemble learning regression method for prediction. It is imported from the sklearn package with ensemble learning and variables are assigned to it. This algorithm is by no exception without limitation as studied (Au, 2018) for analysis of the absent level problem on the model's performance, and whose effects have never been thoroughly examined. The random forest regressor is constructed as shown in Figure 2-31 comprising of number of trees from which prediction such as in Figure 2-32 are obtained.

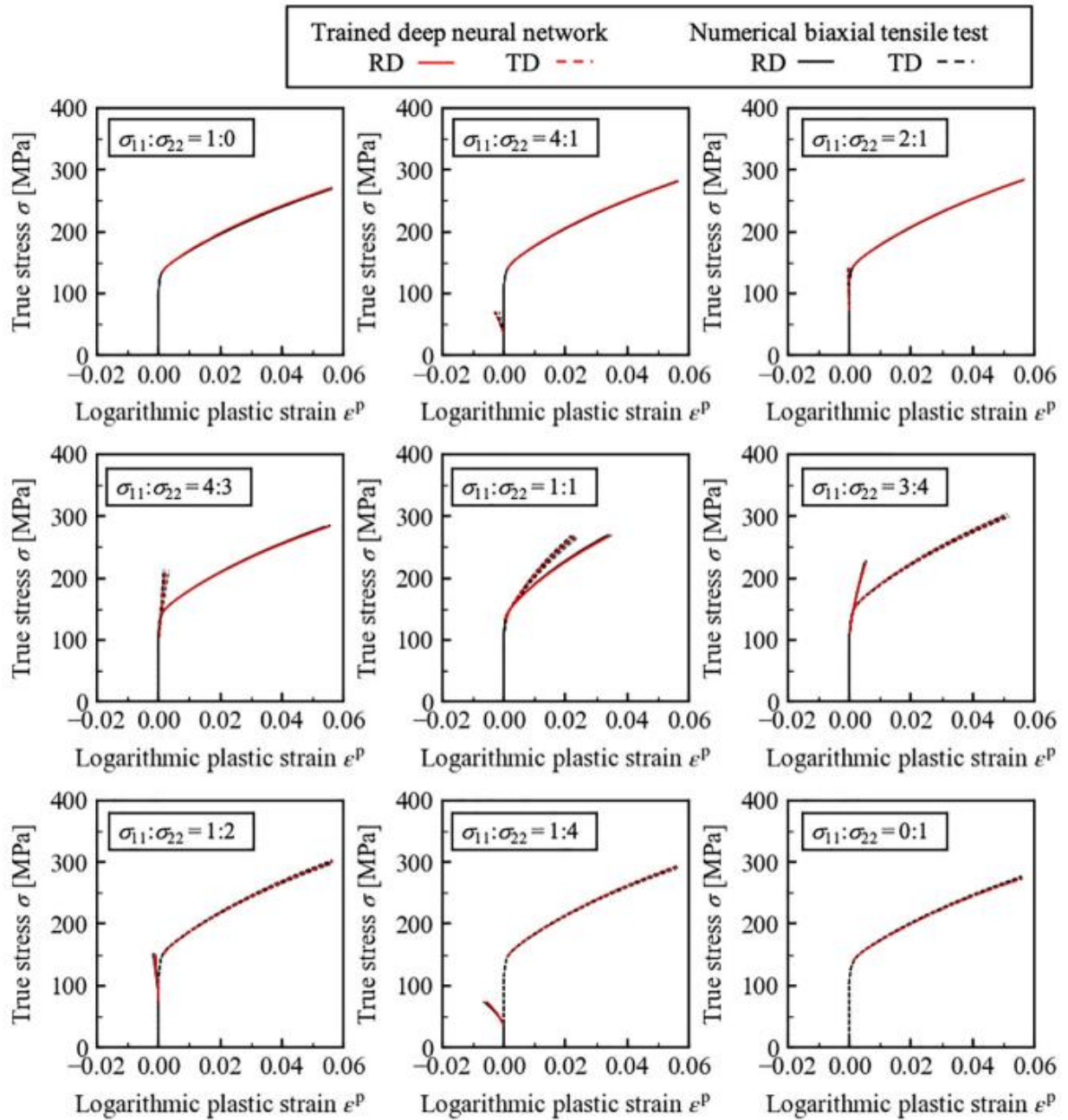


Figure 2-30 Numerical (black) and estimated (red) biaxial tensile curves trained with DNN-2D (Koenuma, Yamanaka, Watanabe, & Kuwabara, 2020).

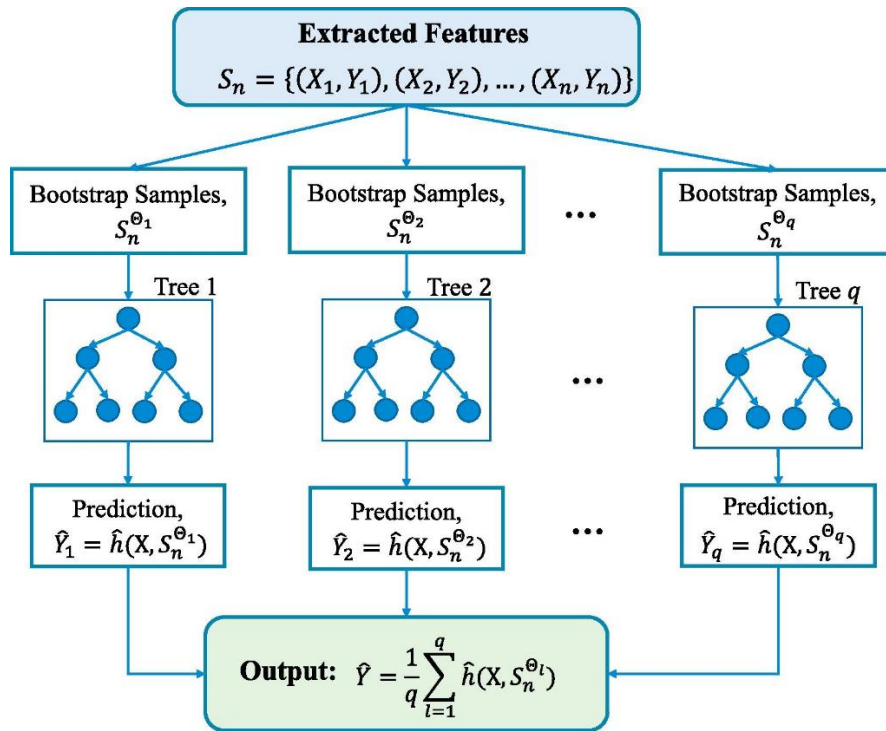


Figure 2-31 Random Forest Regressor sample tree (Li et al., 2018)

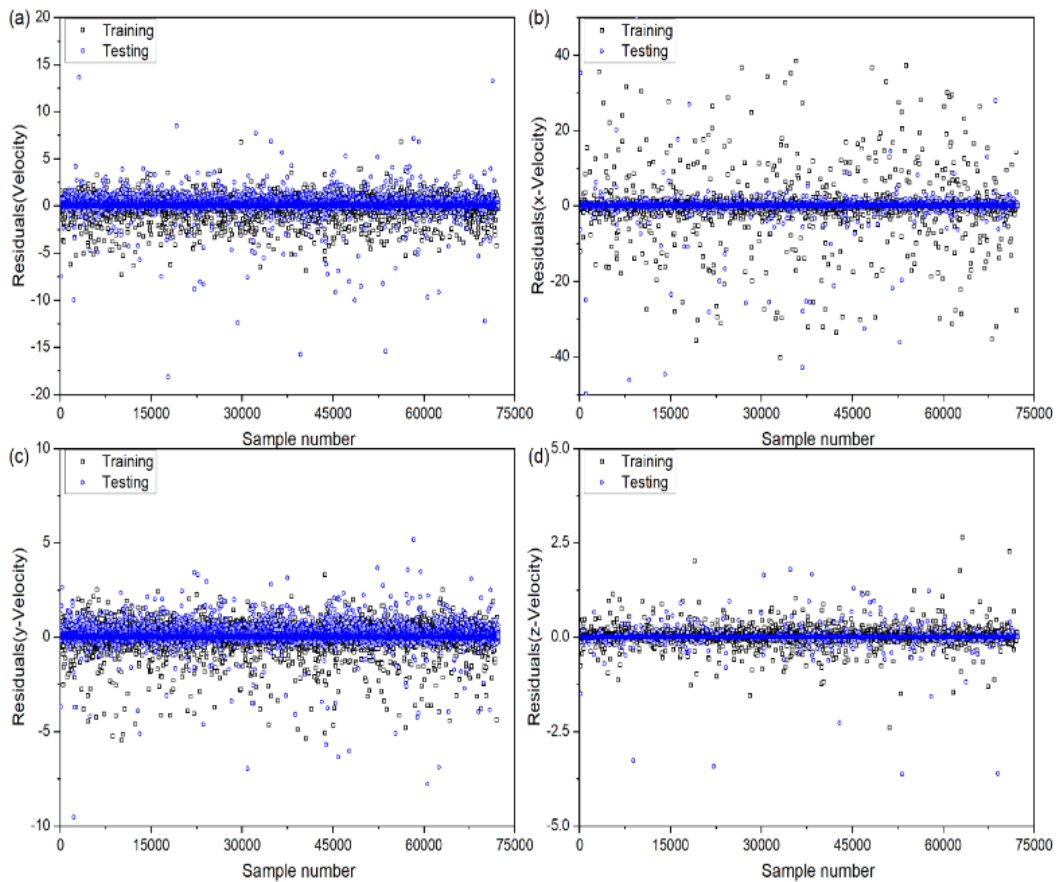


Figure 2-32: Random Forest prediction sample (Ganesh et al., 2021)



## 2.12 Knowledge gap

This work has identified some gaps during the course of the literature review:

- 1) The material characterisation of metallic materials at quasi-static strain rates have been widely studied using established testing procedure, but the determination of material properties under dynamic loading is still very much underdeveloped.
- 2) Researchers have been able to derive the plasticity model of JC constants of X65 steel for modelling in Abaqus but have not been successful in determining the JC ductile damage required for dynamic response simulations. For example:
  - a) (El-Danaf et al., 2013) derived the JC plastic parameters ( $A$ ,  $B$ ,  $n$ , and  $C$ ) of API X65 steel.
  - b) (Cortis, Nalli, Sasso, Cortese, & Mancini, 2022) applied both JC (Johnson, Hoegfeldt, Lindholm, & Nagy, 1983) for the plasticity model and Zerrilli-Armstrong (Zerilli & Armstrong, 1987) model to determine ductile parameters for X65 to model the effect of strain rate and temperature.
- 3) Dislocation evolution has been employed by researchers to analytically predict the flow stress of metals at high strain rates based on irreversible thermodynamics, which at low strain rates is reduced to classical Kocks-Mecking model but did not consider the BCC metal plastic deformation under high strain rates conditions. Examples include:
  - a) (Huang, M., Rivera-Díaz-del-Castillo, Bouaziz, & van der Zwaag, 2009) included the effect of phonon drag - an additional electrical current generated by the interaction between phonons and electrons - to the Kocks-Mecking model to predict high strain rate plastic deformation of FCC metal only.
  - b) (Galindo-Nava & Rivera-Díaz-del-Castillo, 2012) applied dynamic recovery and cell formation effect on the model for BCC metal plastic deformation at quasi-static strain rates.

Given the above gaps, this project seeks:

- 1) To adopt the thermal diffusivity constitutive equation to determine the material behaviour at both quasi-static and dynamic loading conditions.
- 2) To apply both the JC plasticity and ductile damage parameters from experiments to simulate the dynamic behaviour of X65 steel under limited plastic deformation. This requires the JC plastic as well as JC ductile damage

parameters to determine the behaviour of X65 steel under high strain rates condition.

- 3) To adopt the (Galindo-Nava & Rivera-Díaz-del-Castillo, 2012) approach for BCC metal in combination of JC model and temperature rise effect to model the flow stress of BCC metal (X65) at high strain rate.
- 4) To predict fracture toughness material properties using a machine learning algorithm with improved algorithm.

To achieve these aims, the following research proposal was devised:

- 1) A project plan (see Figure 2-33) was designed to determine the material properties of X65 steel combining the analytical, computational, and experimental approaches. To determine the fracture toughness at high strain rates, the analytical approach was adopted to correlate the experimental result and determine the required parameters such as the Johnson-Cook's.
- 2) The tensile tests which comprise of the high strain rate tensile testing, notched and un-notched round tensile testing were employed to determine the properties at high strain rates, which were also used to determine the JC parameters. The dynamic fracture toughness tests were performed using the drop weight test, instrumented Charpy-test, and fracture toughness test to determine properties at high strain rates and the effects of drop mass, change in release angle and change in displacement rates respectively.
- 3) The analytical approach adopted the JC model and thermostastistical model to derive parameters and were validated with the experimental results. These methods were adopted and implemented in the computational approach for accuracy in the model and was validated with the experimental results.

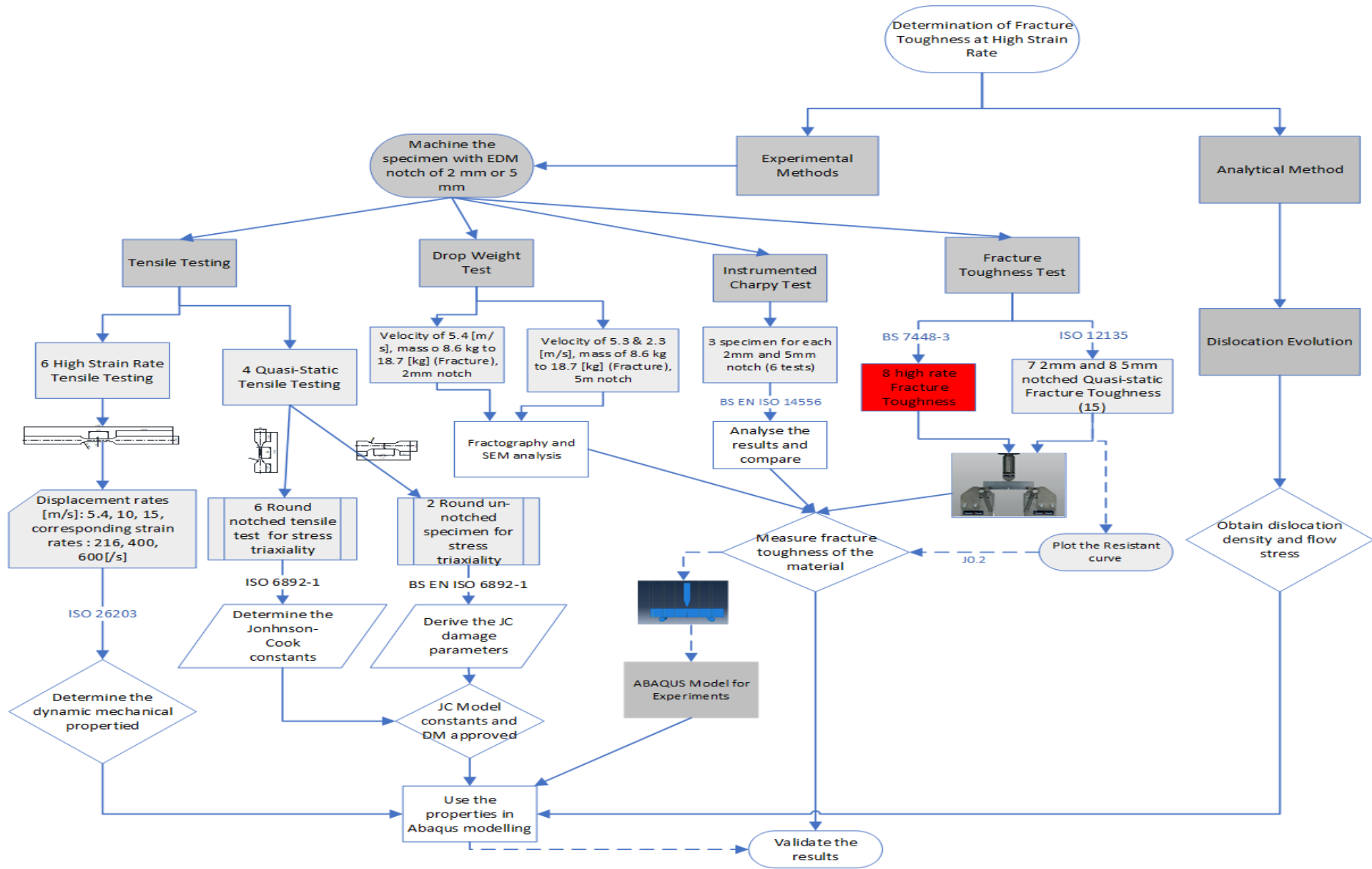


Figure 2-33 Project plan for scientific contribution to dynamic fracture toughness measurement

## 3 EXPERIMENTAL METHODS

### 3.1 Overview

This section explains the different methods employed to characterize the material and determine the fracture toughness at high strain rates. Some mechanical testing were conducted to characterise the required material properties under various loading conditions: -

- Quasi-static tensile testing (round notched and un-notched specimens)
- High strain rate tensile testing (flat specimen)
- Impact drop weight test (Charpy sized specimen)
- Instrumented Charpy test (full blow and low blow)
- Quasi-static fracture toughness test
- Dynamic fracture toughness test

The mechanical testing of materials helps to inform cost-effective design, achieve safe structures, and assist in reducing unexpected failures, as well as failure investigation. The procedure listed in this Chapter was utilised for the testing to fit the purpose and satisfy the knowledge gap identified in Section 2.12.

The API 5L X65 grade steel was the material investigated in this study, and the material chemical composition is shown in Table 2-1. This material finds its application in pipeline production (see Figure 2-1), quenched in water, and tempered at 660°C for 79 minutes with an austenitising temperature of 920°C for 44 minutes as supplied by Tenaris, Italy. The as-received material has the property in Table 3-1. The dimension of the parent material is 355.6 mm outer diameter by 19.05 mm wall thickness, from which all specimens were cut for experiment.

The tensile properties of this material were tested and reported in Section 4.2 to ascertain the properties provided in the mill certificate. The chemical compositions presented in Table 2-1 is as received from the mill certificate with no further testing and analysis. The experiments such as un-notched and notched tensile tests, round, and flat tensile tests, were designed to extract data that satisfy the procedure for deriving the possible Johnson-Cook (JC) constants and JC damage parameters. The JC parameters were applied in finite element analysis of which the method is also introduced in Sections 4.6 and 5.6 for high strain rate tensile testing and dynamic

fracture toughness respectively. The JC parameters formed part of the input in the finite element analysis Abaqus/Explicit to characterize the plastic and ductile damage properties, which was utilised to simulate the material behaviour under high strain rate loading conditions.

**Table 3-1 The X65 tensile properties tested by the supplier with a cylindrical specimen cut from a Longitudinal orientation at 20°C.**

Conditions	Yield strength (YS), MPa	Ultimate tensile strength (UTS), MPa	YS/UTS	Elongation %
Minimum	450	550	Required Max. 0.90	18.0
Maximum	580	760		
Obtained	527	619	0.85	28.9

The fracture toughness tests at high-strain rates were tested using the TWI in-house procedures on the VHS Instron machine, while the DIC was used to capture the displacement (strain) in material during testing. Instrumented Charpy test and impact drop weight tests were conducted for results comparison. The results were correlated with the FEA simulation results. In addition to characterizing the material behaviour at dynamic loading, the obtained fracture toughness data was employed in a machine learning algorithm to predict fracture toughness values.

### 3.2 Introduction

The determination of fracture toughness at high strain rate rates using recent testing machines available at TWI employs two high-speed cameras to capture the impact stages to establish the crack propagation force and strain. X65 steel specimens were machined and prepared for different tests including tensile, the impact drop weight, the instrumented Charpy, and fracture toughness experiments.

Dog-bone (round and flat samples), and Charpy-sized EDM notched (square cross-section) specimen geometries were employed for the experiments to generate the stress-strain data as well as the force-displacement curves to determine the mechanical and fracture behaviour at impact loading. The samples were tested to

investigate the effect of strain rates on the material behaviour at quasi-static, intermediate, and dynamic loading rates. All tests were performed at room temperature ( $\sim 21^{\circ}\text{C}$ ) and strain rates range of  $(1 \times 10^{-5})$  to  $(8 \times 10^2) \text{ s}^{-1}$  at displacement rate loading type using appropriate testing machines for each test. Microstructures are known to have a strong effect on material behaviour depending on the position of the atoms, molecules, and ions in the crystalline material such as the BCC, FCC, and HCP structures. Therefore, each of the crystalline material need to be studied independently for the effect of high loading rates.

**Table 3-2 Experiments conducted for the study.**

<b>Mechanical Test</b>	<b>Johnson-Cook constant</b>	<b>Test Conditions</b>	<b>Data Conditions</b>	<b>Geometry</b>
Round un-notched tensile test	A, B, and n	Room temperature, quasi-static strain rate	2 tests repeated	Round specimen
High strain rate tensile test	C and D <sub>4</sub>	Displacement rates [m/s]: 5.4, 10, 15 corresponding strain rates: 216, 400, 600 [1/s]	6 (3 sets displacement rate)	Flat specimen
Round Notched Tensile Test	D1, D2, and D3	Different notch radius, 3 repeated twice, round specimen	3 repeated twice	Round specimen
Drop Weight Test	-	Mass changed, 8-18kg mass (Force-Time, Force-displacement output)	11 sets of specimens	3-point Bend specimen
Full blow Instrumented Charpy test	-	Fracture toughness test, angle of release $161.4^{\circ}$	3 sets of each $a_0/W$	3-point bend specimen
Low blow Charpy test	-	Release angle changed to $125.7^{\circ}$ and $90^{\circ}$	3 sets of each angle	3-point bend specimen

### 3.2.1 Test specifications

Testing procedure at quasi-static rate has been well established which include BS 12135 (British Standard Institution, 2021) and ASTM E1820 (E1820-23b, 2023). The methods to determine material fracture toughness at high strain rate are somewhat

limited. BS 7448-3 (British Standard Institution, 2005) procedure has detailed fracture toughness testing of metallic material at increased stress intensity factor rate greater than  $3 \text{ MPa}\cdot\text{m}^{0.5}\text{s}^{-1}$ . However, it includes the use of obsolete data acquisition instruments such as an oscilloscope. A typical Charpy-sized specimen of  $10 \times 10 \times 55 \text{ mm}$ , with a span length,  $S$ , of  $40 \text{ mm}$  was employed for three-point bend methods (Figure 3-1 and Figure 3-2), full dimensions shown in Table 3-3 with machine allowances. Two categories of the sample were created, EDM notched samples and EDM notched fatigue pre-cracked samples with mechanical properties shown in Table 3-4 assumed during tests with Figure 3-3 showing the configuration of the impact on the specimen.

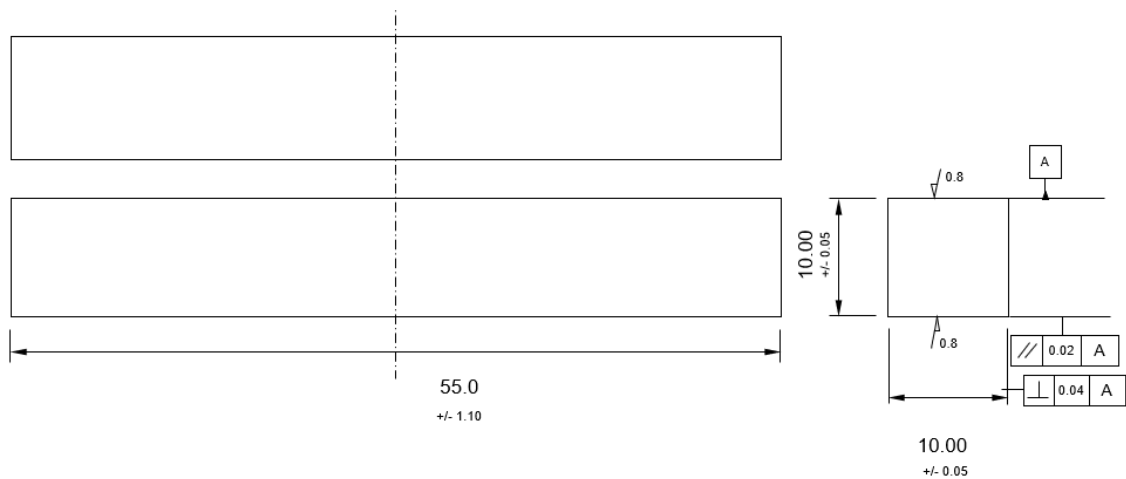


**Figure 3-1 2-D diagram of Charpy-sized specimen.**

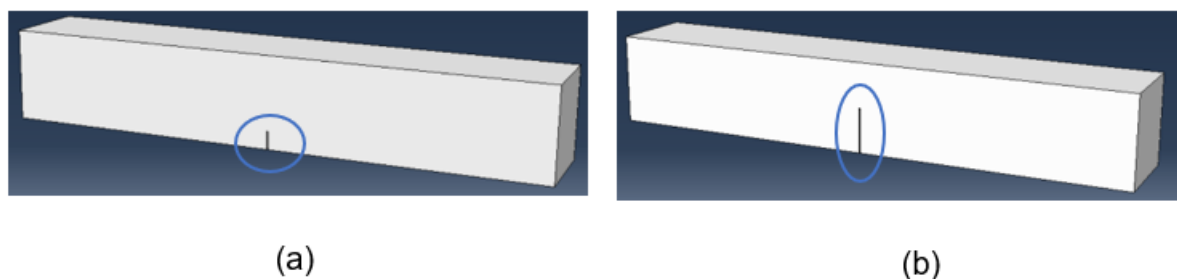


**Figure 3-2 Three-point bend EDM-notched specimens (a)  $a/W_0$  of 0.2( $\approx 2 \text{ mm}$  notch) and (b)  $a/W_0$  of 0.5 ( $\approx 5\text{mm}$  notch)**

**Table 3-3 Three-point bend specimen dimensions with allowable tolerances**

Width	10.0	10.0	mm	+/- 0.05
Thickness	10.0	10.0	mm	+/- 0.05
Length	55.0	55.0	mm	+/- 1.10
a/W	0.2	0.5		
Max Notch width	0.65	0.65	mm	
Notch depth	1.54	3.08	mm	+/- 0.03
Fatigue length	0.51	1.8	mm	

**Table 3-4 Mechanical properties of X65 assumed during testing.**

MECHANICAL PROPERTIES	Measured or assumed, M / A		
<b>:- At test temperature</b>	20.0	°C	
Yield strength, Sys	510.0	N/mm <sup>2</sup>	A
Tensile strength, Sts	680.0	N/mm <sup>2</sup>	A
Young's modulus, E	207000	N/mm <sup>2</sup>	A
<b>:- During fatigue precracking</b>			
Yield strength, Sysp	510.0	N/mm <sup>2</sup>	A
Tensile strength, Stsp	600.0	N/mm <sup>2</sup>	A



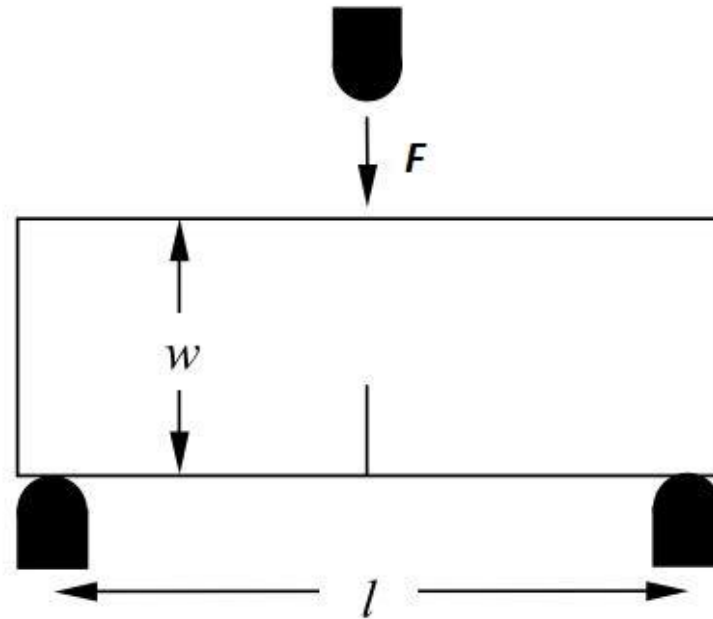


Figure 3-3 Three-point bend configuration showing the point of impact,  $F$ .

### 3.3 Tensile testing

#### 3.3.1 Quasi-static tensile tests

The tensile tests were performed to determine yield and ultimate tensile strength, and elongation. Three types of tensile tests were employed:- round un-notched bar tensile tests, round notched bar tensile tests, (shown in Figure 3-4), and flat tensile test (Figure 3-6). The round bar tests were performed under quasi-static loading ( $10^{-5} \text{ s}^{-1}$ ) and the flat tensile tests under dynamic loading ( $10^2 \text{ s}^{-1}$ ) as shown in Figure 3-4.

The gauge, a centre part of the round bar tensile test specimen that was machined with parallel sides, blended out to broader threaded ends as in Figure 3-5. The tensile specimens were prepared with an extensometer gauge length of 50 mm and the test was performed according to BS EN ISO 6892-1 (British Standard Institution, 2019b). Un-notched and notched round bar specimens shown in Figure 3-4 were tested to determine the stress triaxiality.

As the specimen was loaded under increasing stress, an extensometer was placed across the gauge to measure the extension in the gauge of the specimen Figure 3-5. A uniaxial (quasi-static) increasing load was applied. The load cell to measure applied load applied to the specimen under displacement control, and the extensometer to

measure the strain. The tensile specimen first extended elastically up to the yield point, at which point the specimen began to permanently deform until failure.

The applied load was measured in Newton (N), and the extensometer measured the change in length in mm. By dividing the load by the gauge's cross section area, the load is transformed into an applied stress (measured in MPa or  $\text{N mm}^2$ ). By dividing the length increase by the initial gauge length, which was measured in mm, the extensometer values were transformed into strain readings. In this manner, the results of the tensile test were converted into a stress versus strain curve. The yield strength and ultimate tensile strength were all calculated from the stress-strain curve.

The experiment involved deforming the sample to the maximum deformation until fracture. Following the test, the diameter of the necked region's narrowest point was measured, and the broken test pieces were repositioned next to one another to determine the gauge's final deformed length between the marker points at the point of failure. The difference between the gauge diameter before and after the test, stated as a percentage of the initial gauge diameter, was the percentage reduction in area. The increase in gauge length expressed as a percentage of the initial gauge length is the same as the percentage elongation.

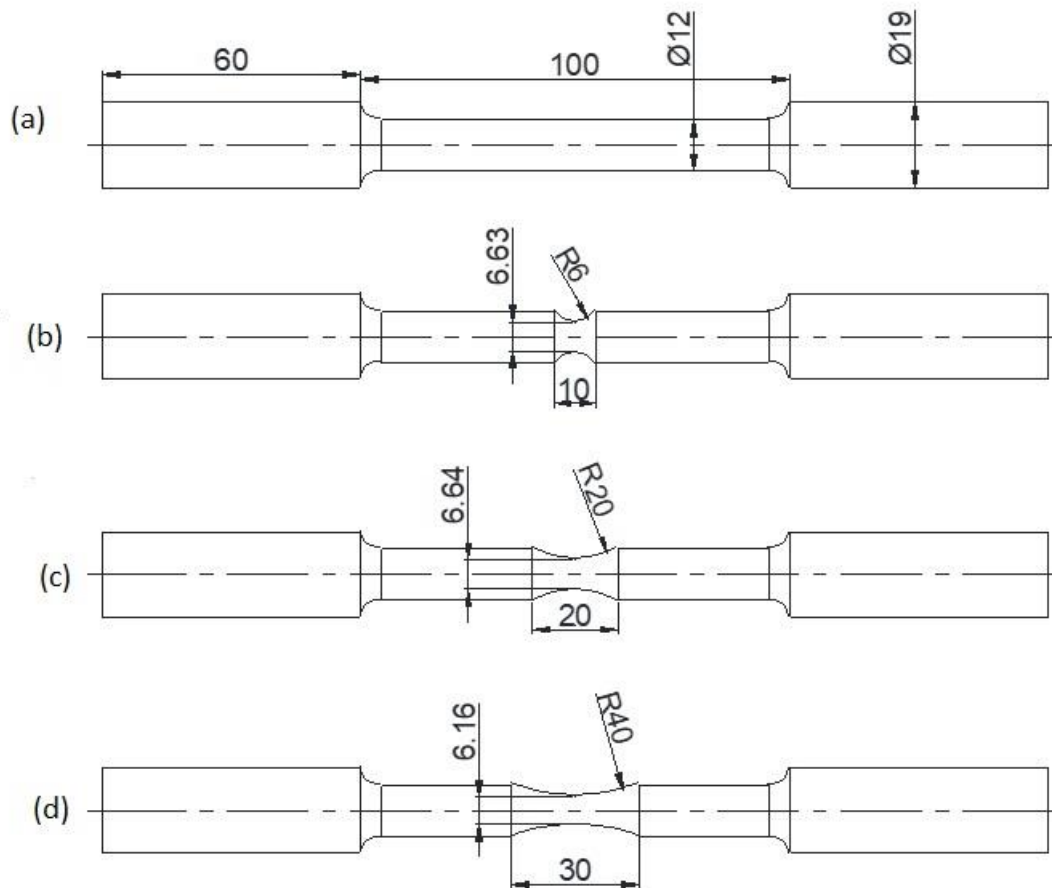


**Figure 3-4 Round dog-bone samples showing the un-notched (a), and notched samples (b, c, & d).**



**Figure 3-5 A tensile test set up showing the extensometer across the gauge on round specimen (© TWI)**

### **3.3.2 High strain rate tensile testing**

High strain rate testing was conducted to investigate the tensile properties of X65 steel under dynamic loading conditions with the servo-hydraulic machine shown in Figure 3-7 according to BS EN ISO 26203 (British Standard Institution, 2011) procedure. The tests were carried out by fixing the bottom end and applying tensile load on the upper part of the sample. The sample required was longer on one side due to machine requirements. The dynamic loading was achieved through exerting a load on the crosshead at a speed of 5400, 10000, and 15000 mm/s which corresponds to strain rates value of about 216, 400, and 600 s<sup>-1</sup> respectively. Table 3-5 has detailed information on all flat samples tested at high strain rates using the B1003 INSTRON VHS machine.

**Table 3-5 Velocity range with corresponding strain rates.**

Velocity, mm/s	Quasi-static	54000	10000	15000
Strain rate, s <sup>-1</sup>	0.00008	216	400	600

An Instron VHS 160 test machine was used in this study to test flat specimens shown in Figure 3-6 for high strain rate tensile properties. The machine has the capacity of 100 kN load with maximum crosshead speed of 20000 mm/s operating under servo-hydraulic technologies located at TWI Ltd, Cambridge. The machine has a patented FastJaw gripping techniques for stability and requires extra space for travel, hence the reason of one side of the sample being longer to accommodate it as shown in Figure 3-7. The flat sample and the machine setup for high-rate tensile testing is shown in Figure 3-6 and Figure 3-7 respectively.

As the loading rate increases, data acquisition becomes difficult as conventional strain gauges are unable to capture the data. Therefore, specialized high speed recording equipment is required to record the data. This has made the digital image correlation (DIC) systems becomes relevant in dynamic testing for data acquisition.

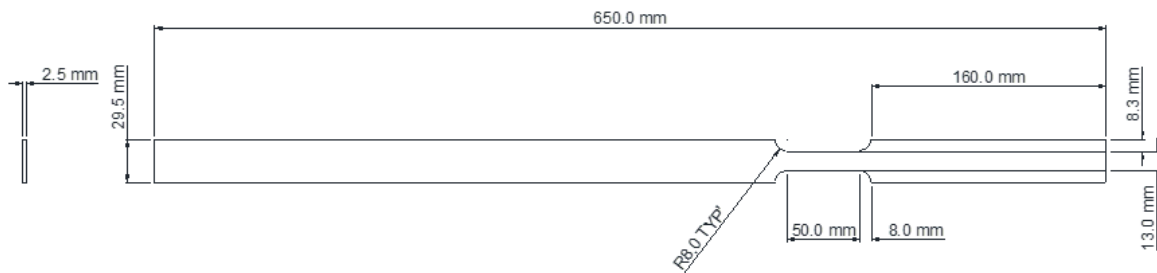


**Figure 3-6 Flat dog-bone sample for high-strain tensile testing.**

Some calibrations were performed on the DIC system for measuring in a certain volume when the trigger pulse from the VHS machine starts the data logger and the high-speed camera. The high-speed cameras were mounted on the left and right of the specimen to capture a continuous image of about 70,000 frames/sec during the elongation, which was analysed using the GOM inspect software as shown in Figure 3-8, Figure 3-9 and Figure 3-10 for different stages. The number of data points

produced during the testing depends largely on camera setup such as frame rate, field of view used and stand-off distance.



**Figure 3-7 Instron machine with sample sprayed with speckle set-up for testing.**

The specimen was sprayed with a speckle pattern within the gauge length to enhance a clear continuous camera capture during the experiment. The speckle pattern was introduced by applying fine spray of distinct paint on a lighter background on the polished surface of the X65 steel. The strain gauges were placed on both the front and back surfaces during testing which measures the localized strain. To generate a full strain map for the dynamic testing, DIC technique was utilised. Two sets of images were captured by the cameras at separate angles. Calibration was performed on the system to determine the event space of which the value was used to correlate the images in order to determine the surface deformation and strain. The captured images were imported into GOM software to correlate the images, the surface component was applied, and an extensometer was constructed across the fractured surfaces. The high

strain rate tensile test data analysed to determine the strain rate effects constants in the JC model employed in the Abaqus/Explicit modelling.

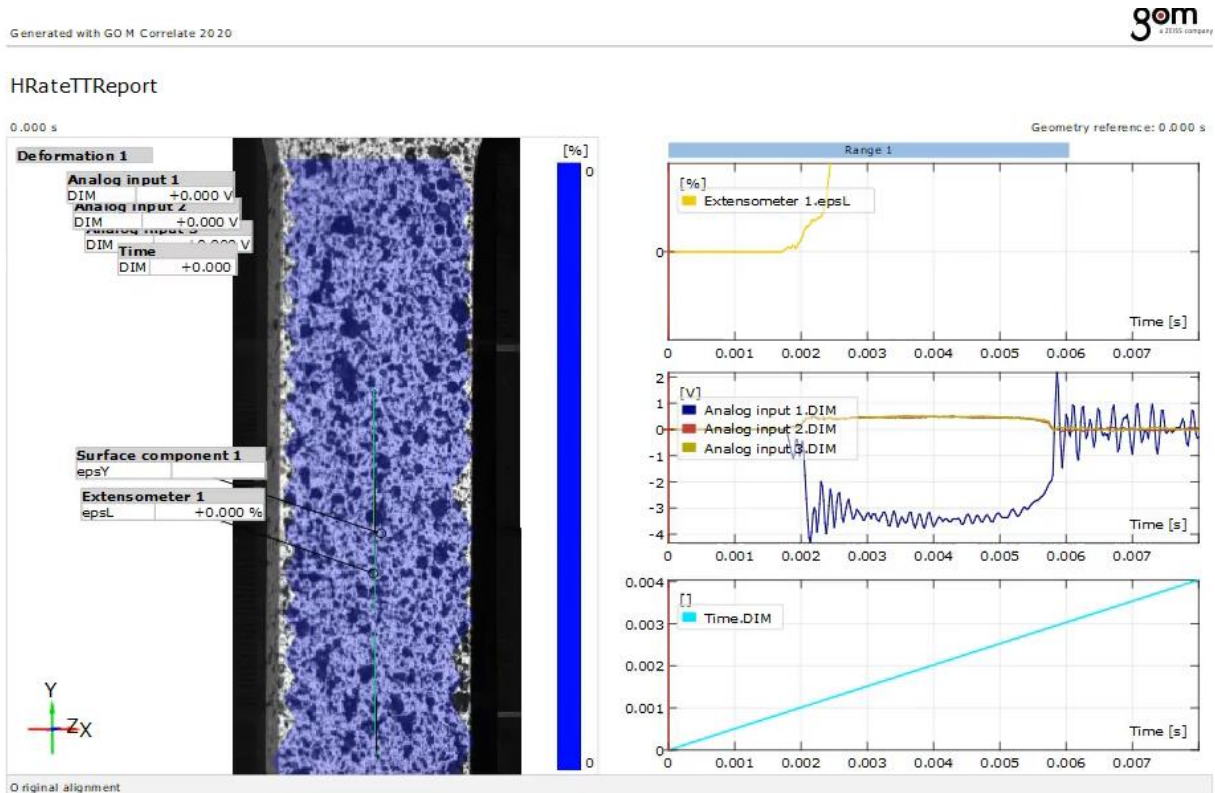


Figure 3-8 GOM data analysis for tensile testing at high strain rate initial stage

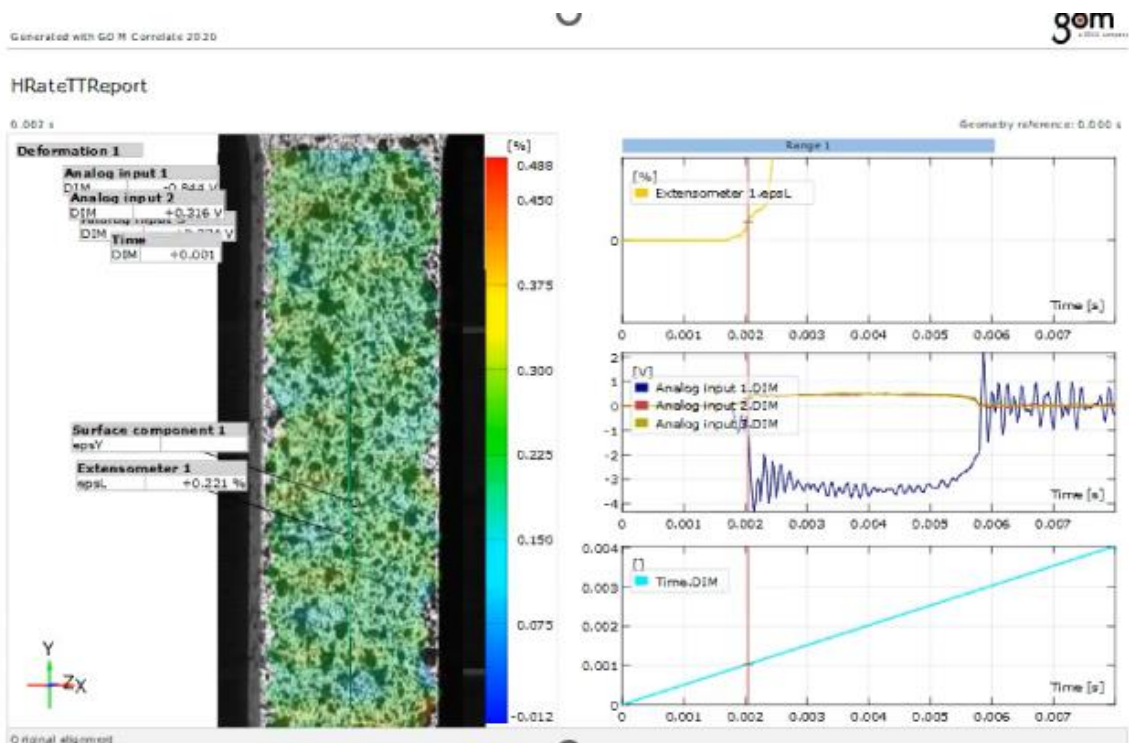


Figure 3-9 GOM data analysis for tensile testing at high strain rate extension stage

## HRateTReport

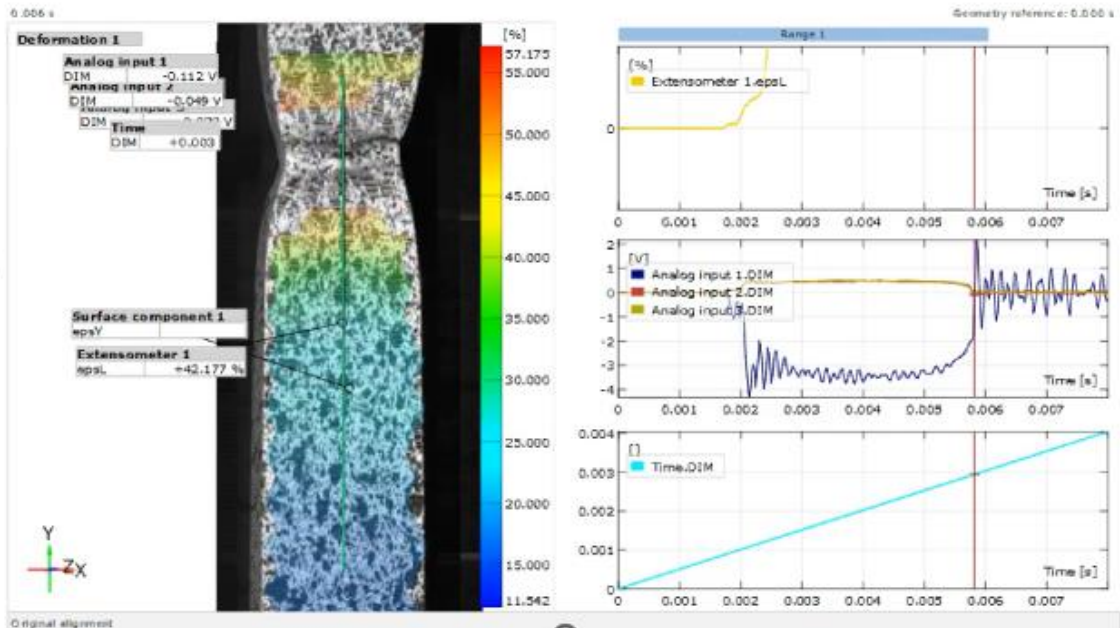


Figure 3-10 GOM data analysis for tensile testing at high strain rate fracture stage

### 3.4 Fracture Toughness Testing

The fracture toughness testing was conducted on notched specimens. The fatigue crack on the fracture toughness sample was introduced to replicate real flaw crack conditions in metallic structures.

A blunt notch was manufactured using EDM (electrical discharge machine i.e. spark erosion) with semi-circular tip radius of 0.1 mm. Fatigue precracking then followed to turn the blunt notch into a sharp one. Two different crack lengths (2 mm and 5 mm) to width (10 mm) i.e.  $a/W = 0.2$  and  $0.5$  respectively were employed.

There are different factors, such as material thickness, constraint, loading rate and temperature which affect fracture toughness. Fracture toughness test is used to determine the resistance to crack extension as a single value of toughness such as stress intensity factor  $K$ , crack tip opening displacement (CTOD), and the J integral or measured a resistance curve. A multi-specimen resistance curve is where the single value of fracture toughness  $K$ , J, or CTOD is plotted against the crack extension as shown in Figure 3-11, and at least six data points are required in each sector.



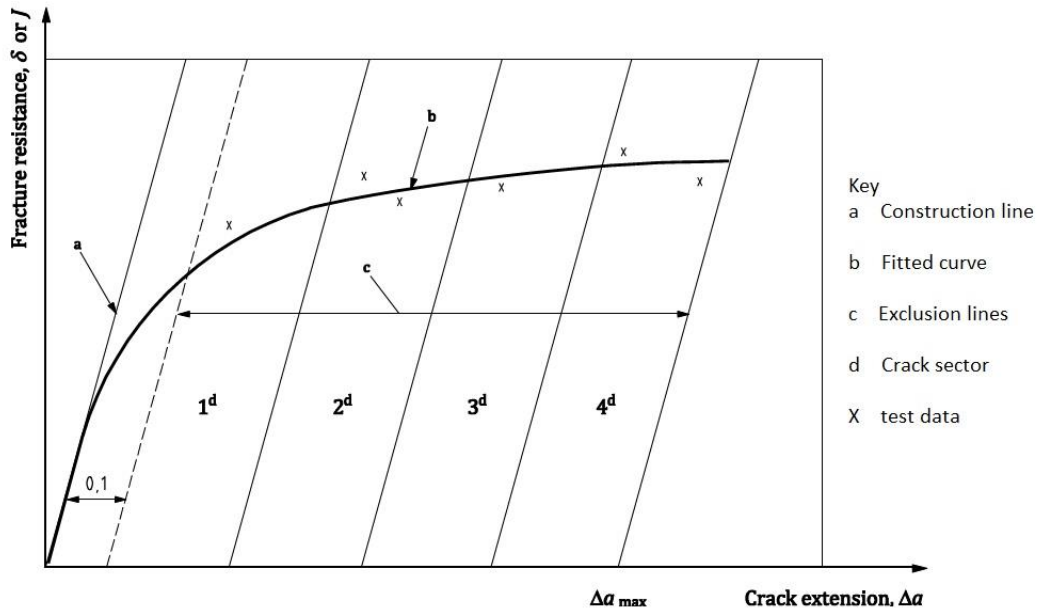
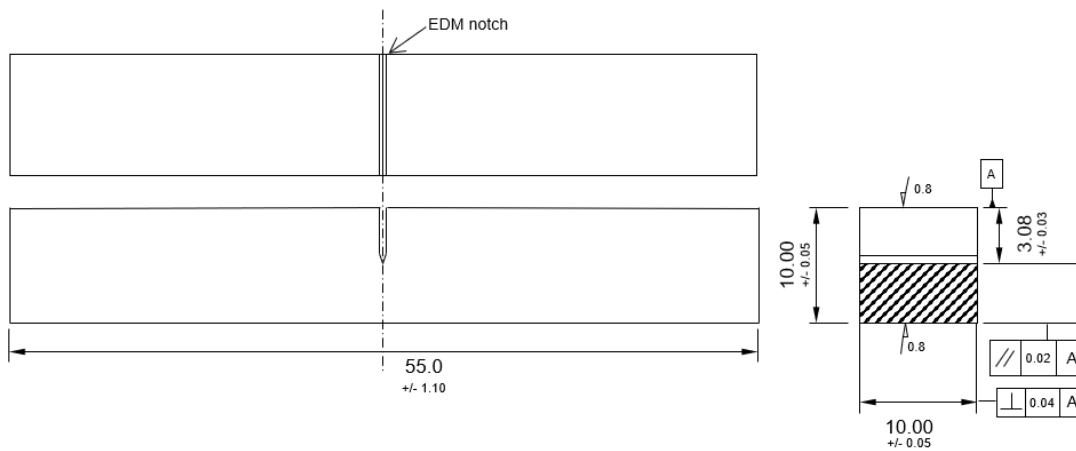


**Figure 3-11 Determination of R-curve and the data spacing (British Standard Institution, 2021)**

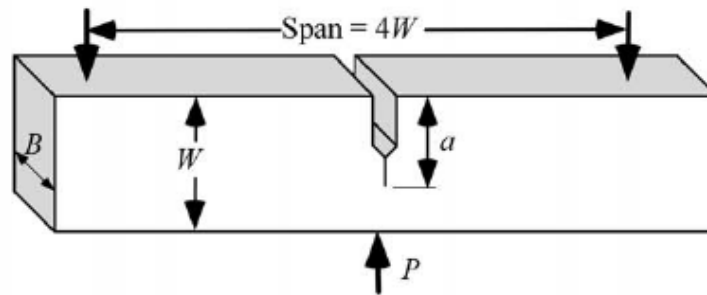
For materials within the linear elastic regime, fracture toughness properties are usually presented as a single point value either as J or CTOD. Ductile materials tear upon loading and their toughness properties are best represented using an R curve.

### 3.4.1 Test specimen preparation

Single edge notched bend (SENB) specimen shown in Figure 3-13 was utilised for this testing. Fracture toughness decreases as thickness increases. When a certain thickness is reached, fracture toughness becomes a material-dependent property.



**Figure 3-12 Engineering diagram of Charpy-sized specimen with EDM notched.**



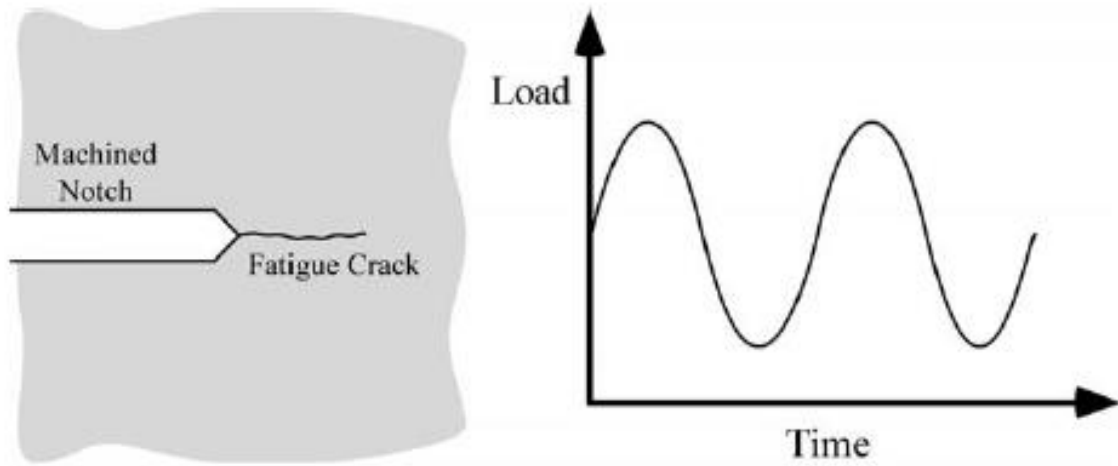
**Figure 3-13 Single edged notched sample showing the three dimensions; crack length (a), the thickness (b), and the width (W).**

Figure 3-13 shows a typical fatigue pre-cracked Charpy v-notched square cross-section specimen expressed as thickness  $B \times$  width  $W$  and length with a span length of  $4W$  used for the bending tests. In this study, specimens with V-notched were not adopted rather those with fatigue precracks of two different crack length ( $a$ ) to width ( $W$ ) ratio of 0.2 and 0.5 as seen in Figure 3-2.

### 3.4.2 Fatigue Pre-cracking

Basically, fracture mechanics theory involves material response in the presence of a sharp crack. To meet this condition with the laboratory specimen, a sufficiently sharp crack is introduced by cyclic loading as shown in Figure 3-14. EDM notch was machined on the specimen, and the low-stress cyclic loading was employed to extend the notch by fatigue pre-cracking (Figure 3-16) process to introduce a sharp crack. The fatigue dimensions are given in Table 3-6.

Reduced fatigue loading from allowable loads will give assured validity results for fatigue pre-cracking but will increase the number of cycles (required time) to achieve the crack. The fatigue loading was limited for pre-cracking test specimen to maintain the material properties and ensure no plasticity is introduced during the process. The fracture toughness specimen was broken open to examine the crack shape as shown in Figure 3-15 (EDM notched specimens) and Figure 3-17 (EDM notched specimens with fatigue pre-cracked) to allow measurement of crack extension, if any.



**Figure 3-14 Fatigue crack of cyclic loading introduced at the tip of a machined notch (Anderson, T. L., 2017)**

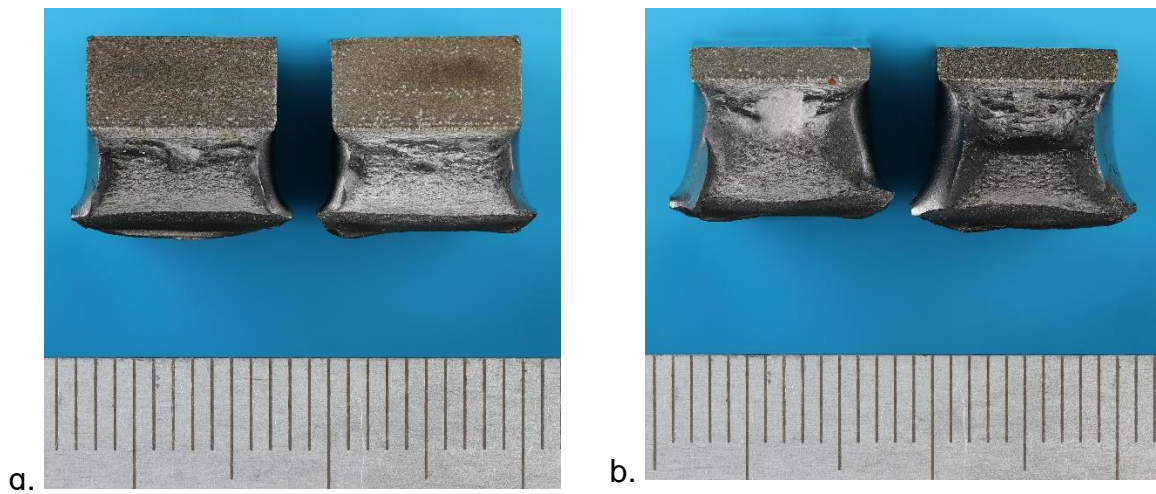


**Figure 3-15 Opened specimen for crack surface shape investigation showing machine notched on top, and ductile fracture bottom. (a)  $a/W$  of 0.5, (b)  $a/W$  of 0.2. (© TWI).**

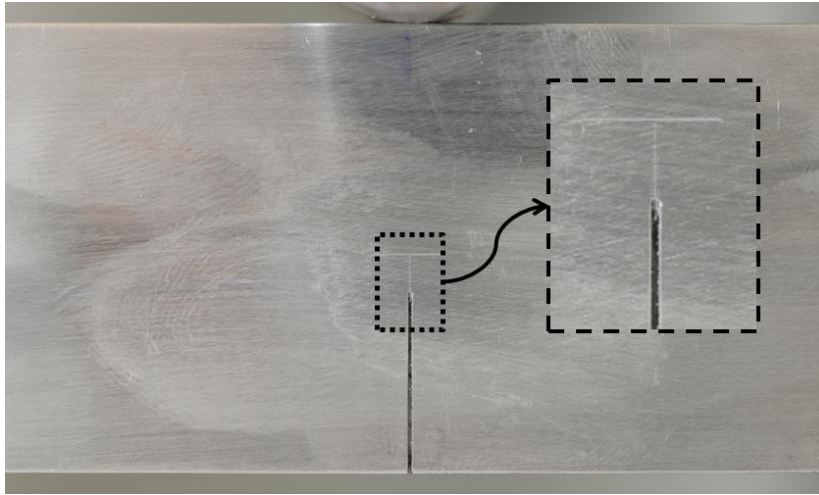


Figure 3-16 SEN(B) sample with EDM notched and the fatigue pre-cracking (image from TWI)

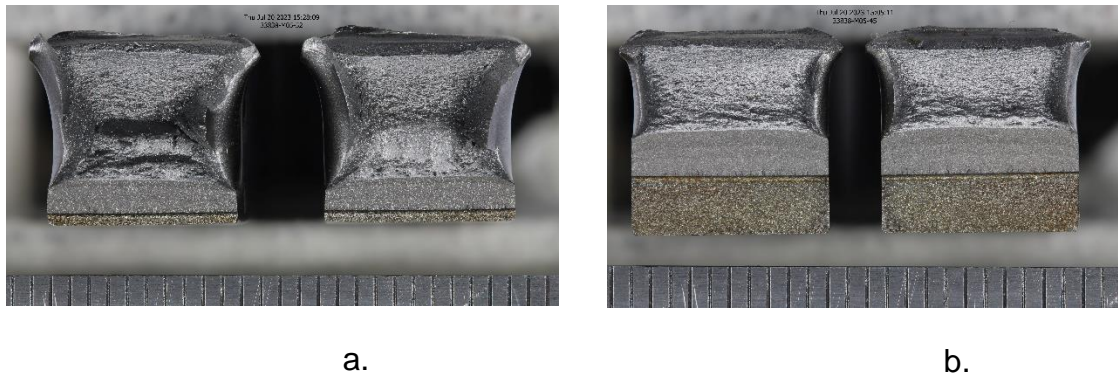


Figure 3-17 Cracked specimens showing the EDM notched, fatigue pre-cracked and fractured surfaces for, (a)  $a_0/W$  of 0.2, (b)  $a_0/W$  of 0.5. (© TWI)

Table 3-6 Fatigue details for the 3-point bend specimens

	$a/W = 0.5$	$a/W = 0.2$	Units
Fatigue load, initial	3.3	6.0	kN
Fatigue load, final	1.7	3.4	kN
Fatigue span (400 mm max)	40.0	40.0	mm
R ratio	0.1	0.1	

### 3.4.3 Testing procedure

The specimens were loaded slowly at a crosshead displacement rate of 0.35 mm/min under three-point bending. During testing, the applied load, crack mouth opening displacement using attached clip gauges, loading rates, and temperatures at the crack tip were recorded. The elastic strain measured by the clip gauges at different heights during the test was used to determine the crack mouth opening as shown in Figure 3-18 allowing the determination of CTOD and providing input for  $J$  determination.

Traces of load versus crack mouth displacement were generated during the test, from which the fracture toughness value was determined from the maximum load reached or the point of fracture if the maximum load was not attained before fracture. The fracture toughness values derived from the maximum load or point of fracture is converted to critical stress intensity factor,  $K_{mat}$  from either J-integral or CTOD fracture toughness values.

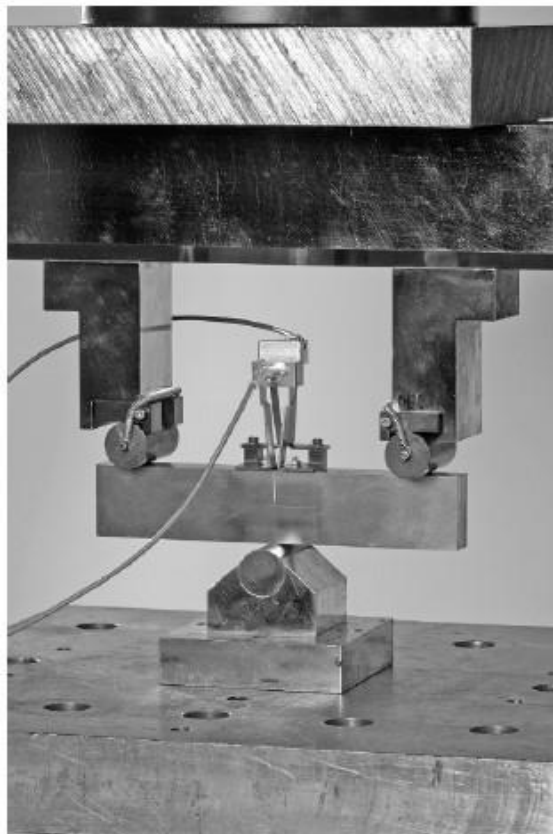


**Figure 3-18 Set up for fracture toughness test with a pre-cracked notch specimen mounted (© TWI).**

Crack extension will deform the plastic zone at the tip of the crack while absorbing energy, thereby increasing the fracture toughness at the tip of the crack of a lower-level tearing. In this case, a tearing resistance curve known as R-curve is used to determine the fracture toughness during crack growth rather than a single point fracture toughness value. An R-curve plots CTOD or  $J$  against the stable tearing to present a rising curve.

Unloading compliance which is the slope of the unloading portion of the curve was used to estimate crack length obtained during repeated partial unloading by estimating crack extension. Also, the R-curve was determined from single fracture toughness value of six identical specimens at different loading levels while measuring the crack extension. Since parent material was being tested, standard procedures such as ISO 12135 and ASTM E1820 were employed for testing guidance for single point fracture toughness and R-curve testing.

### 3.5 Qualitative Toughness Measurement Tests

When components are subjected to rapid loading, controlled impact tests can be used to determine relevant material response. The tests could be conducted using controlled drop weight or instrumented pendulum impact methods.

#### 3.5.1 Impact drop weight test

Impact drop weight testing was conducted to determine the material's ability to resist dynamic loading. The drop weight test was conducted using Zwick/Roell impact drop weight test machine shown in Figure 3-19. Different masses ranging from 8.6 kg to 18.7 kg were employed on Charpy-sized EDM-notched samples (Figure 3-2) with work capacity as seen in Table 3-7, from a specified height at a constant displacement rate of 5296 mm/s.

**Table 3-7 Mass applied and the corresponding work capacity in Joules at a velocity of 5296 mm/s**

<b>Mass (kg)</b>	<b>8.6</b>	<b>9.6</b>	<b>10.6</b>	<b>11.6</b>	<b>12.6</b>	<b>13.7</b>
<b>Work (J)</b>	120.7	134.9	148.9	163.2	177.2	191.4
<b>Mass (kg)</b>	<b>14.7</b>	<b>15.8</b>	<b>16.7</b>	<b>17.7</b>	<b>18.7</b>	

<b>Work (J)</b>	205.8	219.9	234.1	248.1	262.4
-----------------	-------	-------	-------	-------	-------

The evaluation of the test was conducted based on the magnitude of energy absorbed by the specimen. The test recorded the force-time and displacement-time responses.

The drop weight was performed on the specimen with different notches of  $a_0/W$  of 0.2 and 0.5 using different weights to determine the crack propagation and material toughness. Impact loading was applied to obtain the desired high strain rate by dropping the pendulum from a known height to fracture the notched specimen. The testing was performed in accordance with the BS EN ISO 14556 standard with EDM notched samples. In dynamic testing, the maximum force usually occurs far above the normal curve, and this maximum force can be recognized as the dynamic general yield force  $FD_{gy}$ . This causes a rise in yield stress during dynamic loading.

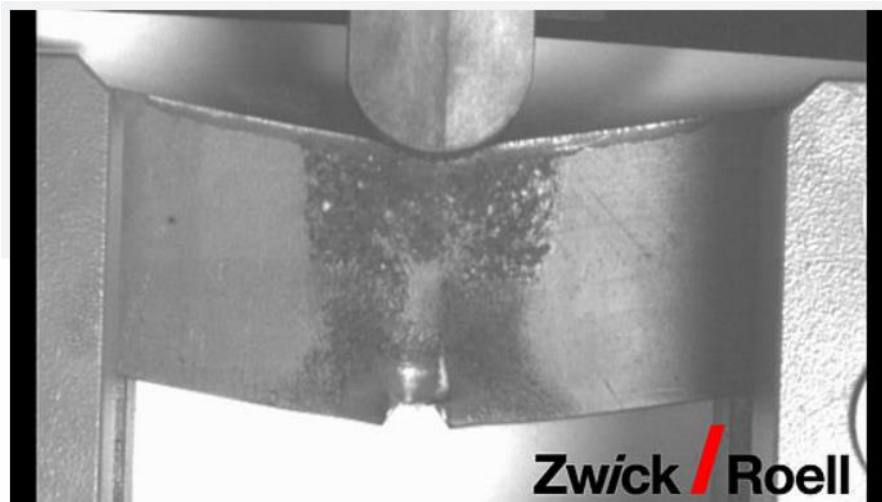


**Figure 3-19 Specimen undergoing impact drop weight testing (Zwick Roell)**

The results obtained from the test of crack length-width ratio of 0.2 mm and that obtained for 0.5 mm were presented in Chapter 5. The impact velocity applied to the test was 5400 mm/s for the crack length to width ratio of 0.2 mm, and 2540 mm/s for the ratio of 0.5. As the 0.5  $a_0/W$  specimen fractured completely when 5400 mm/s was applied, and significant oscillation has been observed on the force-displacement curve. The data were obtained from direct reading during the experiment, as impact software (TestExpert IIIv1.2 Impact tester HIT2000) is combined to an instrumented tup to record data points along the impact curve from which absorbed energy and

speed were calculated. The theoretical work capacity,  $E$  in Table 3-7 energy was estimated from equation (3-1)

$$E = \frac{1}{2}mv^2 \quad (3-1)$$

where  $m$  is the mass and  $v$  is the displacement rate.

### 3.5.2 Instrumented Charpy testing

To prepare the specimen required for Charpy testing, 55 mm X65 steel was cut in a milling machine to a square cross-section of 10 mm by 10 mm. The Electro discharge machining (EDM) technique was utilised to achieve the presence of a crack and the samples were fatigue pre-cracked further using the cyclic loading method to desirable crack lengths of  $\approx 5$  mm and  $\approx 2$  mm. The notch is grounded on the midpoint of the 55 mm length (Figure 3-21), and each sample was labelled properly for easy identification on both ends. Before the experiment, the Charpy machine was checked for interlocker on the protective doors for safety purposes.

The testing was performed at room temperature and was supported on an anvil and impacted with sufficient energy by the moving mass pendulum of a Zwick 750J Charpy T03c test machine shown in Figure 3-20 under displacement control mode. Two types of specimens were employed to check the variations of impact toughness on specimen geometry.



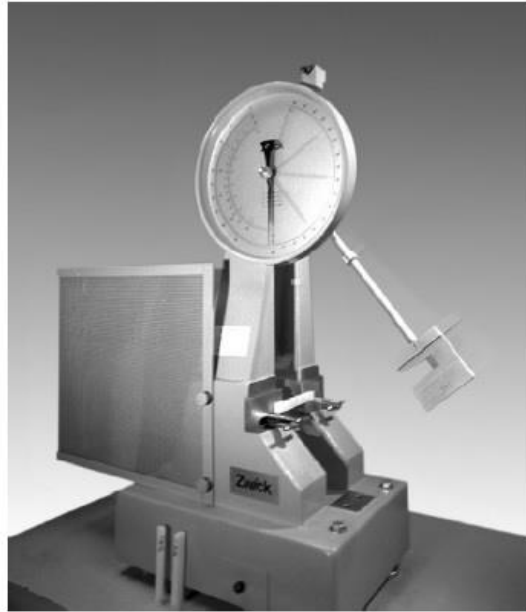


**Figure 3-20 Charpy testing machine with specimen placed horizontally on it (© TWI).**

One set of the samples was the EDM notched with tip radius of 0.1 mm, and the other set of samples was with EDM notched and fatigue pre-cracked to replicate a sharp crack as shown in Figure 3-21. The notched depth was either 2 mm or 5 mm on one face of the sample. Samples were loaded between the Charpy machine anvils while the notch was faced away from the impactor. The locating prong was used to position and adjust the precise location of the samples and the protective doors were properly shut. The striker has a fixed weight end and a rigid arm which is dropped on the back of the notched specimen with a narrow profile to focus the impact force. The striker was held in place to mount the specimen, after which is released from a height and then it swings down to specimen back face while the notch face is in front at the lowest swing point. As the specimen fractures, the energy absorbed by the sample reduces the speed of the swing.

The instrumentation of the Charpy machine was zeroed and the striker impactor was released to fracture the sample. The energy reading was taken from the displayed reading on the machine. The samples were collected after fracturing from the machine and properly stored for fracture surface examination. The same procedure was applied for all the Charpy impact tests at all loading rates. The surface of the fractured specimens was examined and recorded.

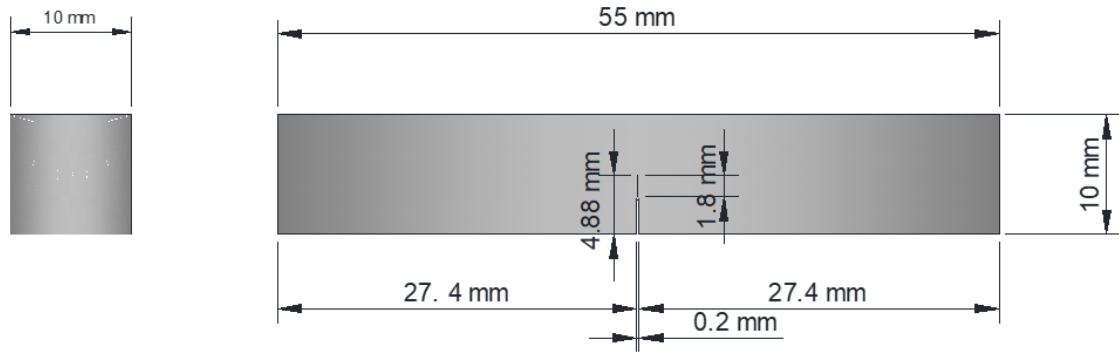


**Figure 3-21 Charpy sample with EDM notched and fatigue pre-cracked.**

The Charpy energy  $C_v$  was determined by measuring the absorbed energy of the tested sample during impact. The measurement of the initial and final value of the potential energy of the mass which is determined by the decrease in motion of the pendulum hammer measured by the scale (dial gauge) determines the absorbed energy, which is known as the impact toughness of the material.

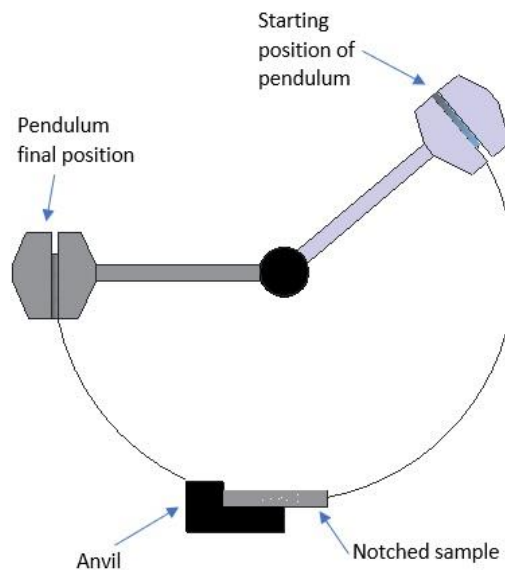


**Figure 3-22 A schematic diagram of the Charpy impact test machine**

Further experiments were conducted at room temperature while varying the displacement rate with the release angles as shown in Table 3-8. The effect of strain rates on the samples and the possible angle of release on the Charpy machine to maintain dynamic loading was the reason for selection.

**Table 3-8 Displacement rate conditions for the tests performed with the Charpy machine**

Theoretical velocity, mm/s	The angle of release $\theta$	Work capacity, J
5420	161.42	749.94
4890	125.71	609.73
3890	90.00	384.90

The temperature in this experiment was kept constant while investigating the effect of strain rate. The empirical relation in equation (3-2) is used to relate Charpy energy  $C_v$  with plain strain fracture toughness  $K_{Ic}$  in the brittle region of the test

$$\frac{C_v}{\sigma_y} = K_{Ic} \quad (3-2)$$

where  $C_v$  is in joules,  $\sigma_y$  yield stress in MPa and  $K_{Ic}$  in  $\text{MPa}\cdot\text{m}^{-1/2}$ . The value of fracture toughness determined with the above equations is considered under slow loading  $K_{Ic}$  conditions. The BS 12135 and ASTM E1820 procedures were employed to analyse the Charpy test data.

Three identical Charpy samples were tested at the same temperature and angle of release. It is usually required to carry out Charpy test at a minimum design temperature, but some production codes would dictate a lower temperature from the design temperature to accommodate Charpy data differences from fracture toughness behaviour. The average of the three data were taken for analysis. Charpy testing are mostly regarded as qualitative since it is not being used for fracture toughness calculations, hence fracture toughness test becomes necessary.

### **3.6 Dynamic Fracture Toughness Measurement Test**

The dynamic fracture toughness test measures the resistant to crack extension under rapid loading. Factors such as inertia effects, reflected stress waves and material rate dependence makes the measurement of dynamic fracture toughness quite complicated. A VHS 160/100-20 Instron servo-hydraulic machine shown in Figure 3-24 that can implement a high displacement rate up to 20000 mm/s at TWI was utilised for the dynamic fracture toughness testing. The machine contains features for high strain

rate tensile tests, as well as 3-point bend fixtures for impact bend tests, and utilised Charpy sized specimen. The support roller is 2 mm in diameter and 20 mm width, while the striker's head has a radius of 2 mm. The specimen is kept on the support 40 mm apart as the span length, and the striker is mounted to the piston as shown in Figure 3-23.

### 3.6.1 Testing Procedure of high velocity test with an impactor

The mechanical behaviour of the material was characterized using high velocity three-point bend test. A Charpy-sized square cross section ( $10 \times 10$  mm) specimen was placed on two supports. The centre of the specimen bears the applied displacement and resulted force is measured.

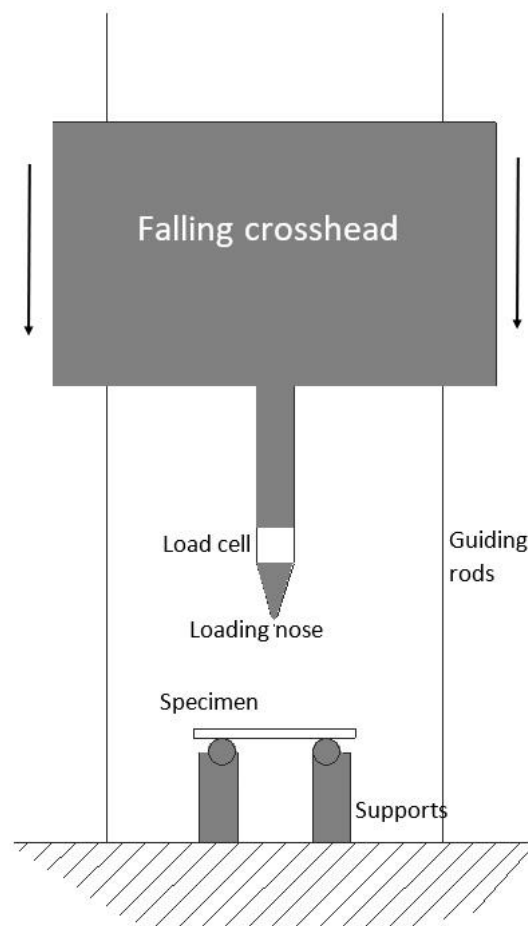


Figure 3-23 Impact drop tower

The impactor is applied to obtain the load displacement curves. A load cell is attached at the tip of the instrumented top to record the load during impact as shown in Figure 3-23. The velocity of the crosshead is recorded as well as the load when the crosshead reached a certain point. From the obtained load recording and time, the force-deflection curve is obtained. The momentum is calculated from applied crosshead in Equation (3-3)

$$m_h a(t) = m_h g - F(t) \quad (3-3)$$

Where  $m_h$  is the crosshead mass,  $a(t)$  is the crosshead's acceleration,  $g$  is the acceleration due to gravity and  $F(t)$  is the force. The integration of the mass gives the velocity  $v(t)$  as in Equation (3-4).

$$v(t) = v_0 + gt - \frac{1}{m_c} \int_0^t F(t) dt \quad (3-4)$$

Where  $v_0$  is the initial velocity. A second integration is performed to obtain the displacement  $x(t)$  of the crosshead in Equation (3-5).

$$x(t) = v_0 t + \frac{1}{2} g t^2 - \frac{1}{m_c} \int \int_0^t F(t) dt \quad (3-5)$$

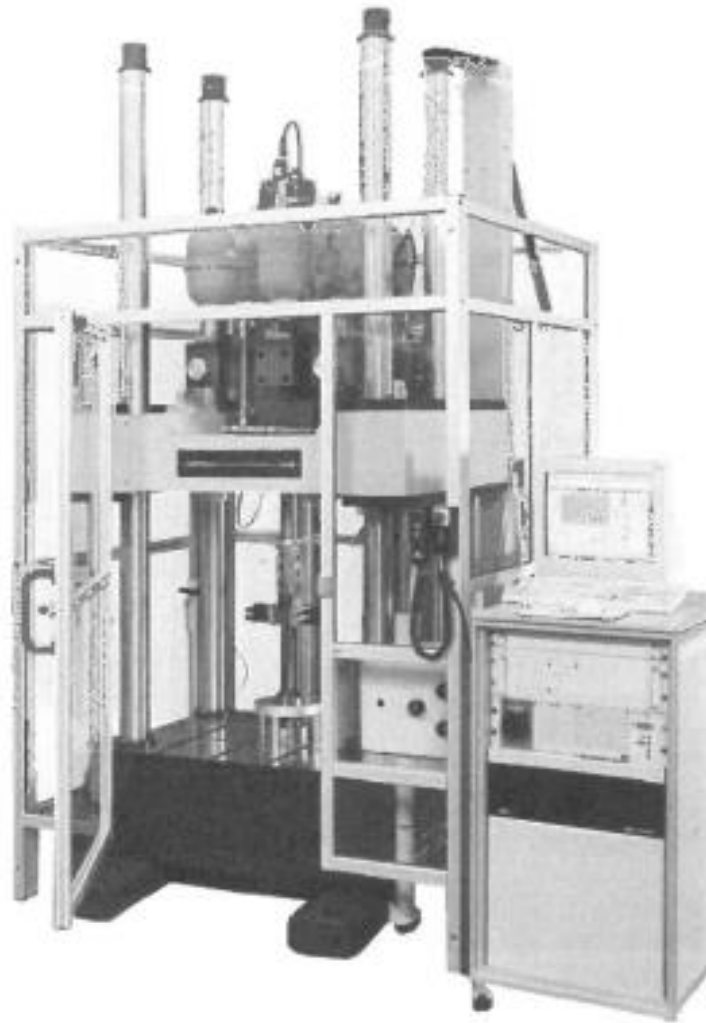


**Figure 3-24 VHS Instron machine (© TWI)**

### **3.6.2 Dynamic Fracture toughness analysis of DIC system with GOM correlate software**

Since high-rate fracture toughness tests last a few milliseconds, a specialized data acquisition tool is required as the conventional tools are inadequate. Hence, the Instron logger and digital image correlation (DIC) systems were both utilised to log the test. Instron logger logs time, load ram displacement while DIC system logs time, DIC images, and load. As DIC is unable to capture sufficient data points at higher velocity, the Instron logger is then programmed to operate up to six or seven times faster than the DIC's maximum speed to record the ringing and aid in correctly filtering the data. Thus, the Instron data set can be filtered properly to eliminate the ringing in the load cell so that it can be lined up with the DIC displacement data. BS 7448 – 3 (British

Standard Institution, 2005) is a procedure for testing dynamic fracture toughness but does not utilise the DIC method to capture data. Rather oscilloscope is applied.

### **3.6.2.1 Procedure for data acquisition**

1. Data from the test is such that it comprises data file from Instron and stage files folder from the DIC. It is the stage files that contains left images, right images, and information of calibration for each frame known as a stage. Calibration block is used for DIC system calibration as it is of known geometry with specific markings. Then, the DIC logging software utilises the known object to calibrate what it sees.
2. GOM correlate software – a DIC analysis software is used in extracting load line displacement from the DIC data by importing the stage files to the software.
3. To track the visible speckled surface of the sample, a surface component is created to enable the surface to be inspected for the vertical (Y) direction displacement.
4. Zero reference stage displacement set across the specimen. Displacement is highest for subsequent stages in the centre of the specimen which is in line with the notch where the striker hits the specimen. A coloured scale is placed by the side to highlight amount of displacement at each stage in different areas.
5. Since highest displacement occurs between the notch tip and hit point of the striker, a point is chosen within this area and the pattern quality is monitored. The displacement of the point of interest is plotted displaying the stage number. Also, the time data is added to the diagram, and all exported as a .csv file with time, load line displacement and stage number.
6. All the relevant data generated from the Instron data and .csv file exported from GOM software are further extracted with another software to derive the data format the normal fracture testing software can analyse.



Figure 3-25 Three bend sample with speckle pattern for fracture toughness test

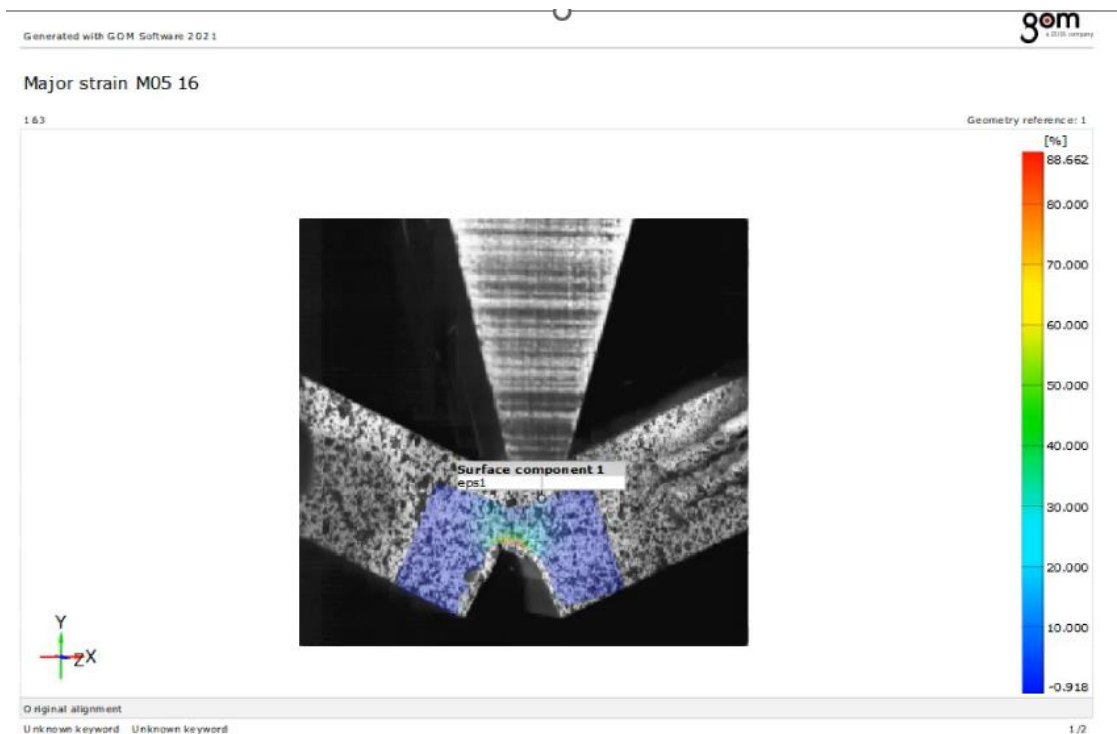


Figure 3-26 Sample with the surface component under high strain rate deformation



### 3.7 Machine learning methodology

Python was used to create the algorithm, and the mathematics of Random Forest regressor was not dealt with in this study. Imports of packages, modules and libraries were made in Python for the model such as Pandas – for data cleaning and analysis, Numpy and Scipy – for statistical analysis, Matplotlib and Seaborn - data visual representation such as bar graphs, pie-charts, and histogram. Random Forest Regressor was imported from sklearn. ensemble and other libraries from sklearn.  $R^2$ \_score/Mean absolute error was used for the model evaluation. GridSearchCV sklearn was applied rather than the basic random forest regression to find a better-performing choice of parameters with 'n\_estimators' of [10,50,100] decision trees that run in parallel without interaction with each other to avoid overfitting to the final output.

In this study, 48 datasets obtained from quasi-static and dynamic fracture toughness experiments were utilised and computed with random forest regressor. The experimental data were applied to ensure the real behaviour of the material was represented in the model without an estimate. The experiments were very expensive leading to fewer number of datasets from the experiments, hence the low number of dataset. Features such as Crack length [mm], Displacement rate [mm/min], Crack Extension [mm], Applied force [kN], and  $K_Q$  [MPa.m<sup>0.5</sup>] were applied to determine the fracture toughness output, J [kJ/m<sup>2</sup>].

To predict the fracture toughness of materials, different work has employed all kinds of machine learning algorithm depending on the available datasets. (Daghighi et al., 2020) applied decision tree regressor in predicting the fracture toughness of a composite material. The various content of the composite was utilised as the factors influencing the fracture toughness of the material (Figure 3-27).

#### 3.7.1 Stress-Strain Prediction using MLPRegressor.

A machine learning prediction of stress-strain curve was determined using Multi-layer Perceptron regressor (MLPRegressor), which is a sklearn neural network. The model was developed from 22 datasets obtained experimentally from notched, un-notched round specimens, high strain rate tensile tests and controlled drop weight tests. The force-displacement curves from drop weight tests were converted to stress-strain curve using beam model analysis. Python was also utilised to model the algorithm. The input entails seven dimensional features which includes: type of test, specimen

geometry, strain rates [ $s^{-1}$ ], mass [kg], initial diameter [mm], initial cross-sectional area [ $mm^2$ ], and temperature [ $^{\circ}C$ ]. The desired output was the stress-strain curves with 200 data points.

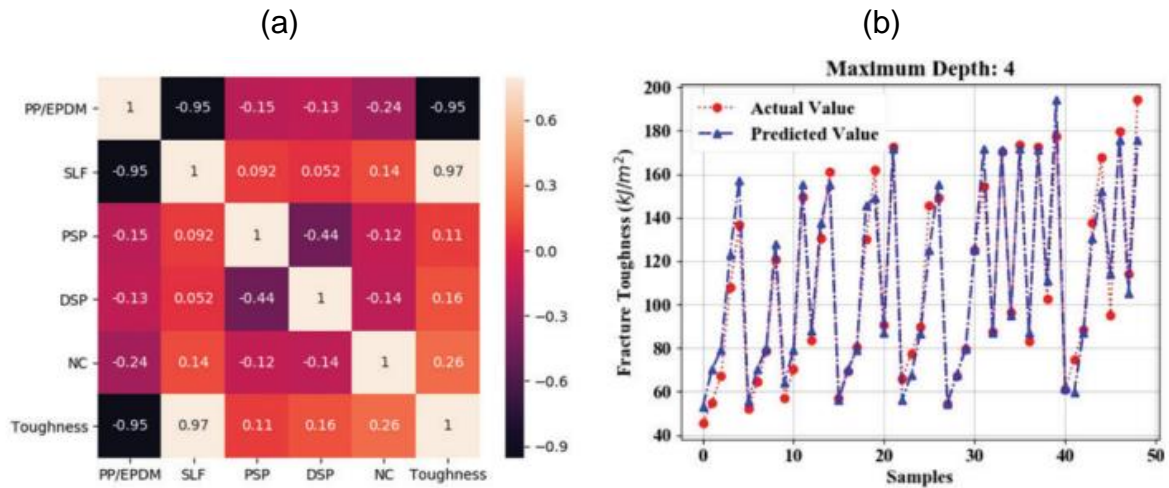


**Figure 3-27 (a) Correlation table showing the applied features (b) Fracture toughness prediction with Regression Tree method (Daghigh et al., 2020).**

The datasets were imported specifying the input and the target in the process and was read as an array. MinMaxScaler was applied to transform the dataset. The data was split into a training and testing sets 70/30 respectively. MLPRegressor was imported and applied to create and train the model with hidden layer sizes of 500, random state of 1 and 50,000 iterations.

Other researchers have applied other deep learning methods such as the convolutional neural network (CNN) for the prediction, but have generated the training data from numerical modelling, rather than the actual experimental data (Koenuma, Yamanaka, Watanabe, & Kuwabara, 2020), and (Yang, Kim, Ryu, & Gu, 2020).

This study has identified the importance of training data in a model with real-life datasets and utilised only the actual experiment data to improve the estimation accuracy. The data points generated from the experiments vary from one experiment to another and this affects the time for training data. To be able to increase the speed of computation and improve estimation accuracy, the values were selected for 200 data points in each experiment to eliminate vague points that will decrease the

accuracy of the prediction through clever filtering and replacing the empty data with zero.

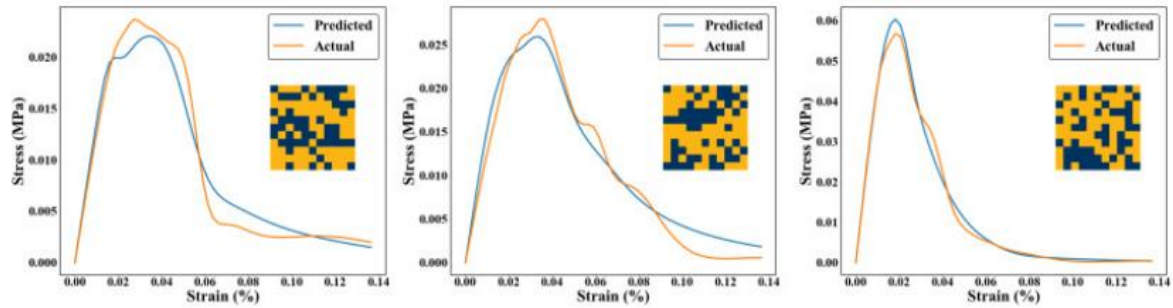


**Figure 3-28** Generated curves from test data of composite with mean squared errors between 25 – 75 % (Yang, Kim, Ryu, & Gu, 2020)

## 4 EXPERIMENTAL ANALYSIS OF X65 STEEL TENSILE PROPERTIES

### 4.1 Introduction

In this chapter, the results from tensile tests have been presented. This section has been divided into three parts. The first part deals with all tensile experiments and discussions covering quasi-static and high-strain rate tensile tests. The results compared the as received tensile properties of the material at room temperature. The strain rate range of the performed tests is quasi-static ( $10^{-5} \text{ s}^{-1}$ ) to dynamic or high ( $600 \text{ s}^{-1}$ ) strain rates.

The second part of this section details the process of determining Johnson-Cook parameters from the experimental results from experiments in Table 3-2. This includes the plasticity JC parameters and the ductile damage JC parameters. The third part details the results of the dislocation evolution effect on flow stress at high strain rates and compares the result of the JC model to characterize the material behaviour at high strain rates.

The result of utilising the thermal conductivity approach to determine the onset of plasticity and sudden flow stress rise as detailed in Section 2.8.6 is presented. The strain rate sensitivity was investigated, and the yield strength was in terms of engineering yield strength taken as the 0.2% proof strength throughout the thesis. It should be noted that all tests but impact drop weight test in this thesis were conducted at TWI, Cambridge.

Furthermore, the experimental results were supported with simulation from finite element analysis in ABAQUS for quasi-static and the high strain rate tensile testing. The JC parameters as well as the experimental data were utilised to input in Abaqus material properties for complete characterization of X65 steel under dynamic loading conditions.

## 4.2 Quasi-static tensile results of X65 steel.

### 4.2.1 Round smooth tensile test

Tensile tests on round specimens were carried out to determine the tensile behaviour of the material under quasi-static conditions. The two tests were conducted using the same cross-sectional area (113 mm<sup>2</sup>) and the average of the results was extracted for further analysis. The designation of M04 was used for the tensile tests in this study and a typical Engineering stress-strain curve obtained from the experiment of X65 steel is shown in **Figure 4-1**. The variation in the two tests was minimal as can be seen in Figure 4-3 and an average of the two was taken. The material properties of the M04 14 have little or no significant difference with those of M04 13 and this is because of errors of variability in the measurement method. The properties extracted from these experiments are presented in **Table 4-1** with the measurement errors shown in **Figure 4-2**. All the testing were repeated with measurement and testing errors occurring due to test set-up, machine calibrations and accuracy of measuring devices which is acceptable at a percentage error of 5 %. Achieving this overall precision required a well-trained and experienced technician. Only two sets of tests were conducted for each strain rate for tensile testing due to limited time available to complete this project and the average was utilised.

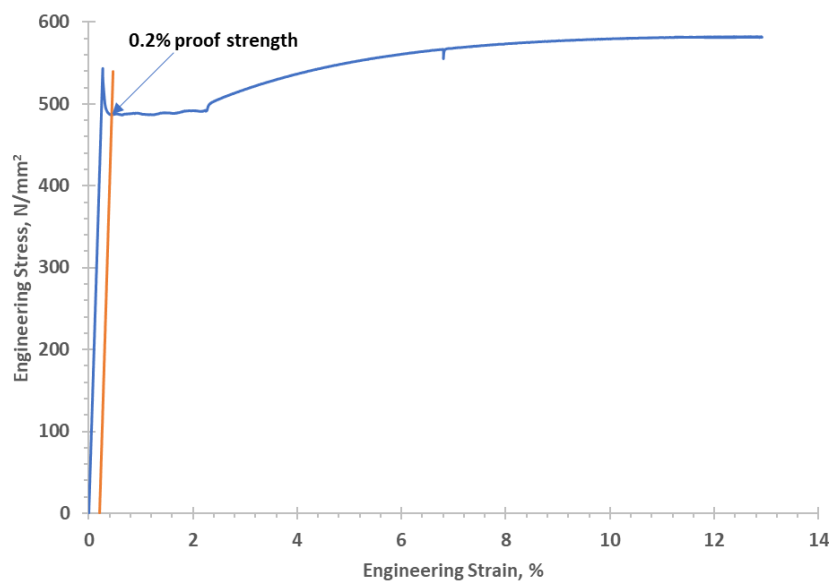


**Figure 4-1 Stress-strain curve of X65 material for static testing**

**Table 4-1 Tensile properties of round un-notched X65 steel tested at 21°C**

Specimen ID	Strain rate, s <sup>-1</sup>	0.2% proof stress, MPa	UTS, MPa	Y/T ratio	Elongation, %	Reduction in area, %
<b>M04 13</b>	8.2×10 <sup>-5</sup>	480.3	579.7	0.83	24.5	77.1
<b>M04 14</b>	8.5×10 <sup>-5</sup>	486.4	581.9	0.84	25.6	77.2

The Y/T ratio was measured as the ratio of the 0.2% proof stress to the ultimate tensile stress from the engineering stress-strain curve. The elongation percentage differs, and this means that elongation should not be generalized as a means of measuring ductility, but rather a mechanical response of the material.

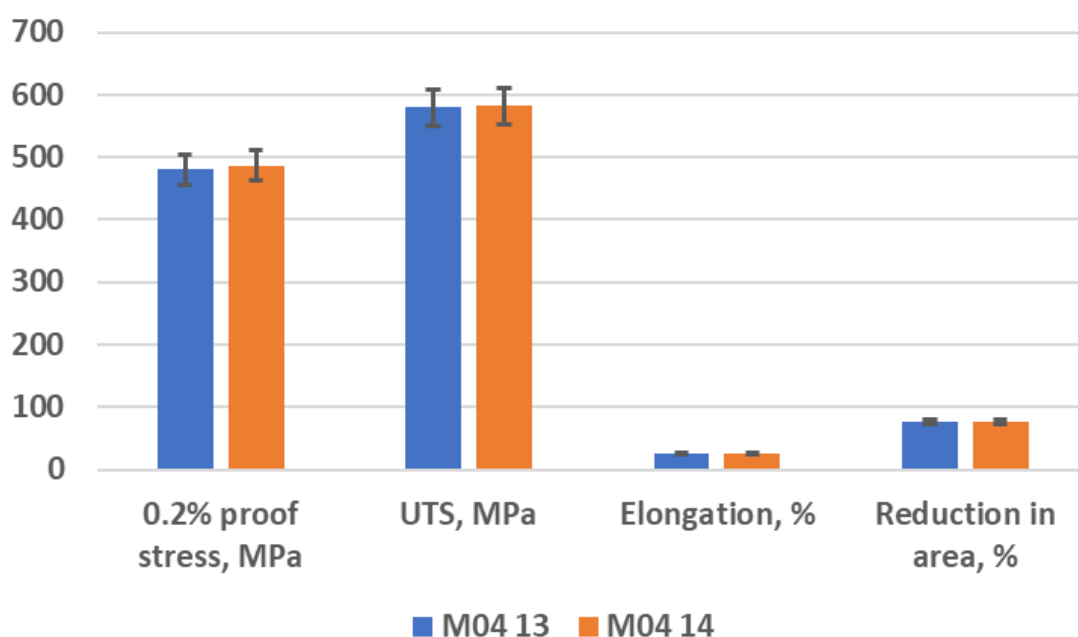


**Figure 4-2 Tensile properties and the measurement errors**

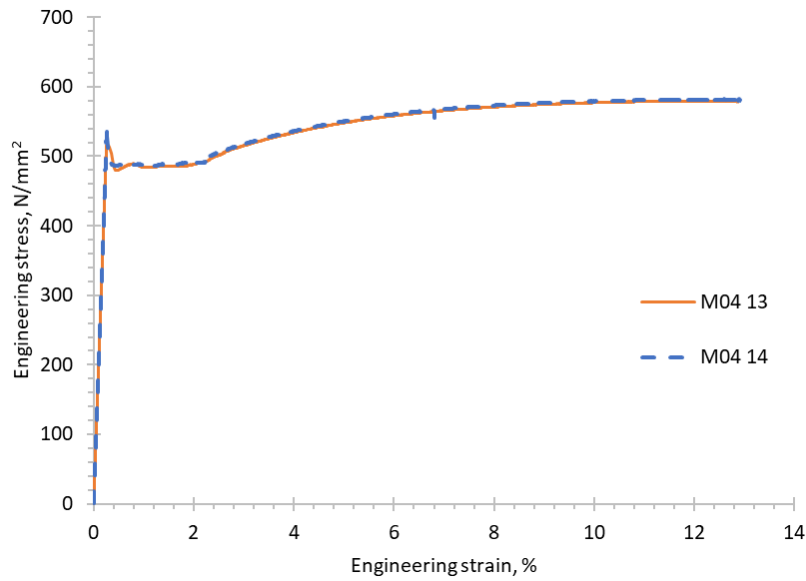


**Figure 4-3 Round Un-notched stress-strain curve showing two identical results of tested specimens M04 13 and M04 14 from X65 steel.**

The conversion from engineering stress-strain was made using equations (4-1) and (4-2) for true stress and true strain, respectively. The resulting stress-strain curves were compared in Figure 4-4.

$$\sigma_{True} = \sigma_{eng} (1 + \varepsilon_{eng}) \quad (4-1)$$

$$\varepsilon_{True} = \ln(1 + \varepsilon_{eng}) \quad (4-2)$$

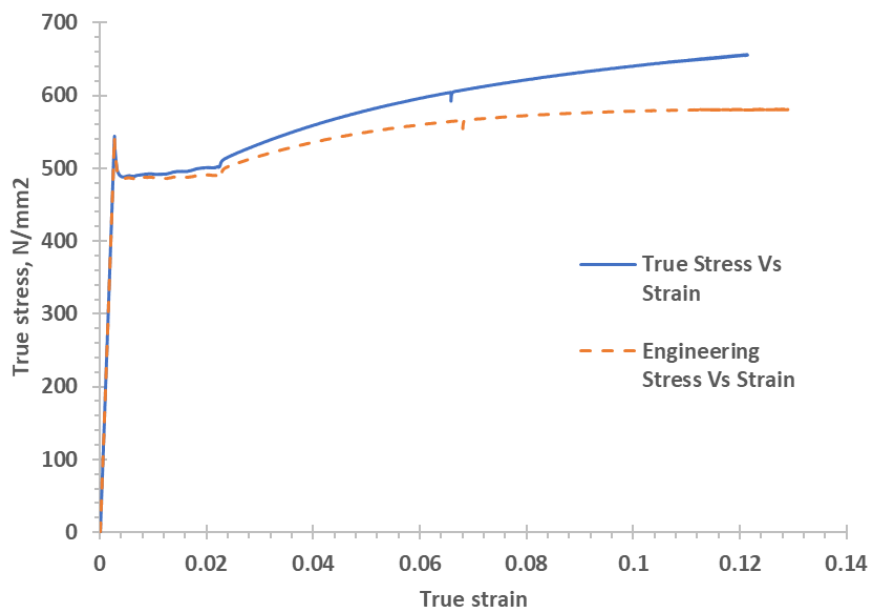


**Figure 4-4 Comparison of Engineering and True stress-strain curves for X65 steel.**

The elastic region in Figure 4-4 is the same in both engineering and true stress-strain curve but starts to deviate at the onset of the inelastic region. True stresses are usually applied in numerical modelling to quantify the plastic behaviour of a material since it considers the instantaneous dimensions of the specimen. The deformation localizes after the ultimate tensile strength and necking begin to take place until fracture.

#### **4.2.2 Round-notched tensile tests**

To investigate the stress triaxiality response of the material, different notch sizes were applied on the extensometer area of the specimen to determine the effect of reduced cross-sectional area and notch radius. Three sets of notched samples were tested with each experiment repeated twice for verification. The quasi-static strain rates were taken directly from the recorded experimental data. The mechanical properties recorded from the experiment are shown in Table 4-2, with the error bar in Figure 4-9.

It was observed that notched samples under quasi-static loading experienced a higher 0.2 % yield strength. The significant deduction is the reduction in area with the 0.2 % yield strength, such that the lower the reduction in area, the higher the resulting yield strength as shown in Figure 4-5. Large cross-sectional area under static loading yielded higher elongation than the reduced area under quasi-static loading. This is because the necking region of the smaller cross-sectional area when compared to the larger cross-sectional area occupies a larger portion of the smaller cross-sectional area. Therefore, the percentage elongation decreases with the cross-sectional area.

The results of notched tensile tests on the six samples are presented in Figure 4-6, and further comparison between the smooth round specimen and the notched round specimen was determined and presented in Figure 4-7. The results show that smooth specimens experience higher elongation before necking. As a result, elongation and area reduction should not be used to measure ductility because they are two different responses to a material's mechanical behaviour. While the reduction in area is a representation of a local plastic work deformation before fracture, uniform plastic elongation is heavily influenced by plastic work hardening.



**Table 4-2 Material properties measured with round notched tensile specimen under quasi-static loading.**

Specimen ID	CSA, mm <sup>2</sup>	Strain rate, s <sup>-1</sup>	0.2 % proof stress, MPa	UTS, MPa	Y/T ratio	Elongation, %	Reduction in area, %
M04 15	35.5	1.3×10 <sup>-4</sup>	592.3	707.2	0.84	4	68.19
M04 16	35.2	1.2×10 <sup>-4</sup>	623.1	738.4	0.84	3.4	67.05
M04 17	34.9	1.1×10 <sup>-4</sup>	579.8	667.1	0.87	4.9	74.32
M04 18	34.6	1.1×10 <sup>-4</sup>	551.0	647.6	0.85	4.9	73.93
M04 19	30.1	1.2×10 <sup>-4</sup>	526.6	632.8	0.83	5.8	74.59
M04 20	30.3	1.3×10 <sup>-4</sup>	519.5	617.5	0.84	6.1	74.92
M04 13	113.3	8.2×10 <sup>-5</sup>	480.3	579.7	0.83	24.5	77.08
M04 14	112.5	8.5×10 <sup>-5</sup>	486.4	581.9	0.84	25.59	77.24

CSA = cross-sectional area of the notched region.

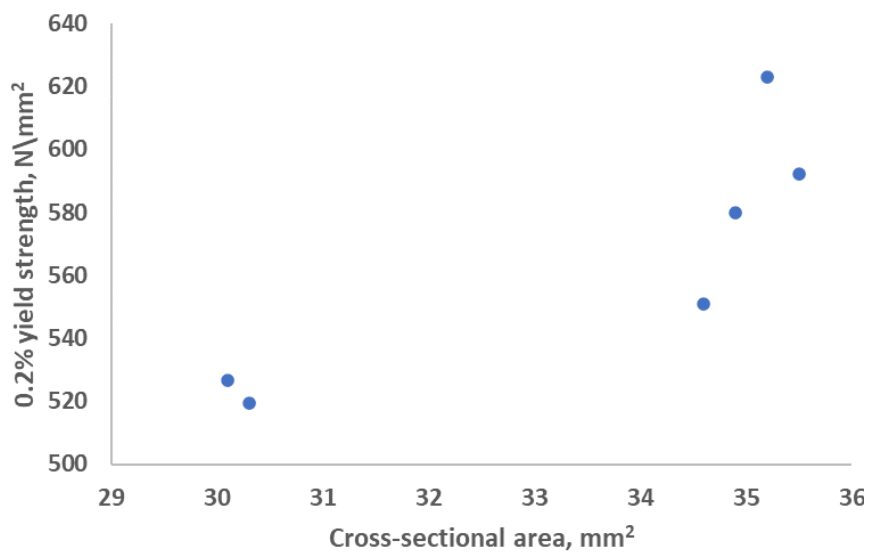


**Figure 4-5 Round (Notched and un-notched) samples variation of yield strength in X65 steel**

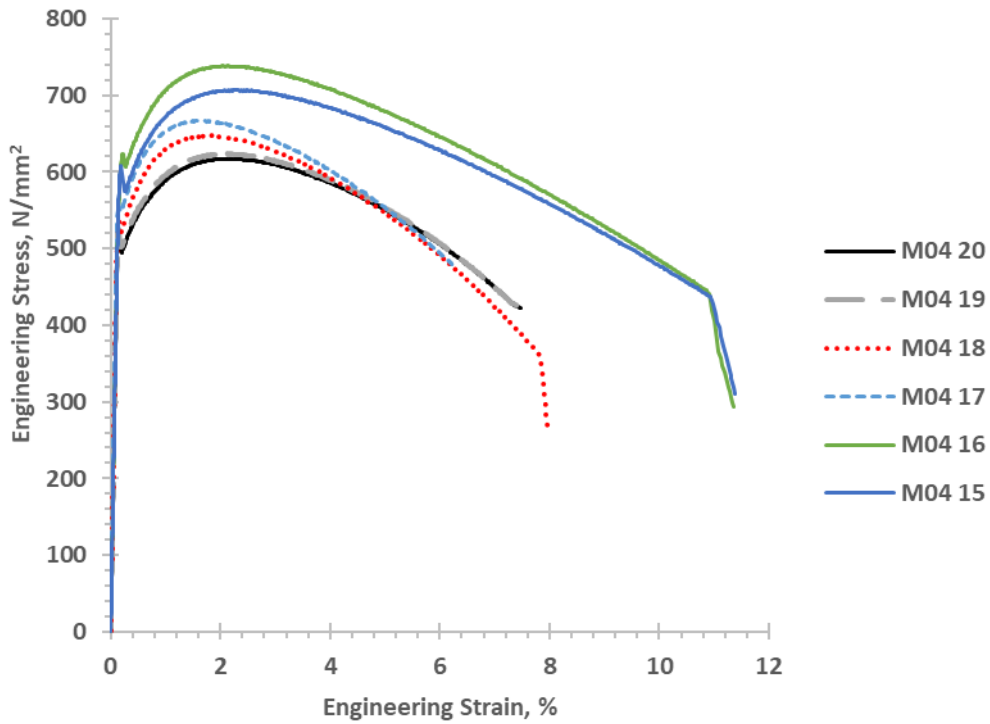


**Figure 4-6 Notched tensile test stress-strain curves.**

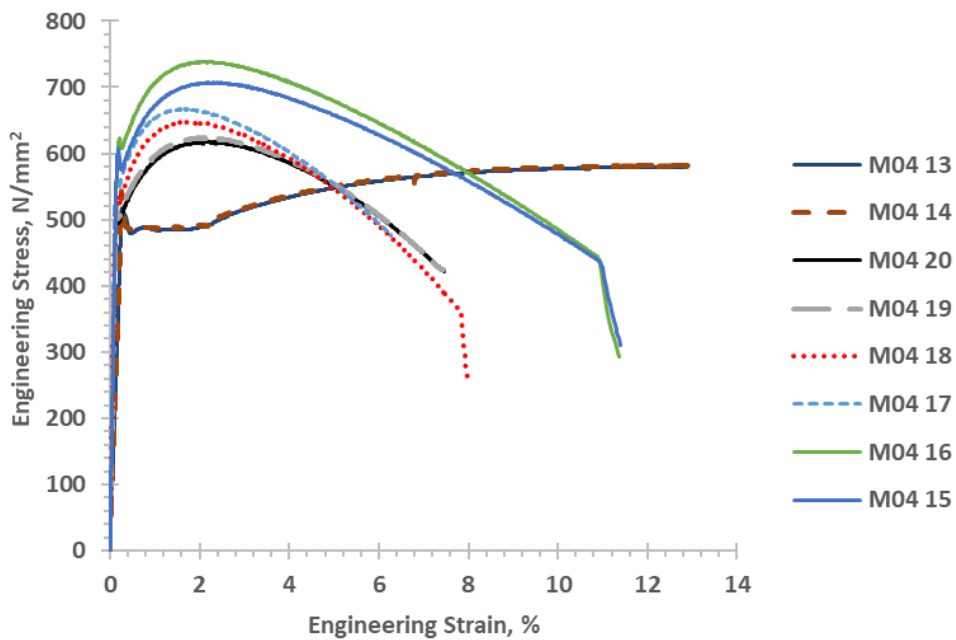


**Figure 4-7 Comparison of the notched and smooth round tensile curve**

According to (Loveday, Gray, & Aegerter, 2004), reduction in area is the most structure-sensitive ductility factor for detecting quality changes in a material's

behaviour following necking. As a result, the specimen geometry and shape (cross sections) before necking formation determine the extent of plastic work deformation and the strain-hardening curve. The resulting stress-strain curves from all the round tensile test including notched samples and un-notched samples is shown in Figure 4-7. Comparison of the notched and smooth round tensile curve Figure 4-7.

### 4.3 High strain rate tensile test results of X65 steel

Two samples were tested for each scenario and the average results were obtained as represented in Table 4-3. When dynamic deformation is being discussed, it is important to remember that the statement strain rate (which is the rate of change of strain with time is obtained from specimen geometry and experimental data, see equation (2-2)) is a critical parameter and not the velocity of deformation.

Figure 4-8 shows that strong oscillations occur as the strain rates are increasing making it difficult to see the true path of the curve. Again, the higher strain rate results show extended strain values compared to quasi-static rates. The results from these experiments were utilised in the determination of JC constant C, and damage parameter D4, as discussed in sections 2.8.4 and 2.8.5 respectively.

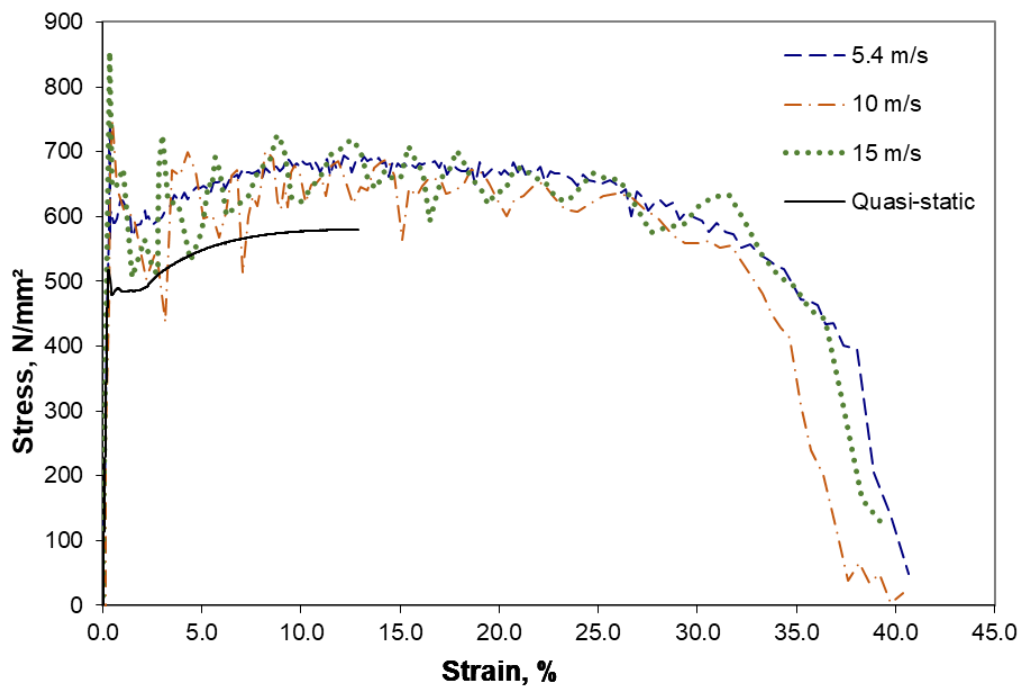


Figure 4-8 Comparison of all stress-strain curves at different displacement rates

**Table 4-3 Material properties measured with flat tensile specimens.**

Specimen ID	CSA, mm <sup>2</sup>	DR, m/s	Strain rate, s <sup>-1</sup>	0.2% PS, MPa	UTS, MPa	Y/T ratio	EI, %	RA, %
M04 01	51.7	5.4	216	599.2	746.7	0.80	29.6	72.8
M04 02	32.4	5.4	216	595.7	723.5	0.82	24.3	69.8
M04 03	31.5	10	400	641.6	747.2	0.86	26.7	62.2
M04 06	31.9	10	400	582.2	702.0	0.83	28.6	71.5
M04 07	31.6	15	600	676.2	849.1	0.80	29.8	67.4
M04 08	32.0	15	600	651.5	855.6	0.76	28.1	68.7

CSA = cross-sectional area, EL = Elongation, RA = Reduction in area, DR = Displacement rate, PS = Proof stress

#### 4.3.1 Summary of the high strain rate tensile test

The results from quasi-static and high strain rate testing shows the mechanical properties in Table 5.1. The material is very ductile exhibiting high plastic deformation prior to failure in a quasi-static tensile test. The plastic nature of the material qualifies it under the category of elastic-plastic fracture mechanics. The 0.2 % yield proof stress and the ultimate tensile strength of X65 steel were compared for varying strain rates in Figure 4-9 and Figure 4-10 respectively which showed increase at increased strain rates.

**Table 4-4 Mechanical properties of X65 grade steel.**

Mechanical properties	Quasi-static	High strain rate
Young's modulus, MPa	205 - 210	240 - 460
0.2 % proof strength, MPa	480 - 510	640 - 688
Ultimate Strength, MPa	580 - 600	740 - 856
Elongation, %	24-26	27 - 30

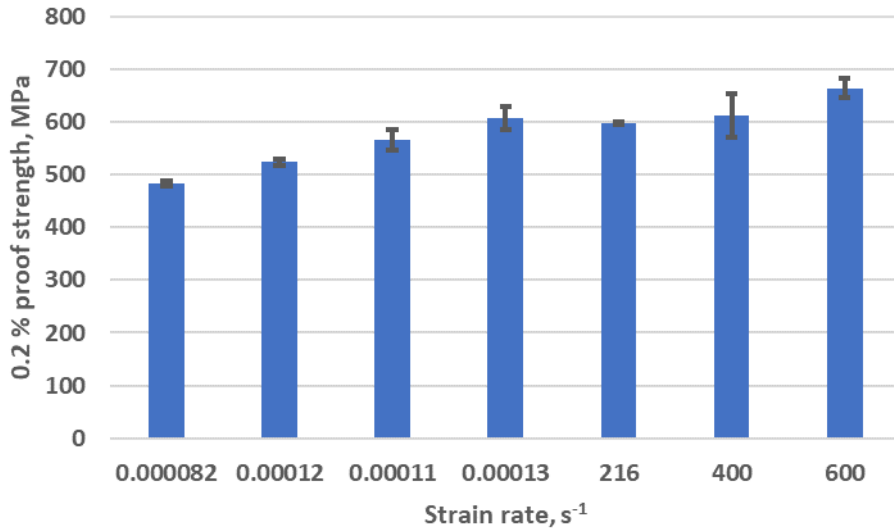


**Figure 4-9 Comparison of yield stress for un-notched, notched round specimen and flat specimens at different strain rates.**

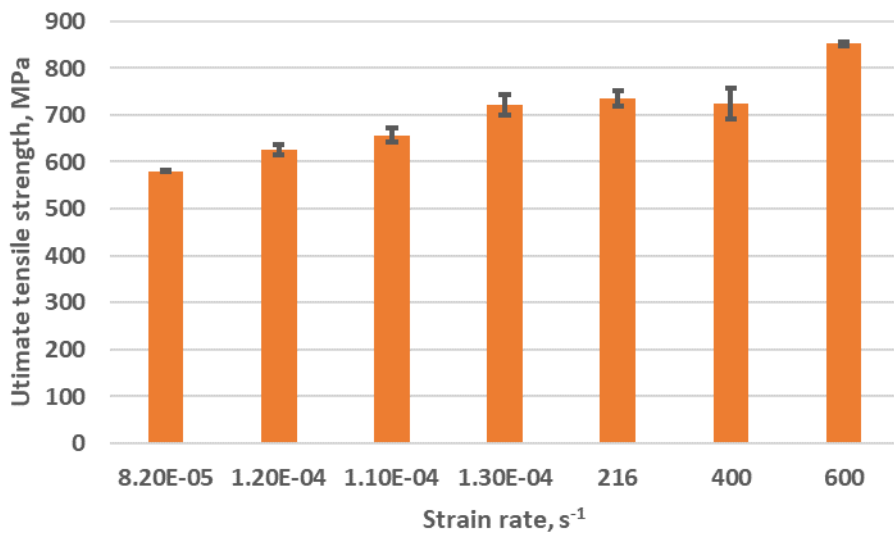


**Figure 4-10: Comparison of ultimate tensile strength for un-notched, notched round specimen and flat specimens at different strain rates which increases with strain rate.**

#### 4.4 Interpretation of tensile test data

During impact loading, the thermal diffusion distant is an important factor in determining the properties of the material. As seen in static testing that the ultimate

tensile strength (UTS) is on the region of the plastic zone, which is different in high strain rate testing as the UTS was reached prior to the plastic deformation. The thermal diffusion distance, therefore, shows the region to obtain these mechanical properties.

Figure 4-11 shows that the whole area under the curve is under the determined thermal diffusion distance and hence the UTS lies within the plastic zone. However, under dynamic loading, the thermal diffusion distance is seen to occur within a short distance under the stress-strain curve, within which the mechanical properties - 0.2 % proof stress and UTS lies before the plastic deformation which shows an increased elongation as shown in Figure 4-8 as a result of increased temperature which was discussed in Section 4.4.6.

#### **4.4.1 Thermal diffusivity effect**

Thermal diffusivity distance explained in Section 2.8.6 was utilised to determine the behaviour of the material and the extent to which heat can travel within a period. The temperature affects the thermal softening of the material. The total duration of time required for the strain to occur will affect the distance of heat diffusion, hence low strain rate loading is considered isothermal whereas the high strain rate is considered adiabatic which leads to thermal softening and shear instability.

Static loading is considered an isothermal process since it requires enough time to allow heat exchange with the environment. The thermal diffusion distance shown in Table 4-5 for the static testing was large enough and extended to both the elastic and plastic region during deformation. Since the high strain rate tests are completed at a very small-time duration, the diffusion distance is also small allowing heat to be trapped within the sample.

The result shows that the higher the strain rate, the lower the thermal diffusion distance during deformation. Figure 4-11, Figure 4-12, Figure 4-13, and Figure 4-14 showed how the thermal diffusion distance relates to the stress-strain curve. Hence, the maximum stress is determined within this distance. It could be seen that there is a sudden increase in the flow stress within the thermal diffusion distance at higher strain rates, and plastic deformation sets in after the thermal diffusion occurrence giving rise to an extended elongation.

**Table 4-5 Thermal diffusion distant at each displacement rates**

Displacement rate, mm/s	$\alpha$ , mm <sup>2</sup> /s	Strain rate, s <sup>-1</sup>	test duration, ms	D <sub><math>\alpha</math></sub> , mm
<b>Static</b>	18.8	0.000085	536410	200.8
<b>5400</b>	18.8	216	1.9	0.38
<b>10000</b>	18.8	400	1.5	0.33
<b>15000</b>	18.8	600	1.2	0.29

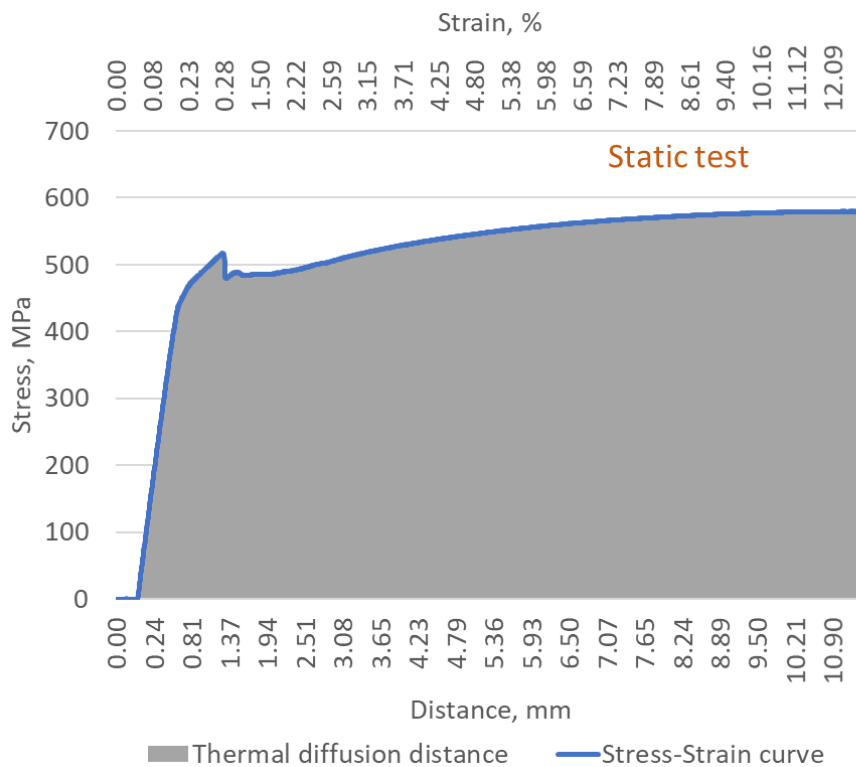


**Figure 4-11 Thermal diffusion distance covered the entire curve.**

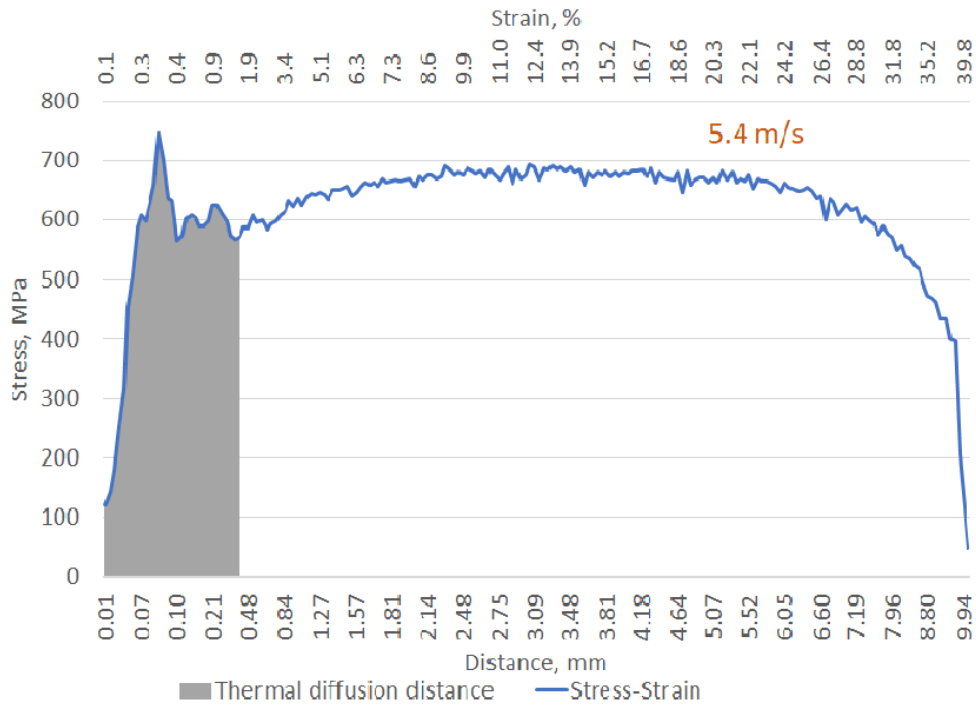


Figure 4-12 Plot to show thermal diffusion distance at 216 s<sup>-1</sup> strain rate.

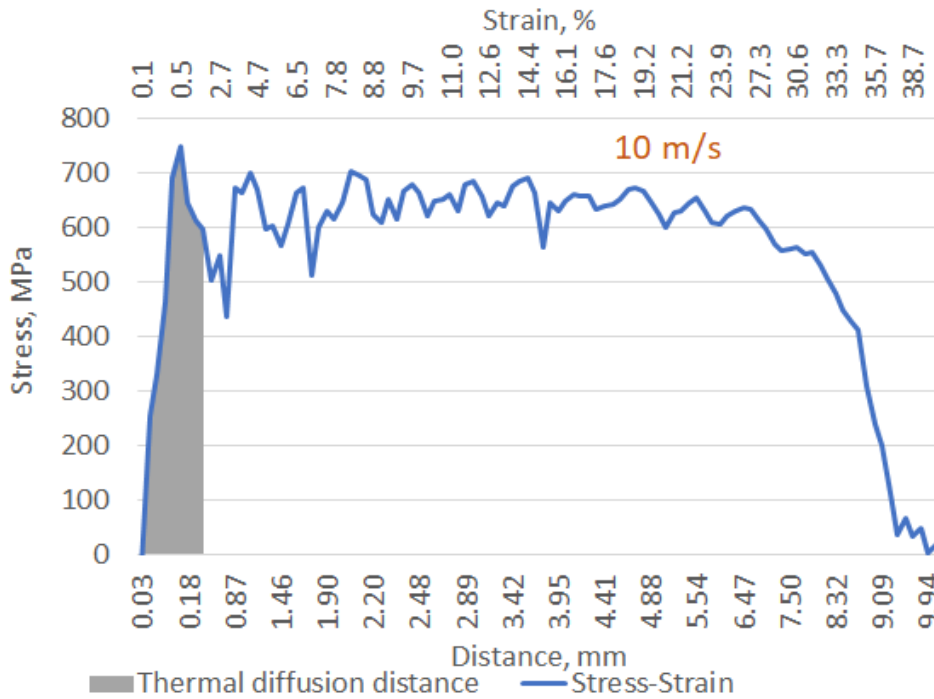


Figure 4-13 Plot to show thermal diffusion distance at 400 s<sup>-1</sup> strain rate



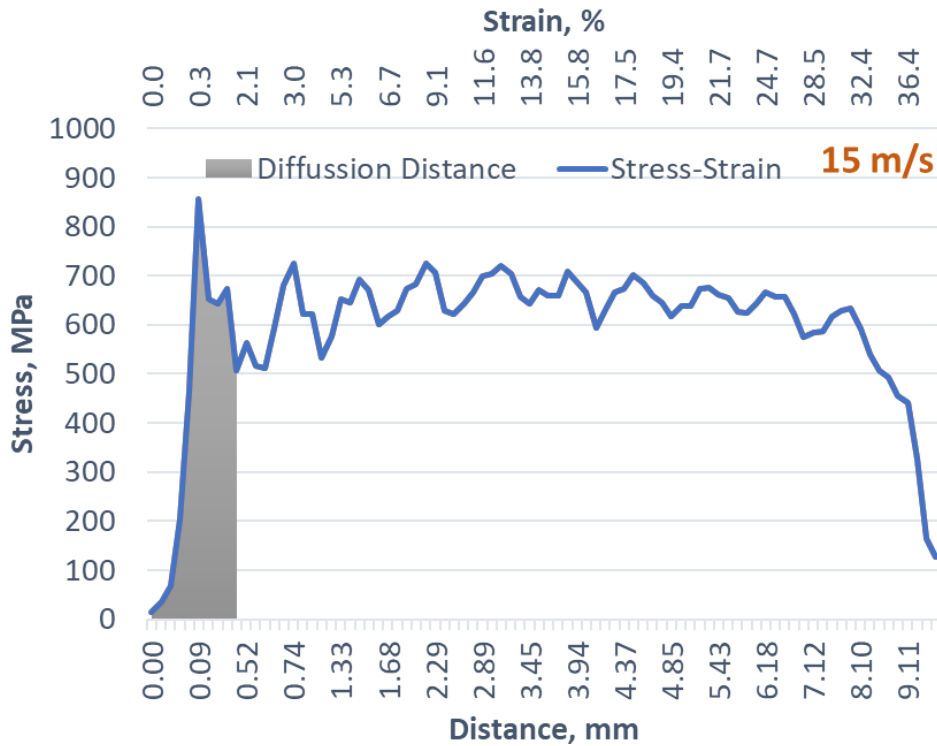


Figure 4-14 Plot to show thermal diffusion distance at  $600 \text{ s}^{-1}$  strain rate.

#### 4.4.2 Johnson-Cook plasticity parameter determination

The effect of strain, strain rate and temperature on the flow stress of a material is very crucial in material characterization to optimize the design of material resistance to fracture. Materials behave differently in different conditions such as low strain rate and high strain rate loading conditions; some could be brittle in low temperature and ductile at room and higher temperature. To be able to characterize the flow behaviour of X65 material under high strain rate deformation, the Johnson-Cook flow stress model was adopted for modelling and prediction of the material behaviour at elevated strain rates. The JC constitutive relation described in Section 2.8.4 was developed and the constants were estimated from experimental results using both numerical and graphical methods.

The material damage behaviour was predicted using the proposed failure model by Johnson and Cook. Several tests were conducted to determine the model parameter using different sample geometries such as un-notched round, notched round, and flat specimens which were tested under quasi-static and dynamic strain rate conditions at

room temperature. Table 4-6 shows the different specimens tested and their condition of testing.

**Table 4-6 Tensile test conditions for JC constants determination at room temperature**

<b>Mechanical tests</b>	<b>JC constants</b>	<b>Test conditions</b>	<b>Specimen geometry</b>
<b>Round un-notched tensile test</b>	A, B, and n	Quasi-static $10^{-5} \text{ s}^{-1}$	Round Un-notched
<b>Round-notched tensile test</b>	$d_1, d_2$ and $d_3$	Quasi-static $10^{-4} \text{ s}^{-1}$	Round notched
<b>Flat tensile test</b>	C and $d_4$	Displacement rates 5.4, 10, and 15 m/s	Flat

The relationship between the flow stress and strain for X65 metallic material was described using the Johnson-Cook model to describe the deformation, strain rate effect, and temperature effect. The flow stress model was split into three parts to obtain the constants  $B$ ,  $n$ , and  $C$ . The  $A$  constant was assumed as the material 0.2 % yield stress for quasi-static testing, and the effective temperature component  $m$  is equal to 1 since elevated temperature was not considered. The reference strain rate was taken as  $1 \text{ s}^{-1}$  to determine the strain rate strengthening coefficient  $C$ .

#### **4.4.3 Determination of JC constants A, B, and n.**

The JC equation was modified to determine the values of  $B$  and  $n$  representing the strain hardening constant and strain hardening coefficient, respectively. The deformation temperature was the same as the reference temperature, and when the strain rate equals the reference strain rate taken as  $1 \text{ s}^{-1}$ , the equation is reduced to **(4-3)**.

$$\sigma = (A + B\varepsilon^n) \tag{4-3}$$

Where  $A$  is the 0.2 % yield stress, while strain rate strengthening, and effects of thermal softening are neglected. To obtain constants, the logarithmic approach was

utilised in which equation (4-3) was further analysed taking the natural logarithm of the yield equation (4-4).

$$\ln(\sigma - A) = n \ln \varepsilon + \ln B. \quad (4-4)$$

Through substitution of the A value and the flow stress values from the experiment, the linear relationship was plotted between  $\ln(\sigma - A)$  and  $\ln \varepsilon$  of which a linear first order regression was fitted to the data as shown in Figure 4-15. The line of best fit was chosen to be a linear line as in equation (4-4) which is linear. The equation of the fit was obtained of which the intercept is  $n$  which is 0.7939, and the exponential of the slope from the fitted curve yields the value of  $B$  as 1043 MPa. It is noted that the regression line fits about 97 % close to the data, and the results is as shown in Table 4-7.

**Table 4-7 Result of B and n from linear regression method.**

A (MPa)	B (MPa)	n
482	1043	0.7939

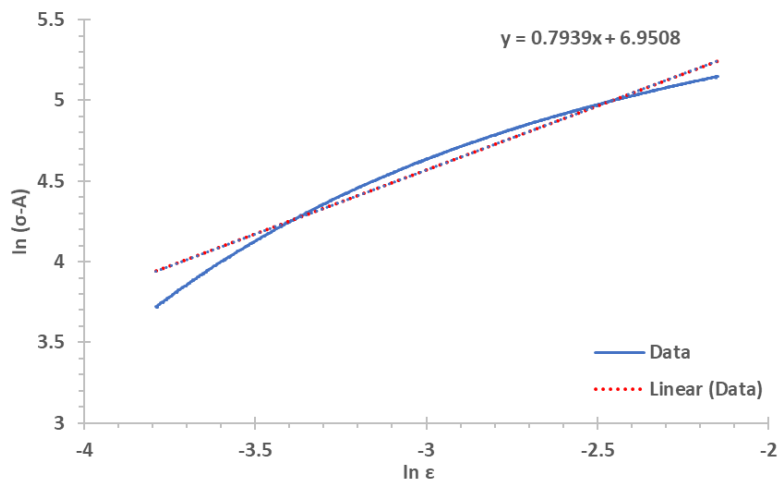


**Figure 4-15 Natural logarithm of flow stress and strain.**

#### 4.4.4 Determination of JC constants C.

At the same temperature with the experiment and reference temperature, the JC equation was reduced to equation (4-5) neglecting the effect of thermal softening.

$$\sigma = (A + B\varepsilon^n)(1 + C \ln \dot{\varepsilon}^*), \quad \text{where } \dot{\varepsilon}^* = \frac{\dot{\varepsilon}}{\dot{\varepsilon}_0} \quad (4-5)$$

Then the above equation was rearranged to obtain the C constant value as shown in equation (4-6).

$$\frac{\sigma}{(A + B\varepsilon^n)} = (1 + C \ln \dot{\varepsilon}^*) \quad (4-6)$$

The already determined values of A, B, and n, were substituted in equation (4-6) such that the plot of  $\frac{\sigma}{(A+B\varepsilon^n)}$  versus  $\ln \dot{\varepsilon}^*$  was plotted at different strain rates (216 s<sup>-1</sup>, 400 s<sup>-1</sup> and 600 s<sup>-1</sup>). The slope of the curve shown in Figure 4-16 is the C value estimated to be 0.0319 at an intercept of 1 as seen in (4-6).

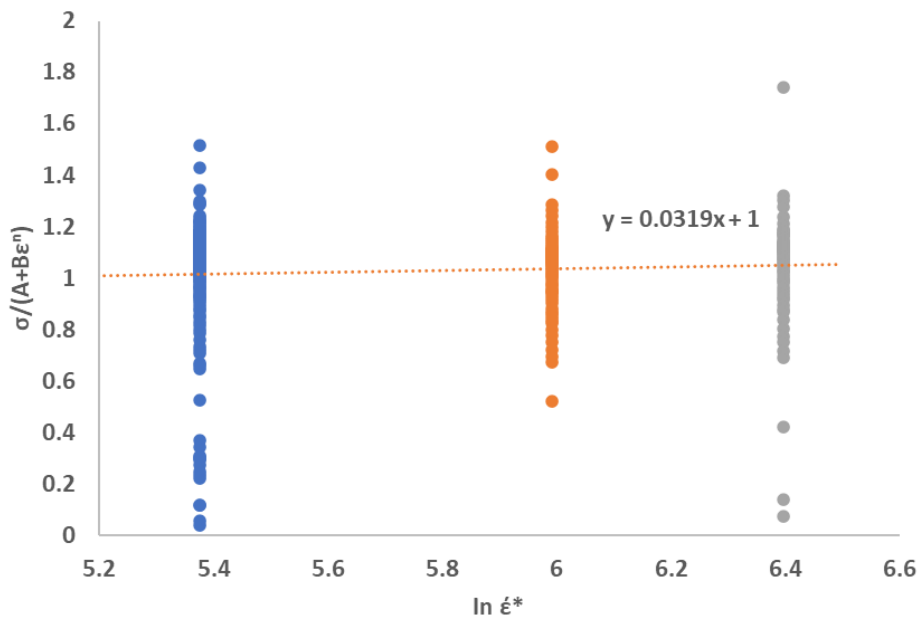


**Figure 4-16 Plot for obtaining the Johnson-Cook C constant.**

Being that the reference temperature is the same as the experiment, the value of m equals 1. The linear fitting in Figure 4-16 was performed to satisfy equation (2-35) to obtain parameter C. Hence, all derived Johnson-Cook parameters utilised in the FEA Abaqus model is as shown in Table 4-8 Regular JC obtained Table 4-8. The parameters were confirmed by comparing JC model with the experimental data and the results were presented in Figure 4-21 and Figure 4-22.

**Table 4-8 Regular JC obtained parameters.**

A (MPa)	B (MPa)	n	C	m	T (K)
482	1043	0.7939	0.0319	1	295

Utilising the Johnson-Cook constants obtained in this work and those obtained in literature in simulation, the comparison showed that this model has closer correlation of about 3% differences with the Cortis results, and 30% with the El-Danaf results. The simulations were done with the determined Johnson-Cook ductile damage parameters ( $d_1 - d_5$ ) in this project. The differences could be error obtained due to testing machines and calibration. It is therefore recommended to use the values with a complete set of JC parameters for simulation.

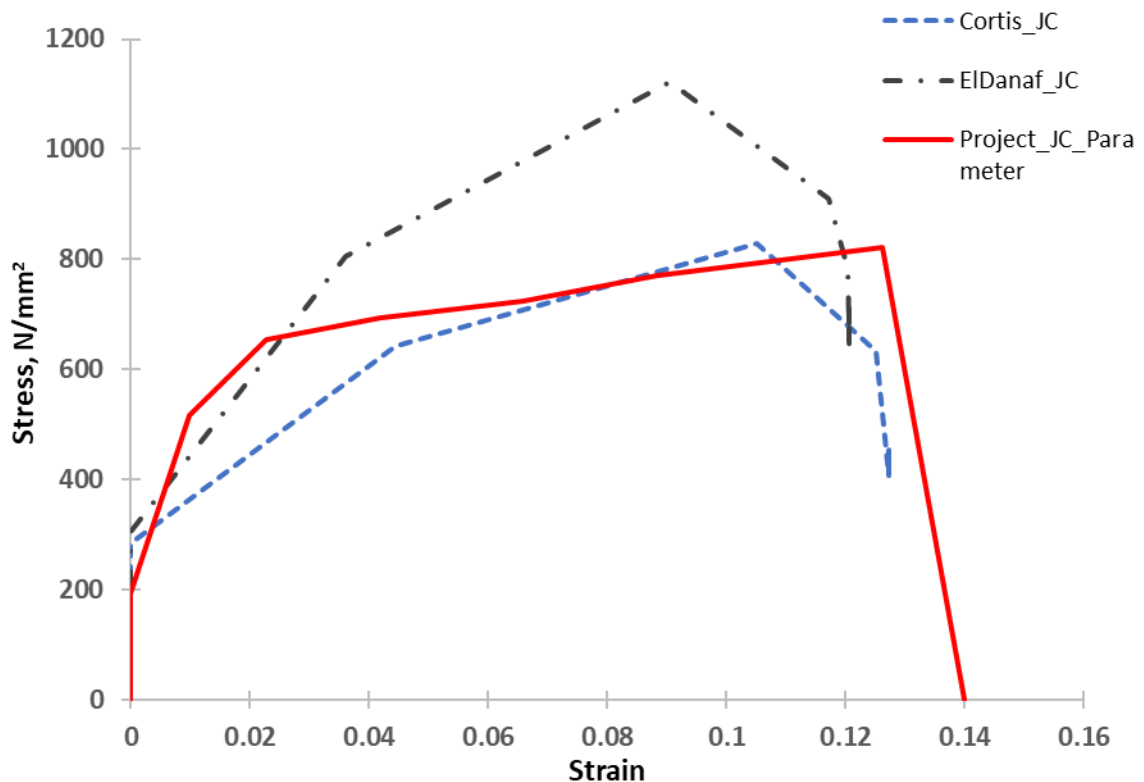


**Figure 4-17 Comparison of obtained X65 steel Johnson-Cook parameters with (Cortis, Nalli, Sasso, Cortese, & Mancini, 2022) and (El-Danaf et al., 2013) JC parameters using same ductile damage parameter ( $d_1 - d_5$ )**

#### 4.4.5 Determination of Johnson-Cook ductile damage parameter

Johnson and Cook's proposal require that fracture strain depends on three variables which include stress triaxiality ratio, strain rate, and temperature. The model has been explained in Section 2.8.5 and is applied to obtain the damage model constants ( $d_1 - d_5$ ). The quasi-static experiments performed on round bar specimens (un-notched and pre-notched) were used to describe the effect of stress triaxiality on X65 steel material.

The Bridgeman's analytical model in equation (4-7) was applied to obtain the stress triaxiality for the JC damage model.

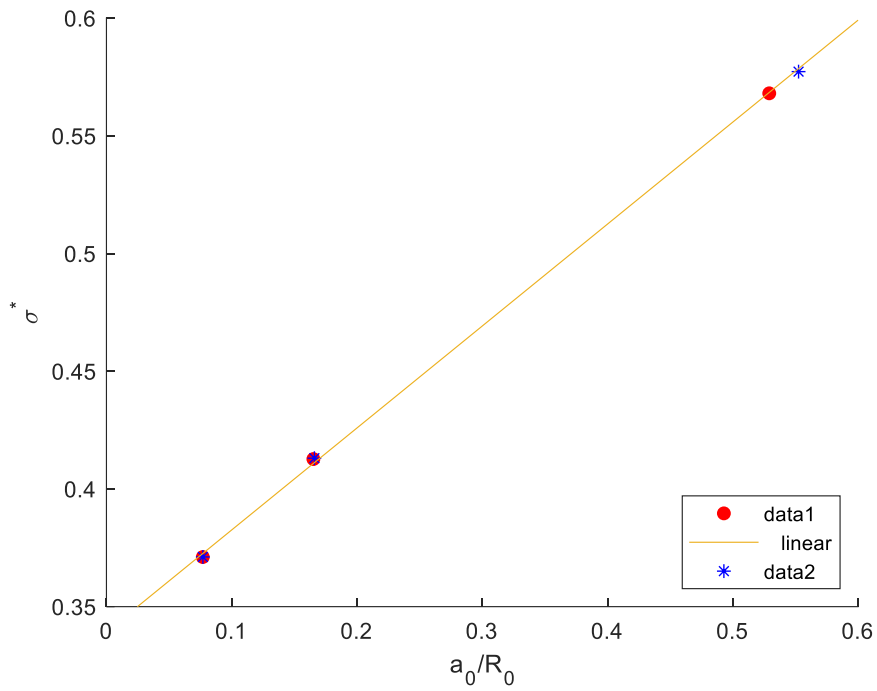
$$\sigma^* = \frac{1}{3} + \ln\left(1 + \frac{a_0}{2R_0}\right) \quad (4-7)$$

Where,  $\sigma^* = \frac{\sigma_m}{\sigma_{eq}}$  is the stress triaxiality,  $a_0$  is the smallest area of the radius, and  $R_0$  is the radius of the circumferential notch. With the values of stress triaxiality known, it was substituted in equation (2-26) first part of the equation, while neglecting strain rate and temperature effects to yield fracture strain equation (2-37)

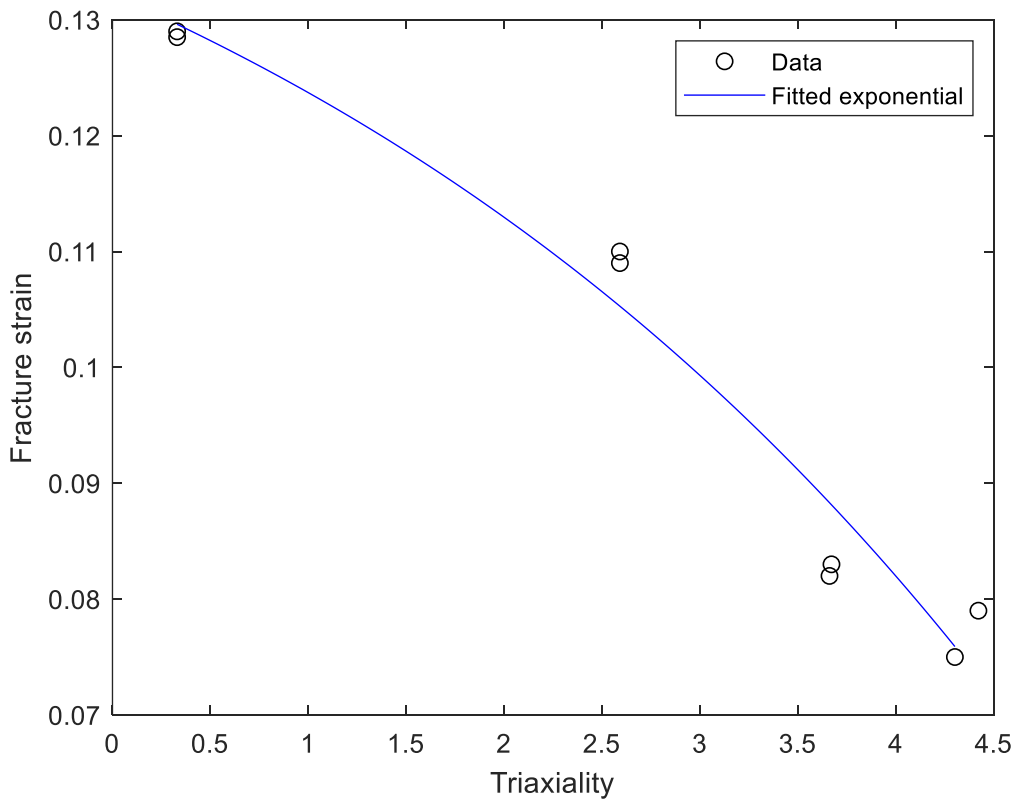
$$\varepsilon_f = (d_1 + d_2 \exp(d_3 \sigma^*)) \quad (4-8)$$

Figure 4-18 shows the six variables from different samples that were employed to determine the stress triaxiality of X65 steel. This aspect shows that stress triaxiality increases with  $\frac{a_0}{R_0}$  ratio.

Fracture strain values and corresponding stress triaxialities were substituted into equation(2-37) to establish the relationship plot in Figure 4-19 to derive the model parameters  $d_1$ ,  $d_2$ , and  $d_3$  shown in Table 4-9. Further analysis of the fracture strain variation was performed to determine the  $d_4$  parameter. The temperature effect was not considered in this study hence  $d_5$  equals zero.



**Figure 4-18 Different stress triaxialities obtained from experimental data**



**Figure 4-19 Fracture strain Vs stress triaxiality plot fitted for round tensile tests.**

**Table 4-9 JC ductile damage parameters (dimensionless)**

Derived damage parameters					
d <sub>1</sub>	d <sub>1</sub>	d <sub>2</sub>	d <sub>3</sub>	d <sub>4</sub>	d <sub>5</sub>
0.1638	-2.569	2.705	0.005	0.0031	0

#### **4.4.6 Rise in temperature during plastic deformation**

The temperature increase has been investigated in terms of the flow stress,  $\sigma$ . Figure 4-20 shows an increase in temperature at varying strain. It is observed that the quasi-static loading rate has little temperature rise and can fracture at a very small strain of about 0.12 as seen in Figure 4-8, which will yield an insignificant temperature rise of about 5 K.

However, high strain rate deformation which is often adiabatic experiences a significant rise in temperature at increased strain, such that the deformation work is converted into heat. Since this temperature rise leads to thermal softening, it therefore, has a profound effect on the material behaviour. The temperature rise derivation from the constitutive equation was discussed in Section 2.8.6 and has been employed to determine the result presented in Figure 4-20, showing the significant rise in temperature as the strain rate increases. The equation (2-42) which comprises of the temperature effect with the flow stress,  $\sigma$  from JC equation were inputted into the equation to determine the final rise in temperature plotted in Figure 4-20 against the strain.



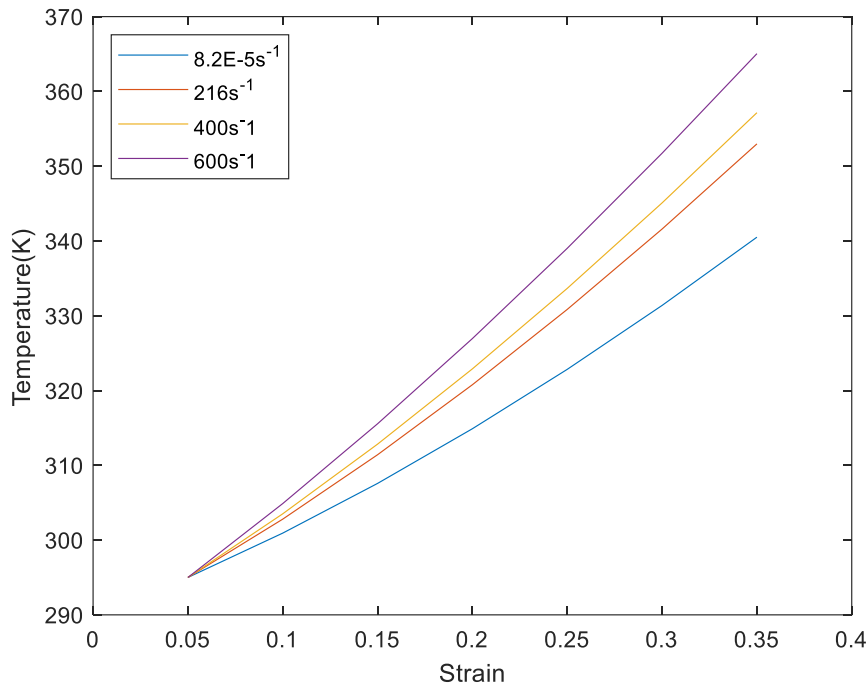


**Figure 4-20 Analytical temperature rise comparison for different strain rates.**

#### **4.5 Analytical approach to thermostatistical model in BCC metals**

This study incorporated the effect of rising temperature during dynamic loading to model the dislocation density from generation, glide and annihilation during deformation. This was possible to determine using the dislocation evolution theory (Section 2.9) equation adopted from (Galindo-Nava & Rivera-Díaz-del-Castillo, 2012). The dynamic loading was considered adiabatic as it has less time for heat dissipation to take place with the environment. The resulting comparison is shown in Figure 4-21 and Figure 4-22 for the JC model (equation (2-35)), dynamic recovery method in BCC metals (equation (2-31)), and the experimentally derived data. When the effect of temperature was considered in the dynamic recovery method of BCC metals (equation (2-47)), the result is as shown in Figure 4-23 and Figure 4-24 comparing the temperature and non-temperature effects.

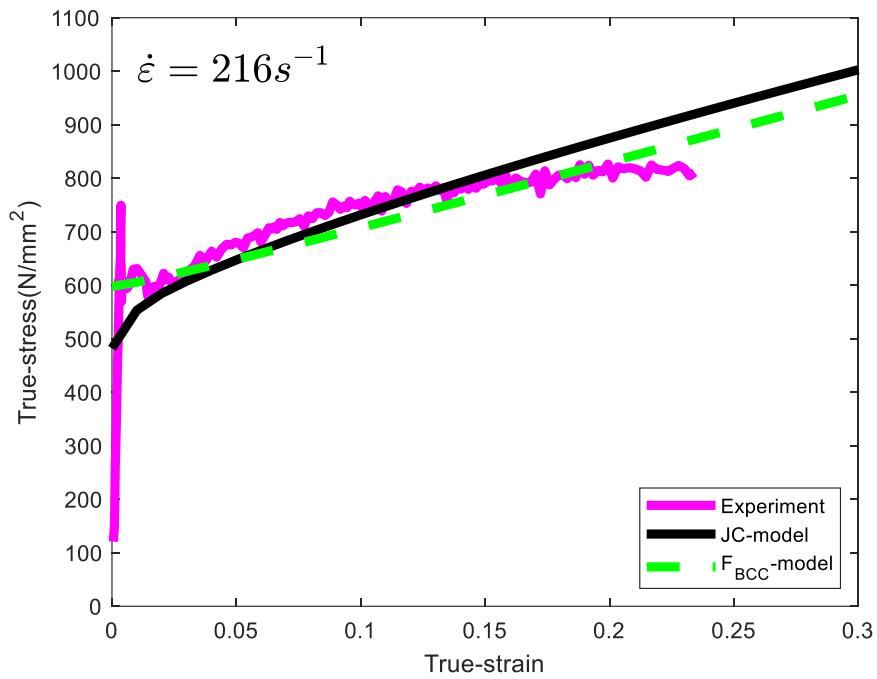


Figure 4-21 Two models compared with the experimental data at 216 s<sup>-1</sup>.

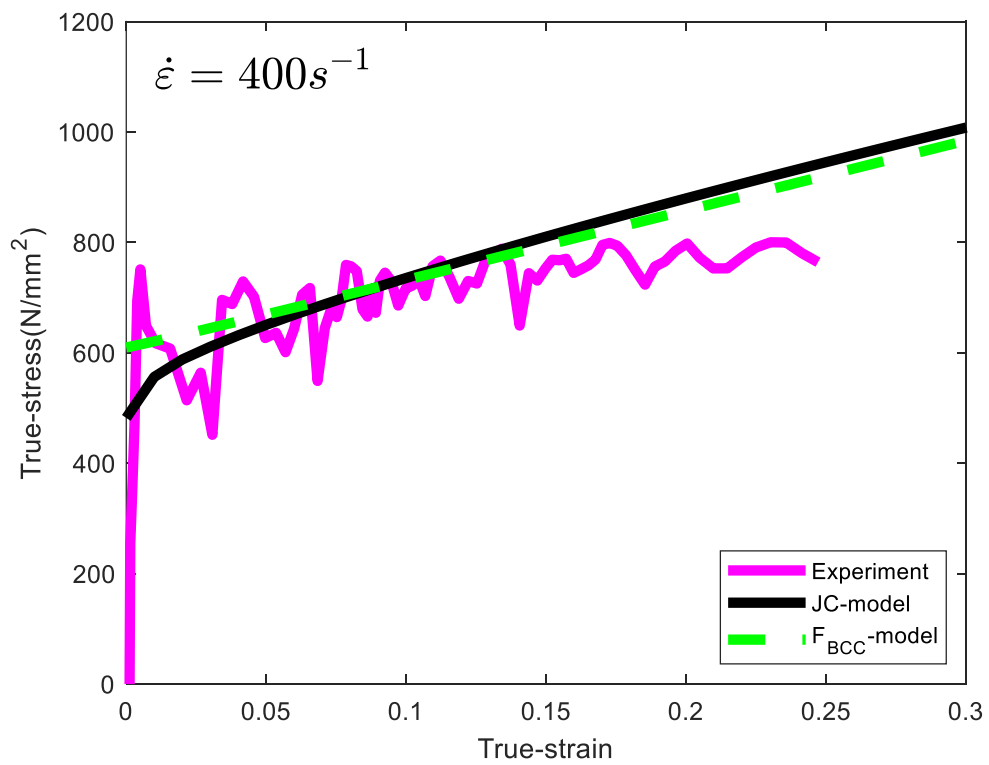


Figure 4-22 Two models compared with the experimental data at 400 s<sup>-1</sup>.

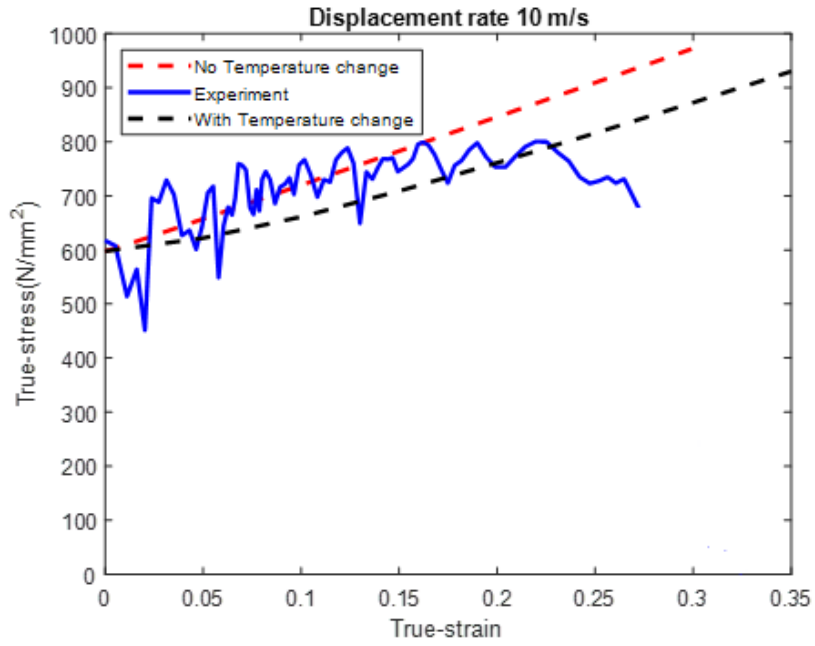


Figure 4-23 Stress-strain curve comparing the effect of temperature rise at 400 s<sup>-1</sup>.

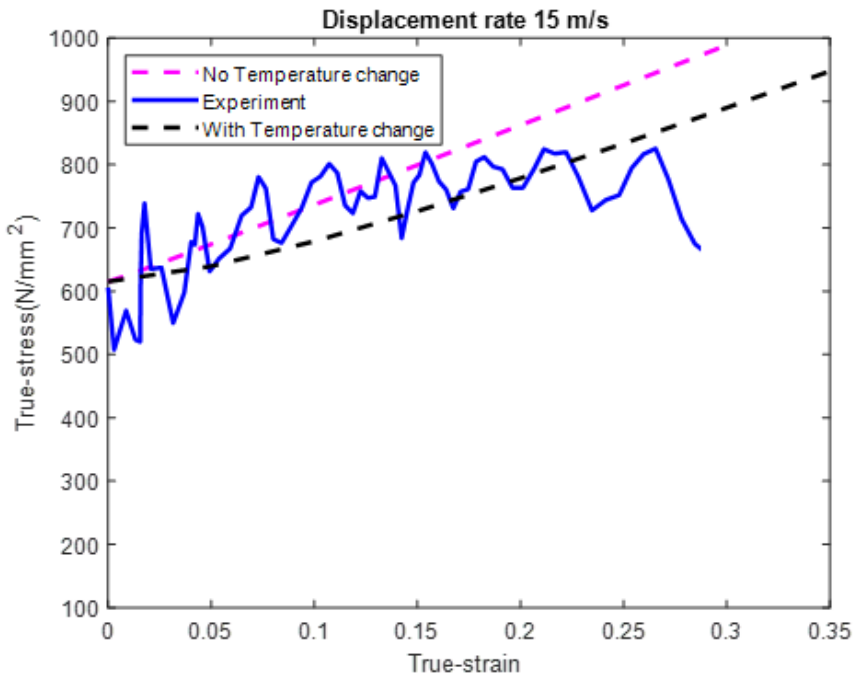


Figure 4-24 Stress-strain curve comparing the effect of temperature rise at 600 s<sup>-1</sup>.

## 4.6 FEA modelling of tensile tests

FEA modelling aids to design new testing model without building a prototype to save cost, and it allows easy modification in an existing design to affect new functions in order to solve problems with manufacturing processes such as forming processes and assembly stresses. These processes help in design verification and validation from most economical design to avoid expensive failure. Abaqus/CAE software was utilised in this project for modelling and simulation as it provides interactive access to fracture-specific tools like focused meshes, defining q-vectors or normal to the crack front, selection of crack front and tip among others.

The X65 material properties determined from experimental data was implemented in simulation to verify fracture strain from the experiment as shown in Figure 4-28, taken from the Von Mises stress in the simulation close to necking region. In addition to the experimental and analytical methods, the computational method was employed to predict the stress-strain curves at different loading conditions. Figure 4-27(a) and Figure 4-28 show the model and its corresponding curve respectively. The gauge length was 25 mm (full dimension - Figure 3-4(a)), tensile properties (Table 4-2), and one end was fixed while the other move. Partitioning was carried out so that the gauge area has smaller mesh density to enhance the displacement recorded.

Although, finer mesh aids in obtaining high-definition calculation and improve accuracy of the model, high strain rate model mesh sensitivity is shown in Figure 4-25 and Figure 4-26 for round and flat tensile tests respectively. Mesh of C3D8R: An 8-node linear brick, reduced integration, hourglass control was applied to the tensile samples, with element deletion to enable fracture. The C3D8R mesh was used to reduce the simulation running time as the integration was a single integration point. Fracture strain, stress triaxiality and strain rate were applied as the ductile damage material properties utilising derived experimental stress and plastic strain for the plasticity model. For the notched sample, one of the notch radii was modelled in Abaqus as shown in Figure 4-29 and the plot obtained was compared to the true stress-strain curve in Figure 4-30.

The high strain rate tensile test was modelled with a flat specimen shown in Figure 4-31 with dimension in Figure 3-6, and two strain rates ( $400$  and  $600 \text{ s}^{-1}$ ) were simulated with resulting plots in Figure 4-32. The JC damage parameters were applied

in the material property of the model. The yield stress representing JC constant A changes depending on the strain rate being modelled as obtained from experimental results. The boundary condition applied was the ENCASTRE for the fixed end, and displacement/rotation for the tensile end extending at an applied U2 direction with amplitude. A Dynamic/Explicit analysis was performed with element deletion enabled to aid fracture.

**Table 4-10 FEA elements distribution in mesh sensitivity analysis with round tensile specimen.**

<b>No. of elements</b>	<b>Linear hexahedral element type</b>	<b>Maximum stress (MPa)</b>
<b>10528</b>	C3D8R	577.30
<b>21164</b>	C3D8R	578.53
<b>70784</b>	C3D8R	579.47
<b>128436</b>	C3D8R	579.47
<b>589593</b>	C3D8R	579.47

**Table 4-11 FEA elements and node distribution in mesh sensitivity analysis for the flat specimen.**

<b>No. of nodes</b>	<b>No. of elements</b>	<b>Linear hexahedral element type</b>	<b>Maximum stress (MPa)</b>
<b>1072</b>	462	C3D8R	852.31
<b>3204</b>	1936	C3D8R	850.62
<b>7140</b>	4956	C3D8R	849.47
<b>19690</b>	14952	C3D8R	849.13
<b>37464</b>	29970	C3D8R	849.49
<b>143775</b>	124608	C3D8R	859.57

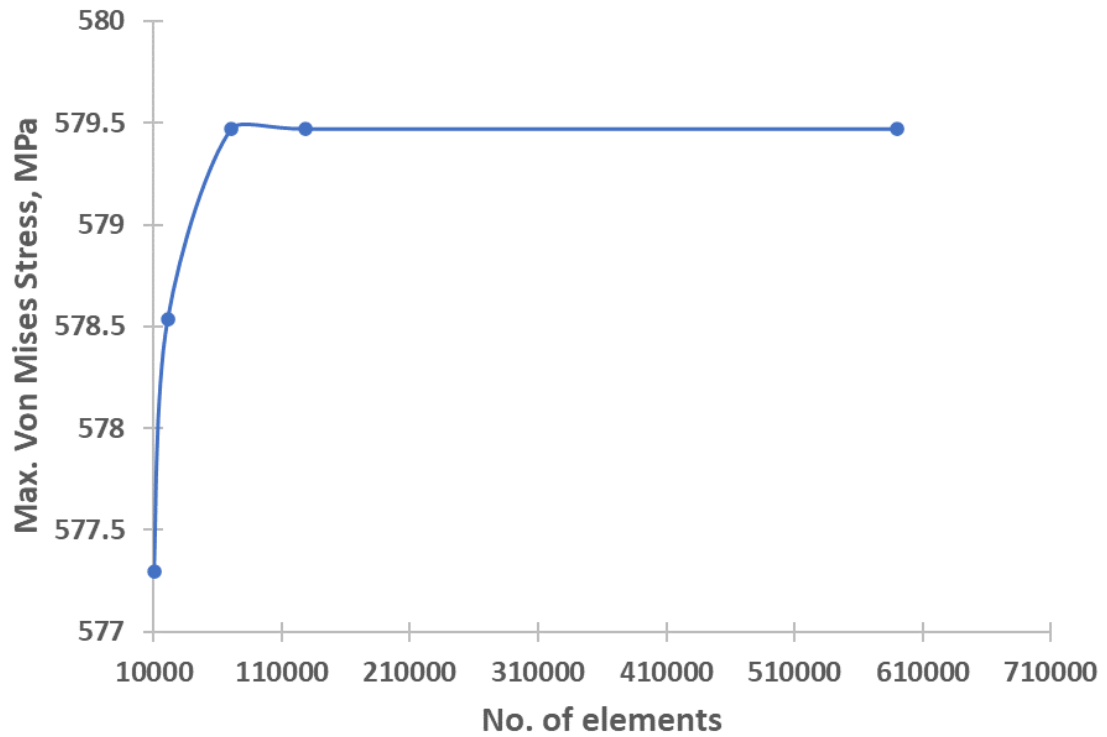


Figure 4-25 Mesh Sensitivity analysis for the round tensile specimen

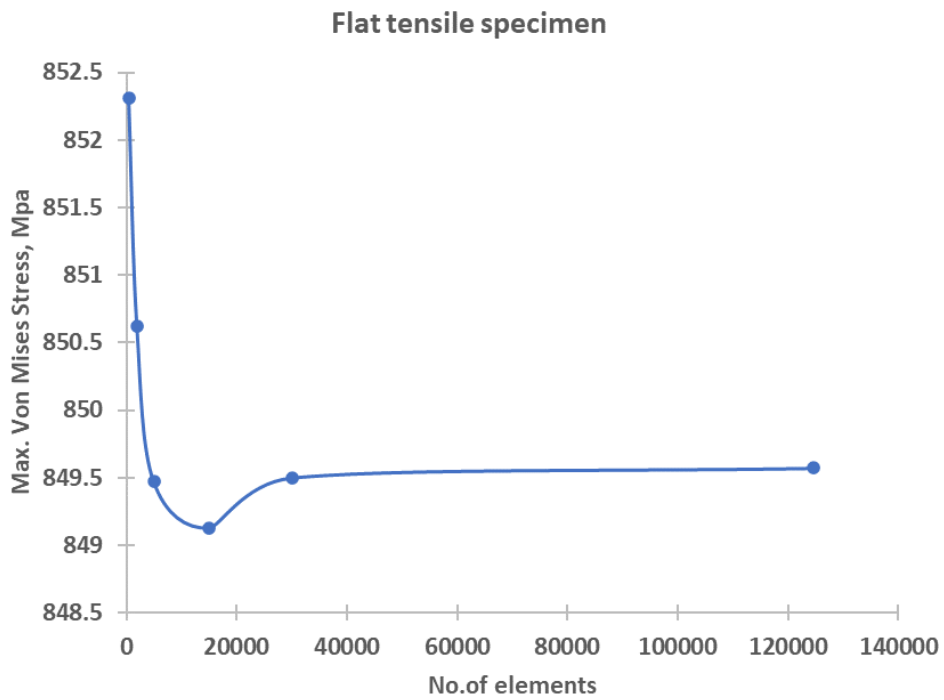


Figure 4-26 Mesh Sensitivity analysis for the flat tensile specimen at 600 s<sup>-1</sup> strain rate

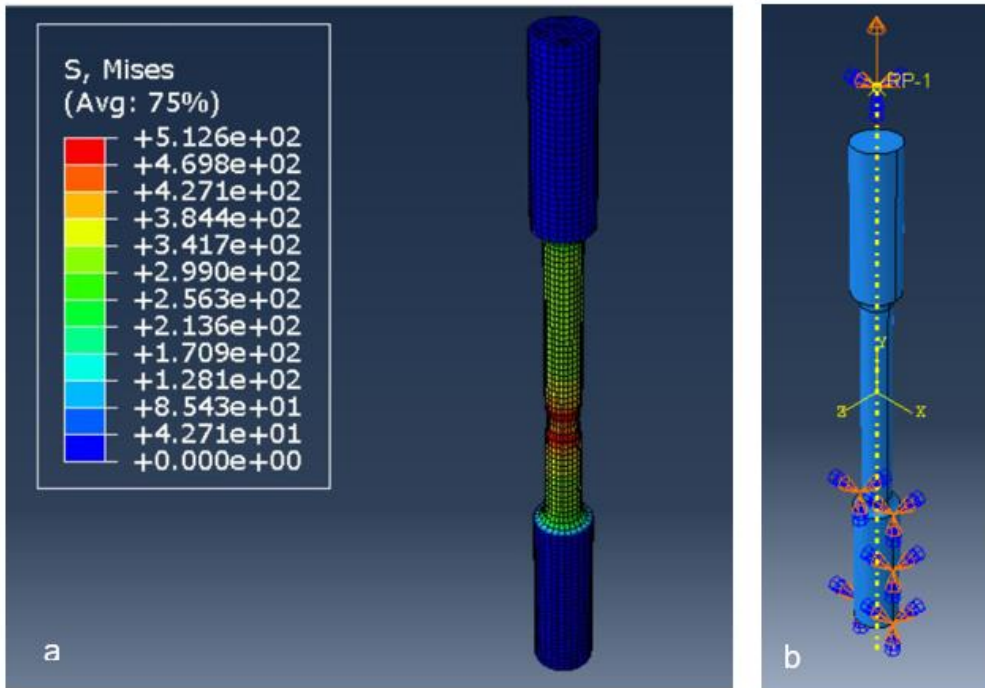


Figure 4-27 FEA model of un-notched round specimen (a) showing the location of stress (b) showing the boundary conditions.

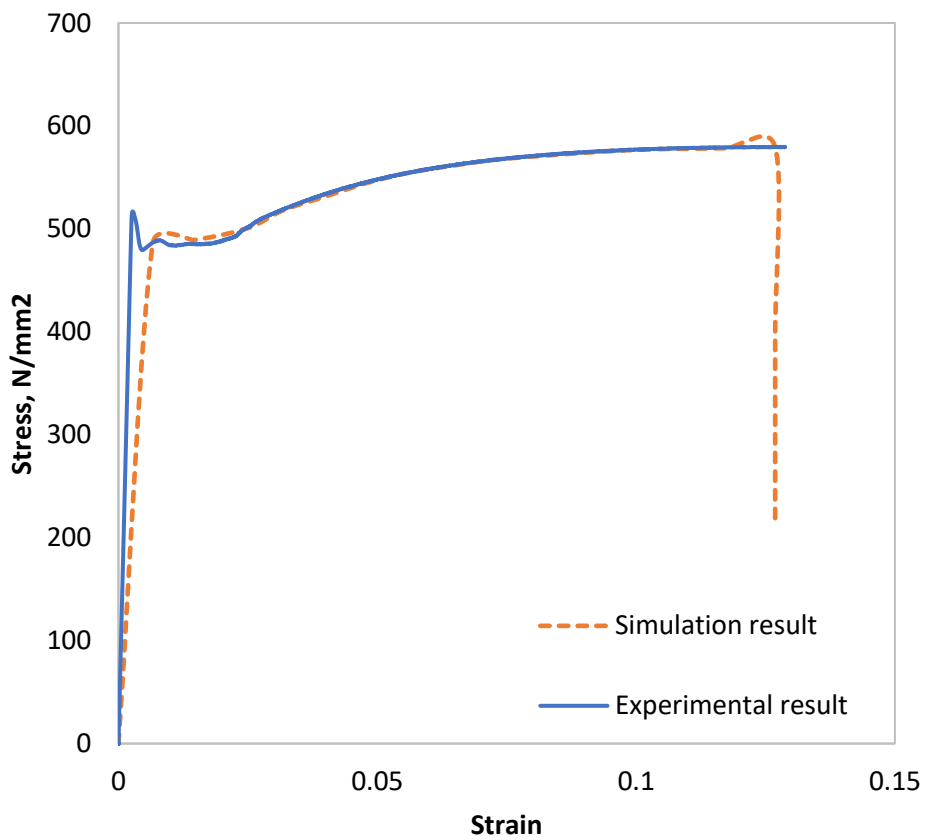


Figure 4-28 FEA Model simulation and experimental data for un-notched sample

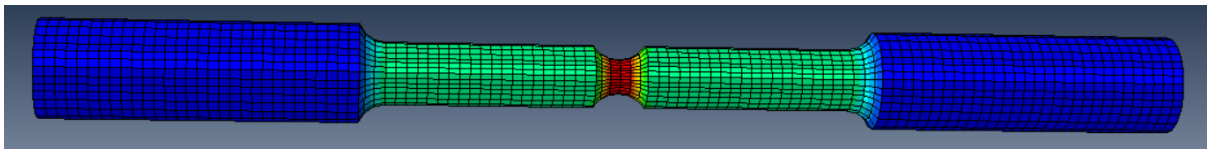


Figure 4-29 Notched Tensile testing sample in FEA model simulation.

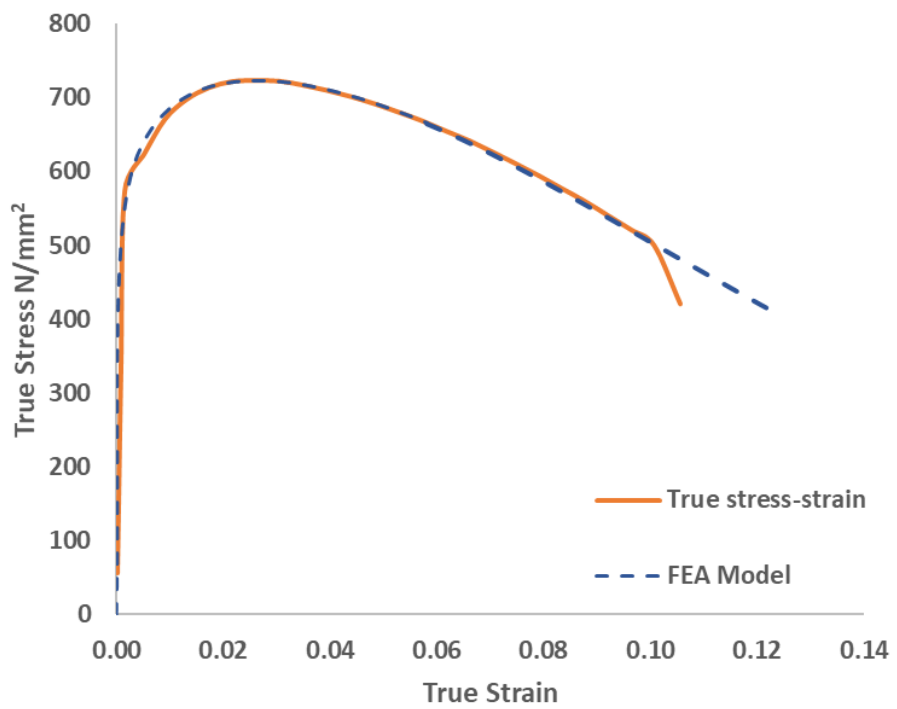


Figure 4-30 Round notched sample comparing different data set.

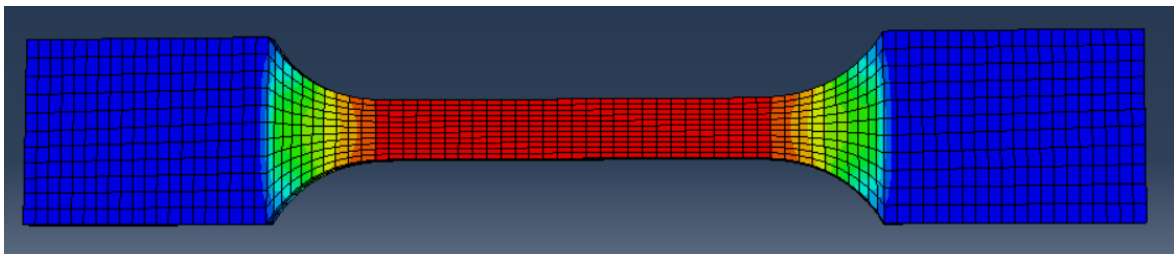
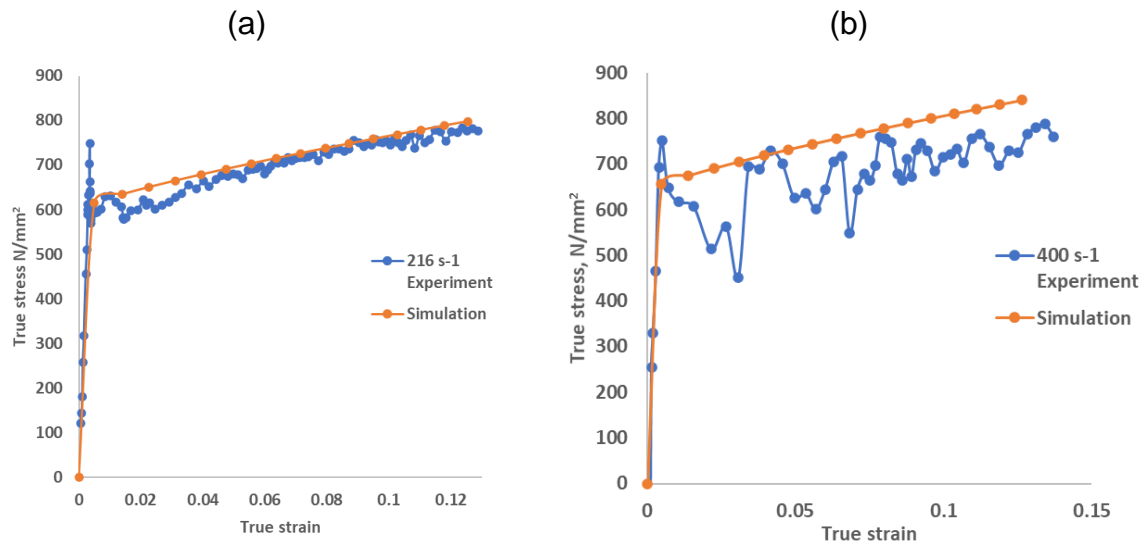


Figure 4-31 Flat tensile specimen FEA modelled in Abaqus.





**Figure 4-32 Comparison of simulation and experiment for (a) 216 s<sup>-1</sup> and (b) 400 s<sup>-1</sup> with flat specimen.**

## 4.7 Discussion on Tensile Testing Analysis

### 4.7.1 Different methods of high strain rate testing

There are different methods that can be used to produce dynamic deformation using experimental techniques discussed in Section 2.4.1 such as Taylor test, the Hopkinson bar test, and expanding ring, depending on the targeted strain rates which is in the range of  $10^3 - 10^5 \text{ s}^{-1}$ . In Section 2.4, a definition and description of strain rates and the ranges of low, intermediate, and high strain rate were given. It was also seen that inertia forces are neglected at lower strain rates to attain an equilibrium, but the effect is considered in higher strain rates due to the propagation of wave effects. At increased strain rates in the range of  $10^5 - 10^8 \text{ s}^{-1}$ , shear wave and shock wave propagation are adopted.

The hydraulic, servo-hydraulic, and screw-driven testing machines are utilised for quasi-static testing in the range of  $10^{-5} - 10^0 \text{ s}^{-1}$ . Testing strain rates in the range of  $10^1 - 10^3 \text{ s}^{-1}$ , is considered dynamic-low experiments of which the high-velocity hydraulic, pneumatic and cam plastometer machines are used. The scope of this work applied an API X65 steel in which its expected real life strain rates effect in offshore condition falls within the dynamic-low strain rate. It is worth noting that dynamic deformation is grouped into three categories including dynamic- low ( $10^1 - 10^3 \text{ s}^{-1}$ ).

Dynamic-high ( $10^3 - 10^5 \text{ s}^{-1}$ ), and high velocity impact ( $10^5 - 10^7 \text{ s}^{-1}$ ) as adopted from (Meyers, 1994).

#### **4.7.2 Effect of strain rate on tensile testing**

It has been traced back to 1905 when Bertram Hopkinson conducted experiment on steel and concluded that dynamic strength was at least twice the strength at low strain rate. Experiments conducted on steels shows that it undergoes a ductile-to-brittle transition at increased strain rate, thus the curiosity on the effect of strain rate on strength of materials. Figure 4-33 and Figure 4-34 has shown that individual materials has varying response to strain rates and therefore becomes necessary to test each material to obtain specific information. (Capelle, Furtado, Azari, Jallais, & Pluvinage, 2013) have reported that the yield strength of X65 steel at low and dynamic loading differs, with increased yield strength and transition temperature occurring at the dynamic loading.

Since the flow stress has dependence on strain rate, some constitutive models have been generated to determine the flow stress. In this work, Johnson-Cook equation in which its parameters have been determined in Section 4.4 was adopted and inputted into computational code in ABAQUS to determine the effect of strain rates on the X65 steel. Other analytical approach was adopted as described in Chapter 2 (thermostatistical model) and a very good agreement was established between the analytical model and experimental result as seen in Section 4.5. The thermostatistical model in which the dislocation movement, dislocation glide and dislocation annihilation was considered as the agent of plastic deformation described the relationship that exist between dislocation velocity and applied stress.

In the tensile test, the different values obtained were as shown in Table 4-1 and Table 4-2. There are quite visible variations in the 0.2 % proof strength for X65 steel. There are certain reasons for these differences to occur but the most significant is the strain rates of the testing. Since the strain rate affects the material behaviour, it was seen that the yield strength increases with the strain rate.

Comparing the values in Figure 4-1 and Figure 4-8, it is observed that stress-strain curve at quasi-static strain rates produce a smooth curve, while the higher strain rates produce significant oscillations. These are due to the effect of inertia on testing

material at high strain rates. This oscillation is observed since the material behaviour depends on the rate of loading applied during mechanical testing. Also, the result shows that the amplitude and the wavelength of the oscillations become greater as the strain rate increases and could be linked with the measuring instrumentation which is unable to record continuous data set during increased loading rates unlike at quasi-static rates. Hence making the number of available data points to be fewer at higher strain rates experimentation.

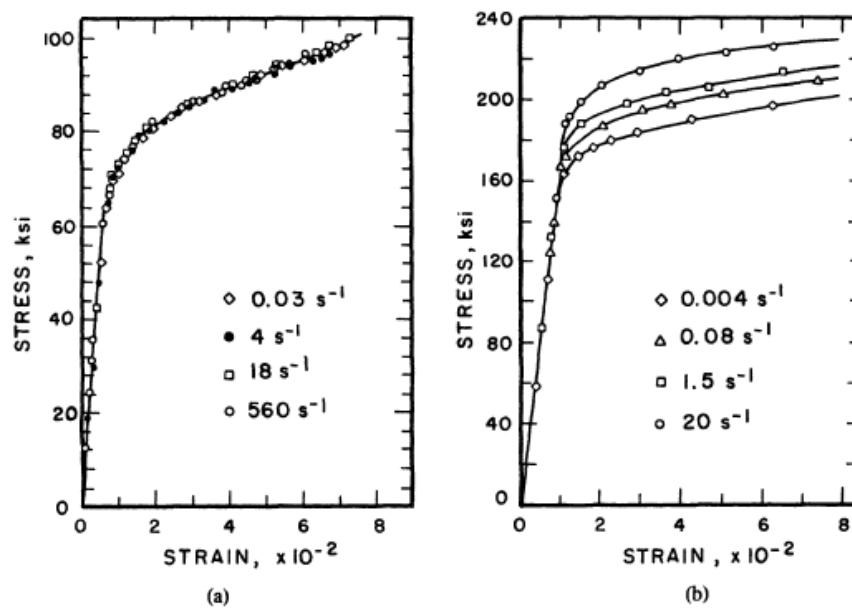


**Figure 4-33 strain rate effect during compression test on cylindrical specimens (a) 7075-T6 aluminium and (b) alloy titanium 6% Al-4% V (Maiden & Green, 1966)**

The varying strain rate experiment has been applied on some metals to determine their behaviour under varying strain rates. Result in Figure 4-33 shows that different material is affected differently when strain rates vary. 7075-T6 aluminium (FCC structure) shows no change in their stress-strain curve and therefore is not affected by strain rates, whereas the alloy titanium 6% Al-4% V showed increasing stress as the strain rate increases. The titanium (HCP) and tantalum (BCC) shows different response to strain rates as seen in Figure 4-34. Hence, this effect is described as *strain rate sensitivity* of material.

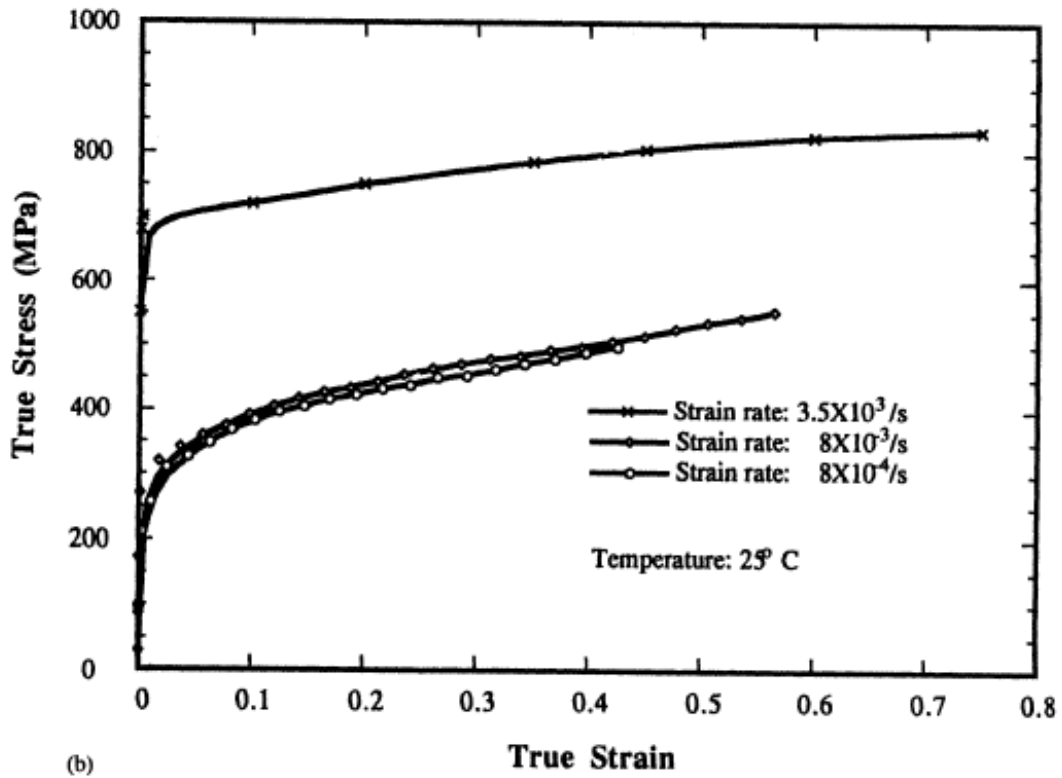
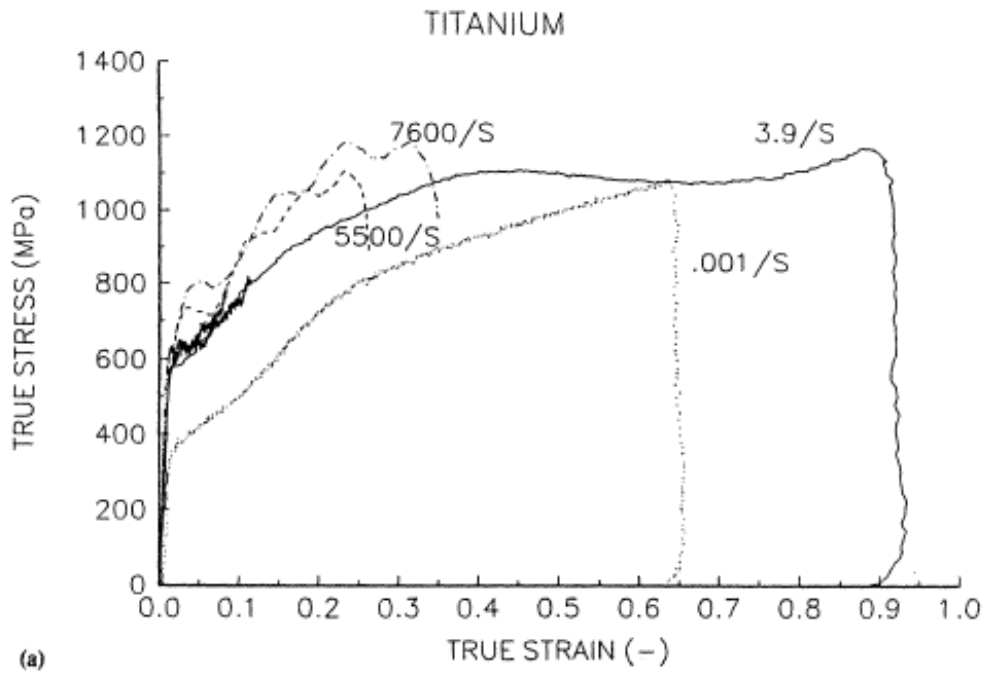


Figure 4-34 Strain rate effect during compression test on (a) pure titanium (b) tantalum (Meyers, 1994)

### 4.7.3 Temperature rise effect on material behaviour during plastic deformation.

As strain rate increase occurs during deformation process, it is observed that the process changes from fully isothermal to adiabatic process. This is because of lack of considerably time for heat generated during the deformation to leave the body at high strain rate which leads to rise in temperature of the specimen and adiabatic shear instabilities in some cases. The deformation work is therefore transformed into heat resulting to thermal softening which has profound effect on the behaviour of the material. Section 4.4.6 results clearly show the rise in this temperature and the thermal diffusivity effect described in Section 2.8.6 on X65 steel (equation (2-42)). An example of such temperature rise was seen in copper during dynamic deformation as show in Figure 4-35, and the same was applied to the API X65 steel.

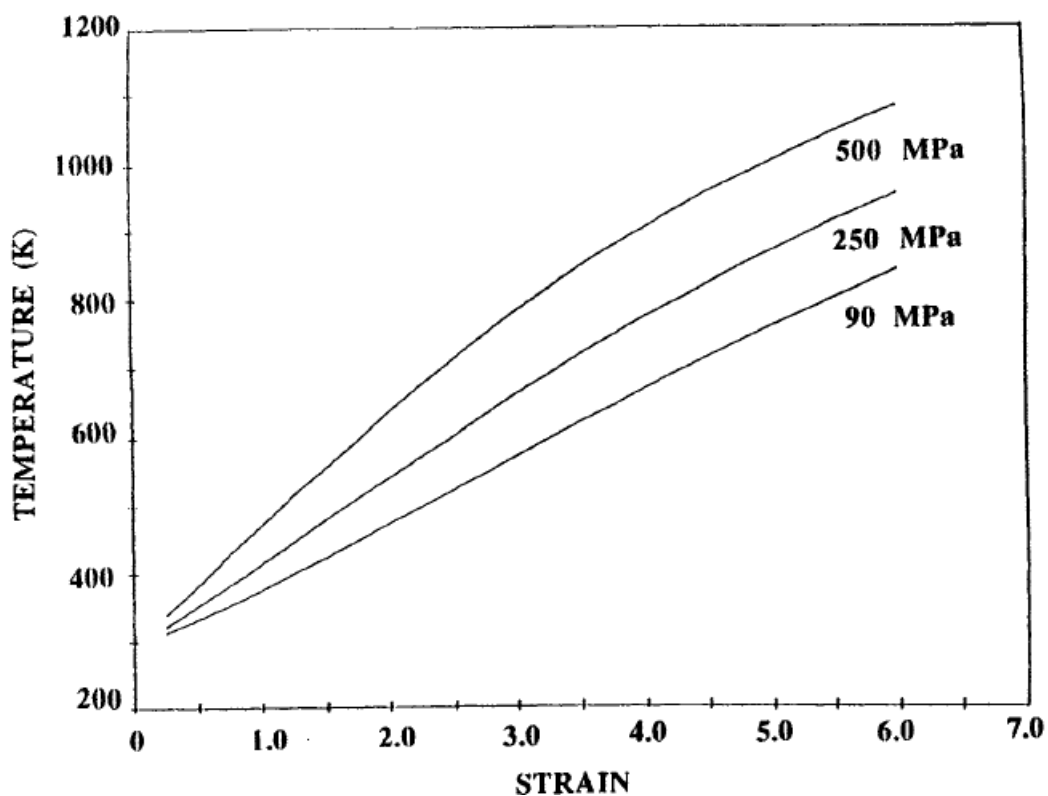


Figure 4-35 Copper tested at  $10^4 \text{ s}^{-1}$  strain rate at initial temperature 298 K, shows variation in the temperature during dynamic deformation (Andrade, Meyers, Vecchio, & Chokshi, 1994).

# **5 FRACTURE TOUGHNESS DETERMINATION AT DIFFERENT LOADING RATES ON X65 STEEL**

## **5.1 Introduction**

Metallic materials are affected by the type of loading which makes the material behave differently in varying conditions, such that a ductile metallic material under a high loading rate behaves as an unstable brittle fracture which is usually represented in a ductile-to-brittle transition curve. As such, the effect of this behaviour could lead to a catastrophic accident and hence requires that material behaviour under different loading rates should be well understood.

In this study, detailed experimental, analytical, and computational work has been conducted to analyse the effect of loading rates on the material properties of X65 steel. This chapter discussed in detail the results from the fracture toughness experiments to quantify the material property at different loading rates.

The results for this chapter were obtained from experiments under quasi-static, intermediate, and high loading rates. The Charpy-sized three-point bend specimen was utilised for the experiments with a square cross-sectional area ( $B = W = 10 \text{ mm}$ ). The crack length-to-width ratio of 0.2 and 0.5 were applied to characterize the behaviour of the material. The resistance curve result for fracture toughness testing results was also presented in this chapter for  $a_0/W$  ratio.

The finite element model was conducted in accordance with ABAQUS/Explicit to derive crack tip stresses and strains that occurs in nonlinear static analysis. So that the crack driving force and crack mouth opening displacement could be determined. This model is required to be able to validate the experimental procedures that have been adopted.

## **5.2 Quasi-static fracture toughness property of X65 steel**

### **5.2.1 Quasi-static fracture toughness testing results of X65 steel**

The quasi-static fracture test conducted at room temperature is discussed in this section. Single point tests were conducted using INSTRON 8801 B910 machine to obtain fracture toughness which was analysed according to BS ISO 12135:2016. The

displacement control, speed of 0.35 mm/min was the control rate of the crosshead with an initial corresponding K-rate value of about  $0.7 \text{ MPam}^{0.5}\text{s}^{-1}$ , and single-point fracture toughness was reported. The tests were repeated for 12 specimens, half of each having a crack length to width ratio ( $a_0/W$ ) of 0.2 and 0.5.

The fracture toughness results from the experiment obtained with a Charpy-sized notched SENB specimen ( $B = W = 10 \text{ mm}$ ) for 5 mm and 2 mm notched are presented in Figure 5-1 and Figure 5-2 respectively. The fracture toughness values were measured in single point crack tip opening displacement (CTOD) and the J integral (energy-based fracture toughness as seen in Table 5-1 and Table 5-2 for  $a_0/W$  of 0.5 and 0.2 respectively).

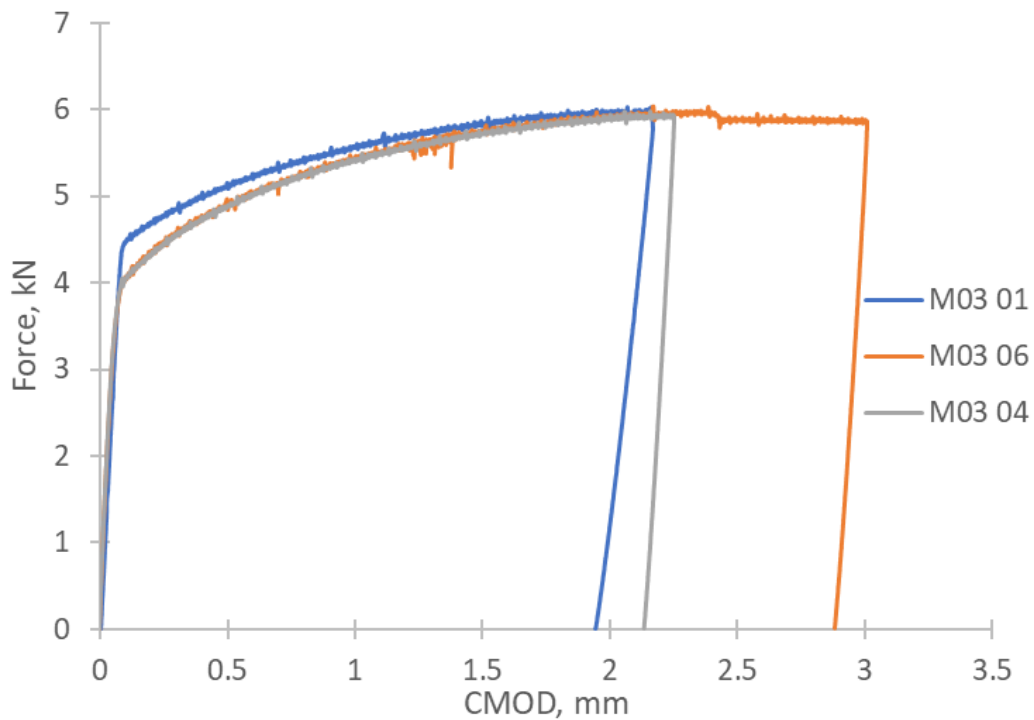


**Figure 5-1 Force-CMOD curve for X65 blunt notch  $a_0/W$  of 0.5**

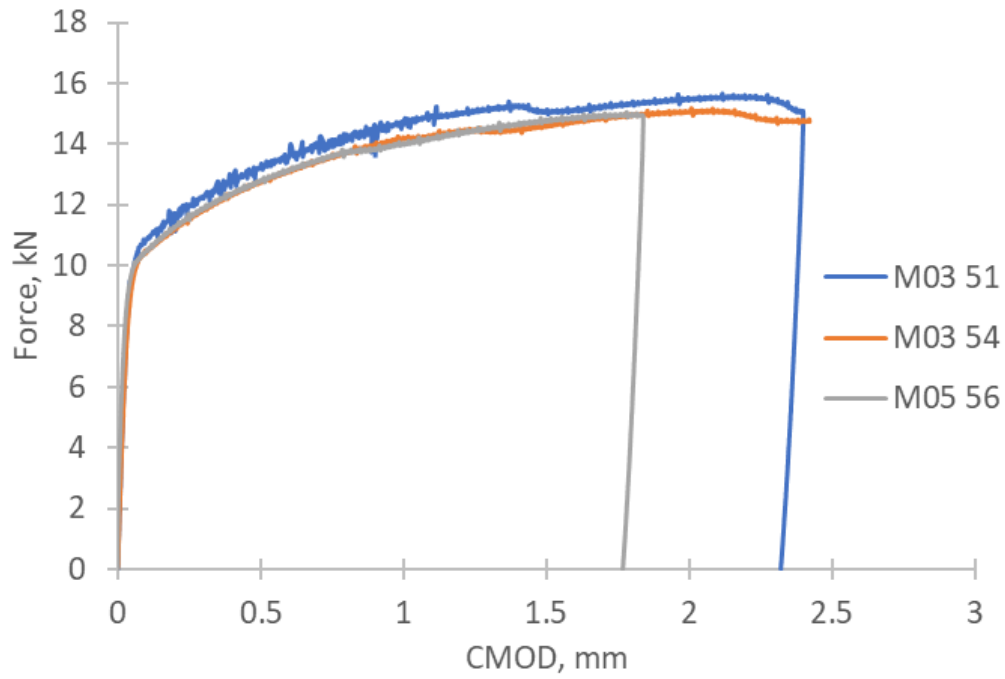


Figure 5-2 Force-CMOD curve for X65 blunt notch  $a_0/W$  of 0.2

Table 5-1 Fracture toughness results under quasi-static loading at room temperature summarised for the  $a_0/W \approx 0.5$ .

Specimen No	$\Delta a$ , mm	CTOD, mm	J, kJ/m <sup>2</sup>
M03-01	0.350	0.513	517.2
M03-02	0.106	0.178	178.8
M03-03	0.188	0.217	217.1
M03-04	0.455	0.569	576.2
M03-05	0.358	0.400	403.5
M03-06	0.631	0.666	678.8



**Table 5-2 Fracture toughness results under quasi-static loading at room temperature summarised for the  $a_0/W$  of 0.2**

Specimen	$\Delta a$ , mm	CTOD, mm	J, kJ/m <sup>2</sup>
M03-51	0.839	1.148	1046.7
M03-52	0.497	0.735	661.1
M03-53	0.226	0.382	339.6
M03-54	1.155	1.275	1182.7
M03-55	0.287	0.552	493.4
M03-56	0.546	0.874	789.5

From the results presented in Figure 5-3, it could be seen that the fracture toughness increases with the change in crack length,  $\Delta a$  under quasi-static conditions.

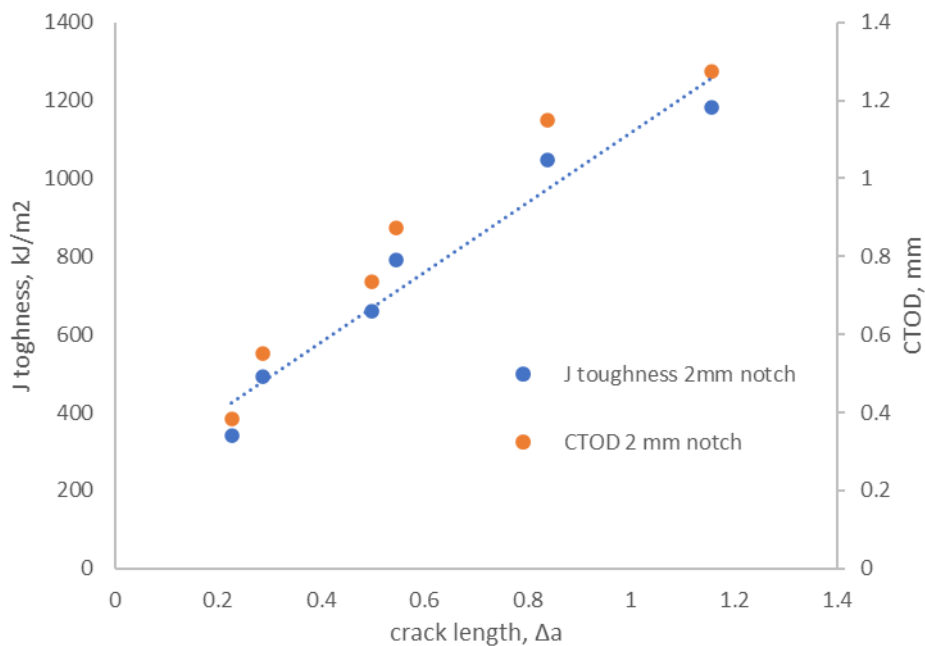


**Figure 5-3 Graphical representation of the fracture toughness values**

### 5.2.2 Resistance curve measurement of fracture toughness

R curve was obtained for the X65 steel since the material fails by ductile crack extension and is therefore expected to exhibit a rising R curve. To obtain the resistance

curve, ISO 12135 formulations were employed. Multiple specimens were utilised to determine the J-R curve.

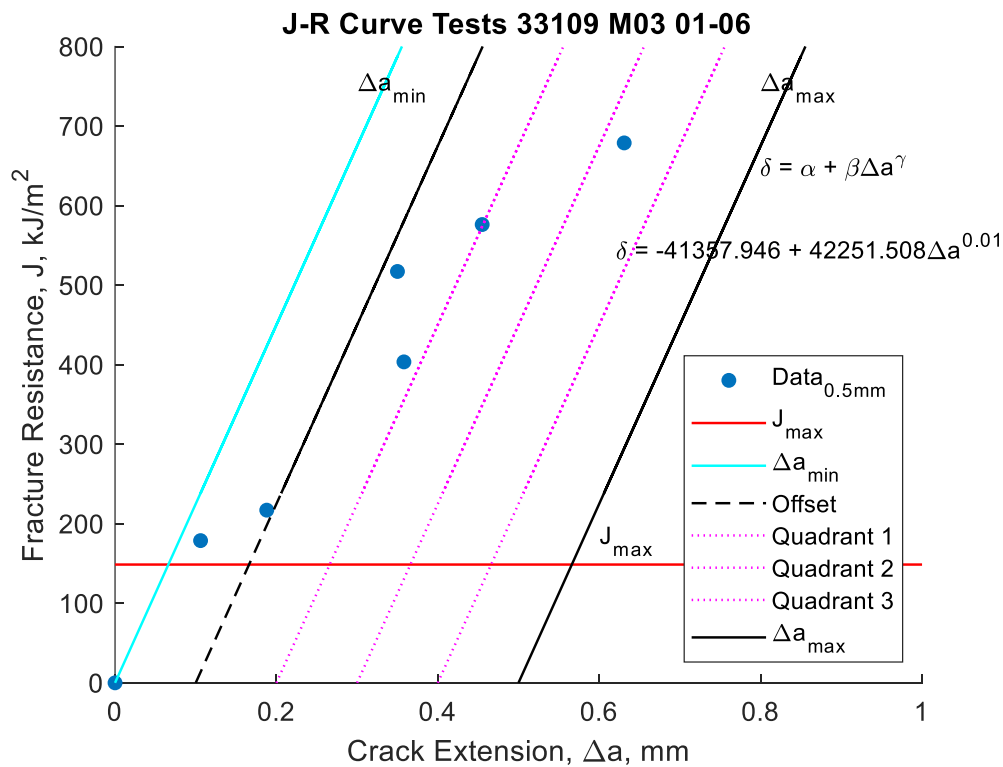


**Figure 5-4 Resistance curve for X65 steel at room temperature with SENB specimen (B=W=10mm) at  $a_0/W = 0.5$  mm**

The BS ISO 12135 was used to analyse and generate a resistant curve shown in Figure 5-4 and Figure 5-5 for crack length to width ratio,  $a_0/W$  of 0.5 and 0.2 respectively. The resistant curve does not show compliance with the ISO 12135 standard which states that at least one of the points need to fall within the four quadrants of the plot for the  $J_{0.2}$  to be measured. This is as a result of the material being very ductile and becomes difficult to reach maximum load during testing.

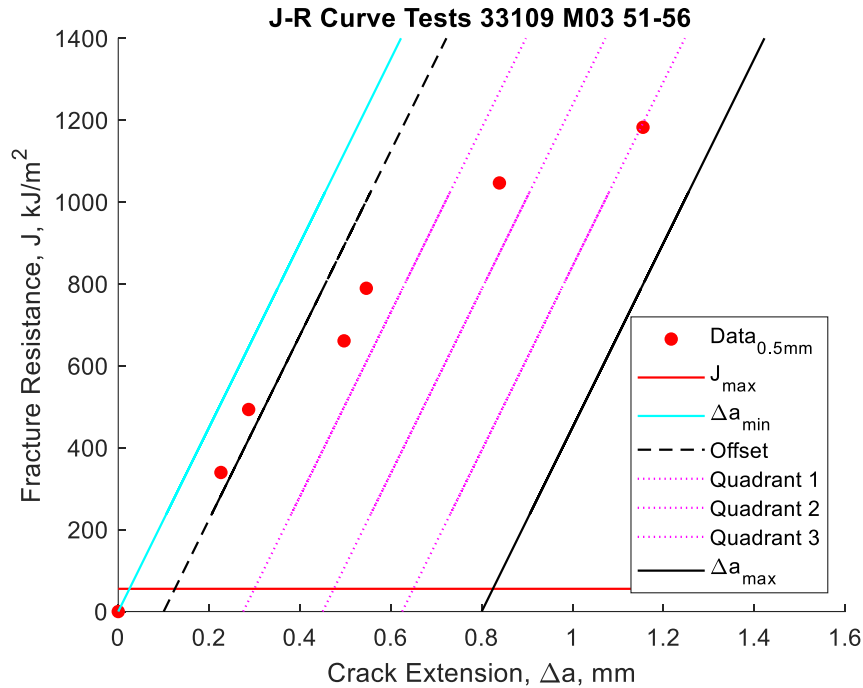


**Figure 5-5 Resistance curve for X65 steel at room temperature with SENB specimen (B=W=10mm) at a/W = 0.2 mm.**

### 5.3 Dynamic/High strain rate fracture toughness results for X65 steel

Dynamic loading leads to an increase in the yield and ultimate stresses which rises with the rate of loading in most metals. High stress level is experienced close to the crack tip which gives insufficient time for proper yielding to occur, resulting in energy being released within a short time which is followed by rapid crack propagation. Hence, dynamic loading can be said to promote brittle fracture as observed in the experiments.

The experiments conducted were a dynamic loading on a solid body which has an initial crack length (fatigue pre-cracked Charpy EDM-notched specimens)  $a_0$  and subjected to a time-dependent loading (displacement rate). In this study, the crack area was characterized by the crack length,  $a_0$  which propagates through a crack path ahead of the crack tip. Three different experiments were conducted to test the fracture toughness of X65 steel under high strain loading which includes Instrumented Charpy test, Low blow Instrumented Charpy test, and Fracture toughness test.

## 5.4 Instrumented Charpy test

The Instrumented Charpy test was performed to determine the impact energy at the crosshead of speed  $V_0 = 5400$  mm/s using the pre-cracked Charpy-sized SENB specimens. The results were presented in Table 5-3. The K-rate value in correspondent with the crosshead speed is about  $10^6$  MPa.m<sup>0.5s</sup><sup>-1</sup> on the tests performed as determined from the machine measurement. Double numerical integration method in accordance with ASTM E2298-18 was used to convert the force-time measurement to force-displacement curve with a rigid striker of 50.9 kg and initial crosshead speed and the velocity expressed as a function of time. Figure 5-6 shows the force-displacement curve derived for  $a_0/W$  of 0.2 and 0.5.

All fatigue pre-cracked specimens of  $a_0/W$  0.2 and 0.5 which were tested to determine the toughness of the X65 steel failed in a ductile fracture with some crack extension,  $\Delta a$  as seen in Table 5-3. The result in Figure 5-6 shows that smaller crack length to width ration,  $a_0/W$  of 0.2 requires higher fracture load than that of the  $a_0/W$  of 0.5 as expected.

**Table 5-3 Fracture test results of dynamic loading of  $V= 5400$  mm/s analysed with ISO 12135:2016 and CTOD of ASTM E1820-20b on SENB specimens.**

Specimen ID	$a_0$ , mm	$\Delta a$ , mm	TT, °C	J, J/m <sup>2</sup>	CTOD, mm	Load, kN
<b>M05-01</b>	5.3	4.7	23	596.4	0.6	6.5
<b>M05-02</b>	5.0	5.0	23	705.4	0.7	7.5
<b>M05-03</b>	5.6	4.4	23	696.1	0.7	5.7
<b>M05-51</b>	2.1	8.0	23	1515.8	1.7	18.8
<b>M05-52</b>	2.2	7.8	23	1490.5	1.7	18.6
<b>M05-53</b>	2.1	7.9	23	1563.0	1.8	18.4

$a_0$  = initial crack length, TT = test temperature,  $\Delta a$  = crack extension, CTOD = crack tip opening displacement.

The force-displacement curves experienced high oscillations and the results of Figure 5-6 were fitted through the oscillations discarding the initial peaks which is normally

one in cases where the specimen is in contact with the anvils, and these loading rates are on the upper shelf region (ductile fracture). The significant oscillations present during deformation were due to the imbalance between the external and internal forces at high rate of loading. The load measured experimentally were the maximum load obtained from the fitted curve through the oscillations in accordance with the ASTM E2298-18.

The Figure 5-7 shows that the fracture toughness of X65 steel is affected by the initial crack size. The lower crack lengths experiences increase in fracture toughness at the same loading rates of  $V = 5400 \text{ mm/s}$  since more energy is required for the specimen to fracture. Thus, the larger the crack size, the less the toughness of the material which leads to early failure of the material.

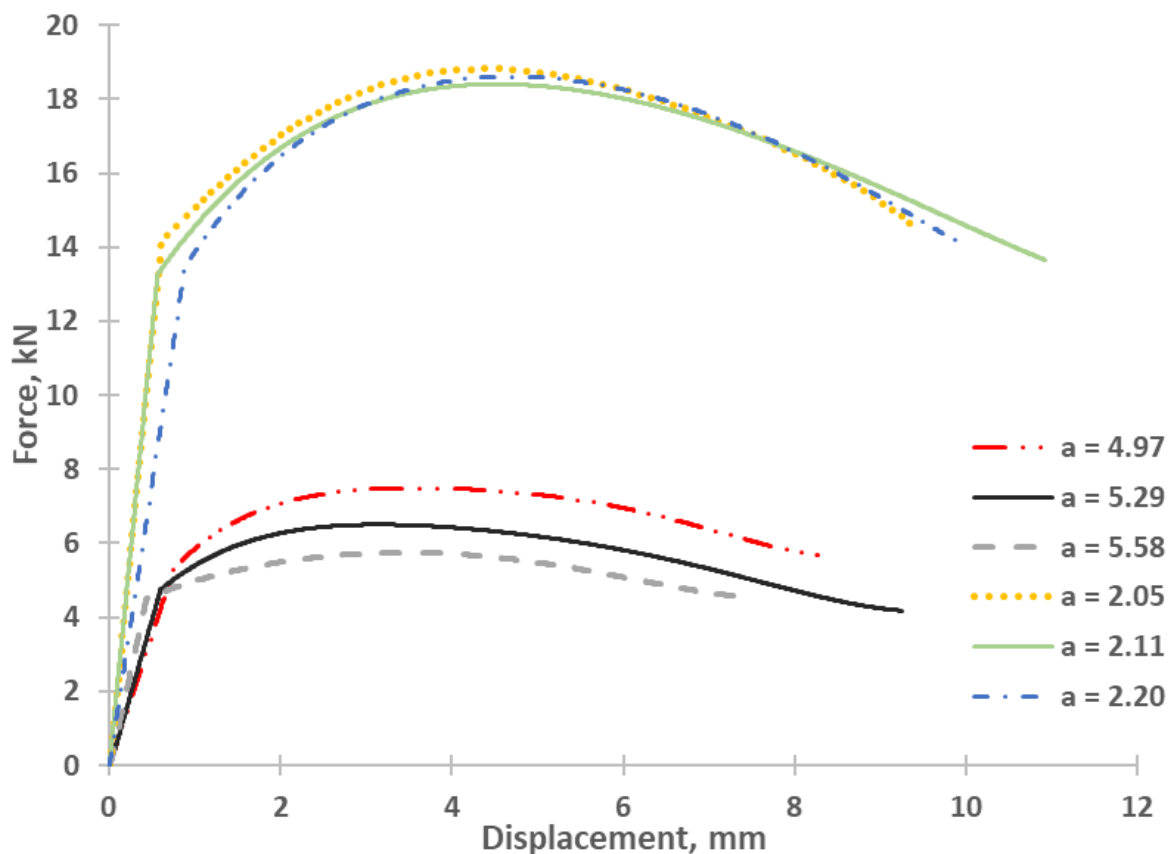


**Figure 5-6 Charpy test result of force-displacement curve at room temperature with varying crack lengths,  $a$  [mm].**

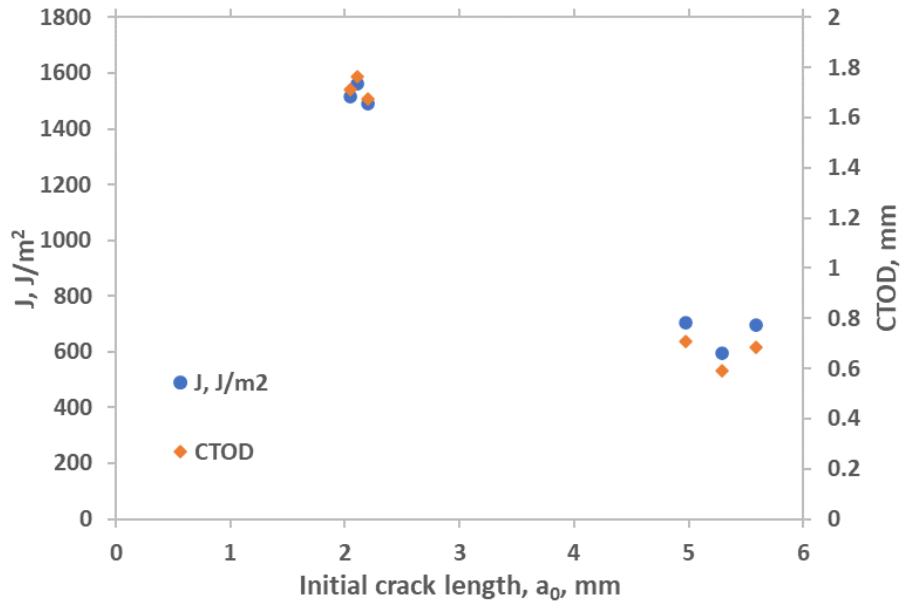


**Figure 5-7 Comparison of fracture toughness for pre-cracked specimen at different crack lengths ( $B = W \approx 10 \text{ mm}$ )**

### 5.5 Low blow Instrumented Charpy test

To check the effect of strain rates on the toughness of X65 steel. The low blow Instrumented Charpy test was performed as discussed in chapter 3, since the high strain rate fracture toughness test did not yield the necessary results needed for analysis. The angle of strike was varied to produce stable crack extension sufficiently to determine the toughness of the material.

Figure 5-8 and Figure 5-9 show the fracture toughness measured with Instrumented Charpy test at a full blow test when the striker angle was not reduced and that when the angle was reduced to decrease the strain rates. It could be seen that a decrease in toughness occurs as the loading rate increase from low blow test to full blow test. The low blow test results showed better fracture toughness results (J and CTOD) than the full blow test, thus, high strain rate testing yields lower fracture toughness results. The difference in full and low blow test were specified in Table 3-2 which is in the height of the pendulum (angle of release).

**Table 5-4 Low blow Charpy test of dynamic loading of V= 5400 mm/s analysed with ISO 12135:2016 and CTOD of ASTM E1820-20b on SENB specimens for  $a_0/W = 0.5$**

<b>Specimen ID</b>	<b><math>a_0</math>, mm</b>	<b><math>\Delta a</math>, mm</b>	<b>Release angle, °</b>	<b>TT, °C</b>	<b>J, J/m<sup>2</sup></b>	<b>CTOD, mm</b>	<b>Load, kN</b>
<b>M05-40</b>	5.3	4.0	125.7	21.0	766.5	0.8	6.6
<b>M05-41</b>	5.3	4.0	125.7	22.0	596.1	0.6	6.6
<b>M05-42</b>	5.1	4.3	125.7	22.0	809.5	0.8	7.4
<b>M05-43</b>	5.3	4.1	90.0	21.0	798.5	0.8	6.8
<b>M05-44</b>	5.3	4.1	90.0	21.0	768.3	0.8	6.8
<b>M05-45</b>	5.3	4.0	90.0	21.0	730.4	0.7	6.8

**Table 5-5 Low blow Charpy test of dynamic loading of V= 5400 mm/s analysed with ISO 12135:2016 and CTOD of ASTM E1820-20b on SENB specimens for  $a_0/W = 0.2$**

<b>Specimen ID</b>	<b><math>a_0</math>, mm</b>	<b><math>\Delta a</math>, mm</b>	<b>Release angle, °</b>	<b>TT, °C</b>	<b>J, J/m<sup>2</sup></b>	<b>CTOD, mm</b>	<b>Load, kN</b>
<b>M05-90</b>	2.6	6.2	125.7	22.0	1563.7	1.7	16.9
<b>M05-91</b>	2.4	6.1	125.7	21.0	1592.3	1.8	17.9
<b>M05-92</b>	2.3	6.3	125.7	21.0	1670.2	1.9	18.4
<b>M05-93</b>	2.2	6.3	90.0	21.0	1650.7	1.9	18.2
<b>M05-94</b>	2.3	6.3	90.0	21.0	1681.9	1.9	18.1
<b>M05-95</b>	2.5	6.5	90.0	21.0	1604.4	1.8	17.3

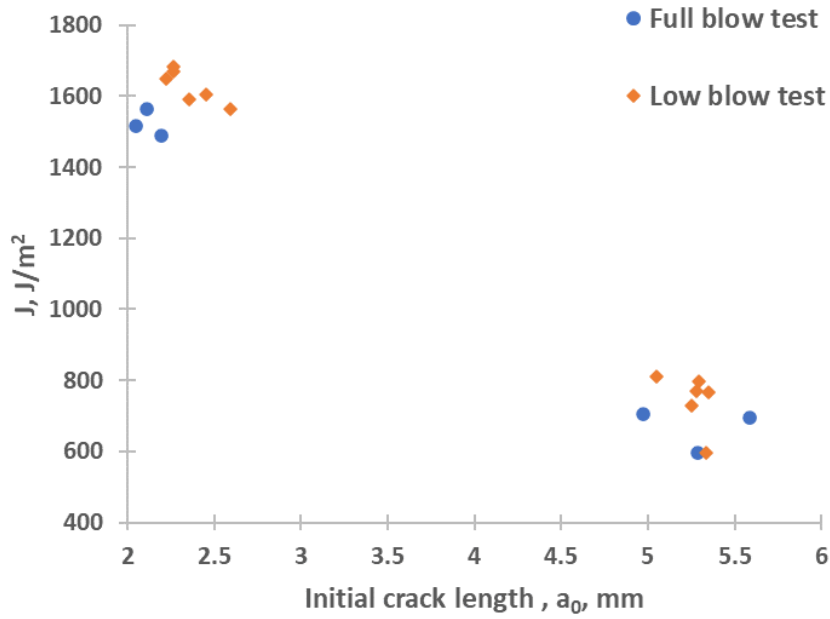


**Figure 5-8 Comparison of J toughness measurement for full and low blow Charpy tests.**

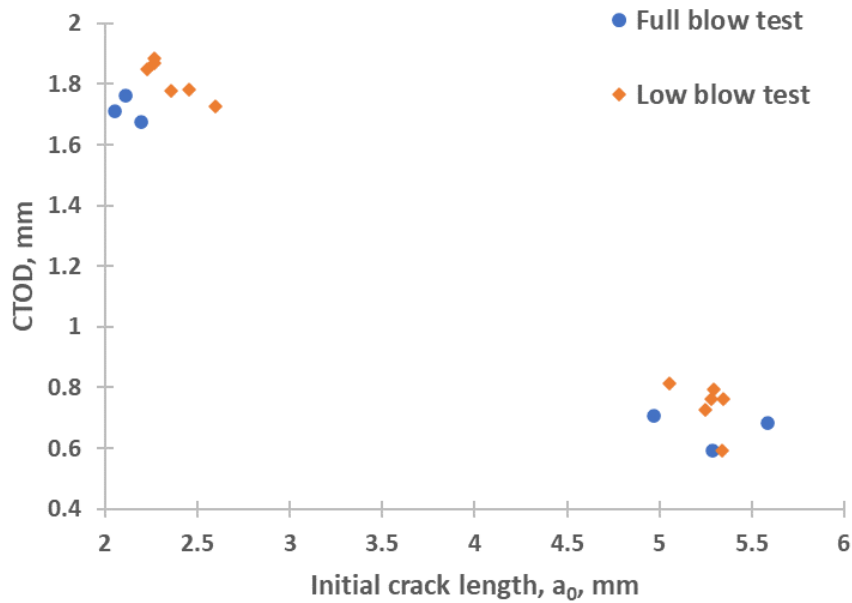


**Figure 5-9 Comparison of CTOD toughness measurement for full and low blow Charpy tests.**

The fracture toughness parameters obtained for CTOD and J for the full blow Charpy test and low blow Charpy test were presented for the case of a/W 0.2 and 0.5. The result shows that the low blow test detailed in Table 3-8 showed a better fracture toughness result for both a/W specimens than the full blow test carried out at 5400



mm/s displacement rate. It indicates that the higher strain rate testing results to lower fracture toughness as expected.

## **5.6 FEA modelling of fracture toughness on SENB sample**

The finite element analysis results for the SENB model for fracture toughness are presented in this section. The model was to predict crack tip strains and stresses in Abaqus/Explicit to determine the effect of rate of loading on the material toughness.

In this dynamic analysis, element deletion method has been applied to predict the crack driving force when the material has absorbed the highest energy required to fracture. As the FE model was to represent the test specimen, the JC parameter determined in Section 4.4 was employed for the ductile damage properties of which the tensile tests FE results have validated the JC properties of the material model.

### **5.6.1 FEA model preparation and the geometry**

The Charpy sized SENB specimen was modelled in commercial finite element modelling software, ABAQUS/CAE 2021.HF9. The full SENB geometry which is Charpy -sized pre-cracked was modelled to represent the real scenario with the impactor falling from a height at a constant velocity. The impactor was modelled as a rigid body since no deformation need to be recorded to save modelling time and efficiency. The two rollers were also modelled as a rigid body and fixed in all directions.

The modelled specimen geometry is shown in Figure 5-10 with enlarged area showing the application of the pre-crack. It is worth noting that the crack length to width ratio  $a_0/W$  was taken as 0.5 for all models. The model was partitioned to allow for different mesh density in order to capture the crack tip region as shown in Figure 5-11. The middle part of the sample was meshed with the smallest element size since the stress concentration from the impactor is highest in the center. The need for finer mesh at the crack tip was to increase the model accuracy and promote high calculation definition. Mesh of C3D8R: An 8-node linear brick, reduced integration, hourglass control was applied for faster simulation. Mesh sensitivity was done to determine the convergence and utilised the suitable element size for the simulation and the plot is shown in Figure 5-12. The fatigue pre-cracked was modelled by creating a special crack and defining the direction of crack in Abaqus/Explicit. The general contact (Explicit) for the hammer is All\* with self, Surface -to-surface contact was applied for

the specimen and the rollers, The interaction contact was applied to all contacts and the friction formulation selected as Penalty while the friction coefficient of 0.25 was applied.

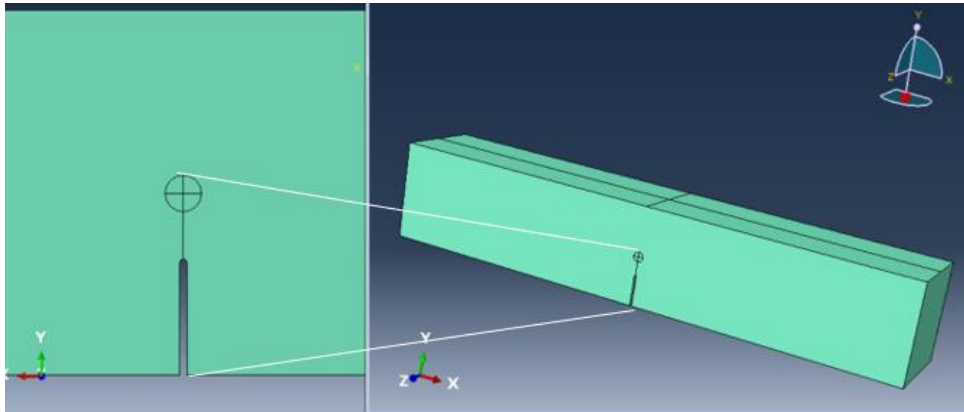


**Figure 5-10 SENB geometry showing the pre-cracked region.**

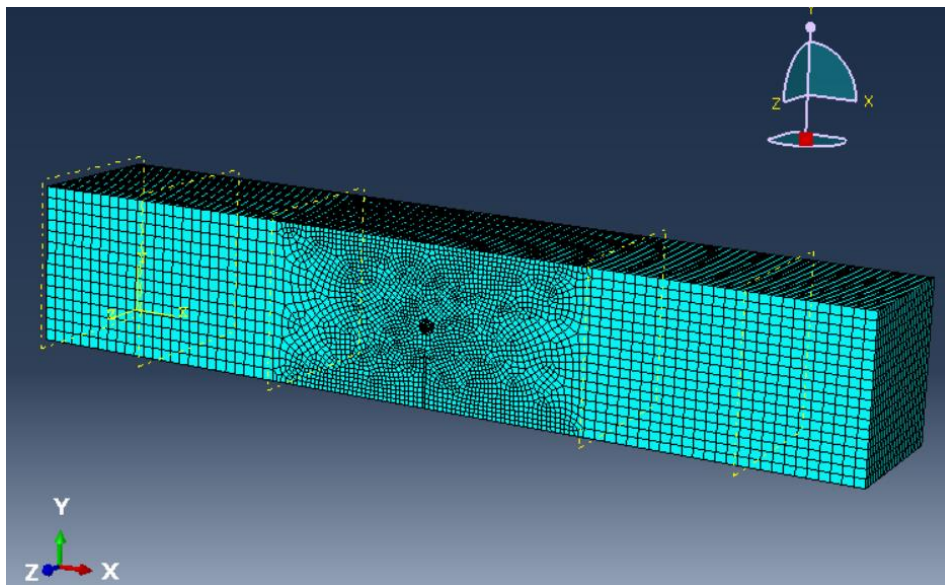


**Figure 5-11 Varying mesh density on different partition.**

**Table 5-6 FEA elements and node distribution in mesh sensitivity analysis for three-point bend sample.**

<b>No. of nodes</b>	<b>No. of elements</b>	<b>Linear hexahedral element type</b>	<b>Maximum stress (MPa)</b>
<b>83117</b>	<b>76392</b>	<b>C3D8R</b>	<b>877.92</b>
<b>103260</b>	<b>95352</b>	<b>C3D8R</b>	<b>795.45</b>
<b>112560</b>	<b>104160</b>	<b>C3D8R</b>	<b>795.14</b>
<b>132939</b>	<b>123150</b>	<b>C3D8R</b>	<b>797.68</b>

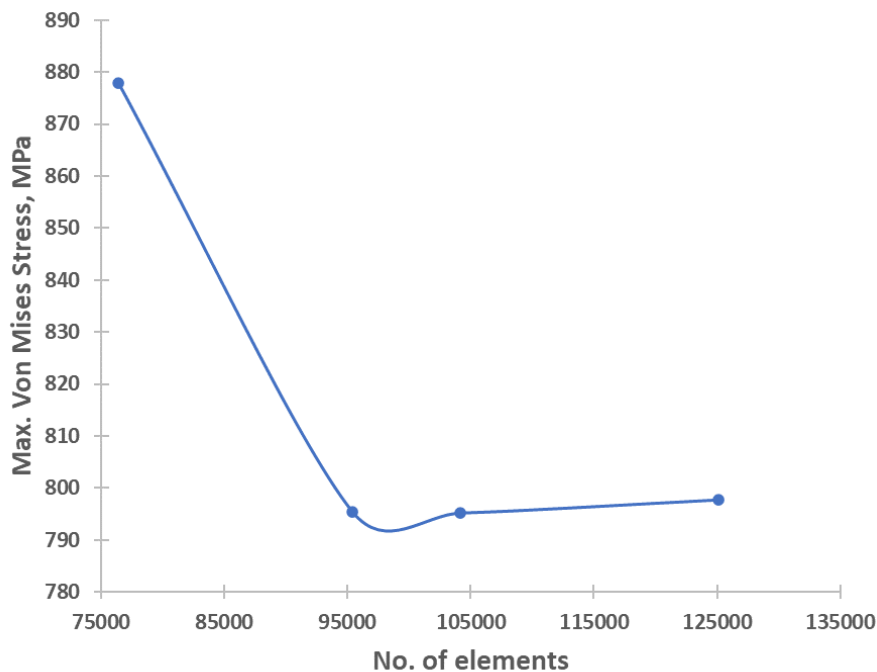


**Figure 5-12 Mesh Sensitivity analysis for the three-point bend specimen**

### **5.7 FEM results on high strain rate model**

The simulated model is shown in Figure 5-13 comprising of SENB specimen, two fixed rollers and an impactor. Boundary conditions were created on the rollers as Symmetry/Antisymmetry/ENCASTRE ( $U1=U2=U3=UR1=UR2=UR3=0$ ) and the initial

velocities set in predefined field manager were imposed on the impactor falling in the negative Y-direction (2 mm).

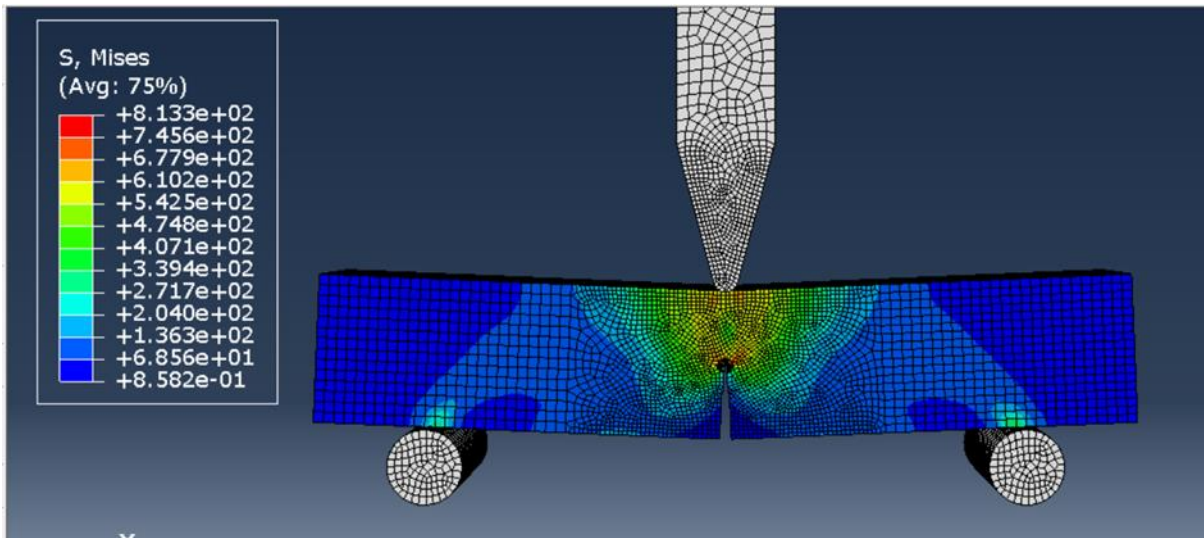


**Figure 5-13 FEA model for 1 m/s displacement rate at 0.002 seconds**

The results in Figure 5-14 and Figure 5-15 show the presence of strong oscillations on the force-displacement curve. As the displacement rate increases, lesser time steps are captured during the testing and the lagging time to capture a value result to oscillations in which the frequency is reduced at higher strain rates with higher amplitudes as seen in Figure 5-16 and Figure 5-17. Hence, for the oscillations in the force-displacement curve during high strain rate testing to be eliminated, a measuring system capable of lower step time is required to overcome this oscillation.

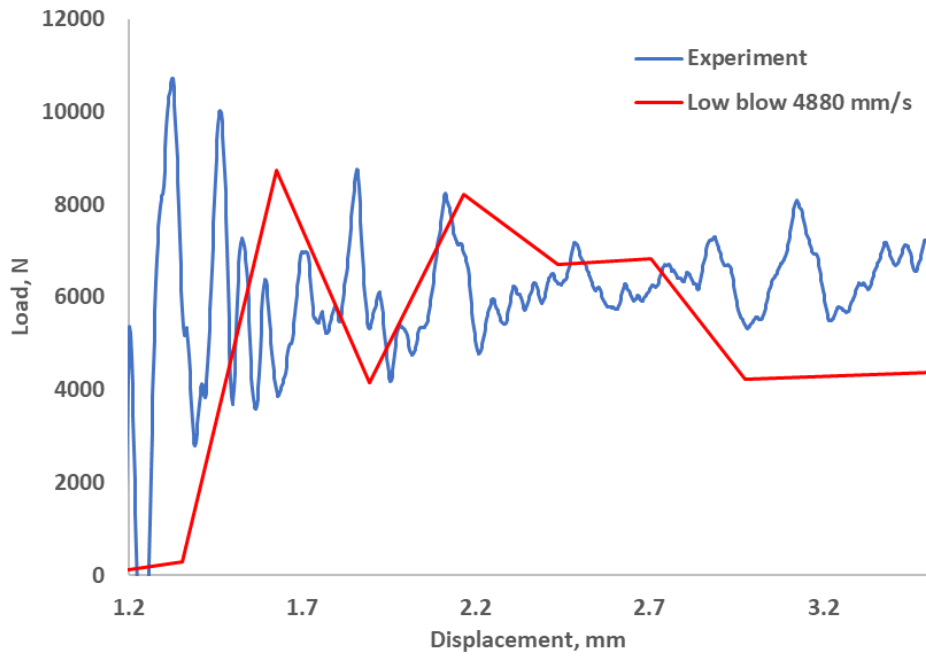


**Figure 5-14 Load versus displacement of X65 steel at 4880 mm/s displacement rate**

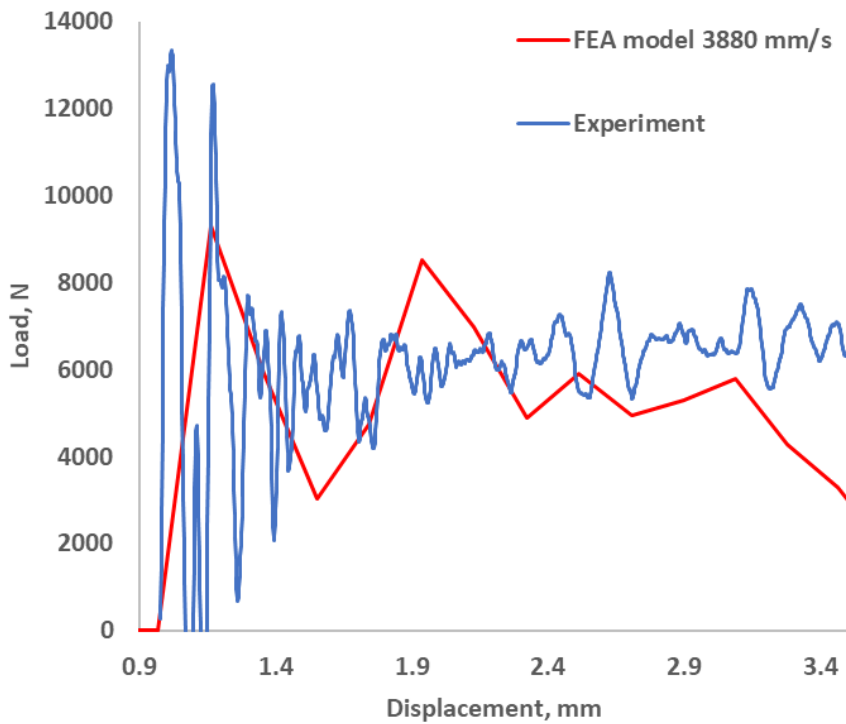


**Figure 5-15 Load versus displacement of X65 steel at 3880 mm/s displacement rate.**

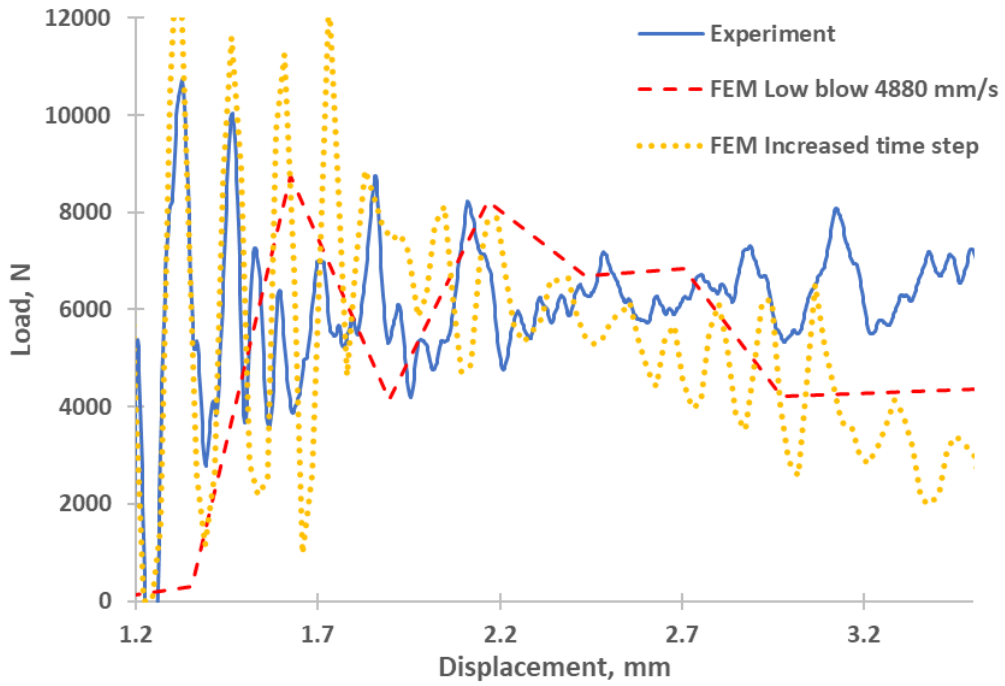


**Figure 5-16 Comparison of time steps with the experiment at 4880 mm/s**

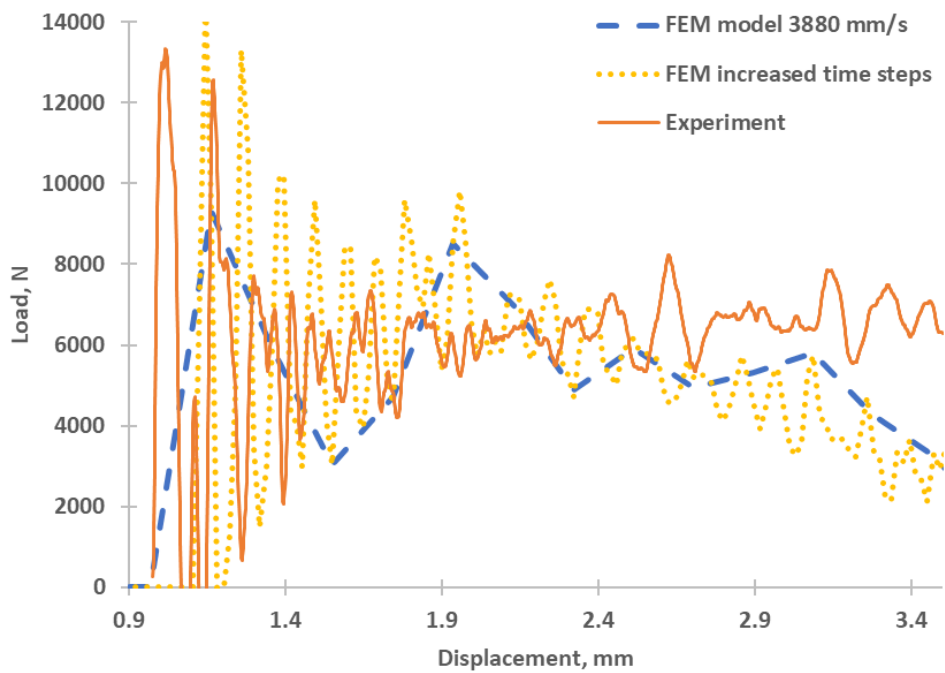


**Figure 5-17 Comparison of time steps with the experiment at 3880 mm/s**

It is therefore difficult to eliminate the oscillations without a steady measuring instrument for the dynamic testing. The energy absorbed by the specimen becomes a better option for measuring the fracture toughness at dynamic testing since an exact

maximum force is difficult to obtain. The results presented showed in Figure 5-16 and Figure 5-17 that time step is a significant factor to consider in modelling dynamic response which validates the analytical model with time to fracture for dynamic analysis in equation (2-18).

### 5.7.1 FEA model prediction at high loading rates

Figure 5-18 shows the absorbed energy from FEA simulations of specimen under varying displacement. The absorbed energy increased with displacement rate as presented with kinetic energy in equation (2-1). The higher the absorbed energy, the lower the fracture toughness of the material. Hence, fracture toughness is reduced with the increase in strain rate with the possibility of the material to fail in a brittle manner. The kinetic energy however decreases with the strain rate.

With the results in Figure 5-16 and Figure 5-17 showing good correlation with the experimental results. A higher displacement rate could not be determined experimentally due to operating limit of test machine. Therefore, the FEA model was applied to determine the effect of higher strain rates on the material properties at the same time (0.002 s) and the same geometry, extrapolating from the results determined at lower strain rates.

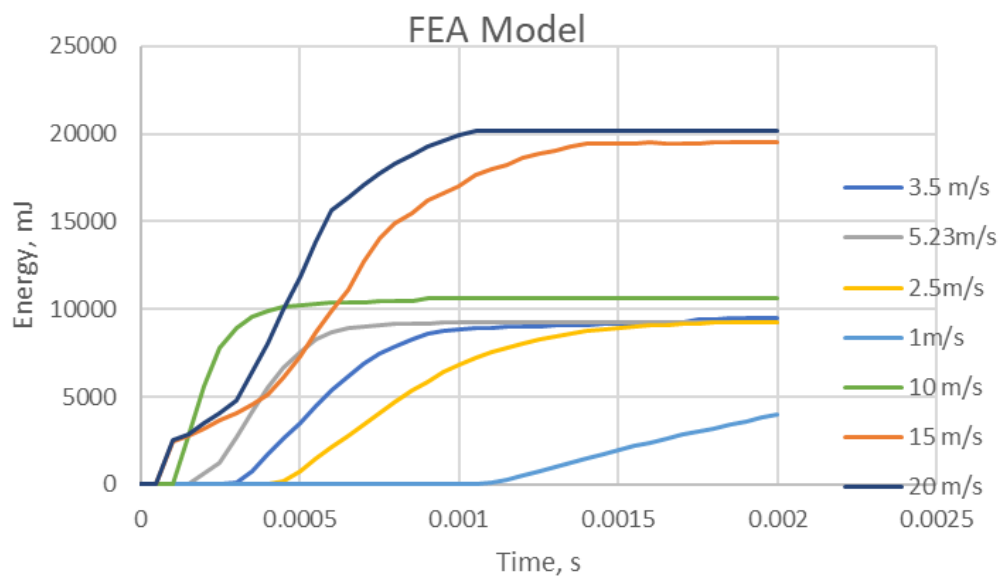
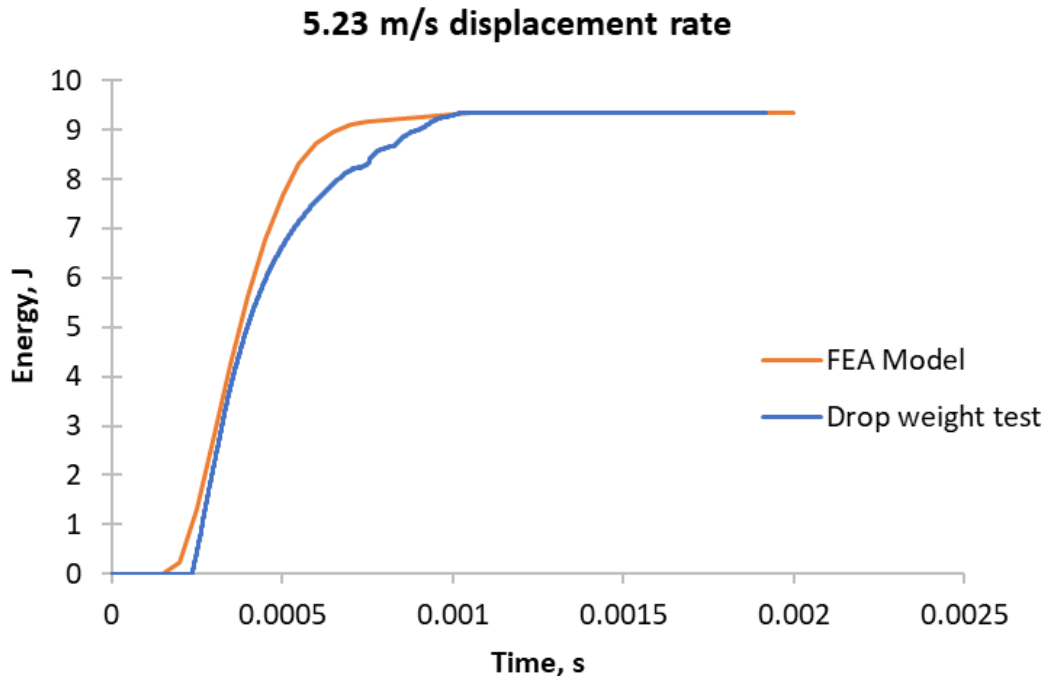


Figure 5-18 Energy increase with the displacement rate from the FEA model.

Figure 5-20 shows that bending of the specimen occurs at displacement rates of less than 5.4 m/s and up to 10 m/s. Beyond 10 m/s, there is no evidence of bending occurring as shown in Figure 5-21, Figure 5-22 and Figure 5-23 as predicted by the model. These were determined by applying higher displacement rate on the same model. Figure 5-21 was for displacement rate of 15 m/s at full time step of 0.002 seconds, and the hammer went through the specimen. Figure 5-22 showed the hammer also passed through the specimen at time step of 0.0095 seconds of the displacement rate, 20 m/s, whereas Figure 5-23 showed the distance the hammer has travelled through the specimen at the full-time step of 0.002 seconds.

This implies that at higher strain rates of loading, the impactor moves with higher speed through the material without showing any prior bending making the material fracture in a brittle manner without warning. Hence, a critical strain rate is attained beyond which a ductile material fractures in a brittle manner. To validate the data obtained from FEA model, drop weight test result at 5400 mm/s was compared and it shows a good correlation in Figure 5-19 with minor errors that might result from the measuring instrument.



**Figure 5-19 Comparison of energy obtained from drop weight test with FEA model at 5.23 m/s.**



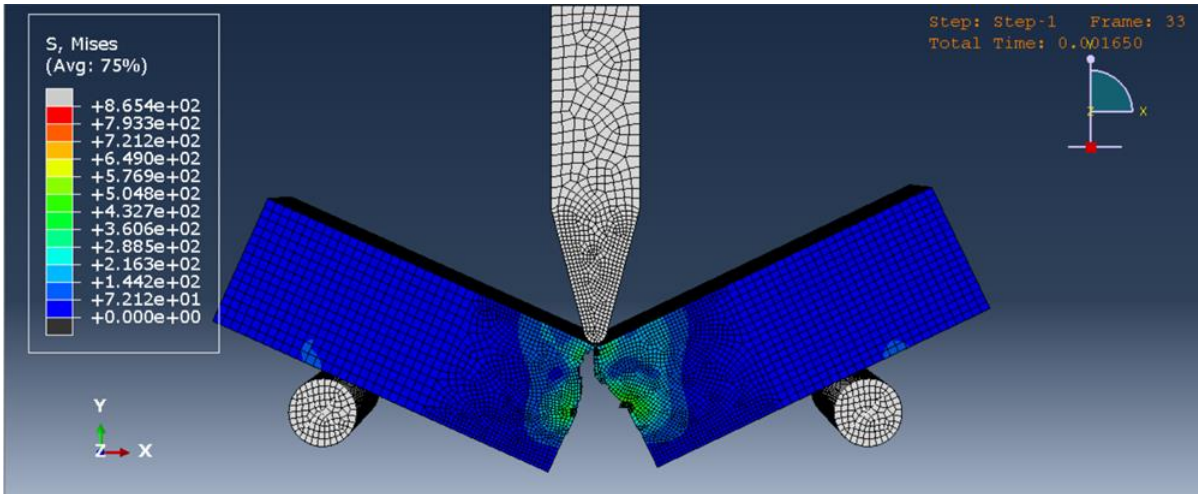


Figure 5-20 FEA model for 5.3 m/s displacement rate at 0.002 seconds

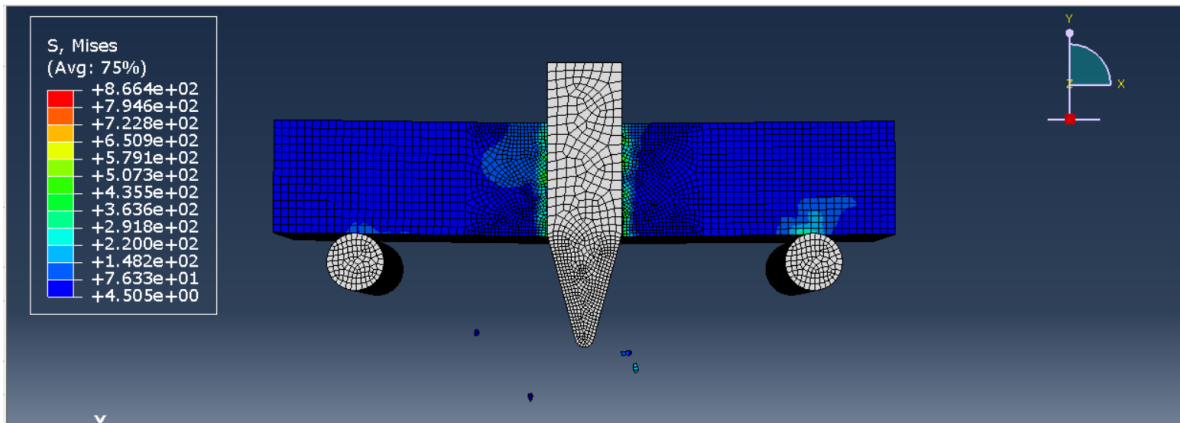


Figure 5-21 FEA result on the 15 m/s displacement rate at 0.002 seconds

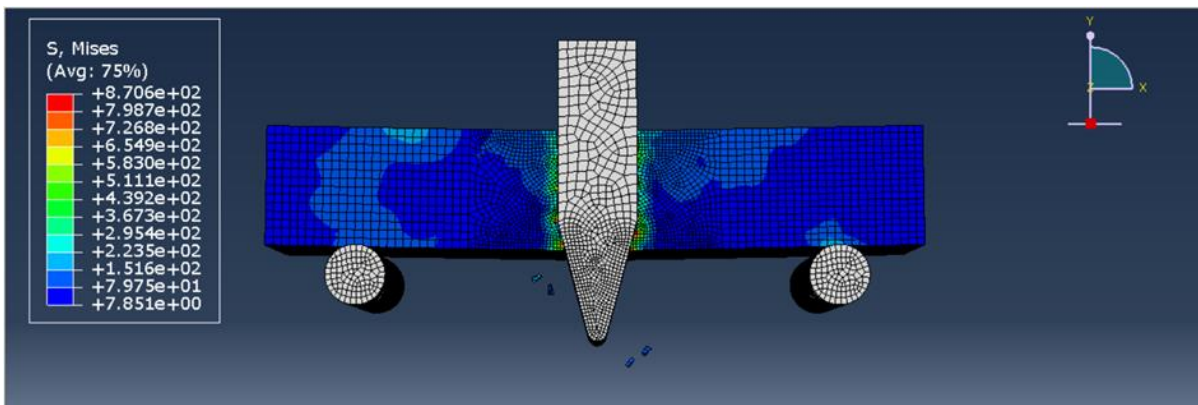
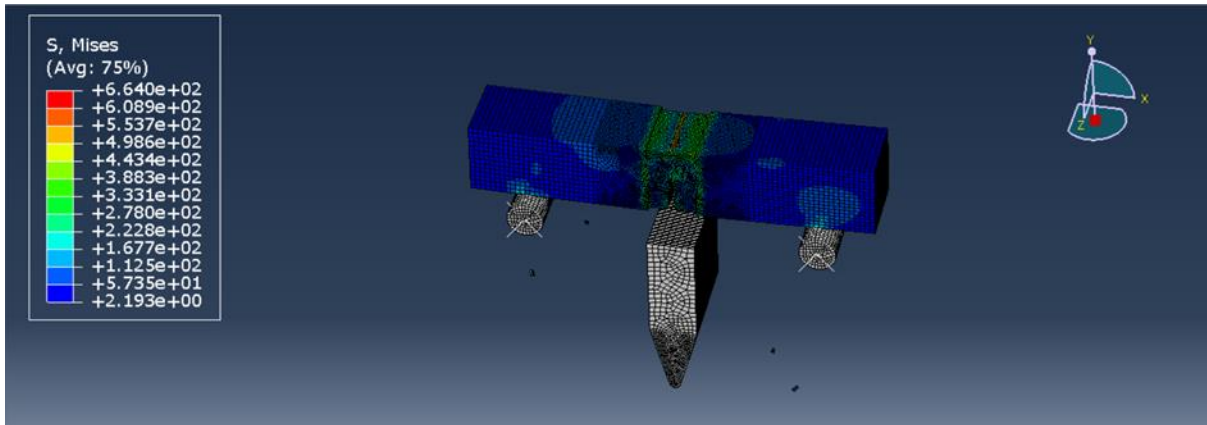


Figure 5-22 FEA model on 20 m/s at 0.00095 seconds, the striker passing through the sample without bending.



**Figure 5-23 The striker cut through the sample with no significant bending at 20 m/s within 0.002 seconds.**

## 5.8 Discussion on Fracture Toughness

Different experiments were carried out and analysed to develop methods of evaluating metallic material at high strain rate and hence determine dynamic fracture toughness. Data was obtained from experiments, and analytical calculations were utilised. Different experiment procedure was applied on varying sample geometry to determine the material properties at dynamic loading rates. Tensile tests were performed using round (notched, and un-notched) and flat samples, as well as instrumented Charpy and fracture toughness test on SENB specimens. Useful data were selected in the form of force-displacement, stress-strain, and time dependent data.

A computational approach using finite element model in ABAQUS were generated to represent each experiment to extract useful information such as time, force, displacement, stress, and strain from different perspective in comparison with the experimental results. Additionally, machine learning algorithms were employed to predict stress-strain curves, as well as fracture toughness property with some given features.

### 5.8.1 Loading Rate Effects on Fracture Toughness of Steel

The structural behaviour is being determined by the influence of both material resistance and the structural response of engineering components which are affected by the dynamic loading rates. The increasing loading rate effect is generally reflected in the increase of strength and with local temperature (established from thermal diffusivity model) increases the strain rate sensitivity. This does not always hold as

there are cases where the dynamic strain aging effects intervenes. Hence, the effect of loading rates on ferritic steels is dependent on the overall behaviour of the material, for example, at temperatures below brittle-to-ductile transition will result to reduced toughness as loading rate increases. Whereas the upper shelf temperatures will result in dynamic initiation toughness increase with strain rate.

Also, around the transition region as discussed in Section 2.6.1 on brittle-to ductile transition curve (Figure 5-24), increasing loading rates can lead to the material behaviour shifting from fully ductile at quasi-static loading to brittle behaviour at elevated loading rates. A typical loading rate effect on the fracture behaviour of a HY80 steel is shown in Figure 5-25, where the J integral (material resistance) is increased with the strain rates at a given crack extension.

The effect of loading rate in steel is seen in its material properties where the yield and tensile strength increases with the loading rate leading to a reduction of cleavage fracture toughness. This is seen in the Charpy testing which involves impacting a SENB specimen with a pendulum with an initial displacement rate of  $5400 \text{ mm s}^{-1}$ . To determine the effect of loading rate on the impact toughness determination, a low blow Charpy test was conducted and the result in Figure 5-8 and Figure 5-9 shows the reduction of fracture toughness at higher displacement rates.

Due to complexity in testing the dynamic fracture toughness of the material, the low blow Charpy tests were adopted to replicate the test at lower strain rates through the deviation of the angle of release. An EDM notched fatigue pre-cracked specimen was applied for the Charpy test rather than the normal Charpy blunt V-notched to replicate the sharp fatigue cracks for more accurate fracture mechanics-based testing, since the striker was instrumented.

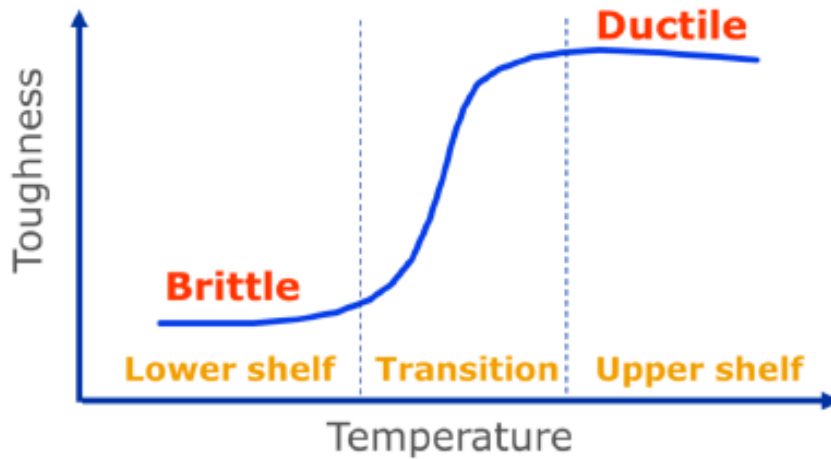


Figure 5-24 Ductile to brittle transition curve for ferritic steels (© TWI).

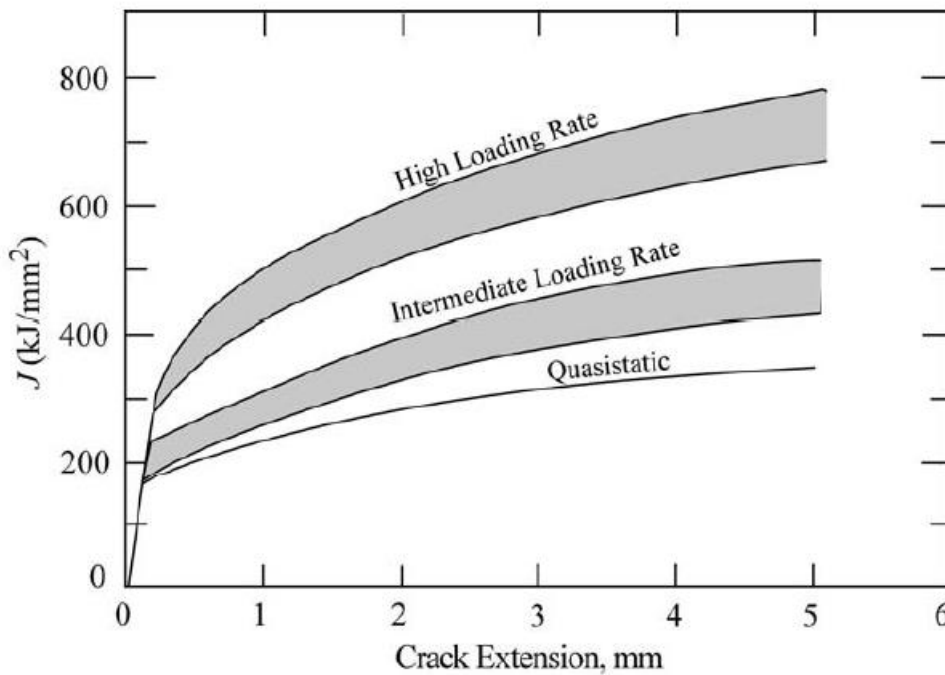


Figure 5-25 Loading rate effect on HY80 steel (Anderson, T. L., 2017)

### 5.8.2 Effect of loading rate on testing procedure

Loading rates are limited by the machine capability, sensor, and available recording devices. These factors affect the comfortable zone in which sufficient data is extracted for analysis. For every testing standard, the effect of strain rate is considered and

hence the need for maximum loading rate beyond which the testing procedure is no longer valid. It is important that loading rate at which a structure will be subjected to is determined and testing in such loading rate using the correct testing procedure. Since it has been observed that cleavage fracture toughness decreases with the loading rates due to the increase in the yield strength that increases the crack tip stresses to reach a critical condition at a lower load level compared to the quasi-static conditions.

The British standard BS 6729:1987 was the first testing procedure for dynamic loading rates of fracture testing in which the approach is based on static procedure with some allowances to represent the dynamic condition. This however was replaced with the BS 7448:3 to be applied for  $K_{Ic}$  and K-rate extending from quasi-static to K-rate of  $3000 \text{ MPa m}^{0.5} \text{ s}^{-1}$ . Beyond this K-rate, an appendix in BS 6729 could be applied to guide on the testing method. However, the issue with these testing procedures is such that the conventional instrumentation is not sufficient to record the actual condition the specimen experiences. The load time plot in Figure 5-26 shows a typical problem encountered in testing dynamic loading rate with conventional load cell attached to the specimen directly, of which the static condition gives an identical reading (Figure 5-26 (a)), but the dynamic condition is dominated by inertial effects (Figure 5-26 (b)).

The VHS INSTRON machine at TWI designed to test up to  $20 \text{ m s}^{-1}$  displacement rate employs a Charpy-sized specimen for fracture toughness test and a high-speed camera on both left and right to capture the deformation stages which is analysed in GOM software, and it is an advanced machine in testing dynamic fracture toughness test. The FEA results showed that there is a threshold rate of  $10 \text{ m/s}$  beyond which no significant bending in the specimen. The VHS machine with  $20 \text{ m/s}$  limit requires high speed camera, tedious preparation, and does not always guarantee sufficient data points. Current testing procedures assume there are sufficient data points but provide no guidance to extrapolate results to predict material response above strain rate employed during testing. Hence, instrumented Charpy testing was employed as it is recommended in ASTM E1820 and E1921.

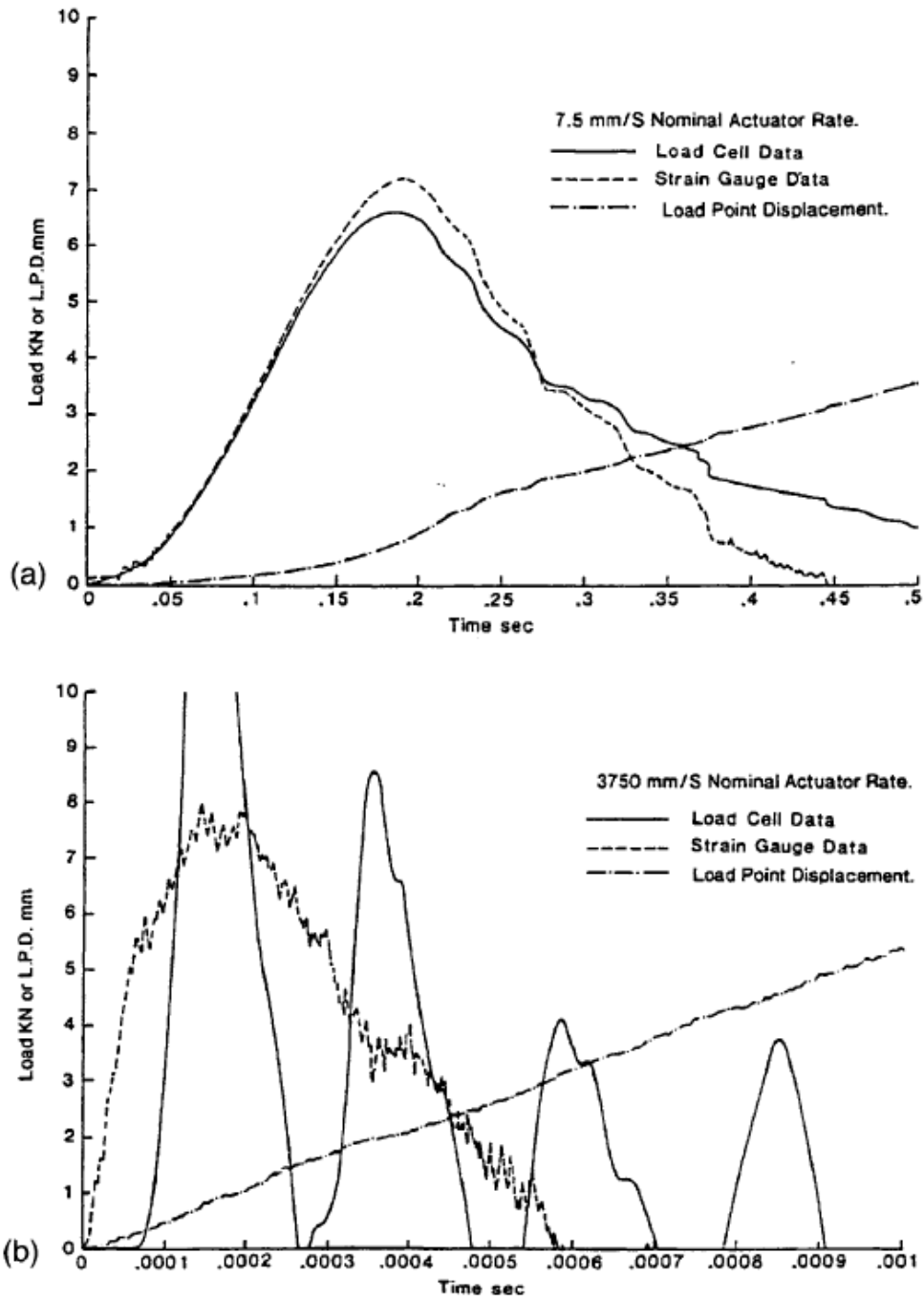


Figure 5-26 (a) Quasi-static Load-time plot (b) Dynamic Load-time plot (Wiesner & MacGillivray, 2019)

### 5.8.3 Concluding remarks

Several attempts and calibrations were made to obtain data from the dynamic fracture toughness testing. The Instron machine was used for the dynamic fracture toughness experiment but was unable to capture relevant data needed for the GOM analysis.

This resulted in the incomplete analysis of dynamic fracture toughness experiment. Hence no result was obtained in the dynamic toughness testing to correlate with the FEA model analysis. This error led to the choice of utilising Instrumented Charpy test to determine the effect of high strain rate on the behaviour of X65 steel material. From the result of Charpy test, it could be seen that strain rate affects the toughness of the material leading to decreased toughness. Also crack length affects the fracture toughness, as the 2 mm crack length has better toughness than the 5 mm crack length.

## **5.9 Machine learning results for toughness and stress-strain curve predictions**

### **5.9.1 Fracture toughness prediction**

Random Forest regressor, a supervised learning algorithm used for classification and regression using ensemble learning method was adopted in this model. The target of this model was a single point fracture toughness; hence Random Forest Regressor was selected for the model for easy interpretation and low overfitting. This model helps with the prediction of the fracture toughness of the material when the input features are known where no experimental data are available. In this study different factors were attributed to the actual experiment to determine the effect of strain rate on the fracture of X65 steel predicted by ML algorithm as seen in Pearson matrix Figure 5-27 which agrees with the result shown in Figure 3-27, but differs in choice of the applied features. It is therefore possible to predict the fracture toughness depending on the features being considered and available datasets for training.

The Pearson correlation matrix which evaluates how strongly two variables are related linearly between the range of -1 and +1 in a descriptive statistic was applied to determine the features affecting fracture toughness. The value of -1 means a negative linear correlation, while the value of 0 means no correlation, and +1 is a total positive correlation. Figure 5-27 shows the Pearson matrix results that was used to select the features with good correlation with the fracture toughness of which five of them were selected as the features for the model as earlier stated.

The machine learning model was developed through a multi-process including data collection from experiments and preparation, preparing features for input to derive

output, training data sets, training, evaluation of the performance, and iteration. The sampling method was a simple random sampling, the data processing was the MinMaxScaler to normalize the data. GridsearchCV was used to obtain the best estimator of 50 for this model and the R-squared scoring method was utilized. The data was split for training and testing with a test size of 0.2 splitting the data into a training set of 80% and a testing set of 20%. The result of the fracture toughness prediction is shown in Figure 5-28 which fitted 3 folds for each of 3 candidates, totalling 9 fits. The mean absolute error for the model was 45.74 and the R<sup>2</sup> score for the model was 0.95.

---

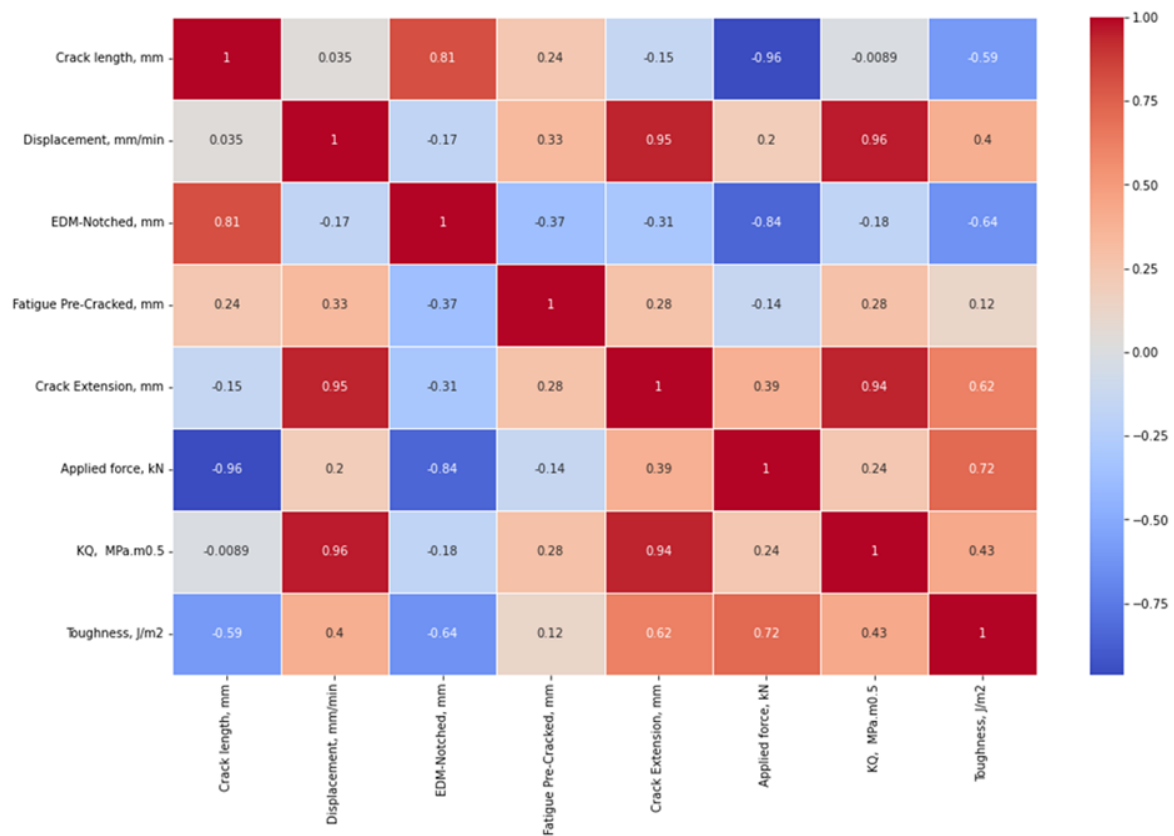


**Figure 5-27 Pearson matrix showing the correlation of the features applied for the machine learning prediction.**



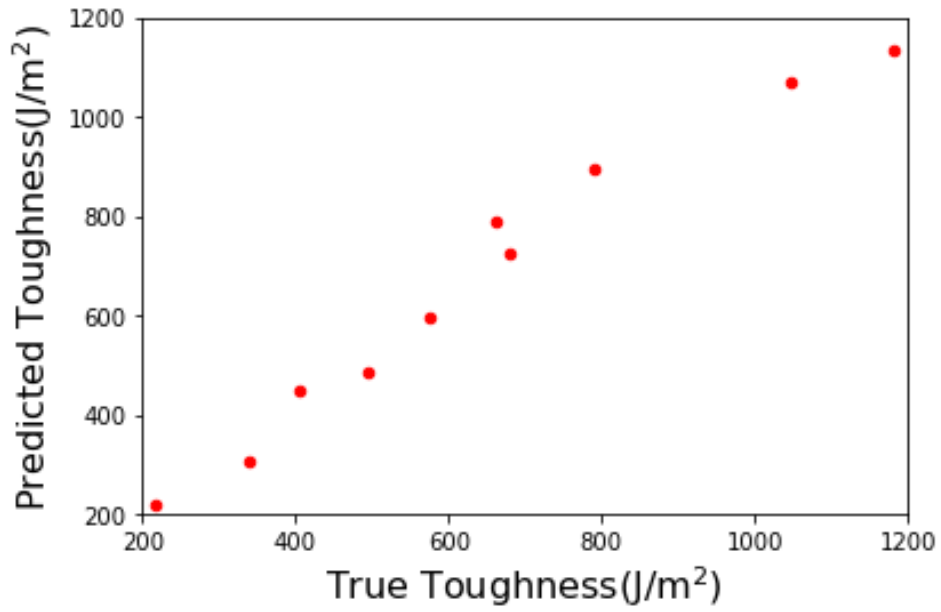


**Figure 5-28 Prediction of fracture toughness values with Random Forest Regressor ML results showing the true and predicted toughness values.**

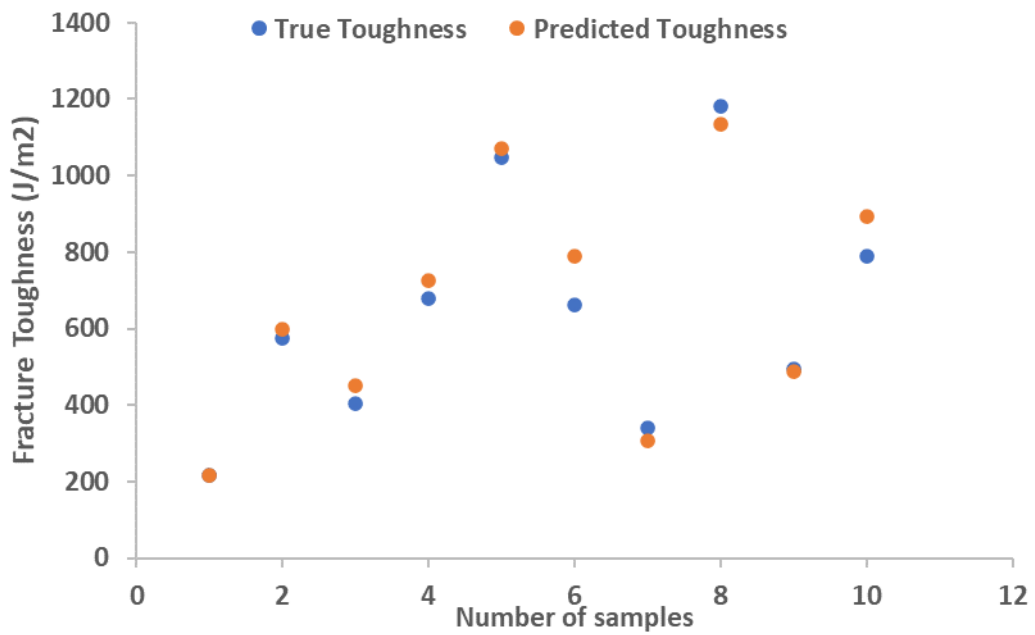


**Figure 5-29 Comparison of predicted fracture toughness with the true toughness result.**

### 5.9.2 Stress-Strain Prediction using machine learning.

A machine learning prediction of stress-strain curve was determined using Multi-layer Perceptron regressor (MLPRegressor), which is a sklearn neural network. The model was tested with different data sets unseen by the model. The model performance was obtained with the regression score of 0.28. Figure 5-30, Figure 5-31 and Figure 5-32 shows a good agreement between the trained and true data for different experimental specimen geometry. This was done so that machine learning could learn the pattern of the stress-strain curves from which physical properties such as tensile strength, elongation, and hardness could be predicted.

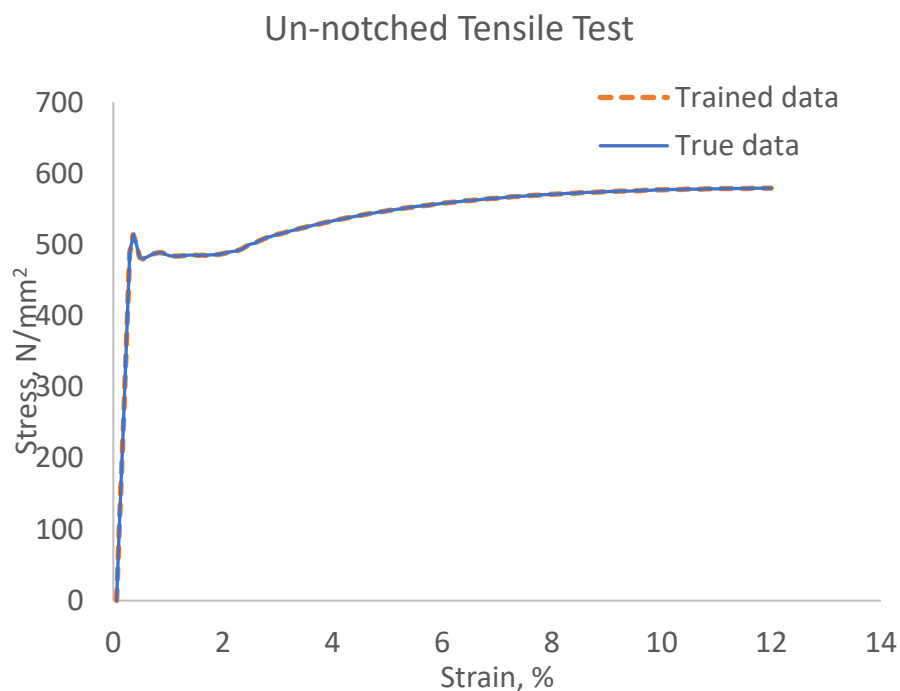


**Figure 5-30 Un-notched tensile tests plot of trained and true dataset**

The stress-strain curve of materials has been extensively studied using the experimental, analytical, and finite element method solutions to obtain mechanical properties from the curve. Analytical solution utilises simple formula, while the numerical method estimates quantitatively the stress-strain curve. Both analytical and numerical methods utilise some experimental values in their solutions. However, the numerical estimation of stress-strain curve is computationally expensive. A machine learning approach is therefore adopted for the prediction. The model was trained from already generated stress-strain curves from experiments using MLPRegressor in machine learning.

Since a given set of inputs were used to predict a real-valued quantity, the MLP regression was deemed suitable. The curves from experiments were converted from the pixels of the image to a reduced row of data which is fed into an MLP.

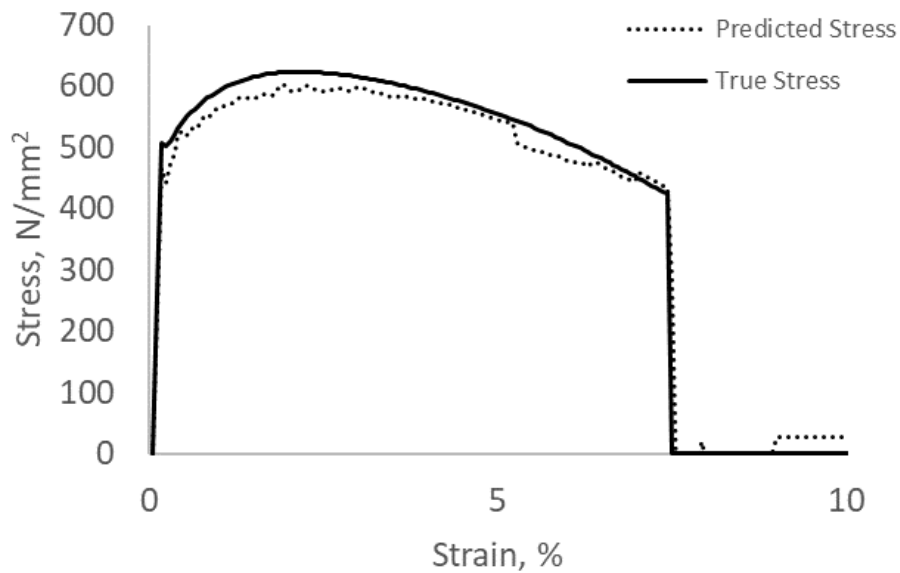


Figure 5-31 Round notched tensile tests plot of trained and true dataset.

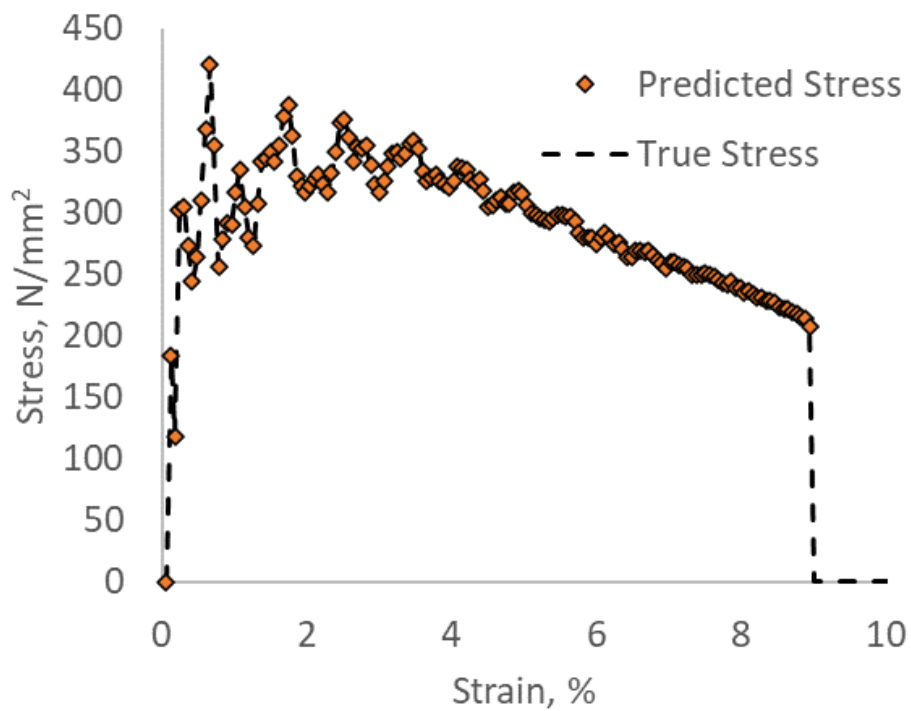


Figure 5-32 Controlled drop weight tests plot of trained and true dataset.

### **5.9.3 Machine learning Summary**

A deep learning method was built that can predict stress-strain curve using small datasets with small error. Specific features or conditions and sample specification can be utilised to predict a stress-strain curve of X65 steel from trained data. Also, the model can be retrained and transferred to other materials with known features, though, additional training data will be applied. The machine learning model satisfied the objectives with reasonable score which can improve with more datasets available for this study. Some curve details were difficult to obtain accurately, and this can improve as the amount of data increases. The model has a limitation of extremely small amount of data, which makes the model extensibility remains in doubt.



## 6 CONCLUSIONS

A range of tests were carried out in this study to determine methods for fracture toughness measurements. To fit the various steps taken, tensile tests were performed to determine the material properties such as the 0.2 % proof stress, elongation, ultimate tensile strength, and modulus of elasticity. The obtained results from the experiments were utilised for analytical calculations and determination of Johnson-Cook ductile and damage parameters. The JC parameters were further utilised for FEA modelling under dynamic loading to validate the analytical and experimental results.

While testing fracture toughness at high strain rates, instrumented Charpy test was utilised which has a limit to which the material can be tested at about 5240 mm/s displacement rate resulting to  $216 \text{ s}^{-1}$  strain rate. Fracture toughness testing at high strain rates were performed with issues resulting from the data acquisition on Instron VHS machine. This high strain rate fracture toughness test requires technical expertise to set up the testing procedure and fixtures. The measuring device which consists of high-speed camera was unable to obtain reasonable data points at higher strain rates.

Hence, the choice of low blow instrumented Charpy test was made to determine fracture toughness at different strain rates. The current testing procedure has no provision for extrapolating results at higher strain rates and are limited to the provided strain rates stated in the procedure, making it difficult to determine fracture toughness at higher strain rates. The material characterisation has been enumerated in Section 6.1.1 and compared with results from other sources.

Some processes that were followed to achieve aims and objectives of this study are as follows:

### 6.1.1 Material characterisation

- The tensile properties of X65 steel were tested and characterised at varying strain rates ( $10^{-5}$  to  $10^2 \text{ s}^{-1}$ ) with the yield strength and ultimate tensile strength shown to be higher at increased strain rates which is similar to what was reported in literature.
- The stress-strain curve of the tensile testing at higher strain rates was affected by strong oscillations that mask the true path of the curve, of which the amplitude increases with strain rate.

- The temperature rise under quasi-static and dynamic strain rates were considered and the temperature rise increases with the strain rate. The thermal diffusivity distance decreases at higher strain rates giving room for thermal softening which could lead to shear instability.
- The experimental data shows that strain rate sensitivity affects X65 material, and the behaviour of metallic material requires testing in both quasi-static and dynamic conditions. This is to optimise the application of the material while considering the real-life loading conditions to reduce catastrophic fracture at dynamic loading conditions.
- The analytical characterisation of flow stress using dislocation evolution theory shows a reasonable agreement with the experimental data and could be used to predict tensile behaviour at increased strain rates that might otherwise not be practicable to be tested in the laboratory.

### **6.1.2 Fracture behaviour**

The fracture behaviour of the material was tested and analysed under different loading conditions ranging from quasi-static to dynamic loading. This required intensive testing including tensile testing with round specimens (un-notched and varying radii notched), the drop weight test, instrumented Charpy tests (full blow and low blow testing), and the fracture toughness tests (static and dynamic).

The results from the experiment were utilised in the analytical solutions to determine the effect of high strain rates. The JC equation, thermostatistical model and thermal diffusivity theory were applied to analyse the high strain rate effects and correlated with the experimental results. The conclusion from these methods is as follows:

- The objective on determining material behaviour at high strain rate has been realised based on the experimental and analytical results of X65 steel during deformation. The 0.2 % proof strength obtained for quasi-static condition ranges from 580 - 600 MPa and 740 – 856 MPa under high strain rate conditions. The result from thermostatistical model mean that flow stresses are predicted from the model. It is important to mention that the yield strength at different strain rates was obtained from experimental datasets to predict accurately the plastic deformation analytically.

- The rise in temperature affects material behaviour during plastic deformation. Little rise in temperature is experienced during quasi-static loading, which becomes very prominent at elevated strain rates (about 80 K for the  $600 \text{ s}^{-1}$  at 0.3 strain). This temperature rise is utilised to characterise material behaviour which undergo isothermal process at quasi-static condition to fully adiabatic process at high strain rates incurring thermal softening and increased elongation. This changes in temperature during plastic deformation was also reflected in the dynamic recovery coefficient in the thermostatistical model at high strain rates.
- The instrumented Charpy test was utilised to determine the effect of loading rate on the fracture toughness in which low blow Charpy tests were performed to derive the varying strain rates using the Charpy sized pre-cracked samples. The  $a_0/W$  of 0.2 and 0.5 was utilised and it shows that crack length affects fracture toughness ( $1400 - 1600 \text{ J/m}^2$  and  $596 - 810 \text{ J/m}^2$  respectively) of metallic material as expected. It is worth noting that fracture toughness decreases during dynamic loading than in quasi-static loading conditions.
- The material initiation toughness,  $J_{0.2}$  was difficult to obtain from J-R curve using the Charpy-sized pre-cracked specimen under quasi-static loading conditions. This shows the effect of ductility on the material properties of X65 steel; thus, this work gives insight on the factors capable of affecting the generation of J-R curve.

### **6.1.3 Finite element analysis and machine learning**

The study was further explored using FEA to model the material behaviour at high strain rates. The JC parameters determined was applied in the material property section of ABAQUS/Explicit analysis for dynamic loading modelling. The FEA results were validated against the experimental results and were further extrapolated to higher strain rates. The FEA model applied was successfully used to determine the crack driving force and fracture energy at varying loading rates which was validated using results from instrumented Charpy experiment and developed model for X65 steel.

The FEA accurately predicted the load displacement curve using ABAQUS/Explicit analysis and element deletion method and can be further applied to higher strain rates provided the Johnson-Cook parameters are determined for the ductile and damage



model. Further analysis of elevated strain rates up to  $20 \text{ m s}^{-1}$  using FEA established that little or no significant bending was experienced at higher strain rates from the FEA model making the material to behave from fully ductile material to fully brittle material. The FEA simulations and experiments have shown that there is a limited strain rate in which the laboratory is suitable for the testing, beyond this critical strain rate a full-scale testing is required.

On application of machine learning algorithm, it was found that the machine learning algorithm identifies the best features and possible causes of result variations for determining fracture toughness presented in the Pearson correlation matrix. It is possible to predict fracture toughness at dynamic loading condition when the model is fully established to reduce the high cost associated with experiment and computational methods.

In conclusion, this research examines various methods to determine material properties at high strain rates using both tensile and fracture toughness tests. The finite element analysis was used to support the experiment and validate the fracture toughness SENB model for the prediction of force displacement and stress-strain curve under the condition of high loading rates using ductile and fracture criteria (Johnson-Cook equation) derived from experimental tension test analysis.

The prediction of stress-strain curve and fracture toughness property using some features were presented and analysed using machine learning algorithms. The results of experimental, analytical, computational and machine learning approaches achieved the main aim of this research which was to determine the fracture toughness of metallic material at high strain rates under the condition of limited plastic deformation.

Some major achievements in this research includes:

1. This study has been able to address and innovate a unique way of measuring the material properties under high strain rate with the approach of thermostatistical model and thermal diffusivity at high strain rates. The results presented in Section 4.4 shows how thermal diffusion distant was embedded in the stress-strain curve and the effect of strain rate to this distance which reduces with increasing strain rates. The region covered by the thermal distance determines the area of the stress-strain curve useful in the analysis, as the mechanical properties (0.2 % yield strength, ultimate tensile strength,

and the elastic modulus) were obtained within the region. The static curve has no limit to the distance as the process is considered isothermal without significant rise in temperature, while the high strain rate deformation undergoes adiabatic process.

2. The effect of temperature rise during high strain rate deformation was explored and found that temperature increases as the strain rate increases, thus, this was implemented in the analytical approach for dislocation density evolution in BCC metal, as material response at high strain rates has connections with the evolution of microstructure. The effect of temperature was applied in deriving the dynamic recovery coefficient and a good correlation was seen in Section 4.5 (Figure 4-23 and Figure 4-24). That identified how important temperature rise affects the material properties tested at dynamic loading. The findings differ from previous studies (Figure 4-21 and Figure 4-22) of which constant temperature was assumed for all loading conditions. This was also compared by obtaining the JC parameters for plastic deformation employing experimental data and it was correlated with both experiment and analytical methods. The JC model parameters were also implemented in FEM analysis to model the material behaviour at dynamic loading conditions, and accurate results were obtained.
3. The machine learning approach was also studied to predict stress-strain curves and dynamic fracture toughness. New features for training data were considered different from previous studies to explore the determination of dynamic fracture toughness under high strain rate loading. The results in Section 5.9 were promising with lower  $R^2$  score resulting from the limited availability of experimental data.
4. The existing testing procedure for fracture toughness tests of metallic materials at increased stress intensity factor outlined in BS 7448: part 3 which uses conventional load cell instrumentation for measuring dynamic load-time values produces a significant inertia effect. The BS 7448: part 3 procedure which was last reviewed in 2005 is obsolete and a review to adopt new improved procedure is required, which will implement modern technology in recording experimental data. It is recommended that recent available machine with high-speed cameras capable of capturing all stages be implemented to determine a

load-time plot with less noise and oscillation, making the true path of the curve available for assessment.

## 7 RECOMMENDATION FOR FUTURE WORK

The application of API X65 steel is seen more in high-pressured, long-distance pipelines transportation in offshore, and this requires that it is at best performance when combined strength and hardness to support the high pressures. The condition in marine environment needs to be tested under both quasi-static and dynamic loading condition to withstand the external forces on the structure.

To fully characterise the mechanical performance of metallic steel at dynamic loading conditions, more research work is needed. As the scope of this research determines the tensile and fracture toughness properties at high strain rates of the parent material, research on the fatigue and weldments are required to fully integrate the performance in Engineering Critical Assessment for enhanced safety of the structure.

Meanwhile, it is necessary that the testing procedure for dynamic fracture toughness up to a displacement rate of  $20000 \text{ mm s}^{-1}$  be determined to establish the best procedure for laboratory material testing to be extendable to other materials at dynamic condition. It is therefore recommended that:

1. Other dynamic testing methods such as Hopkinson's pressure bar experiment could be adopted in conjunction with instrumented Charpy testing which has limit of  $5420 \text{ mm s}^{-1}$  displacement testing rate to improve for improving test methods to determine dynamic fracture toughness. This will require the use of high-speed camera or other recording devices to capture experimental data which will further be analysed to desired fracture toughness results at higher strain rates.
2. More testing on tensile tests (smooth round, notched round, and flat specimens) for each strain rates is recommended to at least three sets of testing which is compatible to capture the inherent scatter in the data.
3. Further work is necessary on the use of machine learning approach for prediction of dynamic fracture toughness. As the limitation is based on the available data, it is important to generate a testing procedure validated by FEA to generate reasonable data sufficient to increase the performance of the machine learning model.

Finally, the mechanical behaviour of metallic material under dynamic loading has structural implication, that if not properly assessed leads to catastrophic event. As safety is the key factor in every engineering structure, this means that all relevant testing relating to the real-life condition of the applied material need to be tested and integrated in the design of the structure. It is therefore not recommended to rely on the quasi-static performance of metallic material only in an Engineering Critical Assessment. It is necessary that a procedure be established for laboratory testing of dynamic fracture toughness and reviewed continuously depending on the available and recent instrumentation. The Charpy test using the pre-crack specimen is a very good testing approach to be adopted for impact loading but is limited to  $5400 \text{ mm s}^{-1}$  displacement rate which does not cover all the dynamic conditions and therefore the need for dynamic fracture toughness at elevated strain rates. A full-scale testing may be required if laboratory testing does not represent the condition properly to ascertain the behaviour of such material at both quasi-static and dynamic loading conditions as presented in this research work.

## REFERENCES

- Almar-Naess, A., Haagensen, P. J., Lian, B., Moan, T., & Simonsen, T. (1984). Investigation of the alexander L. kielland failure—Metallurgical and fracture analysis.
- Anderson, P. M., Hirth, J. P., & Lothe, J. (2017). *Theory of dislocations* Cambridge University Press.
- Anderson, T. L. (2017). *Fracture mechanics: Fundamentals and applications* CRC press.
- Andrade, U., Meyers, M. A., Vecchio, K. S., & Chokshi, A. H. (1994). Dynamic recrystallization in high-strain, high-strain-rate plastic deformation of copper. *Acta Metallurgica Et Materialia*, 42(9), 3183-3195.
- Au, T. C. (2018). Random forests, decision trees, and categorical predictors: The “absent levels” problem. *Journal of Machine Learning Research*, 19, 1-30.
- Bammann, D. J., & Aifantis, E. C. (1982). On a proposal for a continuum with microstructure. *Acta Mechanica*, 45(1-2), 91-121. doi:10.1007/BF01295573
- Banerjee, A., Dhar, S., Acharyya, S., Datta, D., & Nayak, N. (2015). Determination of johnson cook material and failure model constants and numerical modelling of charpy impact test of armour steel. *Materials Science and Engineering: A*, 640, 200-209.
- Barsanti, L., Pozzoli, G., & Hillenbrand, H. G. (2001). Production and field weldability evaluation of X100 line pipe. Paper presented at the

- Billingham, J., Healy, J., & Bolt, H. (1997). *High strength steels-the significance of yield ratio and work-hardening for structural performance* Great Britain, Health and Safety Executive.
- Bobbili, R., Ramakrishna, B., Madhu, V., & Gogia, A. K. (2015). Prediction of flow stress of 7017 aluminium alloy under high strain rate compression at elevated temperatures. *Defence Technology*, 11(1), 93-98. doi:10.1016/j.dt.2014.08.004
- British, S. I. (2005). *BS 7448-3:2005 fracture mechanics toughness tests. method for determination of fracture toughness of metallic materials at rates of increase in stress intensity factor greater than 3.0 MPa m<sup>0.5</sup> s<sup>-1</sup>*. London: BSI.
- British, S. I. (2011). *BS EN ISO 26203-2:2011 metallic materials. tensile testing at high strain rates. servo-hydraulic and other test systems*. London: BSI.
- British, S. I. (2019a). *BS 7910:2019 guide to methods for assessing the acceptability of flaws in metallic structures*. London: BSI.
- British, S. I. (2019b). *BS EN ISO 6892-1:2019 metallic materials. tensile testing. method of test at room temperature*. London: BSI.
- British, S. I. (2021). *BS ISO 12135:2021 metallic materials — unified method of test for the determination of quasistatic fracture toughness*. London: BSI.
- Buitinck, L., Louppe, G., Blondel, M., Pedregosa, F., Mueller, A., Grisel, O., . . . Varoquaux, G. (2013). API design for machine learning software: Experiences from the scikit-learn project. doi:10.48550/arxiv.1309.0238

- Burdekin, F. M., Zhao, W., Tkach, Y., Wiesner, C. S., & Xu, W. (2004). The effects of dynamic loading on structural integrity assessments. *Health & Executive Research Report*, 208
- Capelle, J., Furtado, J., Azari, Z., Jallais, S., & Pluvinage, G. (2013). Design based on ductile–brittle transition temperature for API 5L X65 steel used for dense CO<sub>2</sub> transport. *Engineering Fracture Mechanics*, 110, 270-280. doi:10.1016/j.engfracmech.2013.08.009
- Chao, Y., & Varma, S. K. (1991). Effect of strain rate on dislocation cell size and hall-petch-type relationship at various strain levels during a uniaxial tensile test in electrical conductor aluminium. *Journal of Materials Science Letters*, 10(11), 630-632.  
doi:10.1007/bf00723360
- Clifton, R. J. (1983). Dynamic plasticity.
- Compbell, J. D., & Cooper, R. H. (1966). Yield and flow of low-carbon steel at medium strain rates.
- Cortis, G., Nalli, F., Sasso, M., Cortese, L., & Mancini, E. (2022). Effects of temperature and strain rate on the ductility of an API X65 grade steel. *Applied Sciences-Basel*, 12(5)  
doi:10.3390/app12052444
- Daghigh, V., Lacy Jr, T. E., Daghigh, H., Gu, G., Baghaei, K. T., Horstemeyer, M. F., & Pittman Jr, C. U. (2020). Machine learning predictions on fracture toughness of multiscale bio-nano-composites. *Journal of Reinforced Plastics and Composites*, 39(15-16), 587-598.
- Dimatteo, A., Vannucci, M., & Colla, V. (2013). Prediction of hot deformation resistance during processing of microalloyed steels in plate rolling process. *International Journal of*



*Advanced Manufacturing Technology*, 66(9-12), 1511-1521. doi:10.1007/s00170-012-4435-2

Dorogoy, A., & Rittel, D. (2009). Determination of the johnson-cook material parameters using the SCS specimen. *Experimental Mechanics*, 49(6), 881-885. doi:10.1007/s11340-008-9201-x

Duesbery, M. S. (1998). Dislocation motion, constriction and cross-slip in fcc metals. *Modelling and Simulation in Materials Science and Engineering*, 6(1), 35-49. doi:10.1088/0965-0393/6/1/005

E1820-23b, A. (2023). *Standard test method for measurement of fracture toughness*. american society for testing and materials;

E1921-22a, A. (2022). *Standard test method for determining of reference temperature T<sub>0</sub> for ferritic steels in the transition range*. american society for testing and materials;

El-Danaf, E., Baig, M., Almajid, A., Alshalfan, W., Al-Mojil, M., & Al-Shahrani, S. (2013). Mechanical, microstructure and texture characterization of API X65 steel. *Materials & Design*, 47, 529-538. doi:10.1016/j.matdes.2012.12.031

Evison, R. D. (1964). Failure of kings bridge melbourne. *New Zealand Engineering*, 19(2), 69-70. Retrieved from <https://search.informit.org/doi/10.3316/informit.180915760150874>  
<https://search.informit.org/doi/pdf/10.3316/informit.180915760150874>  
<https://search.informit.org/doi/full/10.3316/informit.180915760150874>

- Fan, C. Z., Xu, Z. J., Han, Y., Liu, Y., & Huang, F. L. (2023). Loading rate effect and failure mechanisms of ultra-high-strength steel under mode II fracture. *International Journal of Impact Engineering*, 171 doi:10.1016/j.ijimpeng.2022.104374
- Galindo-Nava, E., & Rivera-Díaz-del-Castillo, P. E. J. (2012). Modelling plastic deformation in BCC metals: Dynamic recovery and cell formation effects. *Materials Science & Engineering.A, Structural Materials : Properties, Microstructure and Processing*, 558, 641-648. doi:10.1016/j.msea.2012.08.068
- Ganesh, N., Jain, P., Choudhury, A., Dutta, P., Kalita, K., & Barsocchi, P. (2021). Random forest regression-based machine learning model for accurate estimation of fluid flow in curved pipes. *Processes*, 9(11), 2095. doi:10.3390/pr9112095
- Gangi Setti, S., & Rao, R. N. (2014). Artificial neural network approach for prediction of stress–strain curve of near  $\beta$  titanium alloy. *Rare Metals*, 33(3), 249-257. doi:10.1007/s12598-013-0182-2
- Grady, D. E. (1982). Local inertial effects in dynamic fragmentation. *Journal of Applied Physics*, 53(1), 322-325. doi:10.1063/1.329934
- Griffith, A. A. (1921). The phenomena of rupture and flow in solids. *Philosophical Transactions of the Royal Society of London. Series A, Containing Papers of a Mathematical Or Physical Character*, 221, 163-198.
- Gupta, A. K., Singh, S. K., Reddy, S., & Hariharan, G. (2012). Prediction of flow stress in dynamic strain aging regime of austenitic stainless steel 316 using artificial neural network. *Materials & Design*, 35, 589-595. doi:10.1016/j.matdes.2011.09.060

- Hayes, B. (1996). Six case histories of pressure vessel failures. *Engineering Failure Analysis*, 3(3), 157-170.
- He, Z. F., Jia, N., Wang, H. W., Liu, Y., Li, D. Y., & Shen, Y. F. (2020). The effect of strain rate on mechanical properties and microstructure of a metastable FeMnCoCr high entropy alloy. *Materials Science and Engineering: A*, 776, 138982.  
doi:10.1016/j.msea.2020.138982
- Henthorne, M., & Parkins, R. N. (1966). Some aspects of stress-corrosion crack propagation in mild steel. *Corrosion Science*, 6(8), 357-+. doi:10.1016/s0010-938x(66)80018-5
- Ho, T. K. (1995). Random decision forests. Paper presented at the , 1 278-282.
- Ho, T. K. (1998). The random subspace method for constructing decision forests. *IEEE Transactions on Pattern Analysis and Machine Intelligence*, 20(8), 832-844.
- Huang, M., Rivera-Díaz-del-Castillo, P. E. J., Bouaziz, O., & van der Zwaag, S. (2009). A constitutive model for high strain rate deformation in FCC metals based on irreversible thermodynamics. *Mechanics of Materials*, 41(9), 982-988.  
doi:10.1016/j.mechmat.2009.05.007
- Huang, Z. P., Gao, L. H., Wang, Y. W., & Wang, F. C. (2016). Determination of the Johnson-cook constitutive model parameters of materials by cluster global optimization algorithm (vol 25, pg 4099, 2016). *Journal of Materials Engineering and Performance*, 25(9), 4108. doi:10.1007/s11665-016-2256-4
- Hull, D., & Bacon, D. J. (2001). *Introduction to dislocations* Butterworth-Heinemann.

- Ikenna-Uzodike, C. E., Janin, Y. J., Gintalas, M., Wen, W., Tadžijevs, A., & Rivera-Diaz-del-Castillo, P. E. (2022). An industrial approach to high strain rate testing. *Procedia Structural Integrity*, 42, 1634-1642.
- Inglis, C. E. (1913). Stresses in a plate due to the presence of cracks and sharp corners. *Trans Inst Naval Archit*, 55, 219-241.
- Irwin, G. R. (1947). Fracture dynamics. *Fracturing of Metals*,
- Jasper, T. M., & Manjoine, M. J. (1945). Influence of rate of strain and temperature on yield stresses of mild steel. *Journal of Applied Mechanics-Transactions of the Asme*, 12(3), A186.
- Johnson, G. R., Hoegfeldt, J. M., Lindholm, U. S., & Nagy, A. (1983). Response of various metals to large torsional strains over a large range of strain rates .1. ductile metals. *Journal of Engineering Materials and Technology-Transactions of the Asme*, 105(1), 42-47. doi:10.1115/1.3225617
- Karkalos, N. E., & Markopoulos, A. P. (2018). Determination of johnson-cook material model parameters by an optimization approach using the fireworks algorithm. *11th International Conference Interdisciplinarity in Engineering, Inter-Eng 2017*, 22, 107-113. doi:10.1016/j.promfg.2018.03.017
- Kishimoto, K., Aoki, S., & Sakata, M. (1980). Simple formula for dynamic stress intensity factor of pre-cracked charpy specimen. *Engineering Fracture Mechanics*, 13(3), 501-508. doi:10.1016/0013-7944(80)90081-8

- Kleebe, H., Pezzotti, G., & Ziegler, G. (1999). Microstructure and fracture toughness of  $\text{Si}_3\text{N}_4$  ceramics: Combined roles of grain morphology and secondary phase chemistry. *Journal of the American Ceramic Society*, 82(7), 1857-1867. doi:10.1111/j.1151-2916.1999.tb02009.x
- Klepaczko, J. R., & Brara, A. (2001). An experimental method for dynamic tensile testing of concrete by spalling. *International Journal of Impact Engineering*, 25(4), 387-409. doi:10.1016/S0734-743X(00)00050-6
- Kobayashi, H., & Onoue, H. (1943). Brittle fracture of liberty ships. *Failure Knowledge Database*, 100
- Kobayashi, T., Kim, H. J., & Morita, S. (2001). Progress and development in the instrumented charpy impact test: 100 Jahre Charpy-Versuch. *Materialwissenschaft Und Werkstofftechnik*, 32(6), 525-531.
- Kocks, U. F., & Mecking, H. (2003). Physics and phenomenology of strain hardening: The FCC case. *Progress in Materials Science*, 48(3), 171-273. doi:10.1016/S0079-6425(02)00003-8
- Koenuma, K., Yamanaka, A., Watanabe, I., & Kuwabara, T. (2020). Estimation of texture-dependent stress-strain curve and  $r$ -value of aluminum alloy sheet using deep learning. *Materials Transactions*, 61(12), 2276-2283. doi:10.2320/matertrans.p-m2020853
- Korbel, A., & Świątkowski, K. (1972). The role of strain rate in the formation of dislocation structure and its influence on the mechanical properties of aluminium. *Metal Science Journal*, 6(1), 60-63.

- Kuhlmann-Wilsdorf, D. (1970). A critical test on theories of work-hardening for the case of drawn iron wire. *Metallurgical Transactions*, 1, 3173-3179.
- Kuntiyawichai, K., & Burdekin, F. M. (2003). Engineering assessment of cracked structures subjected to dynamic loads using fracture mechanics assessment. *Engineering Fracture Mechanics*, 70(15), 1991-2014. doi:10.1016/S0013-7944(02)00257-6
- Lambert, D. E., & Allen Ross, C. (2000). Strain rate effects on dynamic fracture and strength. *International Journal of Impact Engineering*, 24(10), 985-998. doi:10.1016/S0734-743X(00)00027-0
- Lavrentev, F. F. (1980). The type of dislocation interaction as the factor determining work-hardening. *Materials Science and Engineering*, 46(2), 191-208. doi:10.1016/0025-5416(80)90175-5
- Lee, O. S., & Kim, M. S. (2003). Dynamic material property characterization by using split hopkinson pressure bar (SHPB) technique. *Nuclear Engineering and Design*, 226(2), 119-125. doi:10.1016/s0029-5493(03)00189-4
- Li, Y., Zou, C., Berecibar, M., Nanini-Maury, E., Chan, J. C. W., Van den Bossche, P., . . . Omar, N. (2018). Random forest regression for online capacity estimation of lithium-ion batteries. *Applied Energy*, 232, 197-210.
- Loveday, M. S., Gray, T., & Aegerter, J. (2004). Tensile testing of metallic materials: A review. *Final Report of the TENSTAND Project of Work Package*, 1

Maiden, C. J., & Green, S. J. (1966). Compressive strain-rate tests on six selected materials at strain rates from 10<sup>-3</sup> to 10<sup>4</sup> in/in/sec.

Malygin, G. A. (2012). Influence of the peierls relief on size effects in plastic deformation of micro- and nanocrystals of body-centered cubic metals. *Physics of the Solid State*, 54(6), 1220-1228. doi:10.1134/s1063783412060212

Marais, S. T., Tait, R. B., Cloete, T. J., & Nurick, G. N. (2004). Material testing at high strain rate using the split hopkinson pressure bar. *Latin American Journal of Solids and Structures*, 1(3), 219-339.

Mason, J. J., Rosakis, A. J., & Ravichandran, G. (1994). On the strain and strain-rate dependence of the fraction of plastic work converted to heat - an experimental-study using high-speed infrared detectors and the kolsky bar. *Mechanics of Materials*, 17(2-3), 135-145. doi:10.1016/0167-6636(94)90054-x

Meyers, M. A. (1994). *Dynamic behavior of materials* John wiley & sons.

Moan, T. (1985). The progressive structural failure of the alexander L. kielland platform. *Case histories in offshore engineering* (pp. 1-42) Springer.

Molinari, A., Mercier, S., & Jacques, N. (2014). Dynamic failure of ductile materials. *Procedia Iutam*, 10, 201-220.

Mott, N. F. (1948). Fracture of metals: Theoretical considerations. *Engineering*, 165, 16-18.

- Murugesan, M., & Jung, D. W. (2020). Johnson cook material and failure model parameters estimation of AISI-1045 medium carbon steel for metal forming applications (vol 12, 609, 2019). *Materials*, 13(24) doi:10.3390/ma13245744
- Nabarro, F. R. N., Basinski, Z. S., & Holt, D. B. (1964). The plasticity of pure single crystals. *Advances in Physics*, 13(50), 193-323.
- Nohring, W. G., & Curtin, W. A. (2017). Dislocation cross-slip in fcc solid solution alloys. *Acta Materialia*, 128, 135-148. doi:10.1016/j.actamat.2017.02.027
- Orowan, E. (1949). Fracture and strength of solids. *Reports on Progress in Physics*, 12(1), 185-232. doi:10.1088/0034-4885/12/1/309
- Osorio-Pinzon, J., Abolghasem, S., & Casas-Rodriguez, J. (2019). Predicting the johnson cook constitutive model constants using temperature rise distribution in plane strain machining. *International Journal of Advanced Manufacturing Technology*, 105(1-4), 279-294. doi:10.1007/s00170-019-04225-9
- Owen, D. M., Zhuang, S., Rosakis, A. J., & Ravichandran, G. (1998). Experimental determination of dynamic crack initiation and propagation fracture toughness in thin aluminum sheets. *International Journal of Fracture*, 90, 153-174.
- Pedregosa, F., Varoquaux, G., Gramfort, A., Michel, V., Thirion, B., Grisel, O., . . . Duchesnay, É. (2011). Scikit-learn: Machine learning in python. *Journal of Machine Learning Research*, 12, 2825-2830. doi:10.5555/1953048.2078195



- Prakash, A., Weygand, D., & Bitzek, E. (2017). Influence of grain boundary structure and topology on the plastic deformation of nanocrystalline aluminum as studied by atomistic simulations. *International Journal of Plasticity*, *97*, 107-125.  
doi:10.1016/j.ijplas.2017.05.011
- Quinn, J. B., Sundar, V., & Lloyd, I. K. (2003). Influence of microstructure and chemistry on the fracture toughness of dental ceramics. *Dental Materials*, *19*(7), 603-611.
- Rice, J. R. (1968). A path independent integral and the approximate analysis of strain concentration by notches and cracks.
- Rokach, I. V. (1998). Modal approach for processing one- and three-point bend test data for dsif-time diagram determination part i-theory. *Fatigue & Fracture of Engineering Materials & Structures*, *21*(8), 1007-1114. doi:10.1046/j.1460-2695.1998.00087.x
- Rubio, L., Fernandez-Saez, J., & Navarro, C. (2003). Determination of dynamic fracture-initiation toughness using three-point bending tests in a modified hopkinson pressure bar. *Experimental Mechanics*, *43*(4), 379-386. doi:10.1007/BF02411342
- Rusineck, A., Zaera, R., & Klepaczko, J. R. (2007). Constitutive relations in 3-D for a wide range of strain rates and temperatures – application to mild steels. *International Journal of Solids and Structures*, *44*(17), 5611-5634. doi:10.1016/j.ijsolstr.2007.01.015
- Sharma, P., Chandel, P., Bhardwaj, V., Singh, M., & Mahajan, P. (2018). Ballistic impact response of high strength aluminium alloy 2014-T652 subjected to rigid and deformable projectiles. *Thin-Walled Structures*, *126*, 205-219. doi:10.1016/j.tws.2017.05.014

Shrot, A., & Baker, M. (2011). Inverse identification of johnson-cook material parameters from machining simulations. *Modelling of Machining Operations*, 223, 277-285.

doi:10.4028/[www.scientific.net/AMR.223.277](http://www.scientific.net/AMR.223.277)

Srinivas, M., & Kamat, S. V. (2001). Effect of strain rate on fracture toughness of mild steel.

*Materials Science and Technology*, 17(5), 529-535. doi:10.1179/026708301101510375

Tam, L. L., & Calladine, C. R. (1991). Inertia and strain-rate effects in a simple plate-structure under impact loading. *International Journal of Impact Engineering*, 11(3), 349-377.

doi:10.1016/0734-743x(91)90044-g

Tan, Y., & Zhu, Y. (2010). Fireworks algorithm for optimization. Paper presented at the 355-364.

Taylor, G. (1948). The use of flat-ended projectiles for determining dynamic yield stress I. theoretical considerations. *Proceedings of the Royal Society of London. Series*

*A. Mathematical and Physical Sciences*, 194(1038), 289-299.

doi:10.1098/rspa.1948.0081

Tiamiyu, A. A., Szpunar, J. A., & Odeshi, A. G. (2019). Strain rate sensitivity and activation volume of AISI 321 stainless steel under dynamic impact loading: Grain size effect.

*Materials Characterization*, 154, 7-19.

Voyiadjis, G. Z., & Abed, F. H. (2005). Effect of dislocation density evolution on the thermomechanical response of metals with different crystal structures at low and high strain rates and temperatures. *Archives of Mechanics*, 57(4), 299-343.

- Wang, J. Q., Atrens, A., Cousens, D. R., & Kinaev, N. (1999). Microstructure of X52 and X65 pipeline steels. *Journal of Materials Science*, *34*(8), 1721-1728.  
doi:10.1023/a:1004538604409
- Wells, A. A. (1961). Unstable crack propagation in metals: Cleavage and fast fracture. Paper presented at the 84. , 1
- Westergaard, H. M. (1939). Bearing pressures and cracks: Bearing pressures through a slightly waved surface or through a nearly flat part of a cylinder, and related problems of cracks.
- Wiesner, C. S., & MacGillivray, H. (2019). Loading rate effects on tensile properties and fracture toughness of steel. *Fracture, plastic flow and structural integrity* (pp. 149-174) CRC Press.
- Yang, C., Kim, Y., Ryu, S., & Gu, G. X. (2020). Prediction of composite microstructure stress-strain curves using convolutional neural networks. *Materials & Design*, *189*, 108509.  
doi:10.1016/j.matdes.2020.108509
- Zerilli, F. J., & Armstrong, R. W. (1987). Dislocation-mechanics-based constitutive relations for material dynamics calculations. *Journal of Applied Physics*, *61*(5), 1816-1825.  
doi:10.1063/1.338024
- Zhang, Y. C., Outeiro, J. C., & Mabrouki, T. (2015). On the selection of johnson-cook constitutive model parameters for ti-6Al-4V using three types of numerical models of orthogonal cutting. *15th Cirp Conference on Modelling of Machining Operations (15th Cmm)*, *31*, 112-117. doi:10.1016/j.procir.2015.03.052

Zhu, X. K., & Joyce, J. A. (2012). Review of fracture toughness (G, K, J, CTOD, CTOA) testing and standardization. *Engineering Fracture Mechanics*, 85, 1-46.

doi:10.1016/j.engfracmech.2012.02.001



# APPENDICES

## Appendix A Experiments Conducted and the Conditions

### A.1 Specimen ID

Table A.1 High strain rate loading condition tensile test data for X65 steel

Specimen ID	Type of test	Strain rate (/s)	Speed (m/s)
M04-01	Flat tensile	216	5.4
M04-02	Flat tensile	216	5.4
M04-04	Flat tensile	400	10
M04-05	Flat tensile	400	10
M04-07	Flat tensile	600	15
M04-08	Flat tensile	600	15
M04-10	Flat tensile	800	20
M04-11	Flat tensile	800	20

**Table A.2 Test data for controlled drop weight test with blunt notch of  $a_0/W \approx 0.2$** 

Specimen ID	Type of test	Weight to 8.6 kg
M03-79	Controlled drop weight	plus 9kg
M03-80	Controlled drop weight, second test	plus 4 kg
M03-81	Controlled drop weight, second test	plus 6kg
M03-82	Controlled drop weight, first test	plus 10kg
M03-88	Controlled drop weight	plus 1kg
M03-89	Controlled drop weight	plus 0kg
M03-90	Controlled drop weight, second test	plus 10kg
M03-91	Controlled drop weight, third test	plus 10kg
M03-92	Controlled drop weight, second test	plus 4kg
M03-93	Controlled drop weight	Plus 8kg
M03-94	Controlled drop weight	plus 7kg
M03-95	Controlled drop weight, first test	plus 6kg
M03-96	Controlled drop weight	plus 5kg
M03-97	Controlled drop weight, first test	plus 4 kg
M03-98	Controlled drop weight	plus 3kg
M03-99	Controlled drop weight	plus 2kg

- Test report from TextXpert III for controlled drop weight test

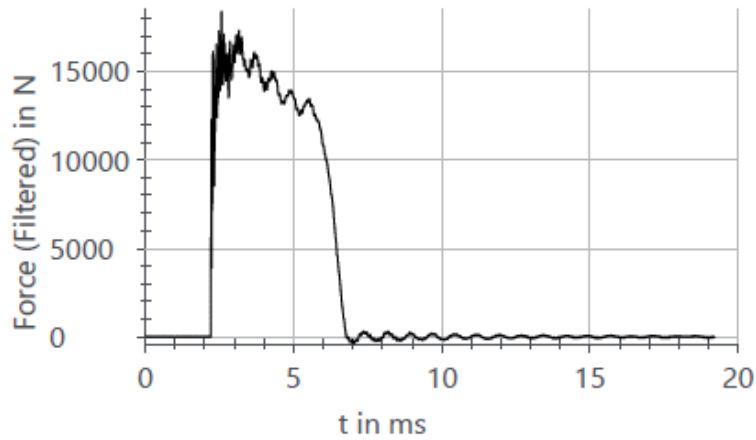
Parameters table:

Customer : Specimen removal :  
 Job no. : Pre-treatment :  
 Tester : Notes :  
 Test standard : Machine data :  
 Material :

Results table:

Legend	No.	Theoretical impact velocity m/s	Total mass kg	Work capacity J
●	2	5.296	8.603	120.65

Curve graph:





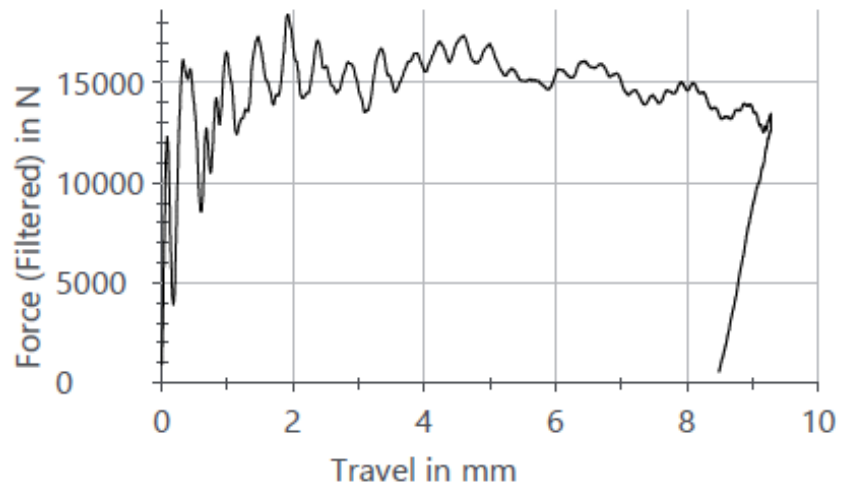








Figure A-1 Impact drop weight tested samples showing the level of crack extension



**Figure A-2 Fractured notch of impact drop weight test samples.**

**Table A.3 Fracture toughness test under quasi-static condition at ambient temperature for  $a_0/W$  0.5 with specimen geometry  $B=W=10$**

Specimen-ID	Total crack length, mm	EDM-Notch, mm	Fatigue crack length, mm	CTOD, mm	Maximum load, kN
M05-32	5.0	3.0	2.0	0.60	5.9
M05-33	5.2	3.1	2.1	0.43	5.5
M05-34	4.8	3.0	1.8	0.84	5.8
M05-35	5.4	3.1	2.3	0.15	4.6
M05-36	5.1	3.0	2.1	0.26	5.5
M05-37	5.1	3.0	2.1	0.50	5.6
M05-38	5.2	3.0	2.2	0.57	5.6
M05-39	5.2	3.1	2.1	0.61	5.5

**Table A.4 Fracture toughness test under quasi-static condition at ambient temperature for  $a_0/W \approx 0.2$  with specimen geometry  $B=W=10$**

Specimen-ID	Total crack length, mm	EDM-Notch, mm	Fatigue crack length, mm	CTOD, mm	Maximum load, kN
M05-81	2.1	0.6	1.5	1.55	15.1
M05-82	2.4	0.7	1.8	0.79	13.6
M05-83	2.3	0.6	1.7	1.13	14.3
M05-84	2.4	0.7	1.7	1.44	13.6
M05-85	2.3	0.6	1.7	0.34	12.6
M05-86	2.3	0.6	1.6	0.57	13.7
M05-87	2.4	0.6	1.8	0.96	14.2

M05-88	2.1	0.5	1.6	1.28	15.1
M05-89	2.3	0.5	1.8	1.08	14.5

**Table A.5 Instrumented Charpy test data and the absorbed energies for  $a_0/W \approx 0.5$**

Specimen-ID	Initial crack length, mm	Crosshead disp, m/s	Applied force, kN	Impact energy, J/m <sup>2</sup>
M05-01	5.3	5.4	6.5	596
M05-02	5.0	5.4	7.5	705
M05-03	5.6	5.4	5.7	696
M05-40	5.3	4.9	6.6	767
M05-41	5.3	4.9	6.6	596
M05-42	5.1	4.9	7.4	810
M05-43	5.3	3.9	6.8	799
M05-44	5.3	3.9	6.8	768
M05-45	5.3	3.9	6.8	730

**Table A.6 Instrumented Charpy test data and the absorbed energies for  $a_0/W \approx 0.2$** 

Specimen-ID	Initial crack length, mm	Crosshead displacement, m/s	Applied force, kN	Impact energy, J/m <sup>2</sup>
M05-51	2.1	5.4	18.8	1516
M05-52	2.2	5.4	18.6	1491
M05-53	2.1	5.4	18.4	1563
M05-90	2.6	4.9	16.9	1564
M05-91	2.4	4.9	17.9	1592
M05-92	2.3	4.9	18.4	1670
M05-93	2.2	3.9	18.2	1651
M05-94	2.3	3.9	18.1	1682
M05-95	2.5	3.9	17.3	1604



## A.2 Experimental results from TWI

- Pre-cracked SENB specimen configuration for Charpy test certificate using X65 steel at room temperature for  $a_0/W \approx 0.5$ .

UKAS TESTING 0088		TWI	
<b>SENB FRACTURE TEST 33109 M05-01</b>			
Client	Project leader	PhD	Yin Jin Janin
		Signed:	
<b>Data source</b>			
Data logging program		testXpert II V3.6 2016	
Program used to calculate CTOD/J		LVGENPLOT V 1.64.10 12-Jul-2021	
Calculation date of CTOD/J		20 Jul 2021	
<b>Specimen details</b>			
Material		X65	
Specimen type		Subsize, SENB	
Crack plane orientation		UNKNOWN	
Type of notch tip		Fatigue	
Notch tip location		Parent material	
Specimen width		9.990 mm	
Specimen thickness		9.990 mm	
Initial crack length		5.287 mm	
Side-grooved?		NO	
Original PM 1 thickness		19.40 mm	
<b>Test details</b>			
Test standard(s)		ISO 12135:2016	
Test date		19/07/2021	
Test time		09:31:00	
Test technician		Martin Gilder	Signed:
Test machine		Zwick 750J Charpy T03c	
Test environment		Air	
Test temperature		23.0 °C	
Soak time @ test temperature		0.0 minutes	
Knife edge heights		N/A mm	
Knife edge attachment spacing		N/A mm	
Initial K-rate		539448.2 MPa.m <sup>3/2</sup>	
Crosshead displacement rate		325137.98 mm/min	
Loading span		42.0 mm	
Double roller diameter		2.00 mm	
Single roller diameter		4.00 mm	
LVGENPLOT V 1.64.10 12-Jul-2021		Page 1 of 5	SI/FRA/F/1 Rev 0.1 March 2017

### Material properties

Yield strength for pre-cracking	510.0 MPa	Assumed from data
Tensile strength for pre-cracking	600.0 MPa	Assumed from data
Yield strength for testing	510.0 MPa	Assumed from data
Tensile strength for testing	600.0 MPa	Assumed from data
Poisson's ratio	0.3	Assumed
Young's modulus	207 GPa	Assumed

### Fatigue details

Stress ratio, R	0.100
Final force, F <sub>f</sub>	1.70 kN
Final K	20.0 MPa.m <sup>1.5</sup>
Fatigue temperature	20.0 °C
Loading span, S	40.0 mm

### Analysis details

Method of determining Load Point Displacement, q	RAM
Lower knife edge height check	N/A

**Compiled by:** Alex Pargeter

**Signed:**

Result relates only to specimen tested.

Tensile properties are not determined as part of this test and are not part of the accredited result.

Result falls within the bounds of TWI's flexible scope of accreditation.



## SENB FRACTURE TEST 33109 M05-01

### Qualification checks

		Value	Allowed
<b>ISO 12135:2016 5.4.2.4.1</b>			
Fatigue stress ratio $\leq 0.1$	<b>Pass</b>	0.1	0.1
<b>ISO 12135:2016 5.4.2.4.3</b>			
Final precracking force $\leq F_p$	<b>Pass</b>	1.7	2.25
<b>ISO 12135:2016 5.6.4</b>			
Single roller diameter	<b>Pass</b>	4	3.33 - 9.99
Double roller diameter	<b>Fail</b>	2	5.00 - 9.99
<b>ISO 12135:2016 5.7.1.1</b>			
Loading speed	<b>Fail</b>	42	29.6 - 40.4
<b>ISO 12135:2016 5.7.5</b>			
Initial K-rate between $0.2 \text{ MPa}\cdot\text{m}^{1/2}\cdot\text{s}^{-1}$ and $3.0 \text{ MPa}\cdot\text{m}^{1/2}\cdot\text{s}^{-1}$	<b>Fail</b>	539448.152	0.2 - 3
<b>ISO 12135:2016 5.8.2</b>			
ag/W check (a)	<b>Pass</b>	0.53	0.45 - 0.7
Fatigue crack shape (b)	<b>Pass</b>	0.1	0.53
Minimum fatigue length (c)	<b>Pass</b>	1.8	1.3
Fatigue crack within envelope (d)	<b>Pass</b>		
<b>ISO 12135:2016 5.8.3</b>			
Final crack shape	<b>Pass</b>	0	1



### SENB FRACTURE TEST 33109 M05-01

Test date	19/07/2021
Technician	Martin Gilder
Test machine	Zwick 750J Charpy T03c
Control mode	Displacement

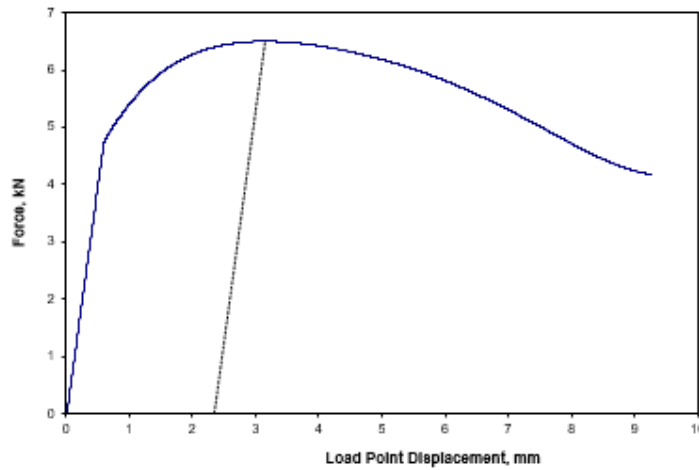
Client	PhD
Project leader	Yin Jin Janin
Investigator's signature	
Compiled by	Alex Pargeter

Selected point coordinator for plot	
	2.336
	3.142
	0.000
	6.503

SPECIMEN DETAILS	
Force, F	6.50 kN
Width, W	9.990 mm
Thickness, B	9.990 mm
Crack length, a <sub>0</sub>	5.287 mm
Loading span, S	42.0 mm
Yield strength	510.0 MPa
Young's modulus	207 GPa
Poisson's ratio	0.300
Test temperature	23.0 °C

RESULTS	
σ	N/A mm
Elastic K @ calculation point	80.2 MPa.m <sup>0.5</sup>
F <sub>max</sub> /F <sub>0</sub>	1.35
K <sub>0</sub>	59.45 MPa.m <sup>0.5</sup>
Total area under Force vs q	16.67 kNm
J <sub>y</sub> from RAM	596.42 kJ/m <sup>2</sup>
Plastic area Force vs q	14.05 kNm
Type of result	UJ <sub>0</sub>
Test standard(s)	ISO 12135:2016
Result qualified to standard(s)	NO

Slope for clip 1	0
Clip 1 offset	0
Slope for clip 2	0
Clip 2 offset	0
Y func	2.92762d
Offset from upper clip	0
F <sub>q</sub>	4.823192
Q type	1
Number of clips	1
Area under load vs C	14.050941
Number of paper in	0 1
K Unit	0
Stress unit	0
E unit	1
J unit	0
Sample type	0
Type of result	8
Type of test	1
Hide UCAS logo	0 1
Graph X axis title	Load Point Displacement, mm



**SENB FRACTURE TEST 33109 M05-01**

**Diagram of fracture face**

			1	2	3	4	5	6	7	8	9	
<b>Specimen width, W</b>		3.930										
<b>Specimen thickness, B</b>		3.930										
<b>Machined notch depth, M</b>		2.960										
<b>Machined notch width, b</b>		0.360										
<b>Surface crack length, a<sub>s1</sub></b>		4.860										
<b>Surface crack length, a<sub>s2</sub></b>		4.920										
<b>a<sub>max</sub></b>		5.415										
<b>a<sub>min</sub></b>		4.730										

**Comments**

DRAFT

Measurement Line	Fatigue crack length a <sub>f</sub> , mm	Slow stable crack extension + fatigue crack a <sub>s</sub> , mm	Slow stable crack extension including stretch zone, Δ <sub>s</sub> , mm
1	4.730	3.930	5.200
2	5.225	3.930	4.765
3	5.360	3.930	4.630
4	5.415	3.930	4.575
5	5.415	3.930	4.575
6	5.380	3.930	4.610
7	5.345	3.930	4.645
8	5.285	3.930	4.705
9	4.945	3.930	5.045
<b>Weighted Average</b>	<b>5.287</b>	<b>3.930</b>	<b>4.703</b>

**Measured by:** Martin Gilder

**Signed:**

- Charpy test certificate for Pre-cracked SENB specimen configuration using X65 steel at room temperature for  $a_0/W \approx 0.2$ .

			
<b>SENB FRACTURE TEST 33109 M05-51</b>			
Client		PhD	
Project leader		Yin Jin Janin	
		Signed:	
<b>Data source</b>			
Data logging program		testXpert II V3.6 2016	
Program used to calculate CTOD/J		LVGENPLOT V 1.64.10 12-Jul-2021	
Calculation date of CTOD/J		20 Jul 2021	
<b>Specimen details</b>			
Material		X65	
Specimen type		Subsize, SENB	
Crack plane orientation		UNKNOWN	
Type of notch tip		Fatigue	
Notch tip location		Parent material	
Specimen width		10.020 mm	
Specimen thickness		10.010 mm	
Initial crack length		2.051 mm	
Side-grooved?		NO	
Original PM 1 thickness		19.40 mm	
<b>Test details</b>			
Test standard(s)		ISO 12135:2016	
Test date		19/07/2021	
Test time		09:57:00	
Test technician		Martin Gilder	
		Signed:	
Test machine		Zwick 750J Charpy T03c	
Test environment		Air	
Test temperature		23.0 °C	
Soak time @ test temperature		0.0 minutes	
Knife edge heights		N/A mm	
Knife edge attachment spacing		N/A mm	
Initial K-rate		632723.8 MPa.m <sup>1.5</sup> /s	
Crosshead displacement rate		324974.63 mm/min	
Loading span		42.0 mm	
Double roller diameter		2.00 mm	
Single roller diameter		4.00 mm	
LVGENPLOT V 1.64.10 12-Jul-2021		Page 1 of 5	
		SI/FRA/F1 Rev0.1 March 2017	

<b>Material properties</b>			
	Yield strength for pre-cracking	510.0 MPa	Assumed from data
	Tensile strength for pre-cracking	610.0 MPa	Assumed from data
	Yield strength for testing	510.0 MPa	Assumed from data
	Tensile strength for testing	600.0 MPa	Assumed from data
	Poisson's ratio	0.3	Assumed
	Young's modulus	207 GPa	Assumed
<b>Fatigue details</b>			
	Stress ratio, R	0.100	
	Final force, F <sub>f</sub>	1.70 kN	
	Final K	8.1 MPa.m <sup>0.5</sup>	
	Fatigue temperature	20.0 °C	
	Loading span, S	40.0 mm	
<b>Analysis details</b>			
	Method of determining Load Point Displacement, q	RAM	
	Lower knife edge height check	N/A	
	<b>Compiled by:</b> Alex Pargeter	<b>Signed:</b>	
<p>Result relates only to specimen tested.</p> <p>Tensile properties are not determined as part of this test and are not part of the accredited result.</p> <p>Result falls within the bounds of TWI's flexible scope of accreditation.</p>			
LVGENPLOT v 1.64.10 12-Jul-2021		Page 2 of 5	SHFRA/F/1 Rev0.1 March 2017



## SENB FRACTURE TEST 33109 M05-51

<b>Qualification checks</b>		Value	Allowed
<b>ISO 12135:2016 5.4.2.4.1</b>	Fatigue stress ratio $\leq 0.1$	<b>Pass</b>	0.1
<b>ISO 12135:2016 5.4.2.4.3</b>	Final precracking force $\leq F_p$	<b>Pass</b>	1.7
<b>ISO 12135:2016 5.6.4</b>	Single roller diameter	<b>Pass</b>	3.34 - 10.02
	Double roller diameter	<b>Fail</b>	5.01 - 10.02
<b>ISO 12135:2016 5.7.1.1</b>	Loading span	<b>Fail</b>	39.7 - 40.5
<b>ISO 12135:2016 5.7.5</b>	Initial K-rate between $0.2 \text{ MPa}\cdot\text{m}^{1/2}\cdot\text{s}^{-1}$ and $3.0 \text{ MPa}\cdot\text{m}^{1/2}\cdot\text{s}^{-1}$	<b>Fail</b>	0.2 - 3
<b>ISO 12135:2016 5.8.2</b>	$a_0/W$ check (a)	<b>Fail</b>	0.45 - 0.7
	Fatigue crack shape (b)	<b>Pass</b>	0.21
	Minimum fatigue length (c)	<b>Fail</b>	1.3
	Fatigue crack within envelope (d)	<b>Pass</b>	
<b>ISO 12135:2016 5.8.3</b>	Final crack shape	<b>Pass</b>	0



### SENB FRACTURE TEST 33109 M05-51

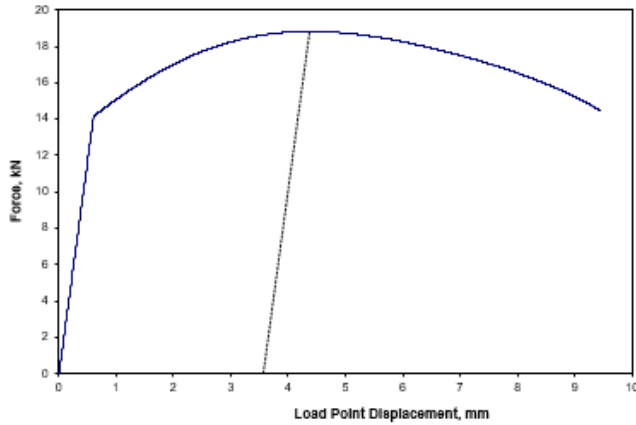
Test date	19/07/2021	Client	PKD
Technician	Martin Gilder	Project leader	Yin Jin Janin
Test machine	Zwick 750J Charpy T03c	Investigator's signature	
Control mode	Displacement	Compiled by	Alex Parqator

Selected point coordinator for plot

3.586  
4.387  
0.000  
18.818

SPECIMEN DETAILS		RESULTS	
Force, F	18.82 kN	σ	N/A mm
Width, W	10.020 mm	Elastic K @ calculation point	93.7 MPa.m <sup>1.5</sup>
Thickness, B	10.010 mm	F <sub>max</sub> /F <sub>g</sub>	1.32
Crack length, a <sub>0</sub>	2.051 mm	K <sub>0</sub>	70.84 MPa.m <sup>1.5</sup>
Loading span, S	42.0 mm	Total area under Force vs q	69.56 kNm
Yield strength	510.0 MPa	J <sub>g</sub> from RAM	1515.73 kJ/m <sup>2</sup>
Young's modulus	207 GPa	Plastic area Force vs q	62.02 kNm
Poisson's ratio	0.300	Type of result	σJ <sub>g</sub>
Test temperature	23.0 °C	Test standard(s)	ISO 12125:2016
		Result qualified test standard(s)	NO

Slope for clip 1	0
Clip 1 offset	0
Slope for clip 2	0
Clip 2 offset	0
Y <sub>func</sub>	1.189881
Offset from upper clip	0
F <sub>g</sub>	14.230879
Q type	1
Number of clips	1
Area under load vs Q	62.01723
Number of pass-ins	0
K Unit	0
Stress unit	0
E unit	1
J unit	0
Sample type	0
Type of result	8
Type of test	1
Hide UCAS logo	0
Graph X axis title	Load Point Displacement, mm



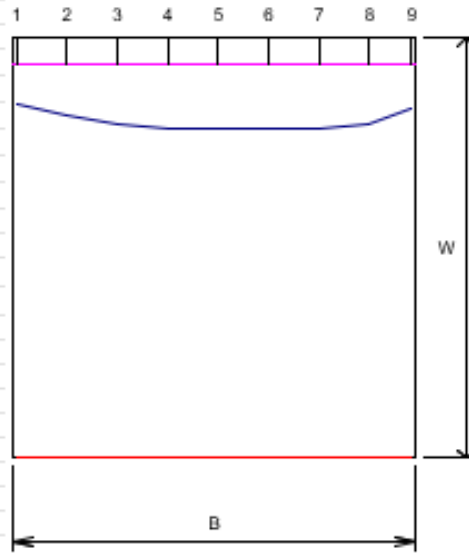
# SENB FRACTURE TEST 33109 M05-51

Diagram of fracture face

Specimen width, $W$	10.020	mm
Specimen thickness, $B$	10.010	mm
Machined notch depth, $M$	0.640	mm
Machined notch width, $h$	0.380	mm
Surface crack length, $a_{s1}$	1.480	mm
Surface crack length, $a_{s2}$	1.540	mm

$a_{max}$	2.200	mm
$a_{min}$	1.580	mm

**Comments**




Measurement Line	Fatigue crack length	Slow stable crack extension + fatigue crack	Slow stable crack extension including stretch zone, $\Delta_s$
	$a_1$ , mm	$a_2$ , mm	zone, $\Delta_s$ , mm
1	1.580	10.010	8.430
2	1.865	10.010	8.145
3	2.085	10.010	7.925
4	2.200	10.010	7.810
5	2.195	10.010	7.815
6	2.190	10.010	7.820
7	2.170	10.010	7.840
8	2.075	10.010	7.935
9	1.680	10.010	8.330
<b>Weighted Average</b>	<b>2.051</b>	<b>10.010</b>	<b>7.959</b>

Measured by Martin Gilder

Signed:

**Table A.7 Fracture test for resistance curve on the blunt notch specimen of  $a_0/W \approx 0.5$  and 0.2**



**SENB FRACTURE TEST RESULTS FOR 33109 M03**


Client : LFR		Material : X65		Compiled by : Phillip Cossey	
Investigator : Yin Jin Janin		Young's modulus : 205 GPa		Signed :	
Test standard : ISO 12135:2016		Poisson's ratio : 0.3			
Notch tip type : Spark Eroded					

Specimen number	Orientation WRT Rolling direction	Yield strength N/mm <sup>2</sup>	Specimen dimensions, mm			Final K <sub>I</sub> Pa.m <sup>1/2</sup>	Initial K-rate Pa.m <sup>1/2</sup> /s	Load kN	V <sub>q</sub> mm	V <sub>p</sub> mm	Test Temp. °C	Notch tip location	Δa mm	K <sub>Ic</sub> Pa.m <sup>1/2</sup>	K @ calc pt. Pa.m <sup>1/2</sup>	J J/m <sup>2</sup>	CTOD mm	Type of Result	Qualified to standard
			W	B	a <sub>0</sub>														
M03-1	Y-X	510.0	9.930	9.920	4.968	0.0	0.74	5.98	2.801	2.658	210	Parent material	0.350	N/A	65.3	517.2	0.513	Unloading	No
M03-2	Y-X	510.0	9.940	9.960	5.044	0.0	0.66	5.15	0.999	0.877	210	Parent material	0.106	N/A	56.9	178.8	0.178	Unloading	No
M03-3	Y-X	510.0	9.950	9.950	4.961	0.0	0.59	5.30	1.224	1.104	210	Parent material	0.188	N/A	56.9	217.1	0.217	Unloading	No
M03-4	Y-X	510.0	9.940	9.940	4.973	0.0	0.59	5.95	3.004	2.877	210	Parent material	0.455	N/A	64.4	576.2	0.569	Unloading	No
M03-5	Y-X	510.0	9.940	9.930	4.974	0.0	0.63	5.81	2.503	2.378	210	Parent material	0.358	N/A	62.9	403.5	0.400	Unloading	No
M03-6	Y-X	510.0	9.950	9.930	4.970	0.0	0.61	5.87	3.890	3.764	210	Parent material	0.631	N/A	63.4	678.8	0.686	Unloading	No
M03-51	Y-X	510.0	9.940	9.940	1.907	0.0	0.58	15.09	3.235	3.149	210	Parent material	0.839	N/A	70.4	1046.7	1.148	Unloading	No
M03-52	Y-X	510.0	9.940	9.930	1.908	0.0	0.63	15.22	1.995	1.908	210	Parent material	0.497	N/A	71.1	661.1	0.735	Unloading	No
M03-53	Y-X	510.0	9.940	9.930	1.939	0.0	0.58	13.83	1.002	0.926	210	Parent material	0.226	N/A	65.2	339.6	0.382	Unloading	No
M03-54	Y-X	510.0	9.930	9.930	2.011	0.0	0.65	14.00	3.991	3.905	210	Parent material	1.155	N/A	67.4	1182.7	1.275	Unloading	No
M03-55	Y-X	510.0	9.940	9.920	1.974	0.0	0.60	14.37	1.502	1.420	210	Parent material	0.287	N/A	68.4	493.4	0.552	Unloading	No
M03-56	Y-X	510.0	9.930	9.930	1.981	0.0	0.65	14.96	2.497	2.409	210	Parent material	0.546	N/A	71.4	789.5	0.874	Unloading	No

07 October 2020 FRAIF/25/REV2.0

**Table A.8 Fracture test for resistance curve on the pre-cracked specimen of  $a_0/W \approx 0.5$**



**SENB FRACTURE TEST RESULTS FOR 33109 M05**

Client : LRF		Material : X65		Compiled by : Jack Bradford	
Investigator : Yin Jin Janin		Young's modulus : 207 GPa		Signed :	
Test standard : ISO 12135:2016		Poisson's ratio : 0.3			
Notch tip type : Fatigue					

Specimen number	Orientation WRT Rolling direction	Yield strength N/mm <sup>2</sup>	Specimen dimensions, mm			Final K <sub>I</sub> Pa.m <sup>1/2</sup>	Initial K-rate Pa.m <sup>1/2</sup> /s	Load kN	V <sub>q</sub> mm	V <sub>p</sub> mm	Test Temp. °C	Notch tip location	Δa mm	K <sub>Ic</sub> Pa.m <sup>1/2</sup>	K @ calc pt. Pa.m <sup>1/2</sup>	J J/m <sup>2</sup>	CTOD mm	Type of Result	Qualified to standard
			W	B	a <sub>0</sub>														
32	Y-X	510.0	9.990	9.990	5.044	18.4	1.06	5.91	3.202	3.074	23.0	Parent material	0.532	N/A	64.1	614.5	0.604	Unloading	No
33	Y-X	510.0	9.990	9.990	5.189	19.3	1.11	5.49	2.202	2.065	23.0	Parent material	0.319	N/A	62.4	438.6	0.432	Unloading	No
34	Y-X	510.0	10.000	9.990	4.843	17.3	1.04	5.82	4.954	4.833	23.0	Parent material	1.216	N/A	59.1	868.9	0.840	Unloading	Yes
35	Y-X	510.0	10.000	10.000	5.363	20.4	1.03	4.57	1.003	0.870	23.0	Parent material	0.126	N/A	54.9	152.4	0.150	Unloading	No
36	Y-X	510.0	10.010	10.000	5.108	18.7	1.04	5.52	1.502	1.370	23.0	Parent material	0.169	N/A	60.7	263.8	0.262	Unloading	Yes
37	Y-X	510.0	10.000	9.990	5.113	18.8	1.05	5.62	2.700	2.561	23.0	Parent material	0.354	N/A	62.1	505.5	0.499	Unloading	Yes
38	Y-X	510.0	10.000	10.000	5.177	19.2	1.05	5.56	3.003	2.866	23.0	Parent material	0.465	N/A	62.7	583.5	0.573	Unloading	Yes
39	Y-X	510.0	10.010	10.020	5.204	19.2	1.03	5.46	3.498	3.359	23.0	Parent material	0.609	N/A	61.8	622.2	0.607	Unloading	Yes

28 September 2021 FRAIF/25/REV2.0

**Table A.9 Fracture test for resistance curve on the pre-cracked specimen of  $a_0/W \approx 0.2$**



**SENB FRACTURE TEST RESULTS FOR 33109 M05**

Client :	LRF	Material :	X85	Compiled by :	Jack Bradford
Investigator :	Yin Jin Janin	Young's modulus :	207 GPa	Signed :	
Test standard :	ISO 12135:2016	Poisson's ratio :	0.3		
Notch tip type :	Fatigue				

Specimen number	Orientation WRT Rolling direction	Yield strength N/mm <sup>2</sup>	Specimen dimensions, mm			Final K <sub>I</sub> Pa.m <sup>1/2</sup>	Initial K-rate Pa.m <sup>1/2</sup> /s	Load kN	V <sub>g</sub> mm	V <sub>p</sub> mm	Test Temp, °C	Notch tip location	Δa mm	K <sub>Ic</sub> Pa.m <sup>1/2</sup>	K @ calc pt Pa.m <sup>1/2</sup>	J J/m <sup>2</sup>	CTOD mm	Type of Result	Qualified to standard
			W	B	a <sub>0</sub>														
81	Y-X	510.0	9.990	9.990	2.134	16.6	0.82	15.09	4.261	4.172	23.0	Parent material	1.299	N/A	73.8	1448.9	1.547	Unloading	No
82	Y-X	510.0	9.990	9.990	2.436	18.0	0.87	13.59	2.002	1.913	23.0	Parent material	0.496	N/A	71.9	721.8	0.786	Unloading	No
83	Y-X	510.0	9.990	9.990	2.296	17.4	0.82	14.28	3.028	2.942	23.0	Parent material	0.701	N/A	73.0	1044.5	1.135	Unloading	No
84	Y-X	510.0	9.980	9.980	2.364	17.7	0.88	13.55	4.721	4.635	23.0	Parent material	1.568	N/A	70.5	1372.8	1.437	Unloading	No
85	Y-X	510.0	9.980	9.980	2.331	17.5	0.83	12.56	1.001	0.920	22.0	Parent material	0.178	N/A	64.8	309.5	0.343	Unloading	No
86	Y-X	510.0	9.990	10.000	2.251	17.1	0.82	13.67	1.497	1.408	23.0	Parent material	0.346	N/A	68.8	518.5	0.573	Unloading	No
87	Y-X	510.0	9.990	9.980	2.372	17.7	0.83	14.18	2.502	2.411	23.0	Parent material	0.588	N/A	73.8	883.2	0.961	Unloading	No
88	Y-X	510.0	9.980	9.990	2.132	16.6	0.77	15.09	3.502	3.424	23.0	Parent material	1.178	N/A	73.8	1197.9	1.285	Unloading	No
89	Y-X	510.0	9.990	9.990	2.287	17.3	0.81	14.55	2.700	2.613	23.0	Parent material	0.748	N/A	74.0	996.0	1.080	Unloading	No

## Published Paper

Ikenna-Uzodike, Chiamaka Emilia, Yin Jin Janin, Marius Gintalas, Wei Wen, Artūras Tadžijevs, and Pedro EJ Rivera-Diaz-del-Castillo. "An Industrial Approach to High Strain Rate Testing." *Procedia Structural Integrity* 42 (2022): 1634-1642.  
<https://doi.org/10.1016/j.prostr.2022.12.206> (Ikenna-Uzodike et al., 2022)